

Functionalized Carbon Nanohoops: Nitrogen-Doped Partial Belts, Macrocyclic Ligands, and The
Inherent Strain That Affects Their Chemical Properties

by

Tavis William Price

A dissertation accepted and approved in partial fulfillment of the
requirements for the degree of
Doctor of Philosophy
in Chemistry

Dissertation Committee:

Michael M. Haley, Chair

Ramesh Jasti, Advisor

Amanda K. Cook, Core Member

Benjamín Alemán, Institutional Representative

University of Oregon

Fall 2023

© 2023 Tavis William Price
This work is licensed under CC BY 4.0
Attribution (United States) License.



DISSERTATION ABSTRACT

Tavis William Price

Doctor of Philosophy in Chemistry

Title: Functionalized Carbon Nanohoos: Nitrogen-Doped Partial Belts, Macrocyclic Ligands, and the Inherent Strain That Affects Their Chemical Properties

Cycloparaphenylenes and related nanohoos offer a new topology to organic chemists to expand the catalogue of electro-responsive materials. Developments in their synthesis have made many functional groups and arenes accessible for insertion into the bent nanohoop backbone. It is necessary to continue expanding our synthetic toolbox for developing more nanohoos with emergent properties for use in future devices and fundamental exploration of the electronic processes in organic materials. As more diverse nanohoos are developed, it important to characterize their optical and electrochemical properties to advance the field in reliable structure-property relationships. Computational analysis of these exact structures offers a glimpse into these emergent properties to narrow down the list of possible structures. Corroboration with experimental measurements can ameliorate flaws in computational predictions by explaining the delocalized character of π -electrons in the cyclic π -system. Fundamentally, we can also gain insight into how inherent strain affects the optoelectronic properties of any arene substituted into the nanohoop backbone.

The following manuscript explains how research on carbon nanobelts has developed over the past 70 years and the nitrogen-doped structures that have come after to tease out more unique properties. The development of synthetic methods leading to pyridinium, quaternary nitrogen, partial belt structures is discussed in the chapter following the history of nanobelts. Chapter 3 presents a new nanohoop ligand using a terpyridine fragment and addresses the optoelectronic differences between the nanohoop-iridium complex and the small molecule analogue. The remaining chapters focus on the computational results of the reactivity of inherently strained molecules, their host-guest properties, and their optoelectronic properties to provide a deeper understanding and relate the structure with the intrinsic properties of strained nanohoop derivatives. These final chapters include previously published co-authored material.

CURRICULUM VITAE

NAME OF AUTHOR: Tavis William Price

GRADUATE AND UNDERGRADUATE SCHOOLS ATTENDED:

University of Oregon, Eugene, Oregon
Cal State Bakersfield, Bakersfield, California

DEGREES AWARDED:

Doctor of Philosophy, Chemistry, 2023, University of Oregon
Bachelor of Science with Honors, Chemistry, 2018, Cal State Bakersfield

AREAS OF SPECIAL INTEREST:

Organic Chemistry
Computational Chemistry
Electrochemistry
Analytical Chemistry

PROFESSIONAL EXPERIENCE:

Instructor of Record, University of Oregon, 2021

Teaching Fellow, University of Oregon, 2018-2021

GRANTS, AWARDS, AND HONORS:

Excellence in Teaching of Chemistry Award, University of Oregon, 2020

PUBLICATIONS:

Colwell, C. E.; Price, T. W.; Stauch, T.; Jasti, R. Strain Visualization for Strained Macrocycles. *Chem. Sci.* **2020**, *11* (15), 3923-3930.

Barker, J. E.; Price, T. W.; Karas, L. J.; Kishi, R.; MacMillan, S. N.; Zakharov, L. N.; Gómez-García, C. J.; Wu, J. I.; Nakano, M.; Haley, M. A Tale of Two Isomers: Enhanced Antiaromaticity/Diradical Character versus Deleterious Ring-Opening of Benzofuran-fused s-Indacenes and Dicyclopenta[*b,g*]naphthalenes. *Angew. Chem. Int. Ed.* **2021**, *60* (41), 22385-22392.

Price, T. W.; Jasti, R. Carbon Nanobelts Do the Twist. *Nat. Synth* **2022**, *1* (7), 1–2.

Fehr, J. M.; Myrthil, N.; Garrison, A. L.; Price, T. W.; Lopez, S. A.; Jasti, R. Experimental and Theoretical Elucidation of SPAAC Kinetics for Strained Alkyne-Containing Cycloparaphenylenes. *Chem. Sci.* **2022**, *14* (11), 2839-2848.

Pedersen, V. B. R.; Price, T. W.; Kofod, N.; Zakharov, L. N.; Laursen, B. W.; Jasti, R.; Nielsen, M. B. Synthesis and Properties of Fluorenone-containing Cyclo-paraphenylenes and Their Late-Stage Transformation. *Chemistry A European J* **2023**, e202303490.

ACKNOWLEDGMENTS

I would like to acknowledge the vast amount of support from my family during my undergraduate and graduate career. They have continually encouraged me to pursue my education to reach my goal of becoming a scientist. I also acknowledge the mentors throughout high school and undergraduate that instilled the idea that a higher education was feasible despite my background as a first-generation college student and guided me through the process, particularly Frank Ripepi and Prof. Dani Solano. Prof. Solano was my first research mentor who welcomed me as an undergraduate and encouraged me to apply to various programs to fund my work in the lab. The MARC-U*STAR program provided significant assistance and training during my undergraduate career to prepare me for graduate school. My summer research experience at UC, San Diego helped provide a preview of the graduate school life and prepare me for the necessary steps prior to becoming a graduate student. I thank all of the mentors, senior graduate students, and lab members during my graduate school career who offered insight, guidance, and friendship these past five years: Dr. Checkers Marshall, Dr. Curtis Colwell, Dr. Joshua Barker, Dr. Jeff Van Raden, Dr. Terri Lovell, Dr. Erik Leonhardt, Dr. Ruth Maust, Dr. Claire Otteson, Dr. James May, Dr. Julia Fehr, Tara Clayton Harrison Reid, Veronica Spaulding, Gaby Bailey, Lan Chen, Victor Salpino, and Vi Baird. Professors Mike Haley and Ramesh Jasti have provided ample guidance and support during my journey as an organic chemist. Particularly Prof. Jasti's determination to host me in his lab and provide an environment to explore a variety of research projects.

DEDICATION

Dedicated in Honor of my father, John Price Jr., who supported my goals and pushed me to pursue a higher education while being an excellent model of hard work and perseverance. I also dedicate this work to my wife Sydney who has always been a loving friend and partner, supporting me throughout many challenges.

TABLE OF CONTENTS

Chapter	Page
I. A REVIEW OF CARBON NANOBELT AND PARTIAL-BELT STRUCTURES	
I.1. Background.....	17
I.2. Cyclacenes	17
I.3. Armchair belts.....	22
I.4. Chiral belts.....	24
I.5. Möbius belt	24
I.6. Nitrogen-incorporated belts	27
I.7. Conclusion	29
I.8. Co-authored content.....	30
I.9. Bridge to Chapter 2.....	30
II. ACCESSING CATIONIC AZA-CARBON NANOTUBE FRAGMENTS VIA INTRAMOLECULAR SN2 AND PYRIDINE-DIRECTED C-H ACTIVATION	
II.1. Introduction	31
II.2. Synthesis and identification of bridged-pyridinium nano hoops	32
II.3. Optical and electrochemical characterization	35
II.4. Computational analysis of bridged-pyridinium nano hoops and their aza[n]CPP analogues	37
II.5. Conclusions	38
II.6. General experimental details.....	38
II.6.1. Computational details.....	39
II.6.2. Synthesis and characterization	39
II.7. Co-authored content.....	53
II.8. Bridge to Chapter 3.....	53
III. TERPYRIDINE-INCLUDED NANOHOOPS AS NOVEL CURVED LIGANDS	
III.1. Introduction	54
III.2. Results and discussion.....	55
III.3. X-ray crystallography	57
III.4. Optical properties of nano hoop and small molecule	57
III.5. Electrochemical properties	58
III.6. Computational results	59
III.7. Conclusion	60
III.8. General experimental details.....	61
III.8.1. Computational details.....	61

TABLE OF CONTENTS

Chapter	Page
III.8.2. Synthesis and characterization	62
III.9. Bridge to Chapter 4.....	65
IV. STRAIN VISUALIZATION FOR STRAINED MACROCYCLES	
IV.1. Introduction.....	66
IV.2. Computational methods	67
IV.3. Results and discussion	71
IV.3.1. Fragments accurately represent the molecule	71
IV.3.2. Energies are expectedly similar to previous results	72
IV.3.3. Local strain energy relates to reactivity	74
IV.4. Unique strain analysis of macrocycles from the literature.....	76
IV.5. Conclusions.....	78
IV.6. General experimental details	78
IV.6.1. Synthesis and characterization.....	79
IV.7. Co-authored content.....	79
IV.8. Bridge to Chapter 5	79
V. COMPUTATIONAL ANALYSIS OF STRAIN PROMOTED REACTIVITIES	
V.1. Background	80
V.2. Experimental and Theoretical Elucidation of SPAAC Kinetics for Strained Alkyne-Containing Cycloparaphenylenes.....	80
V.2.1. Introduction	81
V.2.2. Results and discussion	82
V.2.3. Kinetics of the SPAAC reaction with benzyl azide	83
V.2.4. StrainViz methods for alkyne-containing nano hoops	84
V.2.5. Transition state geometry and energy methods	84
V.2.6. Computational analysis of $[n+1]$ CPP reactivity.....	84
V.2.7. Conclusion to SPAAC Rates of Alkyne-Containing Cycloparaphenylenes	87
V.2.8. Experimental details (computations)	87
V.3. Pinwheel-like Curved Aromatics from the Cyclotrimerization of Strained Alkyne-Containing Cycloparaphenylenes.....	88
V.3.1. Introduction	88
V.3.2. Results and discussion	89
V.3.3. Strain calculations.....	91

TABLE OF CONTENTS

Chapter	Page
V.3.4. Conclusion to Cyclotrimerization of Alkyne-Containing Cycloparaphenylenes	92
V.3.5. Experimental details (computations)	92
V.4. Co-authored content.....	92
V.5. Bridge to Chapter 6	93
VI. PREDICTING OPTICAL AND HOST-GUEST PROPERTIES OF FUNCTIONALIZED CARBON NANOHOOPS	
VI.1. Background	94
VI.2. Synthesis of Water-Soluble Cycloparaphenylenes and Their Supramolecular Chemistry in Aqueous Systems	95
VI.2.1. Results and discussion	97
VI.2.2. Computational results	100
VI.2.3. Conclusion to host-guest properties	102
VI.2.4. Experimental details (computational)	102
VI.3. Synthesis and Properties of Fluorenone-containing Cycloparaphenylenes and Their Late-Stage Transformations	103
VI.3.1. Results and discussion	105
VI.3.2. Experimental and theoretical absorption and fluorescence results	105
VI.3.3. Experimental and theoretical electrochemical results	108
VI.3.4. Conclusion to optoelectronic properties	110
VI.3.4. Experimental details (computational)	111
VI.4. Co-authored content.....	111
VI.5. Bridge to Conclusion	111
VII. CONCLUDING REMARKS	112
REFERENCES CITED	113

LIST OF FIGURES

Figure	Page
I.1. Structure of an [n]cyclacene mapping onto its corresponding zig-zag CNT. Representative resonance structures of an [n]cyclacene where n is an even number	18
I.2. Summarized route to converting C60 to a functionalized [10]cyclophenacene reported by Nakamura <i>et al</i>	23
I.3. a) two different topologies can be created by closing a two-dimensional strip. b) Iterative Wittig reactions and Yamamoto couplings are used to synthesize a (25,25) MCNB	26
I.4. N-doped carbon nanobelt structures reported in the literature	27
II.1. Nitrogen-doped belt structures and partial belts. a) [6.8N ₂] ₃ Cyclacene b) N ₃ -methylene-bridged[6]CPP c) [6.7N](6,6)CNB d) bridged-pyridinium[n]CPPs. (Ar = p-methoxyphenyl)	31
II.2. Single crystal x-ray diffraction results for molecules II.B1 (a) and II.B2 (b) with the space-filling packing structure on the left and the ORTEP drawing on the right (solvent molecules omitted for clarity)	34
II.3. ¹ HNMR spectrum of aza[8]CPP and II.C in CD ₃ CN with representative shifts highlighted.	35
II.4. Left spectra are UV-vis absorbance profiles of A1 and B1 in dichloromethane overlapped with A2 and B2 in acetonitrile (inlay shown as a magnified region for A2 and B2). Right spectra are UV-vis absorbance profiles of C and D in acetonitrile and absorbance and emission profiles of aza[8]CPP and aza[10]CPP in dichloromethane	36
II.5. Cyclic voltammograms of II.D (top left), II.C (bottom left), II.B2 (top right), and II.A2 (bottom right) in acetonitrile for II.D , II.C , and II.A2 or acetonitrile/dichloromethane for II.B2 ; supporting electrolyte: 0.2 M Bu ₄ NPF ₆ , scan rate: 0.2 V/s. All potentials are referenced to the Fc/Fc ⁺ redox couple	37
II.6. Calculated frontier molecular orbital energies and their respective occupancy for each bridged-pyridinium nanohoop (II.D , II.C , II.A2 , and II.B2) and their precursor aza[n]CPP (aza[10]CPP, aza[8]CPP, II.A1 , and II.B1) at the B3LYP/6-31G(d) level of theory (isosurface value set to 0.03)	38
III.1. Summary of established cycloparaphenylene ligand developed by our lab, presenting terpyridine[n]CPPs (tpy[n]CPPs) as a new ligand topology	54
III.2. ¹ H NMR in d ₆ -acetone and ESI-MS of complex III.5 and III.6 from 10 ppm solutions in acetone	56
III.3. Single crystal x-ray diffraction results of tpy[10]CPP III.4 shown in ORTEP drawings, single molecule on the left and packing structure on the right	57

LIST OF FIGURES

Figure	Page
III.4. Absorbance and fluorescence spectra of tpy[10]CPP and 2,2',6',2''-terpyridine in dichloromethane. Absorbance profile presented as molar absorptivity ($10^5 \text{ M}^{-1} \text{ cm}^{-1}$) and emission presented in relative intensity at identical concentrations. Inlays show each molecule in dichloromethane	57
III.5. Absorbance and emission profiles of III.5 and III.6 in acetonitrile. Absorbance profiles shown in molar absorptivity ($10^5 \text{ M}^{-1} \text{ cm}^{-1}$) and emission profiles in relative intensity at identical concentrations. Inlays show solutions of both complexes in acetonitrile at room temperature and $-196 \text{ }^\circ\text{C}$	58
III.6. Cyclic voltammograms of 2,2':6',2''-terpyridine (top left), III.6 (top right), III.4 (bottom left), III.5 (bottom right) in acetonitrile; supporting electrolyte: 0.2 M Bu_4NPF_6 , scan rate: 0.2 V/s. All potentials are referenced to the Fc/Fc^+ redox couple.....	59
III.7. TD-DFT calculations of tpy[10]CPP , III.5 , III.6 , and 2,2':6',2''-terpyridine (tpy) showing the HOMO-LUMO gap and individual energies. The predicted wavelength of the lowest transition is provided above the predicted oscillator strength. Images of the molecular orbitals are shown for each molecule (isosurface value of 0.02).....	60
IV.1. a) Strain energy is calculated by comparing the strained molecule to an unstrained polymer or homodesmotic reaction product resulting in a single strain energy for the entire molecule. b) StrainViz determines strain energy local to every coordinate	67
IV.2. a) This ideal experiment begins with the strained macrocycle and ends with an infinite polymer where the strain has been released. b) By removing part of the molecule, the beginning and end geometries can now be connected by a strain releasing trajectory. This allows the local trajectory of each atom to be determined	68
IV.3. Workflow for strain analysis. The coordinates in each molecule fragment relax to release strain energy that is quantified per coordinate (r : bond length, θ : angle, ϕ : torsional angle)	69
IV.4. Fragments of [8]CPP having 2-7 phenylenes (highlighted in pink) were used in the strain analysis. Fragments retaining 50% or more of the molecule all determined strain energies within 3% of each other. All calculations were performed at the B3LYP/6-31G(d) level of theory unless otherwise noted	71
IV.5. Literature examples of strain energy determinations compared to StrainViz analysis. a) Cycloparaphenylene strain determined by homodesmotic reactions. b) carbon nanobelt strain energy extrapolated from increasing belt sizes. c) [2.2]paracyclophane strain and Bodwell's more strained analogue determined by isodesmotic reaction B3LYP/6-31G(d,p) and M06-2X/Def2TZVP respectively.....	73

LIST OF FIGURES

Figure	Page
IV.6. Torsional angles and total strain of [6]CPP and m[6]CPP . Changing connectivity from <i>para</i> to <i>meta</i> decreases total strain but increases local strain energy.....	74
IV.7. Strain release during bromination of [6]CPP . First bromination activates molecule to be more reactive in the second step	75
IV.8. Möbius molecules have more strain due to an internal twist when compared to a non-Möbius belt. a)The Möbius molecule synthesized in the Tanaka group is more strained than the non-Möbius despite being a larger size. b)In a symmetric Möbius molecule, strain is centered at the twist entry point.....	76
IV.9. Strain energy present in Yamago's nanoball. More strain at the ball corners relative to the edge	77
IV.10. Strain energy in copper-free click reagents. Trans-cyclooctene is more strained than cyclooctyne but has similar strain distribution. Increasing rigidity by addition of a cyclopropyl fusion increases strain energy and shifts it to the reactive site	78
V.1. (a) Examples of strained alkynes developed for copper-free click chemistry. (b) Strained alkynes in the field of carbon nanomaterials. (c) New strained alkyne-containing $[n+1]$ CPPs described in this work	81
V.2. SPAAC second-order rate constants for $[n+1]$ CPPs. These constants were measured <i>via</i> quantitative ¹ H NMR in deuterated DMSO	83
V.3. Strain analysis of the $[n+1]$ CPPs described in this study with the StrainViz script	85
V.4. (a) Transition state structures for each SPAAC reaction with benzyl azide; distances shown in Angstroms (Å). (b) Generalization of the distortion-interaction model and $\Delta E^{\ddagger}_{\text{activation}}$ of each SPAAC reaction broken down into its $\Delta E^{\ddagger}_{\text{distortion}}$ and $\Delta E^{\ddagger}_{\text{interaction}}$ components	86
V.5. Absorbance (solid) and emission (dashed) profiles of fluor[9+1]CPP (yellow) and fluor[9+1] trimer (blue) on the left in dichloromethane. Absorbance (solid) and emission (dashed) profile in dichloromethane (yellow) and dimethylsulfoxide (black)	90
V.6. Calculated orbital energies for fluor[9+1]CPP and fluor[9+1] trimer with the orbital geometries labelled and shown adjacent to each energy level (B3LYP/6-31G(d) level of theory, isosurface of 0.03).....	90

LIST OF FIGURES

Figure	Page
V.7. StrainViz analysis of $[n+1]$ CPPs and their respective trimers at the B3LYP/6-31G(d) level of theory. Table of total strain for each shown below respective structures. Relative strain scale (in kcal/mol) shown on the left	91
VI.1. Typical synthetic route to functionalized cycloparaphenylenes with a variable pyridine in replacement of a phenylene	94
VI.2. Established macrocyclic hosts like cyclodextrins (left) and cucurbiturils (center) have found utility in aqueous supramolecular chemistry. In contrast CPPs (right), while interesting in their own right, have found limited use in this area due to their functionally simple structure .	96
VI.3. DFT models of 4* and 4* \rightarrow C ₆₀ in water highlighting the deformation of the larger nanohoop to optimize vdW interactions between host and guest	101
VI.4. DFT models of 2* and 2* \rightarrow C ₆₀ in water illustrating the tight binding of the complementary π -surfaces to optimize vdW interactions between host and guest.....	101
VI.5. Geometries of the ring-in-ring complexes optimized computationally using Gaussian 09 at the ω B97X-D/6-31G(d,p) level of theory and the self-consistent reaction field using the default Polarizable Continuum Model method with the dielectric constant for water	103
VI.6. Top: $[n]$ Cycloparaphenylene ($[n]$ CPP) and the electron acceptors selected for this study. Bottom, left: Known donor-acceptor conjugated nanohoops. Bottom, right: New structures described herein. Number in brackets corresponds to the number of aromatic rings in the nanohoop. CPP stands for cycloparaphenylene (phenylene in this case meaning aromatic ring, e.g. pyridinium, benzothiadiazole), CP just stands for cyclophenylene as not all rings in the structures are <i>para</i> -substituted (phenylene in this case meaning aromatic ring, e.g. thiophene)	104
VI.7. FMOs of [9]CPP , F[9]CPP , and FM[9]CPP calculated at the B3LYP/def2TZVP level of theory	106
VI.8. UV-Vis absorption spectra of compounds F[9]CPP (blue), F[11]CPP (green), FM[9]CPP (red), and FM[11]CPP (purple) in dichloromethane. Insert: Zoom of most red-shifted absorption bands	107
VI.9. Emission spectra of compound F[9]CPP in toluene (green), heptane (5% CH ₂ Cl ₂) (pink), chlorobenzene (purple), DMSO (red) and CH ₂ Cl ₂ (orange). All compounds were excited at 450 nm	107
VI.10. Cyclic voltammograms of compounds F[9]CPP (blue), F[11]CPP (green), FM[9]CPP (red), and FM[11]CPP (purple) in CH ₂ Cl ₂ at 0.5 mM; supporting electrolyte: 0.1 M Bu ₄ NPF ₆ , scan rate: 0.1 V/s. All potentials are depicted against the Fc/Fc ⁺ redox couple	108

LIST OF FIGURES

Figure	Page
VI.11. Calculated HOMO (orange) and LUMO (blue) energies for compounds F , FM , F[9]CPP , FM[9]CPP and [9]CPP . Arrows indicate contributing orbitals to the HOMO and LUMO energies of the fused compounds F[9]CPP and FM[9]CPP . Orbital energies were calculated at the B3LYP/def2tzvp level of theory. Similar observations are observed for the compounds F[11]CPP , FM[11]CPP , and [11]CPP (see Table VI.5)	109

LIST OF TABLES

Table	Page
II.1. Summary of optical and electrochemical data for each bridged-pyridinium nano hoop in acetonitrile. E_{opt} was calculated from the band edge wavelength (λ_{edge}), which is determined by the steepest slope of the lowest energy transition. The molar absorptivity (ϵ_{max}) was determined from the most intense absorption event	36
IV.1. Reported strain energies of [12]CPP	72
V.1. Summary of strain values (in kcal mol ⁻¹) determined by StrainViz for each $[n+1]$ CPP	85
V.2. Activation free energies for the $[n+1]$ CPPs in this study; reported in kcal mol ⁻¹	96
VI.1. Summary of titration results with [10]CPP, 1, and 2* with fullerene and nano hoop guests in varied solvents with associated binding affinities	98
VI.2. Summary of titration results with [12]CPP and 4* with fullerene and nano hoop guests in water and their associated binding affinity.....	100
VI.3. Summary of interaction energies for the predicted host-guest complexes and their distorted diameters as illustrated in Figures VI.3 and VI.4 in Angstroms.....	101
VI.4. Electrochemical data from differential pulse voltammetry of compounds F, FM, F[9]CPP, F[11]CPP, FM[9]CPP, M[11]CPP, [9]CPP and [11]CPP in CH ₂ Cl ₂ ; potentials in volts vs Fc/Fc ⁺ ; concentrations of 0.5 mM; supporting electrolyte: 0.1 M Bu ₄ NPF ₆ . [a] Irreversible redox event. [b] Not perfectly reversible. [c] Ref. 286, recorded in 1,2-dichloroethane, V <i>versus</i> Fc/Fc ⁺ , supporting electrolyte: 0.1 m Bu ₄ NPF ₆	109
VI.5. Experimental and computational (comp) values. [a] From Table 1. [b] Energy of shoulder from longest-wavelength absorption.....	110

LIST OF SCHEMES

Scheme	Page
I.1. Attempted synthesis of [12]cyclacene by Stoddart <i>et al.</i> with representative structure named when necessary	19
I.2. Itami's attempted synthesis of [12]benzo[12]cyclacene via benzannulation of an arylethynyl macrocycle.....	20
I.3. Peña <i>et al.</i> 's attempted synthesis of [10]cyclacene by reduction of a tetraepoxy-macrocycle on a Cu(111) surface by scanning-tunneling-microscopy (STM)	21
I.4. Synthetic routes to benzo-fused [n]cyclacenes reported by Wang, Itami, and Chi.....	22
I.5. Final step in the synthesis of armchair CNBs from Itami's group, "n denotes the size of the belt for (n,n) CNB).....	23
I.6. Synthesis of armchair (12,12) CNB[42] (top) and chiral (18,12) CNB[42] (bottom) from the Miao group	24
I.7. Synthesis of [6.8N ₂] _n cyclacenes reported by the Wu group. The aryl groups used are specified in the inlay box	28
I.8. Synthesis of a non-alternant N-doped [6]CNB, N ₃ -CH ₂ -bridged[6]CPP, from Chen <i>et al.</i> starting from a functionalized carbazole	29
I.9. Final step of N-doped CNB, [6.7N](6,6)CNB, from Itami <i>et al.</i> accomplished via Buchwald-Hartwig coupling	29
II.1. Synthetic routes to bp[6]CPP II.A2 , dibp[6]CPP II.B2 , isoq[8]CPP II.C , and isoq[10]CPP II.D	33
III.1. Synthesis of tpy[10]CPP III.4 from coupling partners reported in the literature	55
III.2. Synthesis of [Ir(tpy)(ppy)Cl][PF ₆] III.6 and [Ir(tpy[10]CPP)(ppy)Cl][PF ₆] III.5 using the same reaction conditions reported in the literature	56
IV.1. Bromination of m[6]CPP	75
V.1. Strain-promoted azide-alkyne cycloaddition reactions between the [n+1]CPPs described in this study and benzyl azide, a model compound. Yields were determined <i>in-situ via</i> quantitative ¹ H NMR in comparison to an internal standard, dimethyl sulfone	83
V.2. Synthesis of [11+1] trimer , [9+1] trimer , fluor[9+1] trimer , meta-fluor[9+1] trimer from their respective CPP	73
VI.1. Conversion of tetra-ester[10]CPP VI.1 to tetra-carboxylate[10]CPP VI.2 and hexa-ester[12]CPP VI.3 to hexa-carboxylate[12]CPP VI.4 with inlays of their emissive properties in water ..	98
VI.2. Synthesis of FM[n]CPPs (n = 9, 11) by Knoevenagel condensations	105

CHAPTER I

A REVIEW OF CARBON NANOBELT AND PARTIAL-BELT STRUCTURES

I.1. Background

Due to carbon's valence the number of possible structures is innumerable. As a result, a variety of structures have caught the interest of materials chemists because of their potential as electronically active building blocks.¹⁻³ Combining electron-rich and electron-poor units to create organic semi-conductors, molecular magnets, light-emitting diodes, and photoresponsive materials drives the ever-expanding research into novel carbon nanostructures.^{1,3-10} Theory tends to lead experimental interest, so a variety of structures have been predicted decades before experimentalists could catch up.^{11,12} This can guide discoveries in synthetic methodology and then material development towards unique carbon structures.

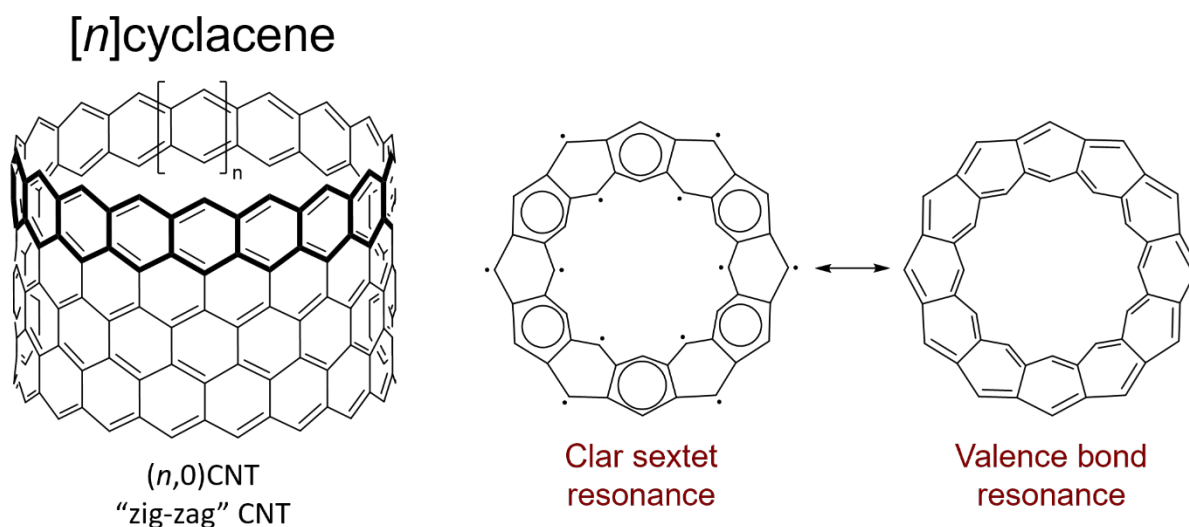
The interest in exploring carbon nanostructures began with the development of carbon-rich small molecules. Cyclophanes, cyclic structures containing at least one aromatic sub-units have maintained significant interest as molecules that impart strain on traditionally planar aromatic molecules.^{11,13-15} As the barrier to more and more strained structures has been surpassed, the goal post has moved to larger exceedingly ambitious structures. This was further motivated by the discovery of curved carbon allotropes. The field of carbon nanoscience exploded with the discovery and continued study of fullerenes and carbon nanotubes (CNTs).¹⁶⁻¹⁸ Because of their useful electronic and thermal properties, chemists have developed the field to functionalize and deconstruct carbon nanomaterials to make more useful topologies for future devices.¹⁹ This has ultimately coincided with cyclophane chemistry as sections of fullerenes and carbon nanotubes resemble such predicted structures hypothesized by Heilbronner and Vögtle.^{11,20} Cycloparaphenylenes (CPPs), the smallest section of an armchair CNT, are prime examples of the emerging utility of carbon nanochemistry as many labs are focused on the functionalization of these inherently strained nanohoops to explore and take advantage of their unique optoelectronic properties.²¹⁻²⁵ Designing interesting or elegant structures and studying their properties has guided organic materials chemists to this day.

Presented herein is the development of carbon nanobelt (CNB) and belt-like molecules, their synthesis, and their properties. This starts with the attempted syntheses of cyclacenes by Stoddart which culminates in successful syntheses of benzo-fused cyclacenes by multiple groups. Second, the theory of armchair CNBs and the syntheses by Itami. Third, chiral CNBs synthesized by Miao which completes the list of molecular analogues of CNTs. Fourth, a Möbius belt that does not map onto any known CNT or represent an intermediate to other CNBs. Fifth, incorporation of heteroatoms into the backbone. Overall, the focus of this review will be on the development of inherently strained aromatic macrocycles.

I.2. Cyclacenes

The first report of cyclacenes as an interesting synthetic target was made by Edgar Heilbronner in 1954, who predicted the eigenvalues and possible molecular orbitals of [12]cyclacene.²⁰ Cyclacenes can be defined as cross-sections of zig-zag CNTs or simply as cyclic analogues of fused polyacenes. The "*n*" in [*n*]cyclacene denotes the number of rings composing the macrocycle, typically six-membered rings but

non-alternant systems exist with five, seven, or eight membered rings that also use the “cyclacene” name. Belt[n]arene is also used as an unambiguous name for discrete “zig-zag” CNT cross sections; however, “[n]cyclacene” and “belt[n]arene” have been used interchangeably in the literature.²⁶ Predictions of the electronic properties were categorized as either valence bond dominant, Clar sextet dominant, or in resonance between the two.^{27–29} It follows that due to the inherent strain of these macrocycles, the valence bond dominant structure could persist for smaller [n]cyclacenes to mitigate the bending of aromatic units in the Clar sextet dominant structure. As seen with large flat acenes, the bonding structure maximizes the number of aromatic units containing six π -electrons.²⁸ In the case of [n]cyclacenes, this would result in

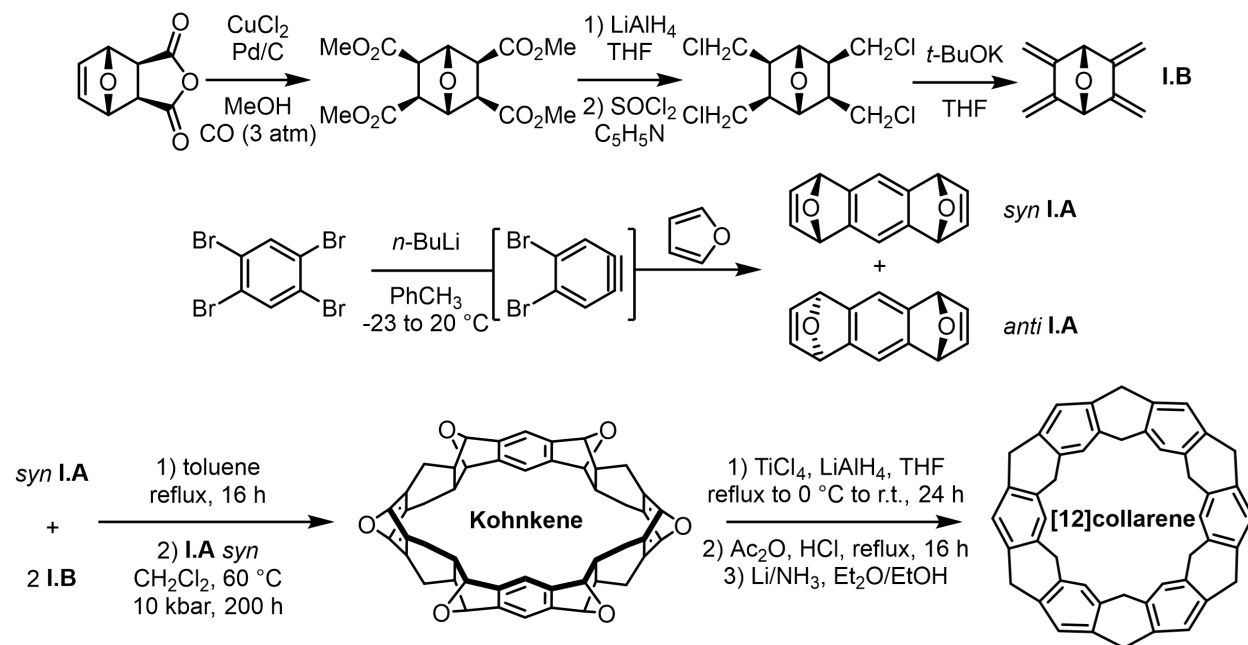


multiradical species as shown in Figure I.1, making them progressively difficult to synthesize.

Figure I.1. Structure of an [n]cyclacene mapping onto its corresponding zig-zag CNT. Representative resonance structures of an [n]cyclacene where n is an even number.

Initial productive attempts at synthesizing [n]cyclacenes relied on multiple stereoselective Diels-Alder (DA) reactions. Oxo-bridged building blocks help direct subsequent DA reactions to favor endotopic products.^{30–32} Stoddart utilized iterative DA reactions to make macrocycles that are arranged to aromatize into the desired [n]cyclacene thanks to the additive curvature of each oxo-bridged subunits. Although the thermodynamic driving force for aromatizing individual six-membered ring is large, the inherent strain of aromatic belts is prohibitively larger for most sizes.^{26,33–36} For example, the [12]cyclacene that was attempted by Stoddart has a predicted strain energy around 110 kcal/mol—similar to [5]cycloparaphenylene, 116 kcal/mol, which is not stable under ambient conditions.^{26,37,38} The synthetic route shown in Scheme I.1 starts with two subsequent non-stereoselective DA reactions between *in-situ* generated 4,5-dibromobenzynes and two equivalences of furan to make an equivalent amount of *syn* and *anti* **I.A** as the major dienophile building block.^{31,32,34} Diene **I.B** was synthesized by step-wise carboxymethylation, reduction, chlorination, and finally β -elimination.^{30–32,34} Refluxing **I.A** and **I.B** in toluene provided a larger diene **I.C** with stereoelectronic selectivity due to the repulsion by the oxo-bridges.³² The

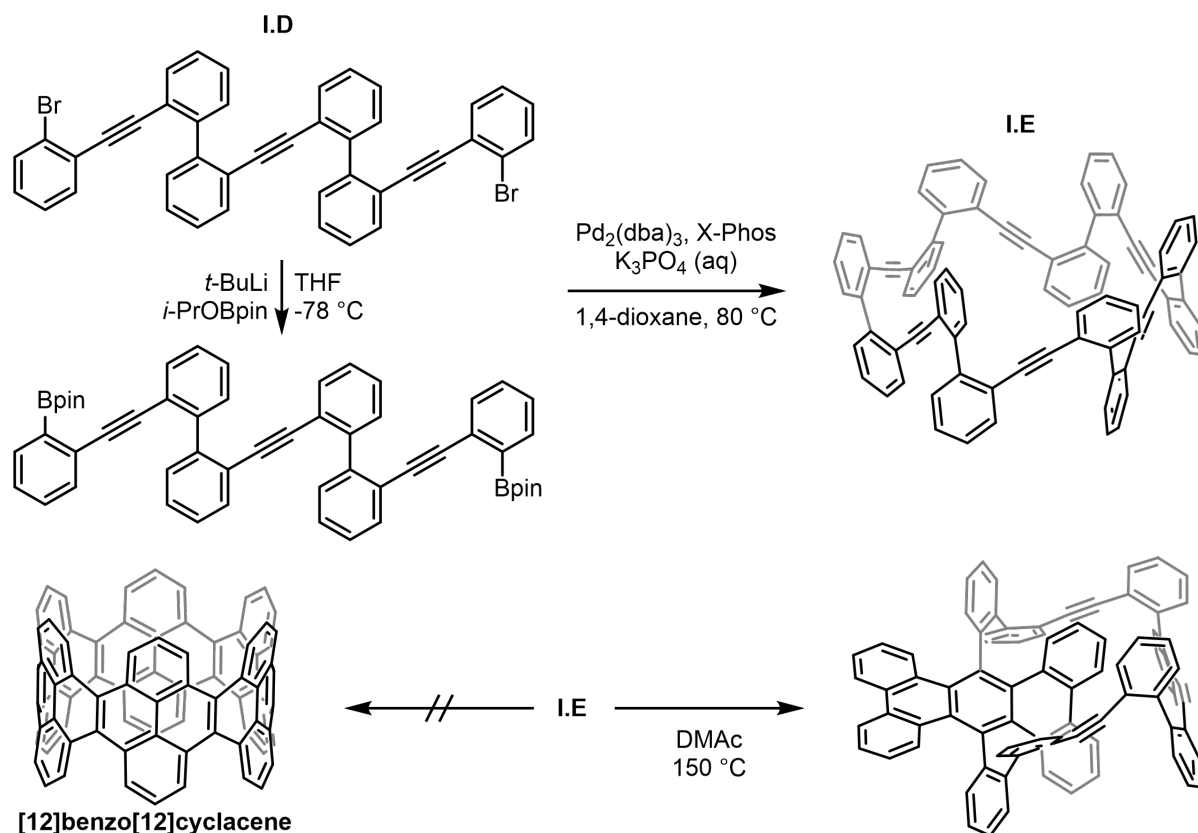
addition of another equivalent of **I.A** under high pressures resulted in a macrocycle with twelve six-membered rings “Kohnkene” poised to be reduced to the final [12]cyclacene.^{31,34} Iterative reduction only afforded the [12]collarene which was unable to fully aromatize to [12]cyclacene.



Scheme I.1. Attempted synthesis of [12]cyclacene by Stoddart *et al.* with representative structure named when necessary.

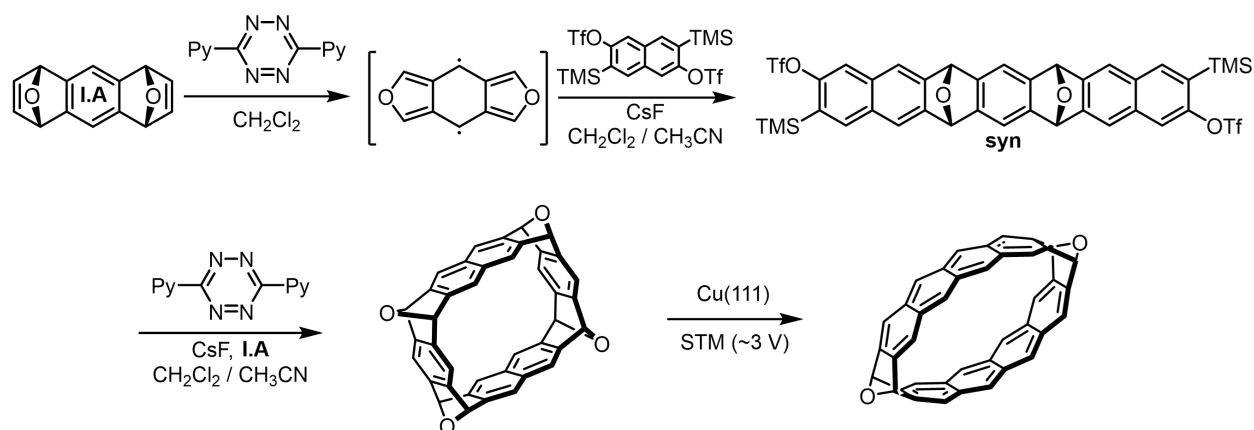
Modern synthetic methodologies have transformed the possible transformations that can impart the necessary strain required for fully aromatized [*n*]cyclacenes. The majority of reported methods have heavily relied on DA reactions via aryne intermediates. Effective separation techniques are required because the reactions are non-stereoselective. Outlined are the notable reports which led to successes in partially aromatized and fully aromatized [*n*]cyclacene derivatives.

The first attempt by the Itami lab relied on a 12-fold annulation strategy to convert an aryl-ethynyl macrocycle into [12]benzo[12]cyclacene, where benzo-fusions localize the bonds to stabilize the resulting nanobelt. This began with an electrophilic borylation then double Suzuki-Miyaura cross-coupling reaction to obtain dibromide **I.D** which is then borylated and reacted with another equivalent of **I.D** to make the aryl-ethynyl macrocycle **I.E**.³⁹ Heating to 150 °C in dimethylacetamide resulted in a product of cycloadditions and electrocyclic ring-opening reactions instead of the desired [12]benzo[12]cyclacene (Scheme I.2).³⁹



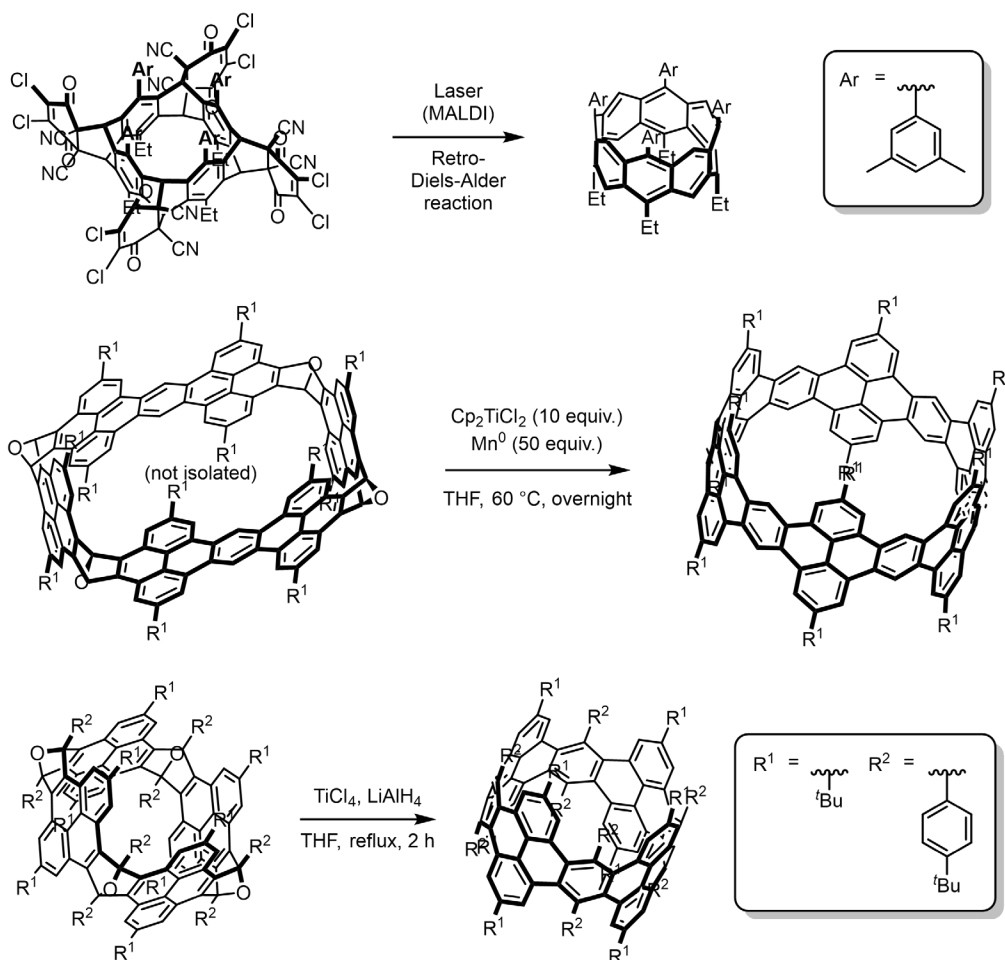
Scheme I.2. Itami's attempted synthesis of [12]benzo[12]cyclacene via benzannulation of an arylethynyl macrocycle.³⁹

Revisiting DA reaction routes, Profs. Dolores Pérez and Diego Peña attempted to reduce an oxo-bridged [10]cyclacene derivative on a Cu(111) surface and visualized only partial deoxygenation.⁴⁰ The macrocycles were made from DA reactions between aryne and iso-furan functionalized arenes, but the tetraepoxy[10]cyclacene was the only macrocycle that could be visualized before and after deoxygenation attempts. Unlike Stoddart's synthetic routes, no stereoselectivity is present in these reactions; however, the only productive pathway is with the *syn*-adduct so the products did not need to be resolved prior to subsequent steps. Synthesis proceeds with the identical dienophile **I.A** that Stoddart used via a tetrazine-mediated retro-DA reaction followed by an *in-situ* two-fold DA-reaction with dinaphthylene generated by reaction of 3,7-bis(trimethylsilyl)naphthalene-2,6-trifluoromethylsulfonate with cesium fluoride (Scheme I.3).⁴⁰ The resulting *syn*-addition adduct was reacted with another equivalent of dienophile **I.A** in the same reaction conditions to generate the tetraepoxy[10]cyclacene. Deoxygenation of Cu(111) using STM tip-induced deoxygenation successfully removed two oxygen atoms in two different orientations, but no fully deoxygenated structures were visualized by AFM or STM.⁴⁰ Synthetically, these examples set the bar closer to realizing a fully aromatic [*n*]cyclacene but required a stronger thermodynamic driving force or strained intermediate to facilitate the final aromatization reaction.



Scheme I.3. Peña *et al.*'s attempted synthesis of [10]cyclacene by reduction of a tetraepoxy-macrocycle on a Cu(111) surface by scanning-tunneling-microscopy (STM).

Back-to-back reports in the literature soon followed with the first successful synthesis of a [n]cyclacene derivative accomplished by the lab of Prof. Mei-Xiang Wang at Tsinghua University. The synthetic route began with an alkene functionalized pillar[4]arene that was converted to the aldehyde functionalized pillar[4]arene.⁴¹ Addition of an aryl-Grignard followed by Friedel-Crafts alkylation produced a collar[8]arene which underwent a DA reaction with DDQ then laser-mediated retro-DA reaction to make the substituted [8]cyclacene.⁴¹ The final product was confirmed by high-resolution mass spectrometry along with partially aromatized products. This result was foundational to future works since it set the precedent that [n]cyclacenes are synthetically accessible under the appropriate conditions. Although this is the only example of a true [n]cyclacene in the literature, other groups have reported successful syntheses of benzo[n]cyclacenes in measurable quantities. Other methods reported in literature follow the DA approach of using functionalized arynes and isofurans to build benzo-fused intermediates that are finally reduced to the benzo[n]cyclacenes. Chi and Itami's group simultaneously reported the first examples of this pathway by utilizing functionalized pyrene units which combine one at a time for Itami's route and symmetrically in the case of Chi's route.^{42,43} Each of these routes are summarized in Scheme I.4 and illustrate the power of the DA reaction to make a variety of [n]cyclacene derivatives. The Miao group soon after reported the synthesis of multiple benzo[n]cyclacenes precursors via the same synthetic methodology.⁴⁴ Miao's [8]benzo[20]cyclacene precursor was successfully aromatized; however, due to the extended acene fragments within the belt it was prone to oxidation in air.⁴⁴ This reflects the barrier to fully aromatic [n]cyclacenes with minimal to no benzo-fusions. As the length of acene fragments decrease, the favorable electronic properties disappear and smaller [n]cyclacene derivatives increase the inherent strain, reducing stability of individual acene fragments.



Scheme I.4. Synthetic routes to benzo-fused $[n]$ cyclacenes reported by Wang, Itami, and Chi.^{41–43}

So far, there are multiple synthetic routes to $[n]$ cyclacene derivatives reported in the literature. The variety of methods and the continued development of new methods offer materials and organic chemists the appropriate tools to expand carbon nanoscience. Success by the groups presented in this chapter could converge to a true $[n]$ cyclacene for studying their intrinsic optoelectronic properties. A significant aspect of $[n]$ cyclacenes that requires experimental investigation is the bond order of the total belt, bond length alternations of the structure, and practical applications as unique semiconducting molecules.

I.3. Armchair belts

Motivations to synthesize armchair belts began with Vögtle and led to many attempts to make the first CPP by desulfurization methods but none were successful. Nakamura took an alternative approach by starting with a larger structure, fullerenes, then dismantled the “top” and “bottom” to make a functionalized [10]cyclophenacene⁴⁵ and Gan used the same methodology to synthesize a Vögtle [10]belt⁴⁶ from C_{60} and C_{70} , respectively. Although the structures they reported are not “belts” because they are closed on both ends, the dominate structural motif maps onto a (5,5) CNB. Iterative methylation then cyanation afforded a partially dearomatized C_{60} that was phenylated and the cyano group was removed to obtain the [10]cyclophenacene derivative (see Figure I.2).

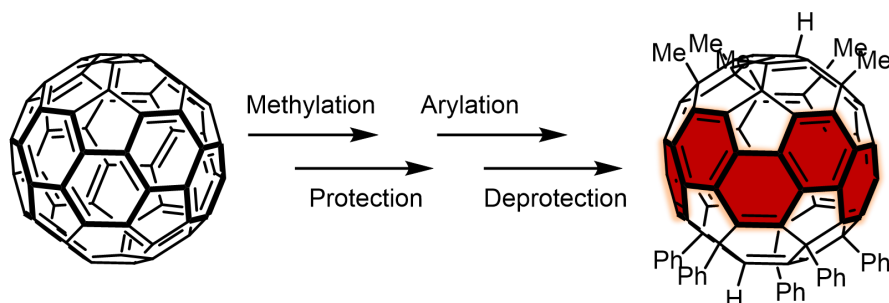
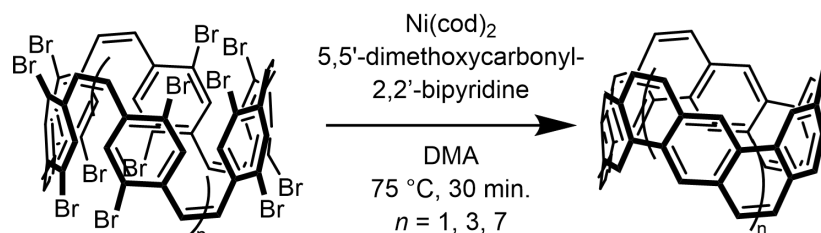


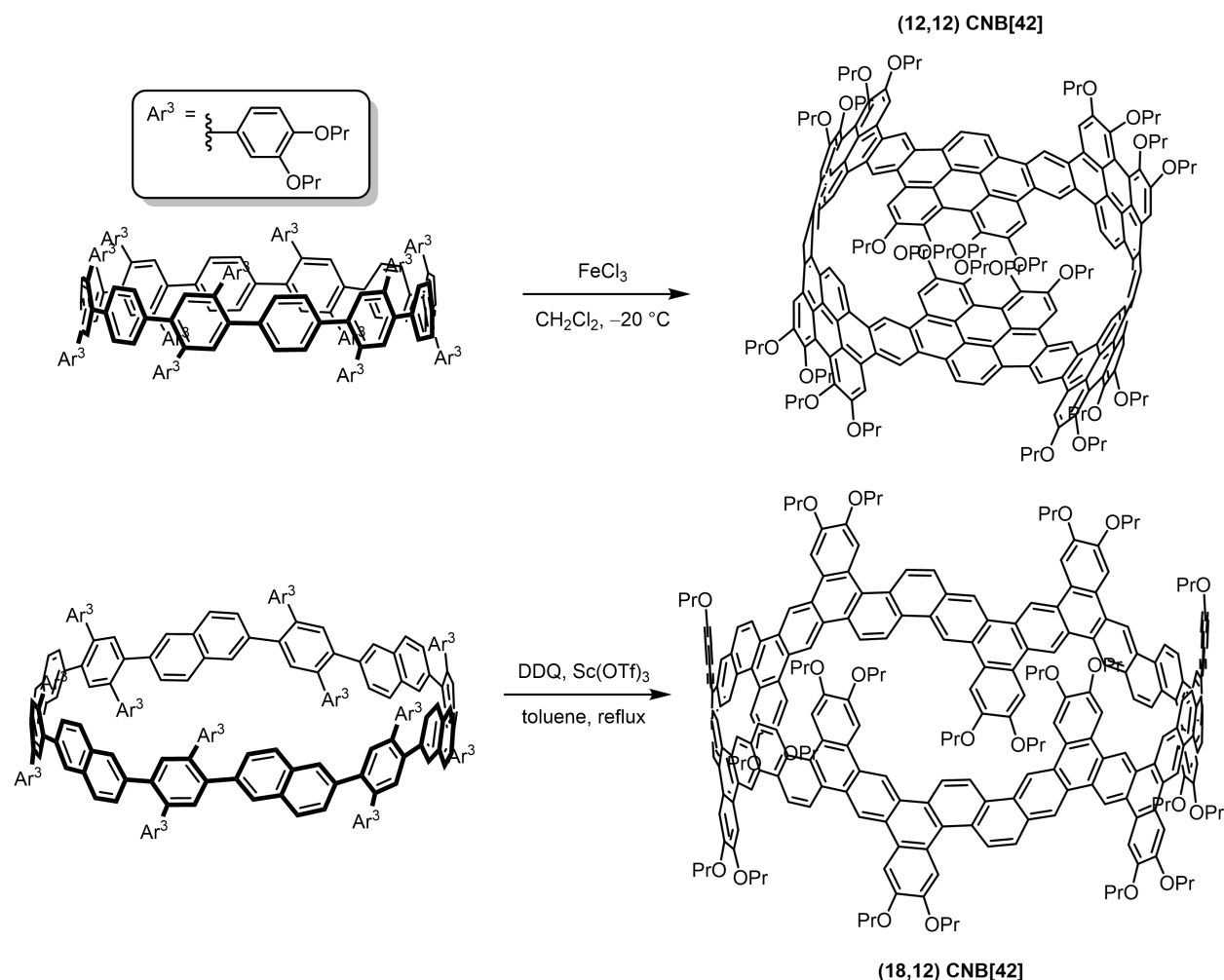
Figure I.2. Summarized route to converting C_{60} to a functionalized [10]cyclophenacene reported by Nakamura *et al.*⁴⁵

After sufficient time and development, the Itami group determined a suitable reaction pathway that could overcome the inherent strain of building up a curved nanobelt. Macrocycles were first constructed from iterative Wittig reactions of appropriately sized vinylbenzene oligomers.^{47,48} A final Wittig reaction of an adequately sized triphenylphosphonium-aldehyde makes a highly-functional vinylbenzene macrocycle which is subjected to a multi-fold reductive coupling to produce the desired armchair CNB. Itami's route has shown to be robust to make CNBs of various sizes, even highly strained derivatives like (6,6) CNB (Scheme I.5). The resulting structures have size-dependent properties like CPPs with emergent properties from the rigidified backbone.⁴⁸ CNBs discussed are highly fluorescent with the (6,6) CNB presented broadly emitting between 550 and 800 nm in dichloromethane.⁴⁷ Although the yields to the CNB are not high, the methods are more convergent than incrementally building in functionality to convert to the belt. The conversion from bromines to carbon-carbon bonds is robust using a multi-fold Yamamoto coupling approach and has low steric repulsion compared to olefin metathesis routes.⁴⁹



Scheme I.5. Final step in the synthesis of armchair CNBs from Itami's group, " n denotes the size of the belt for (n,n) CNB".⁴⁸

Miao took an alternate approach leading to both an armchair CNB or chiral CNB, as will be discussed in the following section, using the same key building block for both routes. This highlights the variety of approaches groups have taken to synthesize molecular CNT fragments. By functionalizing building blocks compatible with CPP synthesis—which I will elaborate on in the coming chapters—a diverse set of belt and belt-like structures have been synthesized.^{49,50} A highly-functionalized [12]CPP derivative with electron-rich arenes was made via non-selective Suzuki cross-coupling conditions followed by reductive aromatization. The electron-rich arene functionalized [12]CPP was subjected to Scholl oxidation conditions to obtain the (12,12) CNB[42], a π -extended version of Itami's (12,12) CNB with electron-rich solubilizing groups (Scheme I.6). Miao's armchair CNB has emissive properties similar to Itami's CNBs.^{48,50}



Scheme I.6. Synthesis of armchair (12,12) CNB[42] (top) and chiral (18,12) CNB[42] (bottom) from the Miao group.⁵⁰

I.4. Chiral belts

Following the same method Miao presented for making the (12,12) CNB[42], by replacing every other phenylene with a functionalized naphthalene they made an (18,12) CNB[42] derivative after reductive aromatization and Scholl oxidation, see Scheme I.6. This, so far, represents the only example of a chiral CNT mimic as a CNB. Although they map onto different CNT structures, the (18,12) CNB derivative has similar optical properties to the armchair CNBs present in the literature, noting the blue-shifted emission due to the larger belt size.⁵⁰ The number of chiral structures are expanded to increase as synthetic methods develop to arrive at functionalized chiral CNBs or different chiral vectors to explore their intrinsic chiroptical properties.

I.5. Möbius belt

Carbon nanomaterials are promising candidates for an array of optoelectronic applications, but traditional synthetic methods result in heterogeneous mixtures of structures, which are often not desirable. Alternatively, synthetic organic chemistry enables fragments of carbon nanomaterials to be prepared with

unprecedented atomic precision, providing a way to access and tune carbon nanomaterials. In particular, synthetic methods to prepare CNB structures that map onto various chirality CNTs have undergone a renaissance in the past few years.²⁶ Using a variety of methods and strategies, all sp^2 -hybridized CNBs have been prepared that map onto armchair, zigzag and chiral nanotubes. With these strategies rapidly evolving, the range of possible topologies of carbon nanomaterials are also increasing and our imagination is truly the only limit.

Itami and co-workers reported a synthetic method to prepare an all sp^2 -hybridized CNB that has a Möbius topology—a Möbius carbon nanobelt (MCNB).⁵¹ Although Möbius objects have appeared in works of art and in mathematics for centuries, the MCNB is the first example of this topology being introduced into a CNB using a rational bottom-up synthetic approach.

A Möbius topology can be envisioned by considering the ways a flat two-dimensional strip can be connected into a cylindrical object.⁵² In a more common scenario, a flat strip can be wrapped around to form a cylinder by connecting the top edge of one side of the strip with the top edge of the other side (Figure I.3a, left). Adding a single twist to the strip such that the top edge meets the bottom edge creates a Möbius strip with a non-orientable surface (Figure I.3a, right). Möbius molecules pose a formidable synthetic challenge as a twist needs to be forced into the molecule before making the final bond that closes the cyclic structure. Not surprisingly, synthetic examples of Möbius molecules are very rare.^{52–55} Theoretical calculations of Möbius π -conjugated molecules also motivate their synthesis due to the potential to investigate basic concepts of aromaticity, which are critical to understanding optical and electronic properties of materials. Hückel aromaticity follows a $(4n + 2)$ π -electron rule whereas Möbius aromaticity follows a $4n$ π -electron rule. The change in the number of π -electrons is a result of the change in p-orbital phases as the molecule makes a twist, cancelling out when they meet back at the point of origin. Experimentally, this results in noticeably different optoelectronic properties of Möbius molecules compared with their Hückel counterparts.^{52,53}

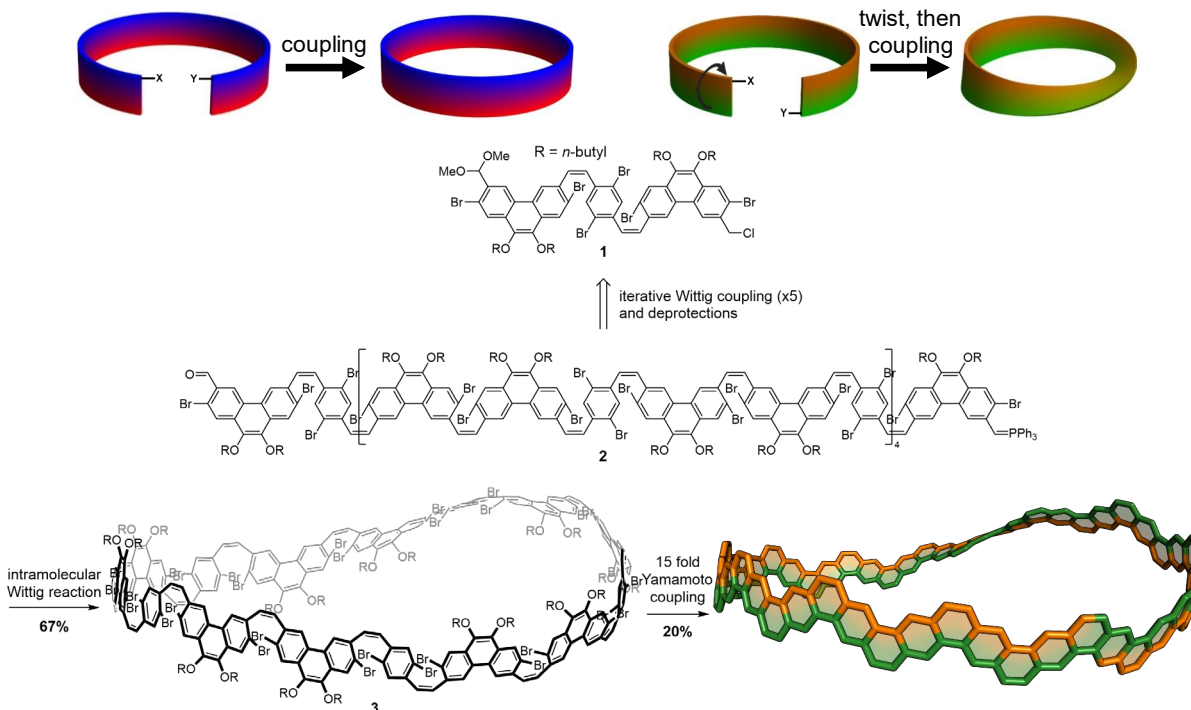


Figure I.3. a) two different topologies can be created by closing a two-dimensional strip. b) Iterative Wittig reactions and Yamamoto couplings are used to synthesize a (25,25) MCNB.

The synthetic approach to the MCNB in this work is an adaptation of previous methods used to make armchair CNBs reported by the Itami group.^{47,48} Based on this earlier work,⁴⁷ the authors surmised that the upper-bound for the build-up of strain energy in the final bond-forming reaction (Yamamoto coupling) is ~ 40 kcal mol⁻¹. As a consequence of this consideration, the Itami group targeted the (25,25) MCNB—this larger Möbius belt alleviates the demand of the synthesis in that the twisted belts are much more strained than the previously synthesized armchair belts. The other key feature in their synthetic strategy is to target a precursor that has two functional groups for macrocyclization that are positioned on opposite edges of the ultimate belt, therefore forcing the twist.

An appropriate precursor to the (25,25) MCNB is key Wittig precursor **1.2** (Figure I.3b); the aldehyde and phosphorus ylide are on opposite edges of the belt precursor, and a Wittig macrocyclization should lead to a macrocycle with a single twist. After macrocyclization, Itami and co-workers envisioned that a sequential Yamamoto reductive aryl–aryl coupling reaction would deliver the target MCNB. In a forward sense, Wittig precursor **1.2** was prepared by sequential Z-selective Wittig reactions using building block **1.1**—this key molecular building block can be converted to a phosphonium ylide via the chloride or an aldehyde by deprotection of the acetal, providing an iterative method to build up a linear structure. As planned, a series of Z-selective iterative Wittig couplings and functional group interconversions enables the preparation of linear precursor **1.2** in good yields. Once the linear molecule **1.2** is prepared, an intramolecular Wittig via a twist is executed to deliver the Möbius nanobelt precursor macrocycle **1.3** in an excellent 67% yield. A one-pot 15-fold intramolecular Yamamoto coupling affords the (25,25) MCNB in a remarkable 20%

overall yield (on average, ~90% for each C–C bond forming reaction).

Interestingly, a (15,15) MCNB belt could also be targeted using the same building blocks, but was unsuccessful in the Yamamoto coupling reaction, presumably owing to the higher strain energy. The (25,25) MCNB was characterized using mass spectrometry and ^1H NMR spectroscopy, which was corroborated by predicted spectra.⁵¹ Increasing the temperature while obtaining the ^1H NMR spectrum results in sharper peaks compared with the room-temperature spectrum, which is consistent with dynamic movement of the twist throughout the belt. The intramolecular Wittig reaction can occur in two orientations and, as a result, the reaction should produce two enantiomers in equal amounts. This prediction was verified by separation of enantiomers and matching of the circular dichroism spectrum to the simulated spectrum of each, further confirming the structure.

This MCNB is a new topological nanocarbon. Notably, the CNB has Möbius topology but does not show obvious Möbius aromatic properties, which would require delocalization through the macrocycle. Although the goal here was to construct an aromatic belt with Möbius topology, further experiments exploring the electronic structure of the reduced or oxidized structure (which may be more globally aromatic) will provide interesting information on Möbius aromatic hydrocarbon belts. Overall, this synthetic approach represents an important advancement in the development of topologically diverse nanocarbons by a bottom-up synthetic approach. And like the recent explosion of CNBs, this breakthrough will inspire many more Möbius π -conjugated molecules with new properties.

1.6. Nitrogen-incorporated belts

Since the development of CNB structures, the interest in incorporating heteroatoms to manipulate the electronic properties of such structures or facilitate their synthesis has been ever present.^{56–62} Nitrogen atom doping in carbon nanostructures has proven to be a valuable method for amplifying their appealing electronic properties. It stands to continue developing nitrogen-doped carbon nanostructures to understand how different isomers affect their applications in future devices. Two N-doped cyclacenes and an N-doped armchair CNB have been reported thus far and their synthesis is elaborated herein (Figure I.4).

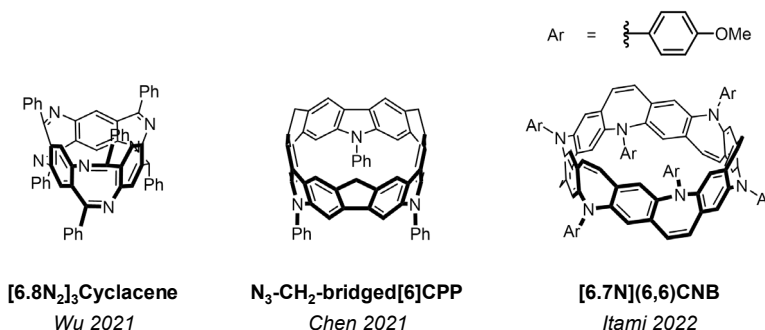
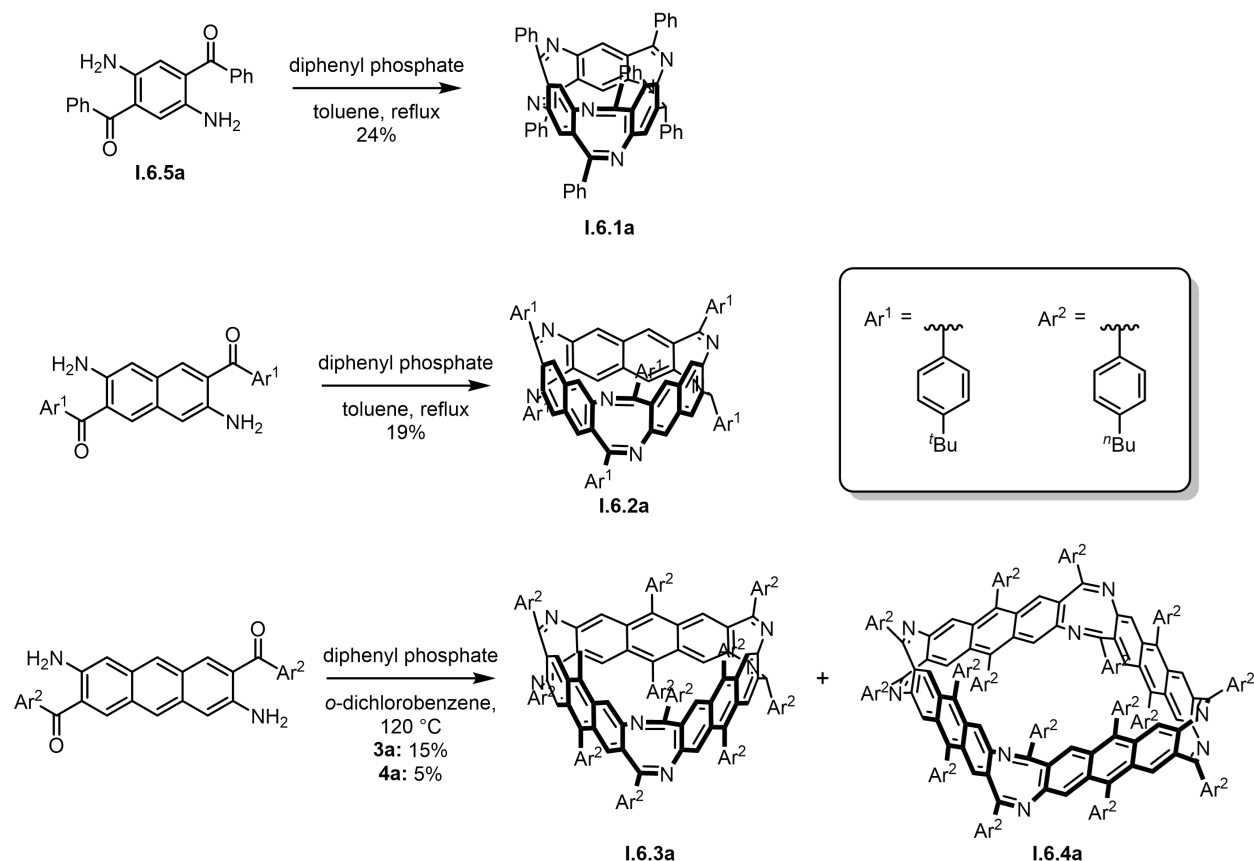


Figure I.4. N-doped carbon nanobelt structures reported in the literature.

The first example of N-doped carbon nanobelt synthesis was reported by the Wu group. They represent a collection of cyclacene derivatives assembled by imine chemistry. Dynamic covalent chemistry has been established as a powerful tool for materials chemists to make a range of thermodynamically preferred structures.⁶³ With the appropriate diketone-diamine, four N-doped cyclacene structures were

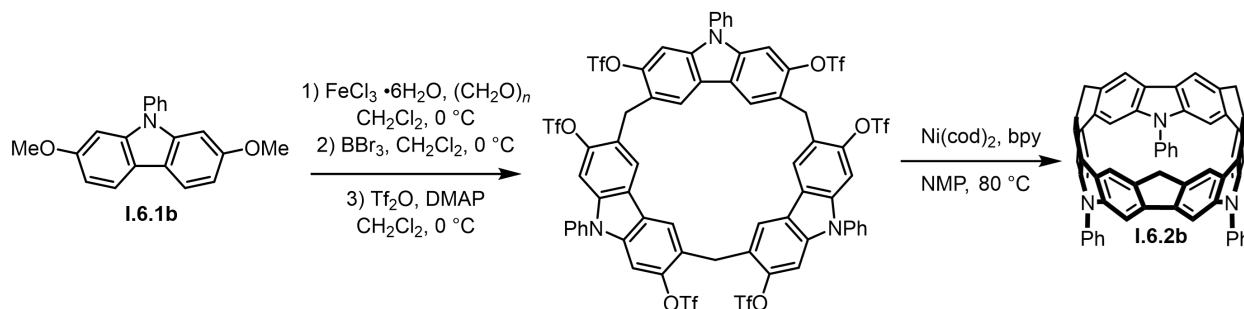
successfully isolated. Standard organic transformations precede the macrocyclization step, and molecule **I.6.5a** is used to make the **[6.8N₂]₃cyclacene** by refluxing in toluene with diphenylphosphate.^{63,64} These conditions have been established for making [1,5]diazocine structures since 1896 and only recently applied to making aromatic macrocycles.⁶³ The larger structures were obtained using the same reaction conditions with the addition of *o*-dichlorobenzene in place of toluene for the two larger structures in order to solubilize the mixture. Structurally, the eight-membered ring results in a triangular macrocycle for **I.6.1a**, **I.6.2a**, and **I.6.3a** and a square macrocycle for **I.6.4a** (Scheme I.7). Larger macrocycles have red-shifting absorbance profiles due to the increased conjugation of the larger acene panels. Expanding this to even larger acene building blocks would be a facile way to solubilize conventionally insoluble electronically active organic molecules.



Scheme I.7. Synthesis of **[6.8N₂]_ncyclacenes** reported by the Wu group. The aryl groups used are specified in the inlay box.⁶⁴

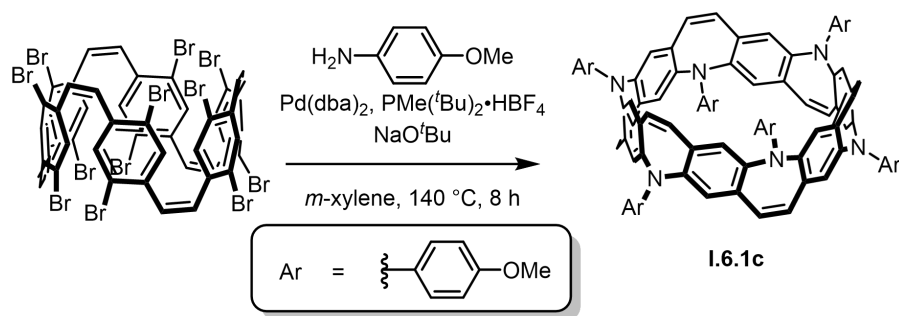
The next example maps onto a [6]CPP, but it has alternating methylene and amino bridging five-membered rings. By condensing a functionalized carbazole **I.6.1b** with paraformaldehyde, Chen *et al.* made calix[3]carbazole which, through functional group conversions, was reductively coupled to form the final carbon-carbon bonds of **I.6.2b**.⁶⁵ The increased conjugation of the final belt structure produces a red-shifted absorbance band from 320 to 450 nm, compared to the starting calix[3]carbazole and nano hoop relative [6]CPP.⁶⁵ Unlike nano hoops of the same size, this non-alternant N-doped belt **I.6.2b** is fluorescent with an

emission from 500 to 600 nm. Electrochemically, **1.6.2b** has multiple reversible reduction and oxidation events in a narrow electrochemical window. Paired with the high-yielding synthesis, this sets precedent for carbon nanobelt structures as viable electronically active materials (Scheme I.8).



Scheme I.8. Synthesis of a non-alternant N-doped [6]CNB, N₃-CH₂-bridged[6]CPP, from Chen *et al.* starting from a functionalized carbazole.⁶⁵

The last example of N-doped CNBs in the literature is a belt with seven-membered rings with one nitrogen synthesized by the Itami lab. They report the successful Buchwald-Hartwig amination of a previously reported precursor to the (6,6) CNB.^{47,66} Using *p*-methoxyaniline, they performed a six-fold Buchwald-Hartwig amination to make **1.6.1c**, the [6.7N](6,6) CNB (Scheme I.9). They report that belts with aromatic units with seven-membered rings or larger help to dissipate the inherent strain, resulting in optoelectronic properties closer to their linear analogues. Belt **1.6.1c** shows an absorption peak at 334 nm and no fluorescent properties and addition of a chemical oxidant results in a growing peak at 520 nm from the dication of **1.6.1c**.⁶⁶ These examples represent inventive ways to synthesize complex unnatural products to understand how new topologies affect electronic and chemical properties of curved aromatic molecules.



Scheme I.9. Final step of N-doped CNB, [6.7N](6,6)CNB, from Itami *et al.* accomplished via Buchwald-Hartwig coupling.⁶⁶

I.7. Conclusion

Since their conception, carbon nanobelts have intrigued organic chemists because of their synthetic challenge and natural beauty. Constructing curved aromatic molecules to study their resulting properties led to many of the examples presented. Although they are not practical for application in devices, continued work will expand our fundamental knowledge in synthetic methodology and structure-property relationships. Overall, we have established many trends in optoelectronic properties as they relate to inherent strain. Not only has the community made molecular analogues of zig-zag, armchair, and chiral CNTs, belts that do not

map onto a CNT have been made. Introduction of heteroatoms has also been accomplished and offer a way to understand how heteroatoms affect bulk properties of carbon nanomaterials. It follows that more varieties of belts and belt-like structures should be investigated to have a complete understanding of intrinsic material properties and continue expanding our synthetic toolbox.

I.8. Co-authored content

This thesis contains co-authored content that was published in peer-reviewed journals and other co-authored content that is unpublished. Work in Chapter 1 was co-authored with Prof. Ramesh Jasti and published under the title “Carbon nanobelts do the twist” in *Nature Synthesis: News & Views*⁶⁷ Work in Chapter 2 was co-authored with Dylan Nguyen, Victor Salpino, Luca Zocchi, Dr. Lev Zakharov, and Prof. Ramesh Jasti and is in preparation for submission. Work in Chapter 4 was co-authored with Dr. Curtis Colwell, Prof. Tim Stauch, and Prof. Ramesh Jasti and published under the title of “Strain Visualization for Strained Macrocycles” in *Chemical Science*.⁶⁸ Work in Chapter 5 has unpublished and co-authored content with Julia Fehr, Tara Clayton, Nathalie Myrthil, Anna Garrison, Dr. Lev Zakharov, Prof. Steven Lopez, and Prof. Ramesh Jasti with the published material listed under “Experimental and theoretical elucidation of SPAAC kinetics for strained alkyne-containing cycloparaphenylenes” in *Chemical Science*.⁶⁹ Work in Chapter 6 has unpublished and co-authored content with Dr. Claire Otteson and Prof. Ramesh Jasti for the unpublished material and Viktor Pedersen, Dr. Nicolaj Kofod, Dr. Bo Laursen, Prof. Ramesh Jasti, and Prof. Mogens Nielsen under the title “Synthesis and Properties of Fluorenone-containing Cycloparaphenylenes and Their Late-State Transformation” in *Chemistry, a European Journal*.⁷⁰

I.9. Bridge to Chapter 2

Belt and belt-like molecules have been reported with emergent properties as the aromatic rings in curved aromatic systems and increased coplanar arrangements. N-doped CNBs have been reported but each have examples with graphitic or imine type nitrogen atoms. In the next chapter, we proposed building pyridinium belt-like nanohoops to study the effect of coplanarization of the pyridinium ring with the rest of the nanohoop.

CHAPTER II

ACCESSING CATIONIC AZA-CARBON NANOTUBE FRAGMENTS VIA INTRAMOLECULAR S_N2 AND PYRIDINE-DIRECTED C-H ACTIVATION

II.1. Introduction

Development of next-generation technologies is dependent on the creation of new materials with emergent properties.^{2,3,9} Organic materials offer synthetic advantages through bottom-up synthetic precision, solution processability, and flexibility as soft materials.^{2,3,6} Many organic materials with appealing electronic properties are continually being developed, but the variety of available organic n-type materials is much less compared to p-type organic materials.^{1,3,6,71,72} Organic photovoltaics (OPVs), organic light emitting diodes (OLEDs), and redox flow batteries rely on a catalogue of organic materials with various electrochemical windows that suit device performance. An organic scaffold that is readily synthesized with a variety of functionalization and does not impair the electronic properties is, therefore, ideal for developing diverse organic optoelectronic materials.

Nitrogen-doped carbon nanomaterials have made promising breakthroughs in functional devices by gradually lowering the energy gap of materials and introducing charge carriers.^{57,73–77} CNTs doped with nitrogen have improved material properties as capacitors, batteries, and electro-catalysts.^{73,74,77} However, it is difficult to make precise structures due to the random replacement of carbon for nitrogen in the doping process resulting in a variety of nitrogen content and valence.^{73,75} Bottom-up approaches to nitrogen-doped materials are ideal for understanding the effect of gradual replacement of carbon atoms with nitrogen of different valences. π -rich pyridinium structures are good candidates for this end because of their established syntheses, modular band gaps, and reversible redox properties. A variety of labs have accomplished syntheses of nitrogen-doped carbon nanobelts (CNB), but none have explored the effect of having quaternary nitrogen atoms in the backbone (Figure II.1).^{64–66}

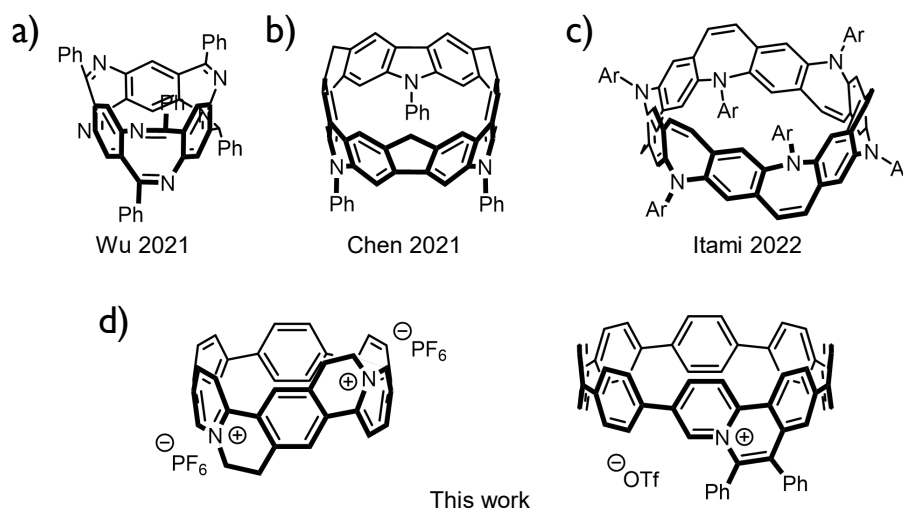


Figure II.1. Nitrogen-doped belt structures and partial belts. a) $[6.8N_2]_3$ Cyclacene b) N_3 -methylene-bridged[6]CPP c) $[6.7N](6,6)$ CNB d) bridged-pyridinium[n]CPPs. (**Ar** = *p*-methoxyphenyl).

Cycloparaphenylene synthesis has developed in recent years to make functional materials with size-dependent properties as well as finely tuned optical and electrochemical properties based on the functional groups appended to the nanohoop.^{25,70,78–90} Aza[n]CPPs, pyridine-included CPPs, mimic all-carbon CPPs in their electronic properties, but they offer a site for discrete functionalization.^{79,91–95} Following previous reports on aza[n]CPPs, the nitrogen has been methylated to make a series of donor-acceptor nanohoops referred to as N-methylaza[n]CPPs or pyridinium[n]CPPs.^{79,93,95} As seen by fully bridged armchair carbon nanobelt structures reported by the Itami lab and partially-bridged nanobelt structure by our lab, increasing the coplanarity of adjacent phenylene results in a decreased HOMO-LUMO gap.^{47–49,96,97} N-methyl aza[n]CPPs show lower reduction potentials indicative of a lower LUMO energy but lack the stability for application. Smaller aza[n]CPPs, which have smaller HOMO-LUMO gaps, have shown to be particularly unstable upon methylation as well as more difficult to methylate in multiple positions.^{79,93} Therefore, we propose incorporating bridged-pyridinium units to increase the coplanarity of the system, reliably alkylate multiple positions, and provide increased stability. Incremental introduction of bridged-pyridinium units is hypothesized to gradually lower the LUMO energy of the resulting nanohoop and provide incremental reduction waves with the hope of reversibility seen by Swager's pyridinium polymers and similar bridging-pyridinium systems.^{2,98,99} These functional units also act to bridge the gap towards pyridinium belt-like structures.

A caveat to the bottom-up synthesis of these molecules is the prefunctionalization of building blocks for each derivative. Incorporating alkyl fragments adjacent to the pyridyl unit in two [6]CPP derivatives, two bridging-pyridinium[6]CPPs have been synthesized. Characterization of their optical and electronic properties was achieved. To rapidly access other pyridinium belt-like structures, we propose using the pyridyl unit in aza[n]CPPs to direct covalent functionalization via pyridine-directed C-H activation.^{100–102} Herein we report the first example of synthesizing functionalized aza[n]CPPs using pyridine-directed C-H activation.

II.2. Synthesis and identification of bridged-pyridinium nanohoops

Precursor aza[n]CPP derivatives were synthesized using techniques familiar to our lab as well as a recently reported method by the von Delius group.^{79,93,95} The key challenges of the synthesis involve isolating a precursor to the aza[n]CPPs with ethanol fragments adjacent to the pyridine units to form the 6-membered ring upon alkylation. Ester groups were the most robust to bring through the syntheses. A pivaloyl group was used for both the mono(bridged-pyridinium)[6]CPP **bp[6]CPP** and the di(bridged-pyridinium)[6]CPP **dibp[6]CPP**. Coupling partners **II.2** and **II.S4** can be obtained in good yields for the Suzuki cross-coupling reaction to make **II.6** (Scheme II.1); however, subsequent steps including the oxidative homo-coupling reaction proceed in low yields unless the boronate, **II.7**, is slowly added to the activated catalyst mixture.¹⁰³ Synthetic steps to afford the bisboronate **II.5** proceed in good yields and cross-coupling reactions to obtain macrocycle **II.9** occur in good yields with the desired structure as the major product. TBAF-mediated desilylation and mild tin-mediated reduction of **II.8** to obtain the aza[6]CPP derivative **II.A1** worked best, but identical conditions with macrocycle **II.9** were not successful. Deprotection

X-ray analysis of the dibp[6]CPP PF₆ salt **II.B2** shows tubular packing of the nanohoops with layers of counter ions. The presence of CH₂Cl₂ molecules in the pores, omitted for clarity, suggest hosting of smaller anions may be possible. Average dihedral angles of [6]CPP, aza[6]CPP, **II.B1**, and **II.B2** are 28.1°, 24.3°, 17.6°, and 17.9° respectively (Figure II.2).^{93,105} As the number of nitrogen atoms within the nanohoop increases, the average dihedral angle between arenes decreases. As a result, the conjugation throughout the nanohoop increases and the HOMO-LUMO gap shrinks.

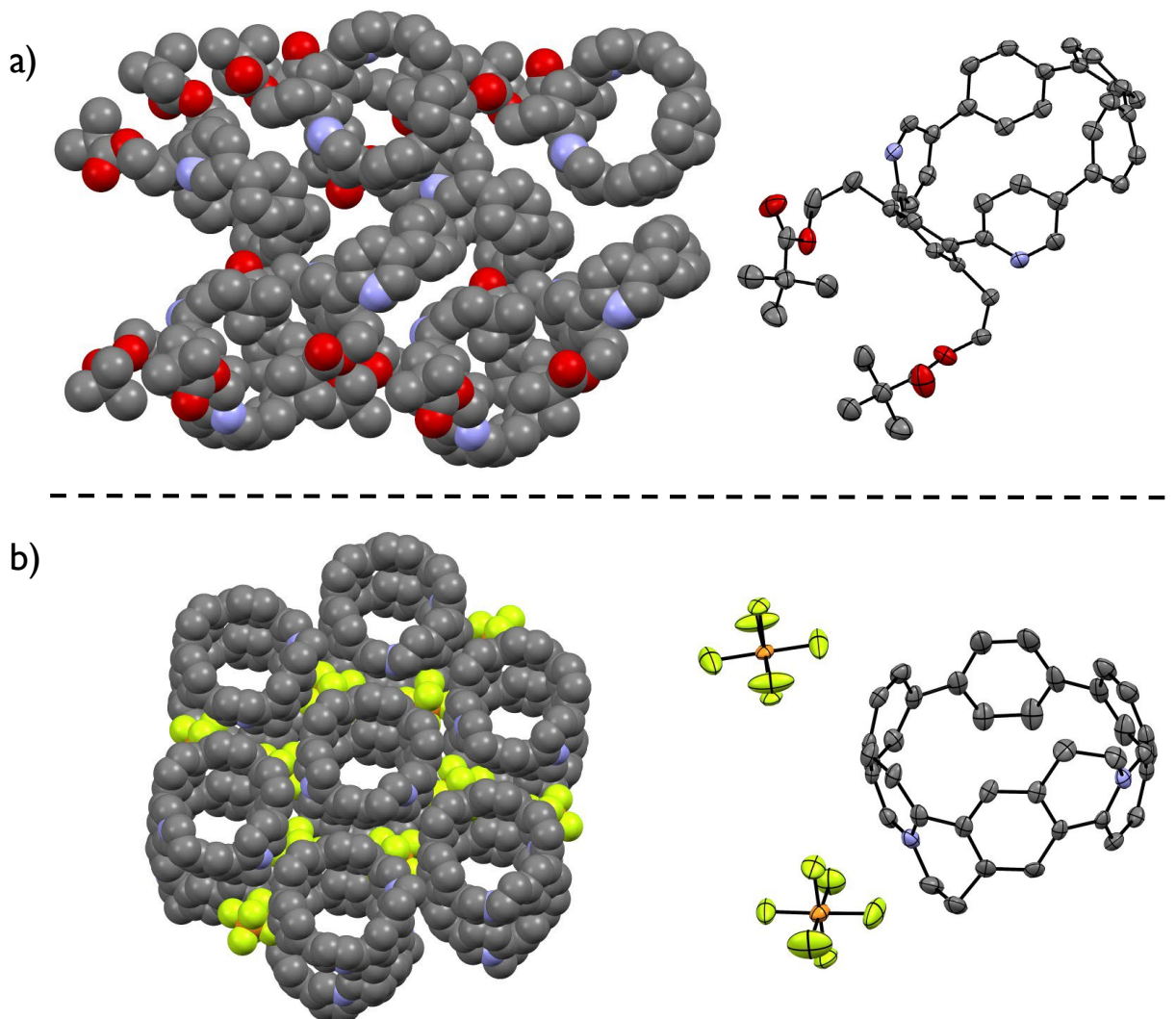


Figure II.2. Single crystal x-ray diffraction results for molecules **II.B1** (a) and **II.B2** (b) with the space-filling packing structure on the left and the ORTEP drawing on the right (solvent molecules omitted for clarity).

Aza[10]CPP and aza[8]CPP were synthesized following reported methods to explore pyridine-directed C-H activation reactions.^{79,95} Attempts to functionalize aza[6]CPP via the same C-H activation reactions were not successful. Following methods developed in the literature,^{100–102} an isoquinolinium fragment was formed via Rh-catalyzed C-H annulation with diphenylacetylene. Each aza-nanohoop was added to a microwave vial along with diphenylacetylene, the rhodium dichloride dimer, and dichloroethane,

then sparged with oxygen gas. Silver trifluoromethyl sulfonate was used to make **II.D** and the combination of copper (II) acetate and potassium hexafluorophosphate were used to make **II.C**, analogous to published methods. The reactions with aza[8]CPP did not typically go to completion unlike the reactions with aza[10]CPP. Annulation was also compatible with other silver salts like silver tetrafluoroborate and silver hexafluorophosphate, but the triflate salt was the most compatible for characterizing **II.D** in acetonitrile like the other pyridinium salts discussed herein. Product **II.D** was obtained in higher yields compared to **II.C**, likely due to the reduced strain of the larger aza[10]CPP compared to aza[8]CPP. The products were obtained after purification by preparative silica TLC. ¹HNMR spectra for **II.C** and aza[8]CPP are elaborated on in Figure II.3. Preliminary experiments with pyridine-directed C-H activation represent a significant development of CPP chemistry since these methods can be used to rapidly functionalize aza[n]CPPs instead of prefunctionalization of requisite building blocks that must survive bottom-up synthetic strategies.

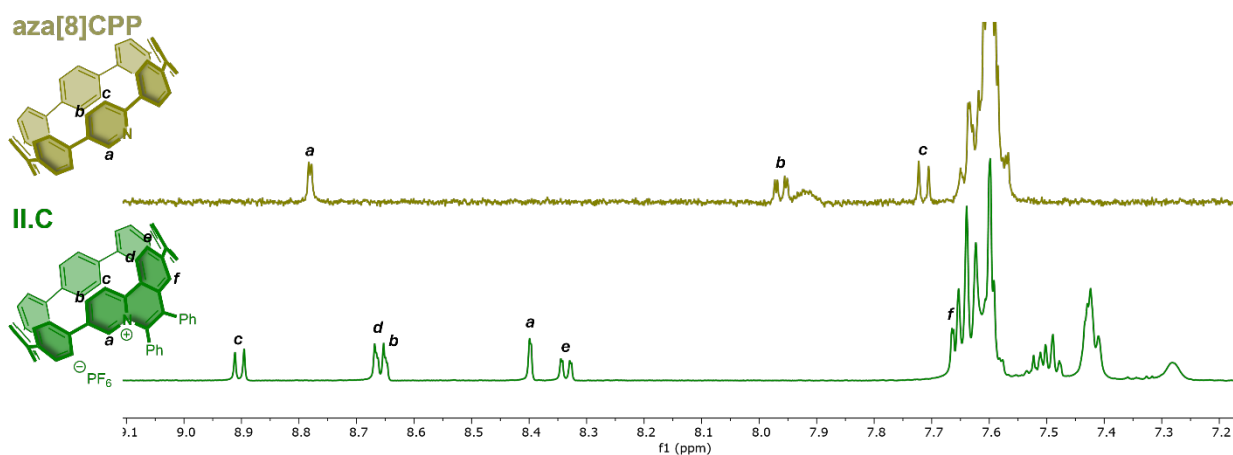


Figure II.3. ¹HNMR spectrum of aza[8]CPP and **II.C** in CD₃CN with representative shifts highlighted.

II.3. Optical and electrochemical characterization

Absorption profiles of the parent aza[n]CPPs show a red-shifting shoulder with increasing number of pyridine units with respect to the size of CPP, see Figure II.4.²⁴ The bridged-pyridinium CPPs have a red-shifted shoulder compared to the parent aza[6]CPPs and a broadening of the absorbance with increasing bridged-pyridinium units. The λ_{max} for the bridging-pyridinium[6]CPPs also red-shifts from their aza[6]CPP counterparts. As the number of pyridinium units increases, the LUMO energy gradually decreases more than the HOMO energy. The increased coplanarity of the pyridinium unit and adjacent phenylene increases conjugation throughout the hoop, effectively further decreasing the HOMO-LUMO gap. Analogously, products **II.C** and **II.D** have red-shifted shoulders from their aza[n]CPP counterparts; however, the λ_{max} are blue-shifted, as seen with the N-methyl aza[10]CPP reported by von Delius.⁹⁵ A note regarding the absorbance profile is that the iodide salts previously reported by our group are more polarized than the hexafluorophosphate salts reported herein. As a result, they exhibit charge transfer characteristics that show a more red-shifted absorbance profile. Attempts to chemically reduce the bp[6]CPPs to study the EPR and absorbance profiles of the reduced structures remain unsuccessful.

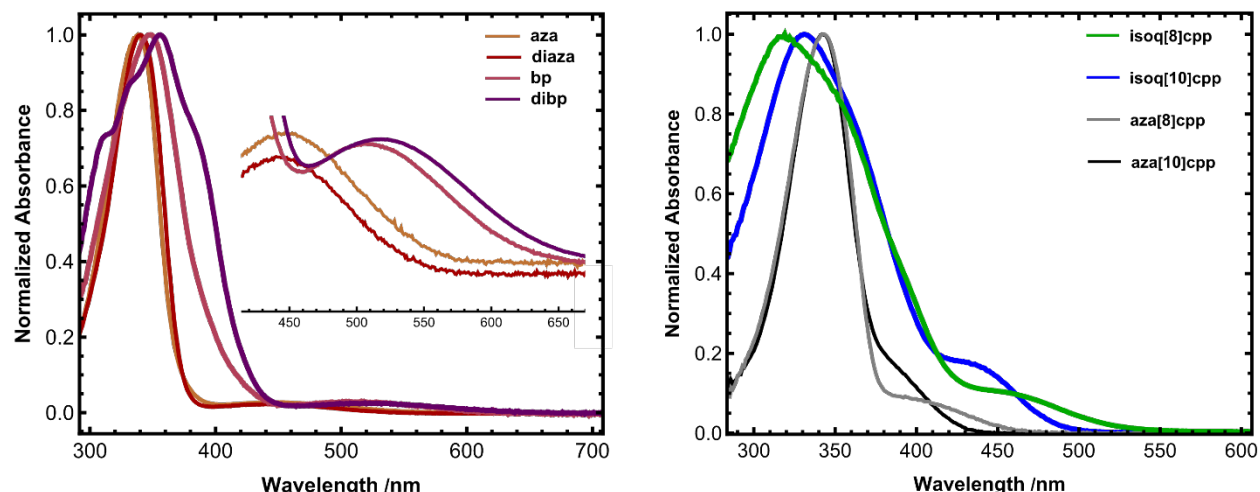


Figure II.4. Left spectra are UV-vis absorbance profiles of **A1** and **B1** in dichloromethane overlapped with **A2** and **B2** in acetonitrile (inlay shown as a magnified region for **A2** and **B2**). Right spectra are UV-vis absorbance profiles of **C** and **D** in acetonitrile and absorbance and emission profiles of aza[8]CPP and aza[10]CPP in dichloromethane.

Cyclic voltammetry was used to probe the electrochemical reduction and identify if the process is reversible for each product. Figure II.5 shows each pyridinium molecule in acetonitrile with 0.2 M NBu_4PF_6 as the electrolyte, with the exception of the dibp[6]CPP which was a 1:1 mixture of acetonitrile and DCM. Although the small molecule analogues of the di(pyridinium)phenylene unit show two reversible reduction events, the pyridinium[6]CPP derivatives discussed here do not have reversible reduction events. This is attributed to the strain of the molecule which greatly increases the reactivity of the reduced structures. The pyridinium[8]CPP and pyridinium[10]CPP derivatives have reversible reduction events but the [10]CPP derivative is not as reversible and resides at the edge of acetonitrile's electrochemical window. Structures **II.C** and **II.D** formed via CH-activation are likely more reversible due to less inherent strain in the larger nano hoops, the added electronic stabilization of the bridging alkene, and the steric protection offered by the phenyl groups on the bridging alkene. Optical and electrochemical data is summarized in Table II.1.

Compound	V_{red} (V)	$E_{\text{g calc}}$ (eV)	E_{opt} (eV)	λ_{edge} (nm)	ϵ_{max} ($10^4 \text{ M}^{-1}\text{cm}^{-1}$)
bp[6]CPP	-0.89	2.53	2.00	620	3.56
dibp[6]CPP	-0.99	2.21	1.92	646	4.12
isoq[8]CPP	-1.92	2.62	2.36	526	1.67
isoq[10]CPP	-2.39	2.62	2.55	486	1.50

Table II.1. Summary of optical and electrochemical data for each bridged-pyridinium nano hoop in acetonitrile. E_{opt} was calculated from the band edge wavelength (λ_{edge}), which is determined by the steepest slope of the lowest energy transition. The molar absorptivity (ϵ_{max}) was determined from the most intense absorption event.

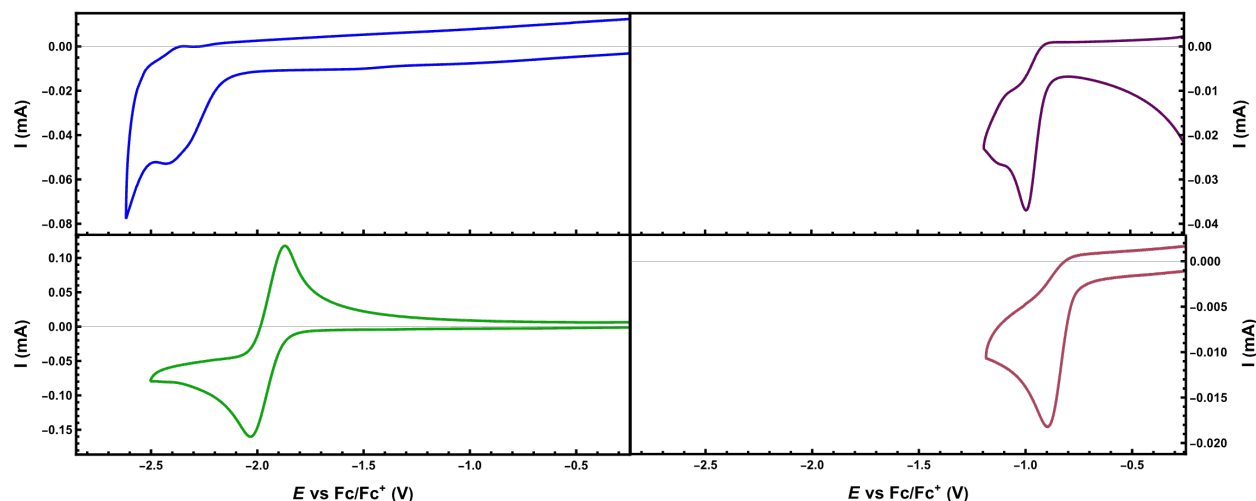


Figure II.5. Cyclic voltammograms of **II.D** (top left), **II.C** (bottom left), **II.B2** (top right), and **II.A2** (bottom right) in acetonitrile for **II.D**, **II.C**, and **II.A2** or acetonitrile/dichloromethane for **II.B2**; supporting electrolyte: 0.2 M Bu₄NPF₆, scan rate: 0.2 V/s. All potentials are referenced to the Fc/Fc⁺ redox couple.

II.4. Computational analysis of bridged-pyridinium nano hoops and their aza[*n*]CPP analogues

DFT calculations were performed on the synthesized molecules as well as other hypothetical derivatives with increasing number of pyridinium units. Computational results were obtained using the Gaussian 09 package¹⁰⁶ with B3LYP/6-31G(d) as the functional and basis set. Results are corroborated with previously reported computational experiments by our lab.^{79,93} Orbital energies are obtained by single point calculations using the same functional and basis set with the default self-consistent reaction field method in the dielectric constant for acetonitrile. The E_g of the aza[*n*]CPPs follow similar trends in energies to their [*n*]CPP counterparts. Upon forming the bridging-pyridinium fragment, the LUMO energy decreases by about one eV while the HOMO energy decreases by different amounts depending on the size of the nano hoop (Figure II.6). Increasing the number of bridging-pyridinium units continues to decrease the LUMO energy with diminishing change in the HOMO-LUMO gap. The HOMO is affected more by increasing the number of pyridinium units since the fragments occupy a larger portion of the nano hoop and reduce the number of bent phenylenes, which are the primary contributors of the HOMO. Orbitals associated with the HOMO and LUMO are shown for each molecule. It has been established that spatially isolated orbitals increase the donor-acceptor character.⁷⁹ The N-methyl aza[*n*]CPPs have greater donor-accepter character due to the localization of the LUMO onto the pyridinium fragment, resulting in their red-shifted absorbance shoulder. Computationally, the structures presented have similar HOMO-LUMO gaps but noticeably different orbital distributions. This results in the LUMO localized to the bridging pyridinium unit more in **II.C** and **II.D** than **II.A2** and **II.B2** making the LUMO energies nearly equivalent to each other and small molecule analogues.

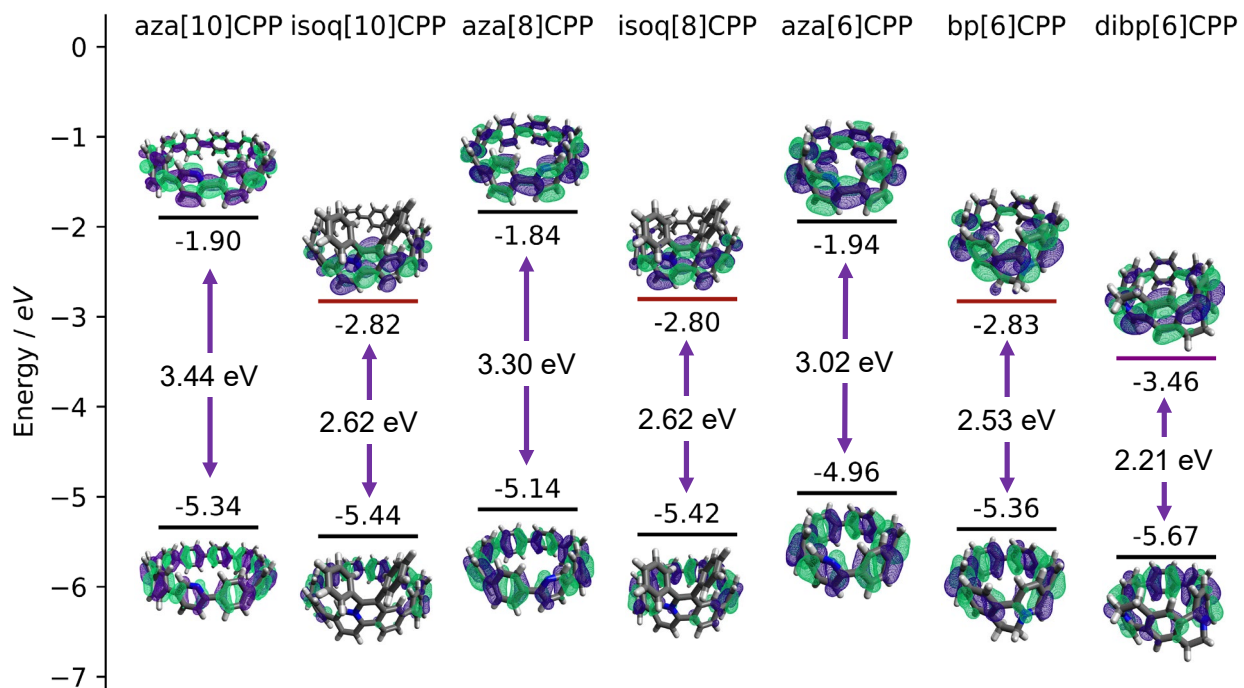


Figure II.6. Calculated frontier molecular orbital energies and their respective occupancy for each bridged-pyridinium nano hoop (II.D, II.C, II.A2, and II.B2) and their precursor aza[*n*]CPP (aza[10]CPP, aza[8]CPP, II.A1, and II.B1) at the B3LYP/6-31G(d) level of theory (isosurface value set to 0.03).

II.5. Conclusions

In conclusion, we have presented two methods for synthesizing bridging-pyridinium nano hoops. Bottom-up methods are synthetically robust enough to incorporate multiple bridging-pyridinium units in highly strained systems, evidenced by dibp[6]CPP. Preliminary pyridine-directed C-H activation reactions have been successful in making bridging-pyridinium units from unfunctionalized aza[*n*]CPPs. This finding is important for rapid development of functionalized aza[*n*]CPPs. So far aza[8]CPP is the most strained nano hoop to undergo C-H activation, but we are continuing to investigate other pyridine-directed C-H activation reactions to develop the scope on aza[*n*]CPPs. These molecules have reduced HOMO-LUMO gaps and lower reduction potentials compared to their parent aza[*n*]CPPs. Computational results support the incremental reduction of the LUMO energy with increasing number of bridging-pyridinium units. Absorbance profiles have red-shifted shoulders upon alkylation of the pyridine for each product discussed, followed by broadening of the absorbance with increasing number of pyridinium units. By bridging the adjacent phenylene with the pyridinium unit, the typically unstable pyridinium nano hoop resulted in a stable salt that can be stored for multiple months in a freezer without noticeable decomposition. With further development, fully fused cationic nitrogen-doped CNBs could be synthesized, resulting in stable and soluble nano hoops with multiple easily accessible reduction potentials.

II.6. General experimental details

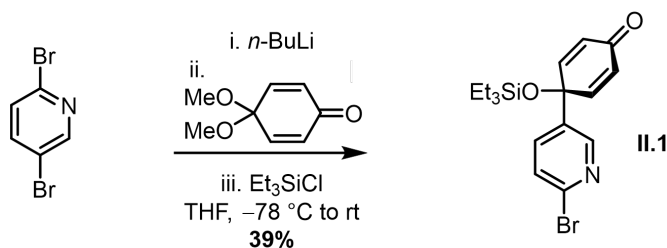
All glassware was flame dried and cooled under an inert atmosphere of nitrogen unless otherwise noted. Moisture sensitive reactions were carried out under nitrogen atmosphere using Schlenk and

standard syringe/septa techniques. Tetrahydrofuran, dichloromethane, dimethylformamide and 1,4-dioxane were dried by filtration through alumina according to the methods described by Grubbs.¹⁰⁷ Silica column chromatography was conducted with Zeochem Zeoprep 60 Eco 40-63 μm silica gel. Automated flash chromatography was performed using a Biotage Isolera One. Thin Layer Chromatography (TLC) was performed using Sorbent Technologies Silica Gel XHT TLC plates. Developed plates were visualized using UV light at wavelengths of 254 and 365 nm. ^1H NMR spectra were recorded at 500 MHz or 600 MHz on a Bruker Advance-III-HD NMR spectrometer. ^{13}C NMR spectra were recorded at 150 MHz on a Bruker Advance-III-HD NMR spectrometer. All ^1H NMR spectra were taken in CDCl_3 (referenced to TMS, δ 0.00 ppm, or residual chloroform, δ 7.26 ppm), methylene chloride- d_2 (referenced to residual methylene chloride, δ 5.32 ppm), or acetonitrile- d_3 (referenced to residual acetonitrile, δ 1.94 ppm). All ^{13}C NMR spectra were taken in CDCl_3 (referenced to chloroform, δ 77.16 ppm), methylene chloride- d_2 (referenced to methylene chloride, δ 53.84 ppm), or acetonitrile- d_3 (referenced to residual acetonitrile, δ 118.31 ppm). Mass spectra were obtained from the University of Illinois at Urbana-Champaign Mass Spectrometry Lab using EI, ESI, or ASAP or from University of Oregon CAMCOR using ASAP or ESI. HRMS was attempted for all compounds, but when not successful, LRMS is reported. Absorbance and fluorescence spectra were obtained in a 1 cm Quartz cuvette with dichloromethane or acetonitrile using an Agilent Cary 100 UV-Vis spectrometer and a Horiba Jobin Yvon Fluoromax-4 Fluorimeter. All reagents were obtained commercially unless otherwise noted. Compounds para-benzoquinone mono-methyl ketal,¹⁰⁸ II.S1,¹⁰⁹ II.S2,⁹⁴ 2-bromo-5-chlorobenzene ethanol,¹¹⁰ Pd PPh_3 Gen III and Pd SPhos Gen III were prepared according to literature procedure.¹¹¹

II.6.1. Computational details

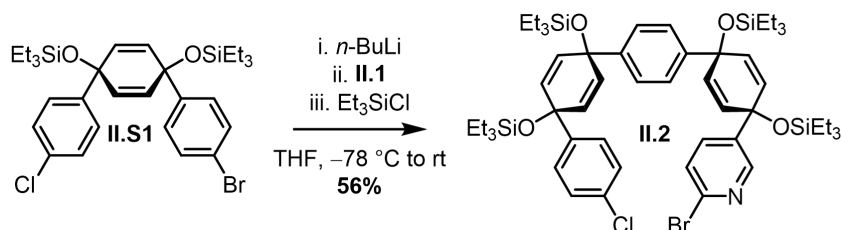
Using Gaussian09 software, computations were performed using Density Functional Theory (DFT) at the B3LYP/6-31G(d) level of theory. All results were solvated using the self-consistent reaction field using the default Polarizable Continuum Model method with the dielectric constant for acetonitrile. All output files are available at: <https://figshare.com/s/08ca10095953cab11d9e>

II.6.2. Synthesis and characterization



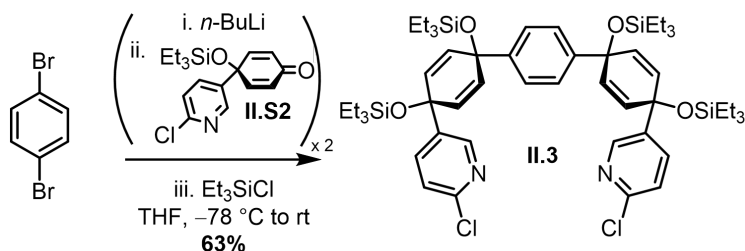
II.1. 20.0 g (84.4 mmol, 1 equiv.) of 2,5-dibromopyridine was added to a flame dried heart-shaped flask. The contents were evacuated, backfilled with nitrogen three times, and capped with a rubber septum under an atmosphere of nitrogen. 20 mL of dry THF was cannula transferred to the heart-shaped flask. 120 mL of dry THF was added to a flame dried round-bottom flask equipped with stirring. The mixture was cooled to $-78\text{ }^\circ\text{C}$ and 34.2 mL (86.1 mmol, 1.02 equiv., 2.52 M) of *n*-BuLi was added to the round-bottom flask. The 2,5-dibromopyridine solution in the heart-shaped flask was cannula transferred dropwise into the

round-bottom flask at $-78\text{ }^{\circ}\text{C}$ and 5.7 mL (84.4 mmol, 1 equiv.) of *para*-benzoquinone monomethyl ketal was transferred immediately after. The mixture was stirred at $-78\text{ }^{\circ}\text{C}$ for 1 hour and then 16.4 mL (92.8 mmol, 1.1 equiv.) of chlorotriethylsilane was added. The mixture was left to stir at room temperature under nitrogen overnight. 30 mL of saturated sodium bicarbonate solution was added slowly and then diluted with 50 mL of DI water. The organic solvent was removed under reduced pressure and the aqueous layer was extracted three times with 50 mL of ethyl acetate. The organic layers were combined and washed with brine and dried over sodium sulfate. Ethyl acetate was removed under reduced pressure and the crude orange-red oil was recrystallized from absolute ethanol to obtain **II.1** as colorless needle-like crystals (12.6 g, 39%). ^1H NMR (500 MHz, Chloroform-*d*) δ 8.51 (d, J = 2.6 Hz, 1H), 7.51 (dd, J = 8.3, 2.6 Hz, 1H), 7.44 (d, J = 8.3 Hz, 1H), 6.78 (d, J = 9.8 Hz, 2H), 6.27 (d, J = 9.8 Hz, 2H), 0.96 (t, J = 7.9 Hz, 10H), 0.66 (q, J = 7.9 Hz, 6H). ^{13}C NMR (126 MHz, Chloroform-*d*) δ 185.06, 150.55, 148.31, 141.99, 136.09, 135.65, 127.96, 127.53, 71.89, 6.97, 6.31. HRMS (ASAP) (m/z): $[\text{M}+\text{H}]^+$ calculated for $\text{C}_{17}\text{H}_{23}\text{NO}_2\text{SiBr}$, 380.0681; found 380.0663. IR (neat): 3089, 3070, 3041, 2957, 2909, 2876, 1690, 1671, 1629, 1604, 1574, 1560, 1448, 1412, 1386, 1359, 1281, 1233, 1198, 1179, 1145, 1137, 1078, 1065, 1026, 1017, 1003, 968, 926, 886, 832, 788, 741.

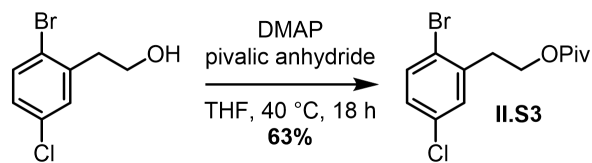


II.2. 6.4 g (10.5 mmol, 1 equiv.) of **II.S1** was added to a 50 mL flame-dried round-bottom flask equipped with stirring. The contents were evacuated, backfilled three times with nitrogen, and capped with a rubber septum under an atmosphere of nitrogen. About 20 mL of dry THF was added and the mixture was cooled to $-78\text{ }^{\circ}\text{C}$. 4.0 g (10.5 mmol, 1 equiv.) of **II.1** was added to a flame-dried heart-shaped flask. The contents were evacuated and backfilled with nitrogen three times. 15 mL of dry THF was added to the heart-shaped flask. 4.43 mL (10.6 mmol, 1.01 equiv., 2.5 M) of *n*-BuLi was added to the round-bottom flask dropwise and the mixture was stirred for 10 minutes before cannula transferring the solution in the heart-shaped flask. The mixture was stirred for an hour at $-78\text{ }^{\circ}\text{C}$ then 1.95 mL (10.7 mmol, 1.02 equiv.) of chlorotriethylsilane was added. The reaction was stirred overnight at room temperature. The mixture was quenched with saturated sodium bicarbonate solution and diluted with DI water. Solvent was removed under reduced pressure and the aqueous mixture was extracted with hexanes. The organic layer was washed with brine and dried over sodium sulfate. The solvent was removed under reduced pressure and the resulting dark oil was eluted through a silica plug using 5% ethyl acetate in hexanes. The solvent was removed under reduced pressure to obtain a yellow oil then recrystallized using ethanol to obtain the product as a white crystalline solid (6.0 g, 56%). ^1H NMR (500 MHz, Methylene Chloride-*d*₂) δ 8.28 (dd, J = 2.6, 0.7 Hz, 1H), 7.39 (dd, J = 8.4, 2.6 Hz, 1H), 7.30 (dd, J = 8.3, 0.7 Hz, 1H), 7.28 (d, J = 2.7 Hz, 4H), 7.26 – 7.23 (m, 4H), 6.13 (d, J = 10.1 Hz, 2H), 6.05 (d, J = 10.1 Hz, 2H), 5.95 (d, J = 10.2 Hz, 2H), 5.92 (d,

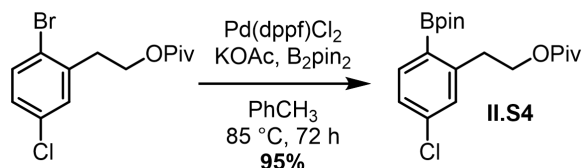
$J = 10.1$ Hz, 2H), 0.99 – 0.88 (m, 36H), 0.71 – 0.52 (m, 24H). ^{13}C NMR (126 MHz, CD_2Cl_2) δ 148.95, 145.98, 145.37, 145.33, 141.71, 141.22, 136.78, 133.36, 133.01, 132.26, 131.85, 131.00, 128.71, 127.90, 127.76, 126.54, 126.29, 71.79, 71.75, 71.48, 70.79, 7.37, 6.98. HRMS (ASAP) (m/z): $[\text{M}+\text{H}]^+$ calculated for $\text{C}_{53}\text{H}_{80}\text{NO}_4\text{Si}_4\text{ClBr}$, 1020.4036; found 1020.3975. IR (neat): 3033, 2953, 2909, 2874, 1573, 1559, 1482, 1849, 1406, 1377, 1353, 1238, 1205, 1188, 1172, 1107, 1061, 1011, 987, 957, 881, 858, 829, 759.



II.3. 0.75 g (3.18 mmol, 1 equiv.) of 1,4-dibromobenzene was added to a 50 mL flame-dried round-bottom flask equipped with stirring. The contents were evacuated, backfilled three times with nitrogen, and capped with a rubber septum under an atmosphere of nitrogen. About 10 mL of dry THF was added and the mixture was cooled to -78 °C. 2.14 g (6.36 mmol, 2 equiv.) of **II.S2** was added to a flame-dried heart-shaped flask. The contents were evacuated and backfilled with nitrogen three times. 10 mL of dry THF was added to the heart-shaped flask. 1.28 mL (3.20 mmol, 1.01 equiv., 2.5 M) of *n*-BuLi was added to the round-bottom flask dropwise and the mixture was stirred for 10 minutes before transferring 5 mL of the solution in the heart-shaped flask. The mixture was stirred for 30 min at -78 °C then 1.28 mL (3.20 mmol, 1.01 equiv., 2.5 M) of *n*-BuLi was added to the round-bottom flask dropwise. The mixture was stirred for 10 minutes before transferring the remaining 5 mL of the solution in the heart-shaped flask. The mixture was stirred for 30 min at -78 °C. 1.13 mL (6.39 mmol, 2.01 equiv.) of chlorotriethylsilane was added. The reaction was stirred overnight at room temperature. The mixture was quenched with saturated sodium bicarbonate solution and diluted with DI water. Solvent was removed under reduced pressure and the aqueous mixture was extracted with hexanes. The organic layer was washed with brine and dried over sodium sulfate. The solvent was removed under reduced pressure and the resulting dark oil was eluted through a silica plug using 10% ethyl acetate in hexanes. The solvent was removed under reduced pressure to obtain an orange oil which was recrystallized using ethanol to obtain the product as a white crystalline solid (1.96 g, 63%) ^1H NMR (500 MHz, Methylene Chloride- d_2) δ 8.33 – 8.29 (dd, $J = 2.5, 0.7$ Hz, 2H), 7.47 (dd, $J = 8.4, 2.6$ Hz, 2H), 7.30 (s, 4H), 7.24 (dd, $J = 8.3, 0.7$ Hz, 2H), 6.12 (d, $J = 10.1$ Hz, 4H), 5.92 (d, $J = 10.1$ Hz, 4H), 0.96 (t, $J = 7.9$ Hz, 9H), 0.90 (t, $J = 7.9$ Hz, 9H), 0.67 (q, $J = 7.9$ Hz, 6H), 0.55 (q, $J = 8.0$ Hz, 6H). ^{13}C NMR (126 MHz, Methylene Chloride- d_2) δ 150.57, 148.30, 145.62, 141.19, 136.99, 132.87, 131.10, 126.43, 124.04, 71.46, 70.73, 7.32, 6.93, 6.84. HRMS (ASAP) (m/z): $[\text{M}+\text{H}]^+$ calculated for $\text{C}_{52}\text{H}_{79}\text{N}_2\text{O}_4\text{Si}_4\text{Cl}_2$, 977.4494; found 977.4504. IR (neat): 2954, 2935, 2910, 2875, 1577, 1562, 1498, 1452, 1408, 1400, 1377, 1365, 1356, 1280, 1238, 1205, 1191, 1140, 1061, 1002, 969, 957, 924, 881, 856, 833, 768.

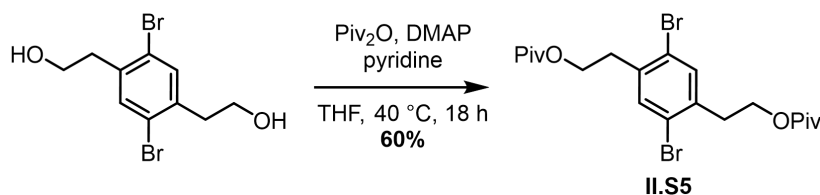


II.S3. 2-bromo-5-chlorophenylethyl pivalate. A 250 mL round bottom flask equipped with stirring was loaded with 9.00 g (14.3 mmol, 1 equiv.) of 2-bromo-5-chlorobenzene ethanol. 0.467 g (3.82 mmol, 0.1 equiv.) of 4-(dimethylamino)pyridine was added to the flask and the contents were evacuated and backfilled with nitrogen three times and capped with a rubber septum under an atmosphere of nitrogen. 130 mL of THF was added to the flask and the mixture was stirred at 40 °C while 11.6 mL (10.7 g, 57.3 mmol, 1.5 equiv.) of pivalic anhydride and 4.61 mL (4.53 g, 57.3 mmol, 1.5 equiv.) of pyridine was added to the reaction flask. The mixture was stirred overnight then cooled to room temperature and quenched with saturated ammonium chloride. The mixture was extracted three times with hexanes. The organic layer was washed with an aqueous copper (II) sulfate solution to remove excess pyridine, then it was washed with a 15% NH₄OH and EDTA solution to remove excess copper (II) sulfate. The resulting organic layer was washed with brine, dried over sodium. The solvent was removed under reduced pressure to obtain a pale-yellow oil. The mixture was purified via a plug of silica by flushing with 5% ethyl acetate in hexanes. The eluent was concentrated under reduced pressure to obtain the desired product as a colorless oil (7.70 g, 63%). ¹H NMR (500 MHz, Chloroform-*d*) δ 7.47 (d, *J* = 8.5 Hz, 1H), 7.24 (d, *J* = 2.6 Hz, 1H), 7.09 (dd, *J* = 8.5, 2.6 Hz, 1H), 4.29 (t, *J* = 6.6 Hz, 2H), 3.06 (t, *J* = 6.6 Hz, 2H), 1.17 (s, 9H). ¹³C NMR (126 MHz, CDCl₃) δ 178.52, 139.35, 134.01, 133.34, 131.33, 128.49, 122.53, 62.87, 38.90, 35.34, 27.30. HRMS (ASAP) (*m/z*): [M]⁺ calculated for C₁₃H₁₆O₂ClBr, 319.0100; found 319.0095. IR (neat): 2970, 2933, 2905, 2871, 1725, 1647, 1585, 1559, 1479, 1462, 1397, 1281, 1229, 1198, 1145, 1098, 1026, 987, 940, 876, 847, 809, 769.

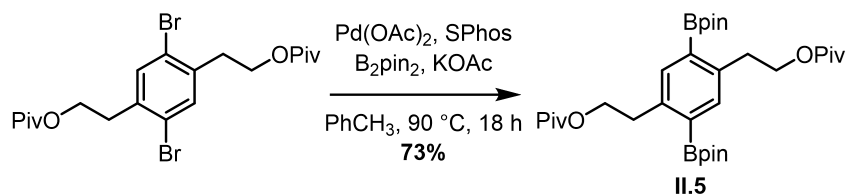


II.S4. 2-boropinacolato-5-chlorophenylethyl pivalate. A 25 mL round bottom flask equipped with stirring was loaded with 6.14 g (62.6 mmol, 5 equiv.) of oven-dried potassium acetate. 4.00 g (12.5 mmol, 1 equiv.) of 2-bromo-5-chlorophenylethyl pivalate, 3.34 g (13.1 mmol, 1.05 equiv.) of bis(pinacolato)diboron, and 0.256 g (0.313 mmol, 2.5 mol%) of [1,1'-bis(diphenylphosphino)ferrocene]palladium dichloride were added to the flask and the contents were evacuated and backfilled with nitrogen three times and capped with a rubber septum under an atmosphere of nitrogen. 30.0 mL of dry toluene was added to the flask and the mixture was stirred at 90 °C over three days (72 hours). The mixture was cooled to room temperature and diluted with toluene. The mixture was filtered through a pad of celite and the solvent was removed under reduced pressure. This was repeated twice with hexanes to remove most of the starting material. The resulting solution in hexanes was filtered through a thin layer of silica (~1 cm) to remove any remaining

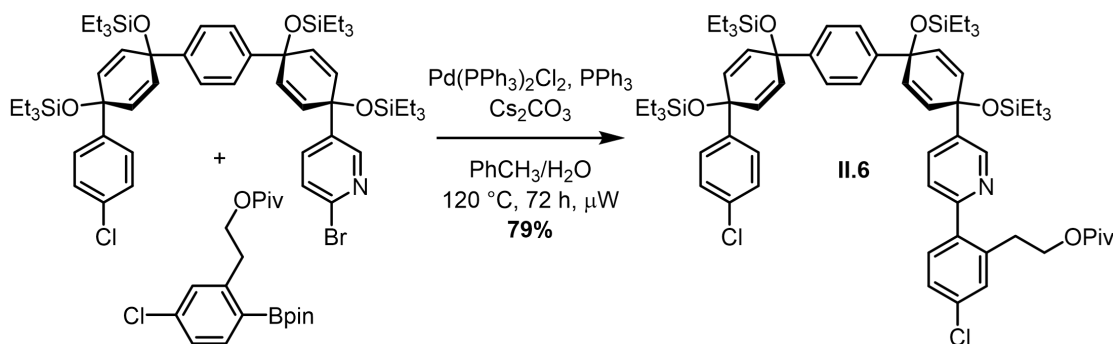
catalyst. The solvent was removed under reduced pressure and the resulting oil was heated under vacuum to sublime any excess B₂pin₂. The desired product was obtained as a colorless oil (2.0 g, 44%). ¹H NMR (500 MHz, Chloroform-*d*) δ 7.82 – 7.66 (d, *J* = 8.1 Hz, 1H), 7.20 (d, *J* = 6.0 Hz, 2H), 4.24 (t, *J* = 6.5 Hz, 2H), 3.20 (t, *J* = 6.6 Hz, 2H), 1.33 (s, 12H), 1.15 (s, 9H). ¹³C NMR (126 MHz, CDCl₃) δ 178.59, 147.14, 137.92, 136.97, 130.56, 126.08, 83.95, 65.59, 38.88, 34.79, 27.33, 25.01. HRMS (ASAP) (*m/z*): [M]⁺ calculated for C₁₉H₂₈BO₄Cl, 366.1769; found 366.1801. IR (neat): 2976, 2933, 2871, 1726, 1590, 1557, 1480, 1459, 1397, 1379, 1372, 1344, 1317, 1281, 1214, 1194, 1143, 1125, 1102, 1070, 1053, 1033, 984, 962, 907, 876, 850, 823, 770, 752.



II.S5. 1,4-dibromo-2,5-phenyldiethyl pivalate. 6.10 g (18.8 mmol, 1 equiv.) of 1,4-dibromo-2,5-phenyldiethanol and 0.46 g (3.77 mmol, 0.2 equiv.) of N,N-dimethyl-4-aminopyridine was added to a flame-dried 250 mL round-bottom flask equipped with stirring. The contents were evacuated and backfilled three times with nitrogen and capped with a rubber septum under an atmosphere of nitrogen. 100 mL of dry THF was added and the mixture was stirred at room temperature while 11.5 mL (56.5 mmol, 3 equiv.) of pivalic anhydride and 4.55 mL (56.5 mmol, 3 equiv.) of dry pyridine were added to the flask. The reaction was stirred overnight at 40 °C under an atmosphere of nitrogen. About 60 mL of DI water was added to quench the reaction, and the THF was removed under reduced pressure. The aqueous layer was extracted three times with 60 mL of ethyl acetate. The organic layer was washed with an aqueous solution of CuSO₄ in water to remove excess pyridine. The organic layer was washed with brine and dried over sodium sulfate. The solvent was removed under reduced pressure to obtain a white greasy solid that was purified via flash column chromatography on silica starting in 5% ethyl acetate in hexanes and finishing with 20% ethyl acetate in hexanes. The desired product was obtained as a white waxy solid (5.60 g, 60%). ¹H NMR (500 MHz, Chloroform-*d*) δ 7.43 (s, 1H), 4.27 (t, *J* = 6.6 Hz, 2H), 3.03 (t, *J* = 6.6 Hz, 2H), 1.16 (s, 9H). ¹³C NMR (126 MHz, CDCl₃) δ 178.41, 137.68, 134.99, 123.10, 62.81, 38.78, 34.64, 27.18. HRMS (ASAP) (*m/z*): [M+H]⁺ calculated for C₂₀H₂₉O₄Br₂, 491.0433; found 491.0435. IR (neat): 3093, 3044, 2970, 2955, 2932, 2870, 1713, 1542, 1474, 1460, 1433, 1397, 1373, 1366, 1325, 1282, 1249, 1229, 1182, 1150, 1054, 1035, 999, 981, 942, 935, 916, 904, 882, 840, 797, 772.

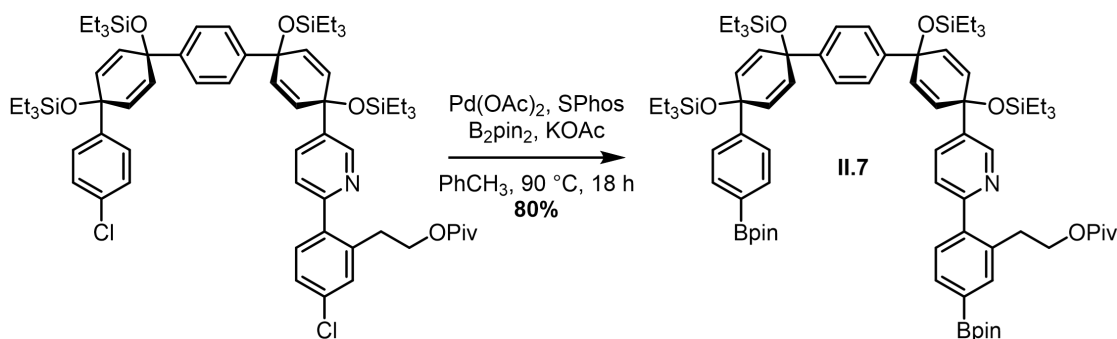


II.5. 1,4-di(boropinacolato)-2,5-phenyldiethyl pivalate. 3.00 g (6.09 mmol, 1 equiv.) of **II.S5**, 6.2 g (24.4 mmol, 4 equiv.) of bis(pinacolato)diboron, 0.068 g (0.305 mmol, 0.05 equiv.) of Pd(OAc)_2 , 0.313 g (0.762 mmol, 0.125 equiv.) of SPhos, and 3.6 g (36.6 mmol, 6 equiv.) of oven-dried potassium acetate were loaded into a 50 mL flame-dried round-bottom flask equipped with stirring. The contents were evacuated and backfilled three times with nitrogen and capped with a rubber septum under an atmosphere of nitrogen. 15 mL of dry toluene was added and the mixture was heated to 90 °C and stirred overnight under an atmosphere of nitrogen. The mixture was removed from heating to cool to room temperature. The contents were diluted with ethyl acetate and filtered through a pad of celite to remove any solids. The resulting solution was concentrated under reduced pressure to afford a dark oil that was sonicated in methanol to obtain the product as a flocculent white solid (2.6 g, 73%) $^1\text{H NMR}$ (600 MHz, Chloroform- d) δ 7.65 (s, 1H), 4.21 (t, $J = 6.7$ Hz, 2H), 3.19 (t, $J = 6.8$ Hz, 2H), 1.32 (s, 11H), 1.15 (s, 9H). $^{13}\text{C NMR}$ (151 MHz, CDCl_3) δ 178.68, 141.93, 138.42, 83.73, 66.15, 38.85, 34.44, 27.39, 25.02. HRMS (ASAP) (m/z): $[\text{M}+\text{H}]^+$ calculated for $\text{C}_{32}\text{H}_{52}\text{B}_2\text{O}_8$, 587.3927; found 587.3983. IR (neat): 2976, 2932, 1723, 1499, 1480, 1458, 1410, 1396, 1379, 1372, 1327, 1301, 1283, 1212, 1142, 1098, 1033, 965, 915, 861, 850, 787, 771, 762, 743.

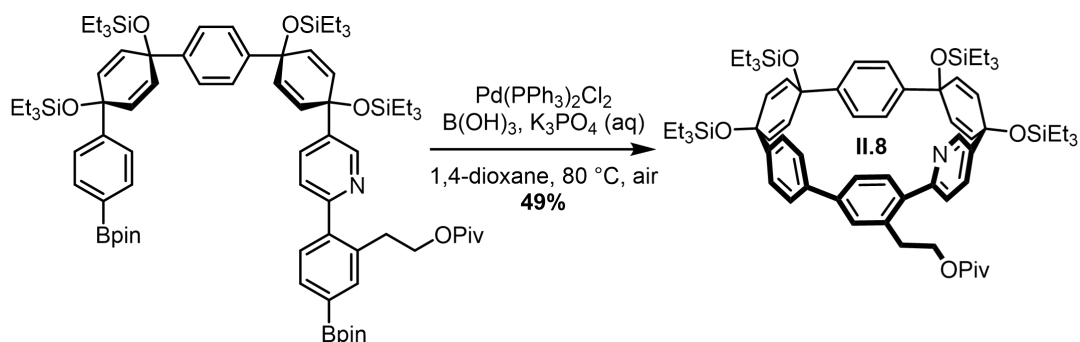


II.6. 1.53 g (1.49 mmol, 1 equiv.) of **II.2** and 0.24 g (0.299 mmol, 0.2 equiv.) of Pd(dppf)Cl_2 were loaded into a 25 mL rb flask equipped with stirring. The contents were evacuated and backfilled three times with nitrogen and capped with a rubber septum under an atmosphere of nitrogen. 0.485 g (1.49 mmol, 1 equiv.) of **II.S3** in 4 mL of toluene and 4 mL of DMF was added under nitrogen. The mixture was sparged with nitrogen for about 30 min. The mixture was heated to 90 °C and 0.8 mL of 2 M K_3PO_4 (aq) was added that was sparged with nitrogen for 1 h before addition. The mixture was stirred for 24 h at 90 °C. The mixture was quenched with water and extracted with diethyl ether three times. The organic layer was washed with 5% LiCl solution then brine. The organic layer was dried over magnesium sulfate and evaporated under reduced pressure to obtain a dark oil. The oil was suspended on celite and purified on a plug of silica using 10% ethyl acetate in hexanes to obtain the product as a colorless oil (1.33 g, 78%). $^1\text{H NMR}$ (500 MHz,

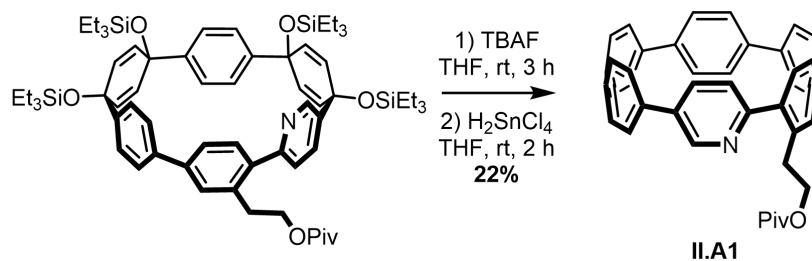
Methylene Chloride- d_2) δ 8.64 (dd, $J = 2.4, 0.9$ Hz, 1H), 7.60 (dd, $J = 8.1, 2.4$ Hz, 1H), 7.35 – 7.15 (m, 12H), 6.13 (d, $J = 10.1$ Hz, 2H), 6.05 – 6.00 (m, 4H), 5.93 (d, $J = 10.1$ Hz, 2H), 4.12 (t, $J = 6.6$ Hz, 2H), 3.03 (t, $J = 6.6$ Hz, 2H), 1.10 (s, 9H), 0.93 (m, 36H), 0.72 – 0.54 (m, 24H). ^{13}C NMR (126 MHz, CD_2Cl_2) δ 178.55, 157.91, 147.80, 145.81, 145.56, 145.35, 140.40, 139.58, 139.21, 134.47, 134.18, 133.27, 132.76, 132.26, 131.87, 131.81, 131.37, 128.64, 127.89, 127.08, 126.45, 126.32, 123.71, 71.78, 71.74, 71.60, 71.01, 64.85, 32.76, 27.46, 7.37, 7.36, 6.98, 6.96, 6.93, 6.90. HRMS (ASAP) (m/z): $[\text{M}+\text{H}]^+$ calculated for $\text{C}_{66}\text{H}_{96}\text{NO}_6\text{Si}_4$, 1180.5692; found 1180.5613. IR (neat): 2953, 2909, 2875, 1727, 1595, 1571, 1480, 1467, 1401, 1377, 1282, 1238, 1189, 1150, 1071, 1004, 959, 881, 859, 820.



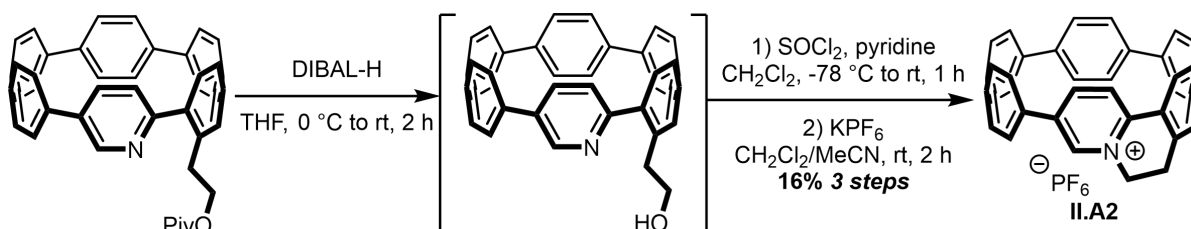
II.7. 1.33 g (1.17 mmol, 1 equiv.) of **II.6** was transferred with 5 mL of dry toluene to a 25 mL flame-dried round-bottom flask equipped with stirring. 0.711 g (2.80 mmol, 2.4 equiv.) of bis(pinacolato)diboron, 0.026 g (0.117 mmol, 0.1 equiv.) of $\text{Pd}(\text{OAc})_2$, 0.120 g (0.292 mmol, 0.25 equiv.) of SPhos, and 0.687 g (7.00 mmol, 6 equiv.) of oven-dried potassium acetate were added, the flask was capped with a rubber septum, and the mixture was sparged with nitrogen for 30 min. The mixture was heated to 90 °C and left to stir under an atmosphere of nitrogen overnight. The flask was removed from heating and left to cool to room temperature before diluting with ethyl acetate and eluting through a pad of celite. The eluent was concentrated under reduced pressure to obtain a yellow-brown oil. The oil was sonicated in 15 mL of methanol to obtain the product as a flocculent white solid (1.23 g, 80%). ^1H NMR (500 MHz, Methylene Chloride- d_2) δ 8.71 (dd, $J = 2.4, 0.8$ Hz, 1H), 7.74 (d, $J = 1.2$ Hz, 1H), 7.66 (dd, $J = 7.5, 1.3$ Hz, 1H), 7.66 – 7.60 (m, 2H), 7.55 (dd, $J = 8.2, 2.4$ Hz, 1H), 7.36 – 7.24 (m, 8H), 6.15 – 6.09 (m, 2H), 6.06 – 5.94 (m, 6H), 4.14 (t, $J = 6.6$ Hz, 2H), 3.04 (t, $J = 6.6$ Hz, 2H), 1.34 (s, 12H), 1.29 (s, 12H), 1.11 (s, 9H), 1.01 – 0.87 (m, 36H), 0.71 – 0.54 (m, 24H). ^{13}C NMR (126 MHz, CD_2Cl_2) δ 178.65, 158.89, 149.67, 147.75, 145.91, 145.38, 143.59, 140.19, 138.23, 136.29, 135.06, 134.35, 133.20, 132.84, 132.14, 131.95, 131.31, 129.84, 126.44, 126.24, 125.72, 123.70, 84.39, 84.26, 72.16, 71.83, 71.65, 71.06, 65.45, 39.09, 32.68, 27.53, 25.26, 25.22, 7.37, 6.94. HRMS (ASAP) (m/z): $[\text{M}+\text{H}]^+$ calculated for $\text{C}_{78}\text{H}_{120}\text{B}_2\text{NO}_{10}\text{Si}_4$, 1180.5692; found 1180.5613. IR (neat): 2956, 2914, 2877, 1726, 1609, 1504, 1458, 1397, 1360, 1321, 1283, 1237, 1212, 1181, 1147, 1107, 1079, 1062, 1052, 1004, 958, 923, 880, 859, 830.



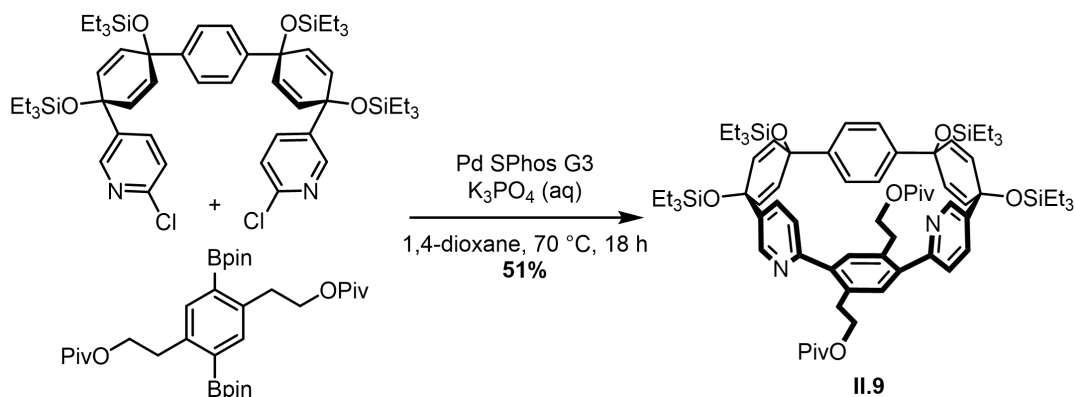
II.8. 0.50 g (0.366 mmol, 1 equiv.) of **II.7** was added to an addition funnel with 30 mL of 1,4-dioxane. 0.113 g (1.83 mmol, 5 equiv.) of boric acid and 0.064 g (0.0916 mmol, 0.25 equiv.) of Pd(PPh₃)₂Cl₂ were added to a 500 mL flask equipped with stirring. 300 mL of 1,4-dioxane was added and the mixture was heated to 80 °C and left to stir open to air for 15 minutes before adding 36 mL of 0.4 M K₃PO₄ (aq). The solution of **II.7** was added dropwise over 30 minutes. The reaction was stirred at 80 °C for 3 hours, but samples taken for NMR analysis showed no further reaction after 1 hour. The flask was removed from heating and the solvent was removed under reduced pressure. The resulting suspension was extracted three times with DCM, the organic layer was washed with brine, dried over sodium sulfate, and evaporated under reduced pressure to yield a dark oil. The mixture was purified via 2000 micron thick preparative silica TLC. The product was eluted from the silica and concentrated under reduced pressure to obtain a colorless oil (0.20 g, 49%). ¹H NMR (500 MHz, Methylene Chloride-*d*₂) δ 8.21 (d, *J* = 2.3 Hz, 1H), 7.85 (dd, *J* = 8.4, 2.3 Hz, 1H), 7.58 (d, *J* = 8.4 Hz, 1H), 7.46 (d, *J* = 2.0 Hz, 1H), 7.41 – 7.36 (m, 3H), 7.29 (d, *J* = 8.6 Hz, 2H), 6.78 (d, *J* = 8.8 Hz, 2H), 6.75 (d, *J* = 8.7 Hz, 2H), 6.21 (dd, *J* = 10.3, 2.5 Hz, 1H), 6.16 (dd, *J* = 10.2, 2.6 Hz, 1H), 6.07 (dd, *J* = 10.1, 2.5 Hz, 1H), 6.00 (dd, *J* = 10.3, 2.5 Hz, 1H), 5.82 (dd, *J* = 10.0, 2.6 Hz, 1H), 5.76 (dd, *J* = 10.2, 2.5 Hz, 1H), 5.60 (dd, *J* = 10.1, 2.5 Hz, 1H), 5.47 (dd, *J* = 10.0, 2.5 Hz, 1H), 4.37 (dt, *J* = 10.7, 6.8 Hz, 1H), 4.29 (dt, *J* = 10.4, 6.6 Hz, 1H), 3.84 (dt, *J* = 13.7, 6.7 Hz, 1H), 3.22 (dt, *J* = 14.0, 6.8 Hz, 1H), 1.16 (s, 9H), 0.93 (dt, *J* = 13.3, 7.9 Hz, 36H), 0.68 – 0.55 (m, 24H). ¹³C NMR (126 MHz, CD₂Cl₂) δ 178.78, 161.11, 145.73, 145.24, 144.75, 143.92, 141.41, 141.29, 139.47, 137.01, 135.97, 135.26, 135.12, 134.38, 133.73, 133.40, 131.88, 130.72, 130.13, 129.48, 128.69, 128.54, 127.23, 125.83, 125.77, 125.63, 119.73, 71.55, 71.19, 70.74, 69.69, 65.82, 39.15, 34.53, 30.28, 27.55, 7.42, 7.38, 7.35, 7.33, 7.07, 7.06, 6.91, 6.86. HRMS (ASAP) (*m/z*): [M+H]⁺ calculated for C₆₆H₉₆NO₆Si₄, 1110.6315; found 1110.6254. IR (neat): 2954, 2909, 2875, 1727, 1583, 1557, 1496, 1458, 1398, 1377, 1283, 1237, 1189, 1151, 1115, 1066, 1004, 957, 878, 859, 821, 801.



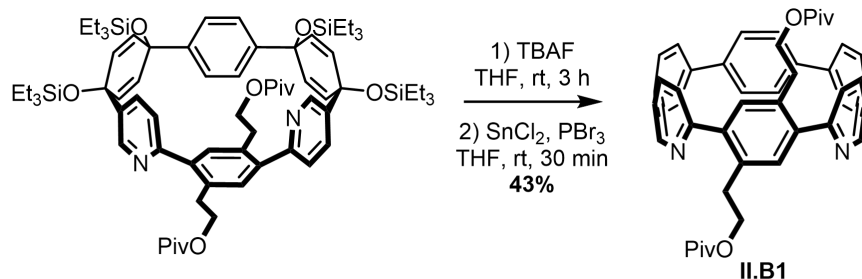
II.A1 (aza[6]CPP benzene ethylpivalate). 0.20 g (0.18 mmol, 1 equiv.) of **II.8** was loaded into a 25 mL round-bottom flask equipped with stirring. The contents were evacuated and backfilled with nitrogen three times and capped with a rubber septum under an atmosphere of nitrogen. 1.0 mL of dry THF was added and the mixture was stirred while 1.08 mL (1.08 mmol, 6 equiv.) of a 1 M solution of tetrabutylammonium fluoride in THF was added. After stirring for three hours, DI water was added to quench the reaction and the resulting precipitate was filtered. The solid was washed with copious amounts of DI water and DCM then placed into a round-bottom flask. A stir bar was added, the contents were evacuated and backfilled three times with nitrogen, and the flask was capped with a rubber septum under an atmosphere of nitrogen. A solution of H₂SnCl₄ in THF was prepared by adding 248 mg (1.10 mmol) of SnCl₂ • 2H₂O into a 25 mL heart-shaped flask. 5 mL of dry THF was added to the heart-shaped flask under nitrogen along with 0.190 mL of concentrated (36%) HCl (aq). The solution was stirred for about 5 minutes. 1.0 mL of dry THF was added to the round-bottom flask and the mixture was stirred while 1.1 mL (0.243 mmol, 2.2 equiv) of the H₂SnCl₄ solution was added dropwise. The reaction was left to stir for 2 hours before quenching with aqueous saturated sodium bicarbonate solution. The mixture was extracted three times using DCM, washed with brine, dried over sodium sulfate, and concentrated under reduced pressure to obtain a pale-orange solid. The crude solid was purified via preparative basic alumina TLC to obtain the desired product as an orange solid (28 mg, 22%). ¹H NMR (600 MHz, Methylene Chloride-*d*₂) δ 8.63 (d, *J* = 2.3 Hz, 1H), 7.85 (ddd, *J* = 9.0, 5.2, 2.2 Hz, 2H), 7.78 – 7.67 (m, 6H), 7.63 (d, *J* = 2.1 Hz, 1H), 7.58 – 7.45 (m, 6H), 7.42 (dd, *J* = 8.9, 2.2 Hz, 1H), 7.33 (dd, *J* = 8.7, 2.1 Hz, 1H), 7.27 (dd, *J* = 8.8, 2.2 Hz, 1H), 7.24 (d, *J* = 8.7 Hz, 1H), 4.48 (dt, *J* = 10.5, 7.0 Hz, 1H), 4.36 (ddd, *J* = 10.6, 7.3, 6.4 Hz, 1H), 4.02 (dt, *J* = 13.6, 6.8 Hz, 1H), 3.32 (dt, *J* = 14.0, 7.1 Hz, 1H), 1.17 (s, 9H). ¹³C NMR (151 MHz, CD₂Cl₂) δ 178.81, 156.24, 148.56, 139.25, 137.71, 137.54, 136.80, 136.50, 136.22, 136.19, 135.99, 135.92, 135.78, 135.33, 133.56, 131.61, 131.13, 130.72, 130.53, 130.30, 129.99, 129.96, 129.72, 129.62, 129.48, 126.59, 126.34, 126.07, 125.94, 125.91, 125.81, 125.67, 125.45, 125.11, 117.64, 66.17, 39.12, 34.66, 30.25, 27.52. HRMS (ASAP) (*m/z*): [M+H]⁺ calculated for C₄₂H₃₅NO₂, 586.2746; found 586.2773. IR (neat): 2956, 2922, 2853, 1719, 1663, 1608, 1569, 1558, 1533, 1516, 1507, 1478, 1456, 1396, 1364, 1283, 1261, 1249, 1200, 1153, 1088, 1033, 1009, 989, 982, 951, 898, 880, 815, 771, 738.



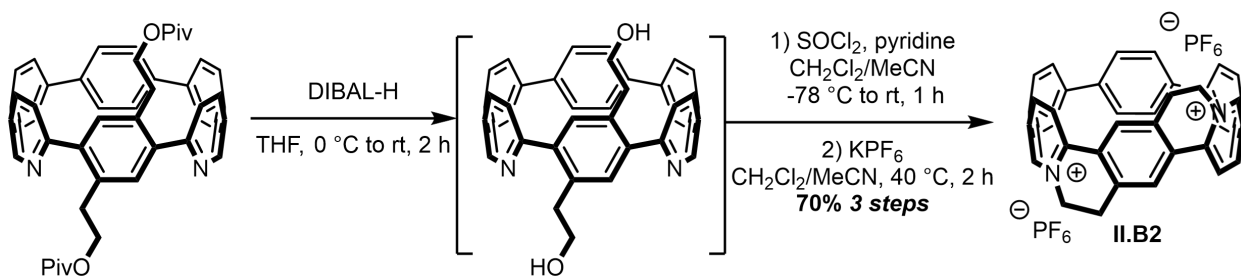
II.A2 (bridged-pyridinium[6]CPP PF₆). 0.012 g (0.021 mmol, 1 equiv.) of **II.A1** was loaded into a 5 ml round-bottom flask equipped with stirring. The contents were evacuated and backfilled three times with nitrogen and the flask was capped with a rubber septum under an atmosphere of nitrogen. 0.5 ml of dry THF was added. The solution was cooled to 0 °C in an ice bath. 0.08 mL (0.082 mmol, 4 equiv.) of 1 M solution of di-*iso*-butylaluminium hydride in hexanes was added dropwise and the ice bath was removed. The reaction was stirred at room temperature for 2 hours. 3 mL of ethyl acetate was added, quenching the reaction. A saturated aqueous solution of sodium potassium tartrate was added, and the mixture was stirred for 10 minutes to break up any emulsion. The mixture was extracted three times with ethyl acetate, washed with brine, dried over sodium sulfate, and concentrated under reduced pressure to yield a red oil. The oil was purified via preparative alumina TLC using 80% DCM and 20% hexanes. The second fraction was eluted with DCM to obtain the alcohol product as a red oil, which was immediately used in the following reaction. Using the round-bottom flask which the oil was concentrated in, a stir bar was added, and the contents were evacuated and backfilled three times with nitrogen. The flask was capped with a rubber septum under a positive pressure of nitrogen. 0.5 mL of dry DCM and 1 drop of dry pyridine was added and the flask was cooled to -78 °C. A 0.5 M solution of freshly-distilled thionyl chloride in dry DCM was prepared. 0.06 mL of the thionyl chloride solution was added to the reaction while stirring. The flask was left to stir at room temperature for 1 hour. All volatile components were removed under high vacuum with a cold trap attached. The resulting dark red solid was dissolved with minimal DCM then precipitated using hexanes. The solid was filtered and washed with water then acetone. The filter paper was washed with DCM to dissolve the chloride salt into a round-bottom flask. 15 mg of KPF₆ in minimal DI water was added and the mixture was stirred for 2 hours at room temperature then filtered. The solution was concentrated under reduced pressure and sonicated with 50% methanol in water solution. The suspension was filtered using a 0.1 mm PTFE syringe filter and eluted with acetone. The solution was concentrated under reduced pressure to obtain a dark-red solid. (2 mg, 16%). ¹H NMR (500 MHz, Acetonitrile-*d*₃) δ 8.80 (d, *J* = 2.1 Hz, 1H), 8.49 (dd, *J* = 9.3, 2.1 Hz, 1H), 8.04 – 7.62 (m, 21H), 4.82 (ddd, *J* = 12.6, 6.2, 2.1 Hz, 1H), 4.65 (td, *J* = 13.2, 6.4 Hz, 1H), 3.66 (ddd, *J* = 19.4, 13.7, 6.2 Hz, 1H), 3.47 – 3.38 (m, 2H). ¹³C NMR (126 MHz, CD₃CN) δ 145.56, 139.04, 138.35, 137.89, 136.08, 135.58, 134.92, 134.36, 133.94, 130.91, 130.39, 129.58, 129.44, 129.36, 129.30, 128.98, 128.91, 128.75, 127.44, 126.84, 126.81, 126.39, 126.36, 126.23, 125.86, 125.64, 125.48, 124.83, 124.20, 123.96, 53.90, 29.31. ¹⁹F NMR (471 MHz, CD₃CN) δ -72.20, -73.70. ³¹P NMR (202 MHz, CD₃CN) δ -137.64, -141.13, -144.61, -148.10, -151.59. HRMS (ASAP) (*m/z*): [M]⁺ calculated for C₃₇H₂₆N⁺, 484.2065; found 484.2020. IR (neat): 3053, 2922, 2853, 1662, 1632, 1603, 1573, 1504, 1486, 1467, 1421, 1383, 1296, 1261, 1250, 1203, 1181, 1161, 1151, 1119, 1081, 1045, 1023, 1005, 920, 894, 873, 817.



II.9. 0.5 g (0.511 mmol, 1 equiv.) of **II.3**, 0.315 g (0.537 mmol, 1.05 equiv.) of **II.5**, and 0.042 g (0.0511 mmol, 10 mol%) of Pd SPhos G3 were added to a 500 mL rb flask equipped with stirring. The contents were evacuated and backfilled with nitrogen three times and the flask was capped with a rubber septum under an atmosphere of nitrogen. 340 mL of dry dioxane was added and the solution was sparged with nitrogen for at least 60 min. The solution was heated to 70 °C and 34 mL of pre-sparged K₃PO₄ was added, and the mixture was stirred overnight. The reaction was removed from heat and cooled to room temperature. The aqueous layer was removed and the dioxane layer was dried over sodium sulfate, filtered, and concentrated under reduced pressure to obtain an orange oil. The crude product was purified via automated flash column chromatography on silica using a gradient of 5% ethyl acetate to 10% ethyl acetate in hexanes. The resulting mixture was heated under vacuum to remove the proto-deborylated **II.5** byproduct. The product was obtained as an oily off-white solid (0.324 g, 51%). ¹H NMR (500 MHz, Methylene Chloride-*d*₂) δ 8.17 (d, *J* = 2.2 Hz, 2H), 7.93 – 7.84 (m, 2H), 7.64 (d, *J* = 8.3 Hz, 2H), 7.12 (s, 2H), 6.82 (d, *J* = 0.9 Hz, 4H), 6.18 (dd, *J* = 10.2, 2.5 Hz, 2H), 6.03 (dd, *J* = 10.3, 2.4 Hz, 2H), 5.80 (dd, *J* = 10.1, 2.5 Hz, 2H), 5.51 (dd, *J* = 10.0, 2.4 Hz, 2H), 4.27 (dt, *J* = 10.7, 6.7 Hz, 2H), 4.18 (dt, *J* = 10.7, 6.6 Hz, 2H), 3.82 (dt, *J* = 13.8, 6.7 Hz, 2H), 3.12 (dt, *J* = 13.9, 6.7 Hz, 2H), 1.14 (d, *J* = 1.0 Hz, 17H), 0.94 (dt, *J* = 12.7, 7.8 Hz, 36H), 0.63 (dq, *J* = 8.8, 6.9, 6.3 Hz, 24H). ¹³C NMR (126 MHz, CD₂Cl₂) δ 178.71, 160.61, 145.40, 144.54, 141.80, 137.36, 136.89, 136.58, 135.91, 135.67, 134.75, 129.52, 129.13, 128.10, 125.83, 119.88, 71.33, 70.08, 65.71, 39.10, 34.04, 27.52, 7.37, 7.36, 7.02, 6.86. HRMS (ASAP) (*m/z*): [M]⁺ calculated for C₇₂H₁₀₆N₂O₈Si₄, 1238.7026; found 1238.6990. IR (neat): 2954, 2910, 2875, 1726, 1683, 1582, 1553, 1539, 1495, 1479, 1458, 1398, 1373, 1283, 1237, 1188, 1150, 1114, 1068, 1004, 956, 875, 858, 831, 760.

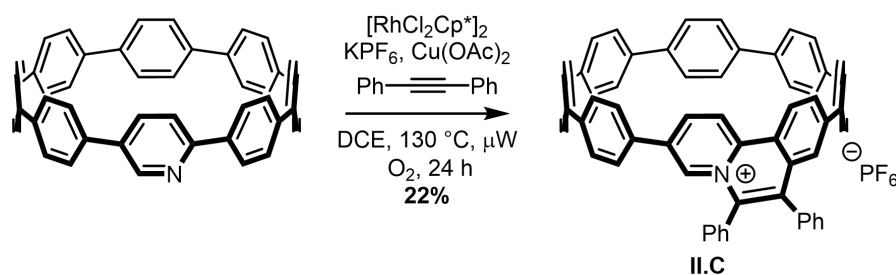


II.B1 (diaza[6]CPP benzene diethylpivalate). 0.360 g (0.290 mmol, 1 equiv.) of **II.9** was added to a 25 mL round-bottom flask equipped with stirring. The contents were evacuated and backfilled three times with nitrogen and the flask was capped with a rubber septum under flow of nitrogen. 3 mL of THF and 1.6 mL (1.45 mmol, 5 equiv.) of a 1 M solution of tetrabutyl ammonium fluoride in THF were added and mixture was stirred for 3 hours at room temperature. Water was added and the mixture was sonicated before filtering. The solid was then washed with DCM and transferred to a round-bottom flask equipped with stirring for the following reaction. 240 mg (1.34 mmol, 5 equiv.) of SnCl₂ was added. The contents were evacuated and backfilled with nitrogen three times and the flask was capped with a rubber septum under a flow of nitrogen. 10 mL of dry THF was added and the mixture was stirred while 0.05 mL (0.800 mmol, 3 equiv.) of phosphorous tribromide (neat) was added. The mixture became dark red and was stirred for 30 min. The reaction was quenched with saturated sodium bicarbonate and extracted with ethyl acetate three times. The organic layer was washed with brine, dried over sodium sulfate, and concentrated under reduced pressure to afford a cloudy red oil. The material was purified via an alumina preparative plate using 2% ethyl acetate in DCM. The product was then eluted and concentrated to afford red crystals. (90 mg, 43%). ¹H NMR (600 MHz, Methylene Chloride-*d*₂) δ 8.70 (d, *J* = 2.3 Hz, 2H), 7.89 – 7.68 (m, 10H), 7.62 – 7.47 (m, 4H), 7.42 (s, 2H), 7.39 (dd, *J* = 8.9, 2.2 Hz, 2H), 4.41 (dt, *J* = 10.5, 7.1 Hz, 2H), 4.31 (dt, *J* = 10.6, 6.6 Hz, 2H), 4.13 (dt, *J* = 13.5, 6.7 Hz, 2H), 3.24 (dt, *J* = 14.1, 7.2 Hz, 2H), 1.14 (s, 12H). ¹³C NMR (126 MHz, CD₂Cl₂) δ 178.25, 147.15, 137.27, 135.87, 135.14, 133.05, 132.69, 130.70, 129.84, 128.86, 128.07, 126.55, 126.38, 125.55, 118.11, 65.44, 38.56, 34.73, 26.98. HRMS (ASAP) (*m/z*): [M]⁺ calculated for C₄₈H₄₆N₂O₄, 714.3458; found 714.3383. IR (neat): 2957, 2930, 2852, 1717, 1674, 1557, 1529, 1478, 1456, 1396, 1362, 1282, 1261, 1253, 1228, 1148, 119, 1082, 1033, 1012, 990, 940, 888, 872, 815, 770, 751, 737, 708, 637, 622, 612, 592, 581, 576, 573, 566, 562, 557, 553.

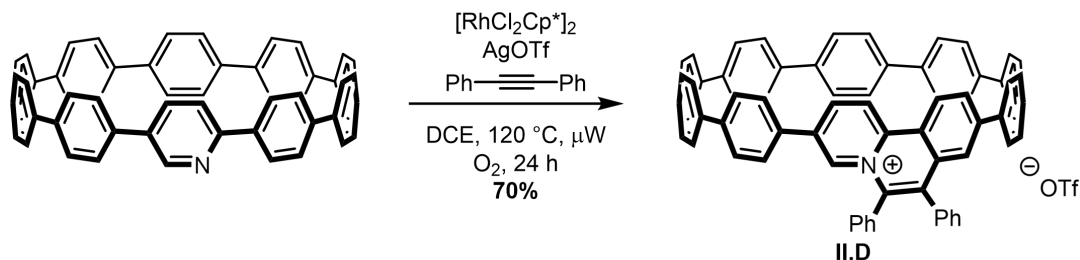


II.B2 di(bridged-pyridinium)[6]CPP PF₆. 0.090 g (0.126 mmol, 1 equiv.) of **II.B1** was loaded into a 25 mL round-bottom flask equipped with stirring. The contents were evacuated and backfilled three times

with nitrogen then capped with a rubber septum under an atmosphere of nitrogen. 5 ml of dry THF was added. The solution was cooled to 0 °C in an ice bath. 1.0 mL (1.01 mmol, 8 equiv.) of 1 M solution of diisobutylaluminium hydride in hexanes was added dropwise and the ice bath was removed. The reaction was stirred at room temperature for 2 hours. A saturated aqueous solution of sodium potassium tartrate was added to quench the reaction and stirred for 30 minutes to assist with extraction. The mixture was extracted three times with ethyl acetate, washed with brine, and dried over sodium sulfate. The organic solution was concentrated under reduced pressure to yield a red oil. The oil was purified via preparative basic alumina plate and immediately continued to the next reaction. The red oil was loaded into a 25 mL round-bottom flask equipped with stirring. The contents were evacuated and backfilled three times with nitrogen then capped with a rubber septum under an atmosphere of nitrogen. 4.6 mL of dry DCM, 4.6 mL of dry acetonitrile, and 0.037 mL (0.461 mmol, 4 equiv.) of dry pyridine was added and the mixture was stirred at -78 °C. 1.84 mL (0.922 mmol, 8 equiv.) of a 0.5 M solution of thionyl chloride in dry DCM was added dropwise. The mixture was removed from the cold bath and stirred at room temperature for 1 hour. The mixture was concentrated under high vacuum with a cold trap attached to remove solvent and excess thionyl chloride. The resulting dark purple solid was dissolved in minimal DCM then precipitated by adding 10 mL of hexanes. The dark solid was filtered and washed with hexanes then acetone. The solid was dissolved with 10 mL DCM and the solution was transferred to a round-bottom flask equipped with stirring. 10 mL of acetonitrile and 0.284 g (1.54 mmol, 15 equiv.) of KPF₆ in minimal DI water was added and the mixture was stirred at 40 °C for 2 hours. The solvent was removed under reduced pressure and redissolved in minimal acetonitrile. The mixture was filtered, and the acetonitrile was removed under reduced pressure. Minimal acetone was added to dissolve the solid, hexanes was added to precipitate the product, and the suspension was vacuum filtered. The solid was then washed with DCM then methanol then water then methanol then DCM again to remove any inorganic salts and impurities. The resulting product was isolated as a dark purple-brown solid. (65 mg, 79%). ¹H NMR (500 MHz, Acetonitrile-*d*₃) δ 8.96 (d, *J* = 2.2 Hz, 2H), 8.65 (dd, *J* = 9.3, 2.2 Hz, 2H), 8.40 (d, *J* = 9.3 Hz, 2H), 8.06 (s, 2H), 8.01 – 7.94 (m, 6H), 7.95 – 7.89 (m, 4H), 7.84 (dd, *J* = 9.1, 2.3 Hz, 2H), 4.81 – 4.74 (m, 4H), 3.58 (dt, *J* = 16.7, 7.4 Hz, 2H), 3.49 (dt, *J* = 16.7, 6.9 Hz, 2H). ¹³C NMR (151 MHz, CD₃CN) δ 145.00, 141.91, 140.14, 139.55, 137.71, 136.10, 135.99, 133.06, 130.99, 129.84, 129.63, 129.59, 129.33, 129.07, 128.76, 128.50, 126.45, 55.21, 28.32. ¹⁹F NMR (471 MHz, CD₃CN) δ -72.09, -73.59. ³¹P NMR (202 MHz, CD₃CN) δ -134.11, -137.59, -141.09, -144.57, -148.06, -151.55, -155.04. HRMS (ES+) (*m/z*): [M+PF₆]⁺ calculated for C₃₈H₂₈N₂F₆P, 657.1894; found 657.1890. IR (neat): 3100, 2924, 1575, 1553, 1506, 1490, 1459, 1427, 1383, 1359, 1297, 1273, 1256, 1213, 1196, 1164, 896, 877, 817, 740, 733, 716, 705, 690, 678, 653, 617, 607, 590, 573, 554.



II.C isoquinolinium[8]CPP PF₆. 0.010 g (0.0164 mmol, 1 equiv.) of **aza[8]CPP** was loaded into a microwave vial equipped with stirring. Following this, 0.002 g (0.00328 mmol, 0.2 equiv.) of [RhCl₂Cp*]₂, 0.015 g (0.082 mmol, 5 equiv.) of KPF₆, 0.003 g (0.0164 mmol, 1 equiv.) of diphenylacetylene, 0.007 g (0.0344 mmol, 2.1 equiv.) of Cu(OAc)₂ were added sequentially to the vial. The contents were sparged with oxygen gas for 5 minutes to ensure a thoroughly mixed solution under an oxygen atmosphere. An appropriate volume of dry DCE was added to the mixture. The flask was then sealed and subjected to microwave irradiation at 130 °C for a period of 24 hours. After completion of the reaction, the mixture was allowed to cool to room temperature. It was then diluted with a sufficient volume of DCM to assist in the extraction process. The mixture was filtered through cotton to remove any solid impurities and obtain a clear filtrate. The filtrate was transferred to a preparative thin-layer chromatography plate pre-coated with silica and eluted with 10% methanol in DCM. After separation, the product-containing band was identified as an orange band and isolated from the plate with 5% methanol in DCM. The isolated product was dissolved in a minimal amount of DCM and filtered through a 0.1 μm syringe filter to remove any remaining silica. This solution was transferred to a rotary evaporator where it was concentrated under reduced pressure to remove the solvent and obtain a concentrated product as an orange solid. (3.4 mg, 22%). ¹H NMR (600 MHz, Acetonitrile-*d*₃) δ 8.90 (d, *J* = 9.6 Hz, 1H), 8.66 (d, *J* = 9.2 Hz, 1H), 8.66 (dd, *J* = 9.6, 1.8 Hz, 1H), 8.40 (d, *J* = 1.8 Hz, 1H), 8.34 (dd, *J* = 9.3, 1.9 Hz, 1H), 7.66 (d, *J* = 1.9 Hz, 1H), 7.66 – 7.58 (m, 24H), 7.53 – 7.47 (m, 4H), 7.44 – 7.40 (m, 6H). ¹³C NMR (151 MHz, CD₃CN) δ 143.71, 140.21, 139.58, 138.20, 138.06, 137.73, 137.59, 137.17, 137.08, 136.91, 136.65, 136.31, 136.03, 135.36, 134.96, 134.83, 133.39, 133.34, 132.95, 130.92, 130.63, 130.36, 129.83, 129.79, 129.50, 128.80, 128.59, 128.08, 127.96, 127.49, 127.44, 127.40, 127.36, 125.85, 125.18, 123.78, 123.02. ¹⁹F NMR (471 MHz, CD₃CN) δ -72.22, -73.72. ³¹P NMR (202 MHz, CD₃CN) δ -137.64, -141.13, -144.62, -148.11, -151.60. HRMS (ES⁺) (*m/z*): [M]⁺ calculated for C₆₁H₄₀N⁺, 788.3311; found 788.3345. IR (neat): 3027, 2927, 2853, 1706, 1596, 1456, 1379, 1255, 1223, 1154, 1075, 1030, 1003, 815, 756.



II.D isoquinolinium[10]CPP OTf. 0.018 g (0.0236 mmol, 1 equiv.) of **aza[10]CPP**, 0.0046 g (0.0260 mmol, 1.1 equiv.) of diphenylacetylene, 0.0015 g (0.00236 mmol, 0.1 equiv.) of $[\text{RhCl}_2\text{Cp}^*]_2$, and 0.013 g (0.0496 mmol, 2.1 equiv.) of silver trifluoromethylsulfonate were added a microwave reaction vial equipped with stirring. 2.3 mL of 1,2-dichloroethane was added and the mixture was sparged with pure oxygen for 5 minutes. The mixture was heated to 150 °C in the microwave reactor for 18 hours. The reaction was cooled to room temperature then diluted with DCM. The mixture was washed with water then brine and dried over sodium sulfate. Solvent was removed under reduced pressure and the resulting dark orange solid was purified via preparative silica TLC using 10% methanol in DCM as the eluent. An Orange band was removed with 5% methanol in DCM and the solvent was removed under reduced pressure to obtain the product as an orange solid. (18 mg, 70%). ^1H NMR (500 MHz, Acetonitrile- d_3) δ 9.05 (d, J = 9.5 Hz, 1H), 8.79 (d, J = 9.2 Hz, 1H), 8.71 (dd, J = 9.5, 1.9 Hz, 1H), 8.54 (d, J = 1.8 Hz, 1H), 8.35 (dd, J = 9.2, 2.0 Hz, 1H), 7.73 (d, J = 1.9 Hz, 1H), 7.70 – 7.59 (m, 32H), 7.52 – 7.38 (m, 10H). ^{13}C NMR (126 MHz, CD_3CN) δ 145.11, 142.02, 141.31, 139.81, 139.23, 138.98, 138.77, 138.61, 138.18, 137.70, 136.51, 135.44, 134.81, 134.61, 134.21, 132.33, 131.99, 131.59, 129.74, 129.66, 129.10, 128.87, 128.79, 128.67, 128.41, 128.38, 128.36, 128.32, 127.06, 125.53, 124.95, 124.25. ^{19}F NMR (471 MHz, CD_3CN) δ -79.33. HRMS (ES+) (m/z): $[\text{M}]^+$ calculated for $\text{C}_{73}\text{H}_{48}\text{N}^+$, 938.3787; found 938.3854. IR (neat): 3044, 2973, 2918, 2013, 1991, 1960, 1733, 1683, 1616, 1558, 1506, 1456, 1419, 1373, 1264, 1084, 1021, 895, 733.

II.7. Co-authored content

The work in Chapter 2 was co-authored with Dylan Nguyen, Victor Salpino, Luca Zocchi, Dr. Lev Zakharov, and Prof. Ramesh Jasti and is in preparation for submission. I drafted the manuscript and performed most of the synthesis and characterization. Dylan Nguyen helped with synthesis and collection of absorption spectra of **isoq[8]CPP** and helped draft the supplementary information. Victor Salpino assisted with screening reaction conditions for C-H activation of aza[n]CPPs. Luca Zocchi helped develop synthetic routes to **bp[6]CPP**. Dr. Lev Zakharov solved crystal structure data for the molecules presented. Prof. Ramesh Jasti edited the manuscript.

II.8. Bridge to Chapter 3

Development of new nitrogen-doped nanohoops have resulted in molecules with unique redox properties due to the electron-accepting pyridinium units. Introduction of nitrogen atoms in a cooperative geometry can also be used to make nanohoop ligands. Chapter 3 addresses the optoelectronic consequences of placing three pyridyl-units adjacent to each other to form a 2,2':6',2''-terpyridine fragment within the nanohoop backbone and its resulting iridium (III) 2-phenylpyridine complex.

III.1. Introduction:

As the global energy demand increases, the need for renewable energy harvesting materials will grow and promote the investigation of new materials.^{1-3,6,72} Dye-sensitized solar cells (DSSCs) represent a cheap and scalable option for capturing solar energy due to the material properties intrinsic to organic dyes.^{5,10,112} Bipyridine or terpyridine metal complexes are common organic dyes present in DSSCs because of the broad visible absorption associated with the metal to ligand charge transfer (MLCT) event. Ligands are typically redox active to facilitate the flow of electrons from dye molecule to the anode, via photoinduced electron transfer, while a redox mediator transfers an electron to the oxidized dye molecule. Terpyridine ligands are particularly appealing due to their multiple accessible reduction potentials.¹¹³⁻¹¹⁸ This allows for better band alignment for electron transfer to the photoanode.

Cycloparaphenylenes represent an interesting scaffold for ligand incorporation due to their shortened HOMO-LUMO gap, increased solubility, and intrinsic curvature that distorts typical ligand geometries.^{79,94,119-124} Strong absorbing properties of CPPs make them viable candidates for exploring photoinduced electron transfer processes relevant to DSSCs. Incorporation of multiple pyridyl units into the backbone of nano hoops results in a variety of ligand topologies. The first examples included 2,2'-bipyridyl (bipy) units that bind metals in a bidentate fashion (Figure III.1). Our lab demonstrated that bipy[n]CPPs have electronic properties different from linear bipy ligands due to the curved geometry and narrow HOMO-LUMO gap.^{94,122}

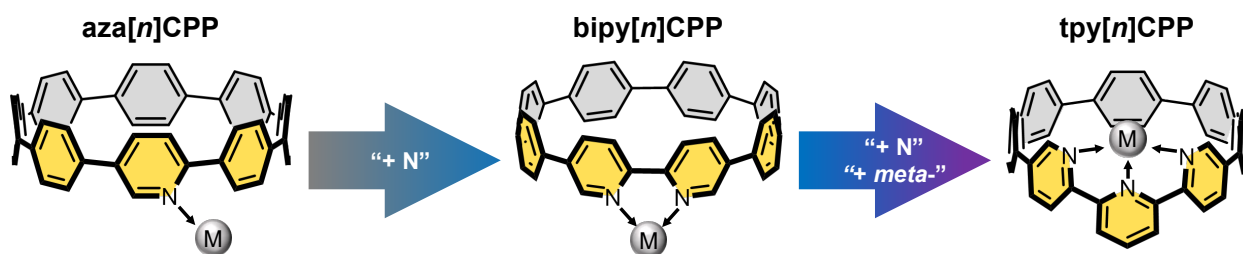


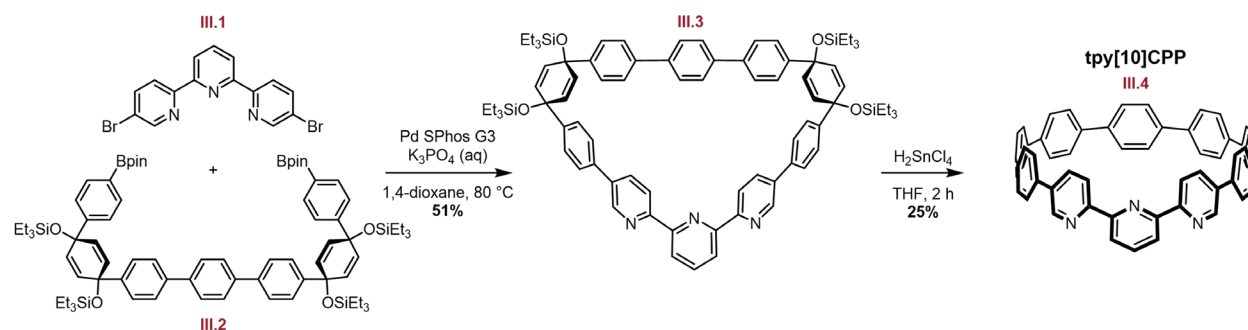
Figure III.1. Summary of established cycloparaphenylene ligand developed by our lab, presenting terpyridine[n]CPPs (tpy[n]CPPs) as a new ligand topology.

It stands that other ligand geometries could be explored to study the effect of the curved π -system on the MLCT, ligand to metal charge-transfer (LMCT), and magnetic properties. Three pyridyl units denoted as a 2,2':6',2"-terpyridine (tpy) fragment is of interest because of the large body of research and increasing interest for metal-tpy complexes for their applications in supramolecular chemistry and as dyes for DSSCs.^{5,114,118,125-127} Tpy ligands are notably difficult to functionalize due to the limited routes to assemble the three pyridyl groups in the correct orientation. Incorporation of a tpy fragment into a nano hoop should change the binding geometry and the frontier molecular orbitals (FMOs) associated with their optoelectronic properties. This offers a unique way to functionalize the tpy fragment via geometric deformation and incorporation of inherent strain. Due to the geometry of the fragment, the metal should also bind in the pore

of the hoop, see Figure III.1. These factors motivate investigating the feasibility of a series of tpy[n]CPP and how metal coordination affects the electronic properties of the nano hoop. Investigation of the absorbance and emission spectra is presented to understand how the π -system and bent ligand geometry compare to the flat tpy ligand. Electrochemical measurements of the nano hoop and resulting complex are also presented to understand how the redox-active tpy fragment affects the redox properties of the parent nano hoop and resulting complex.^{114,128}

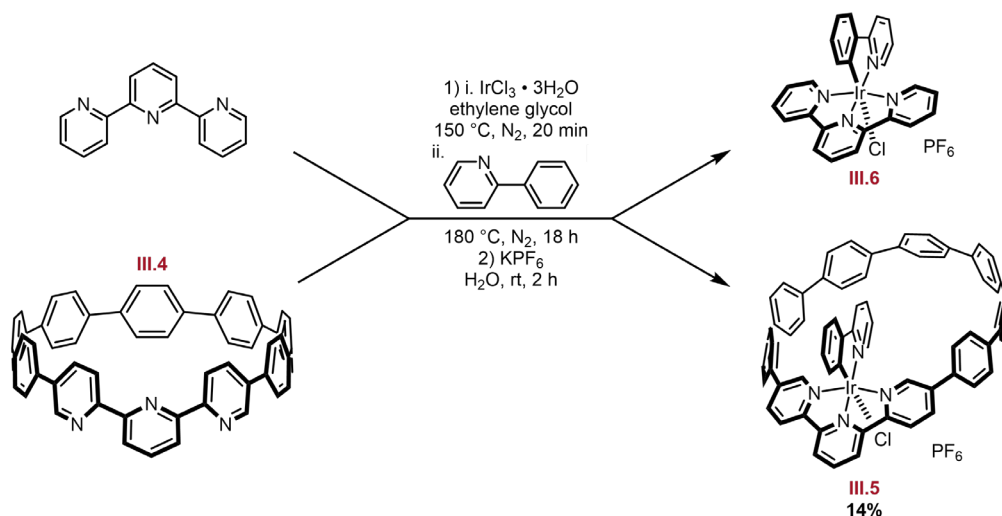
III.2. Results and discussion

A modified published synthesis of functionalized tpy fragments^{129,130} was used to arrive at the core 5,5''-dibromo-2,2':6',2''-terpyridine (**III.1**) in good yields, shown in Scheme III.1. We envisioned multiple target nano hoops with a tpy fragment accessible with this dibromide tpy derivative. Hoops that map onto a *m*[8]CPP, *m*[9]CPP, and *m*[10]CPP would illustrate the size-dependent and geometry-dependent properties of their respective metal complexes. Synthesis of **tpy[10]CPP** produced the most promising results, following a Suzuki cross-coupling route that was successful at making the macrocycle in moderate yields; however, the macrocycle was not stable enough for chromatography. Deprotection and aromatization of **III.3** was successful in good yields to obtain **tpy[10]CPP** (**III.4**), and the structure was confirmed by single-crystal X-ray diffraction (Scheme III.1).



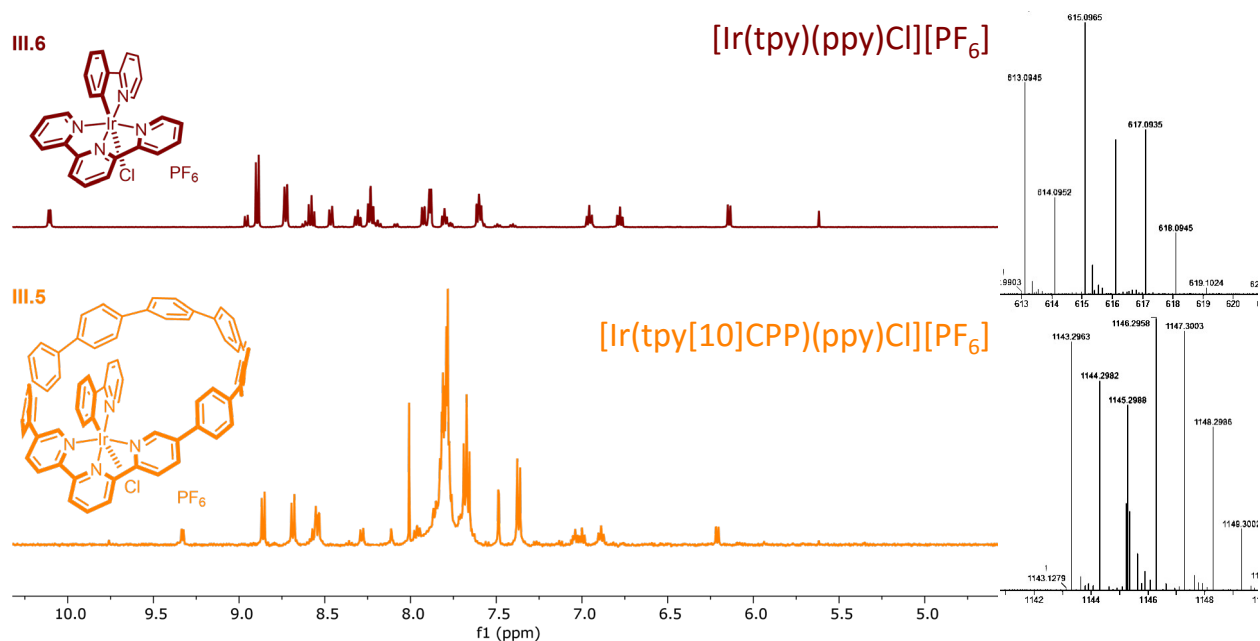
Scheme III.1. Synthesis of **tpy[10]CPP** **III.4** from coupling partners reported in the literature.

Metalation of the tpy[10]CPP was inspired by common terpyridine-metal complexes in literature to best compare the effects from the curved π -system. Fe(II) and Ru(II) complexes are the most appealing because of their broad visible absorption profiles relevant for application in DSSCs.^{5,5,113,131} Ir(III)(2-phenylpyridine) derivatives were also of interest for their luminescent properties and how they would converge with the optical properties of a nano hoop ligand.^{132–134} Initial attempts to form heteroleptic Ru(II) and Fe(II) complexes with 2,2':6',2''-terpyridine resulted in the decomposition of the nano hoop and the formation of homoleptic tpy-complexes. Attempts to complex iridium with tpy[10]CPP were successful, much more stable, and isolable. Refluxing tpy[10]CPP with iridium trichloride trihydrate in ethylene glycol followed by addition of 2-phenylpyridine (ppy) and then KPF₆ in water provided the [Ir(tpy[10]CPP)(ppy)Cl][PF₆] complex as a dark yellow solid that precipitated upon cooling (Scheme III.2).¹³⁴



Scheme III.2. Synthesis of $[\text{Ir}(\text{tpy})(\text{ppy})\text{Cl}][\text{PF}_6]$ **III.6** and $[\text{Ir}(\text{tpy}[10]\text{CPP})(\text{ppy})\text{Cl}][\text{PF}_6]$ **III.5** using the same reaction conditions reported in the literature.¹³⁴

^1H NMR spectra of the nanohoop complex and the literature complex show very similar splitting patterns while many of the shifts coalesce in the nanohoop complex. ^{19}F and ^{31}P NMR show shifts in the correct region in both complexes **III.5** and **III.6** to support successful anion exchange and coordination by the pyridine on the ppy ligand. Mass spectrometry data shows the presence of both complexes as the complete cationic structure—without the PF_6 ion (Figure III.2). The samples were prepared as 10 ppm solutions in acetone and infused via electrospray ionization (ESI) with source parameters around 4.0 mA current and 60 mV cone voltage.



III.3. X-ray crystallography

Single crystals suitable for diffraction were grown by slow diffusion of pentane into chloroform. The structure shows tubular packing with distorted pentane molecules inside the pore. Pyridine units in the terpyridine fragment are distorted from coplanarity unlike in crystal structures of 2,2':6',2''-terpyridine. Distortion of the terpyridine fragment in tpy[10]CPP is characterized by dihedral angles of 33.1° and deviation from planarity of 35° induced by the nano hoop backbone (Figure III.3).

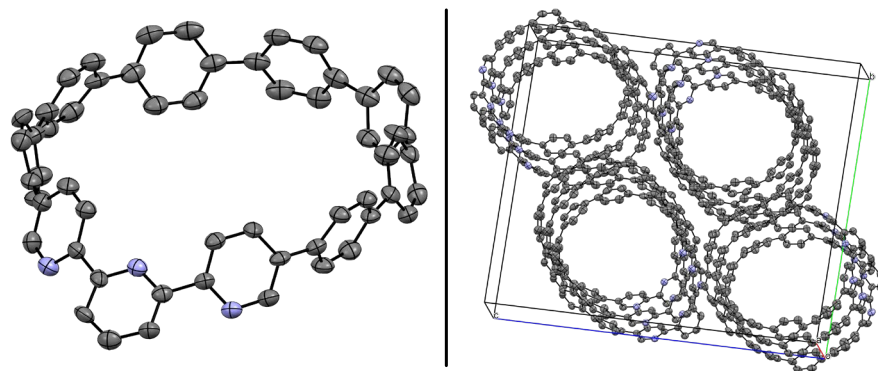


Figure III.3. Single crystal x-ray diffraction results of **tpy[10]CPP** III.4 shown in ORTEP drawings, single molecule on the left and packing structure on the right.

III.4. Optical properties of nano hoop and small molecule

The absorbance and fluorescence spectra of **tpy[10]CPP** and 2,2':6',2''-terpyridine were obtained in dichloromethane. Terpyridine alone has a broad absorbance in the UV and broad, relatively weak, violet fluorescence. Optically, the tpy nano hoop has characteristics more like *m*[10]CPP than the small molecule terpyridine (Figure III.4). This is due to the dominating characteristics of the bent phenylene backbone, which localizes the HOMO while the LUMO is localized onto the terpyridine portion.

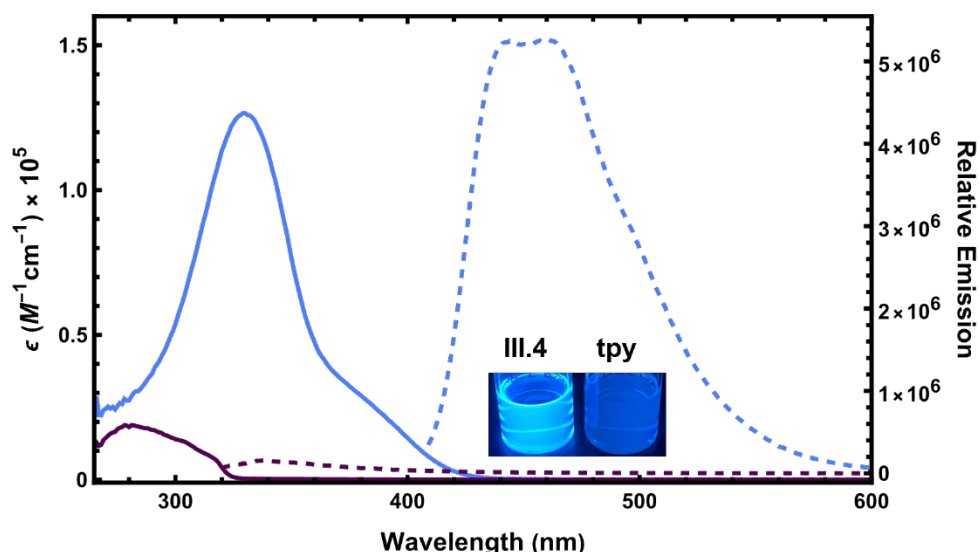


Figure III.4. Absorbance and fluorescence spectra of **tpy[10]CPP** and 2,2':6',2''-terpyridine in dichloromethane. Absorbance profile presented as molar absorptivity ($10^5 \text{ M}^{-1} \text{ cm}^{-1}$) and emission presented in relative intensity at identical concentrations. Inlays show each molecule in dichloromethane.

The coordination geometry and resulting optical properties should be notably different for any nanohoop complex compared to the small molecule complex, since the inherent curvature of the nanohoop backbone will be retained in any organometallic complex with $\text{tpy}[n]\text{CPPs}$. The absorbance and emission profiles of the small molecule and nanohoop complexes were obtained to study how the curvature and electronic properties of the nanohoop affect the optical properties compared to the small molecule analogue. Overall, the molar absorptivity of the nanohoop complex is much larger than the small molecule complex. This is typical for nanohoop structures due to the large π -system of the phenylene backbone, so the same $\pi \rightarrow \pi^*$ transitions are retained in the complex. The broad sloping shoulder around 500 nm extends to the onset of the small molecule's absorbance profile (Figure III.5), suggesting a similar origin of transition. It is established in literature as a mixture of MLCT and ILCT in the small molecule complex,^{132,134} but computational results suggest more MLCT and LMCT character for the nanohoop complex as the HOMO is localized on the bent phenylene backbone. Inverse to the non-metalated terpyridine derivatives, the iridium-phenylpyridine chloride complexes show intense emission from the small molecule complex and much less intense emission from the nanohoop complex. Observationally, cooling solutions of each complex to -196°C increases the brightness of their emission (Figure III.5).

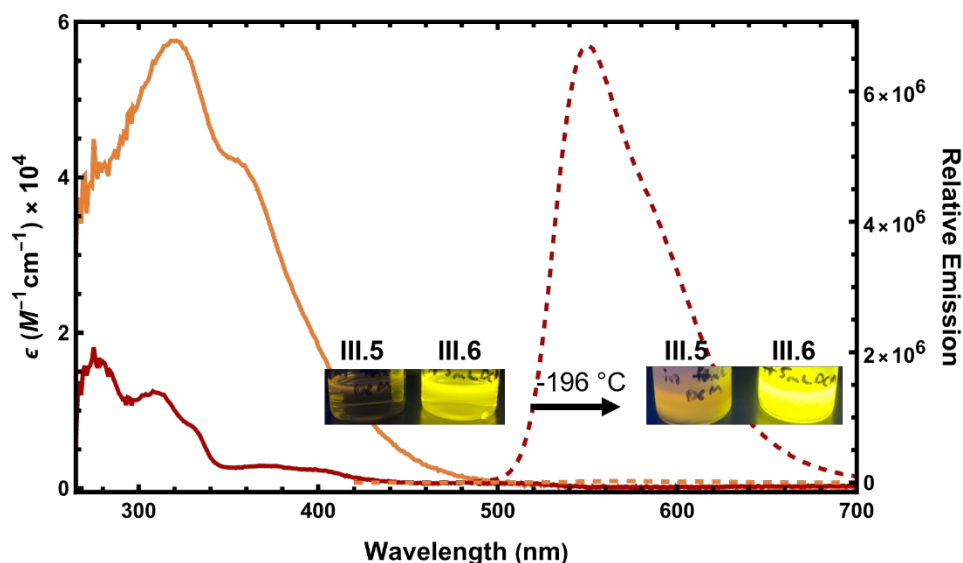


Figure III.5. Absorbance and emission profiles of **III.5** and **III.6** in acetonitrile. Absorbance profiles shown in molar absorptivity ($10^5 \text{ M}^{-1} \text{ cm}^{-1}$) and emission profiles in relative intensity at identical concentrations. Inlays show solutions of both complexes in acetonitrile at room temperature and -196°C .

III.5. Electrochemical properties

Cyclic voltammetry was used to determine how the nanohoop contributes to the reduction of the iridium complex. 2,2':6',6''-terpyridine alone has an irreversible reduction in acetonitrile around at -2.57 V , but $\text{tpy}[10]\text{CPP}$ has a pseudo-reversible reduction around -2.29 V in acetonitrile, see Figure III.6 (left). The curvature of the nanohoop is expected to lower the reduction potential by bending the terpyridine fragment, which directly lowers the LUMO. Unexpectedly, the presence of the terpyridine unit inside the nanohoop backbone slightly stabilizes the reduction such that we see pseudo-reversibility. The iridium(2-

phenylpyridine)chloride complexes of each terpyridine derivative have reversible reduction events in acetonitrile. The waves are very similar to each other, but the nanohoop complex has earlier and broader waves than the small molecule complex. **III.5** has a first reduction wave at -1.36 V whereas **III.6** has a first reduction wave at -1.43 V, and it is more defined and spatially separated from the second reduction event (Figure III.6, right).

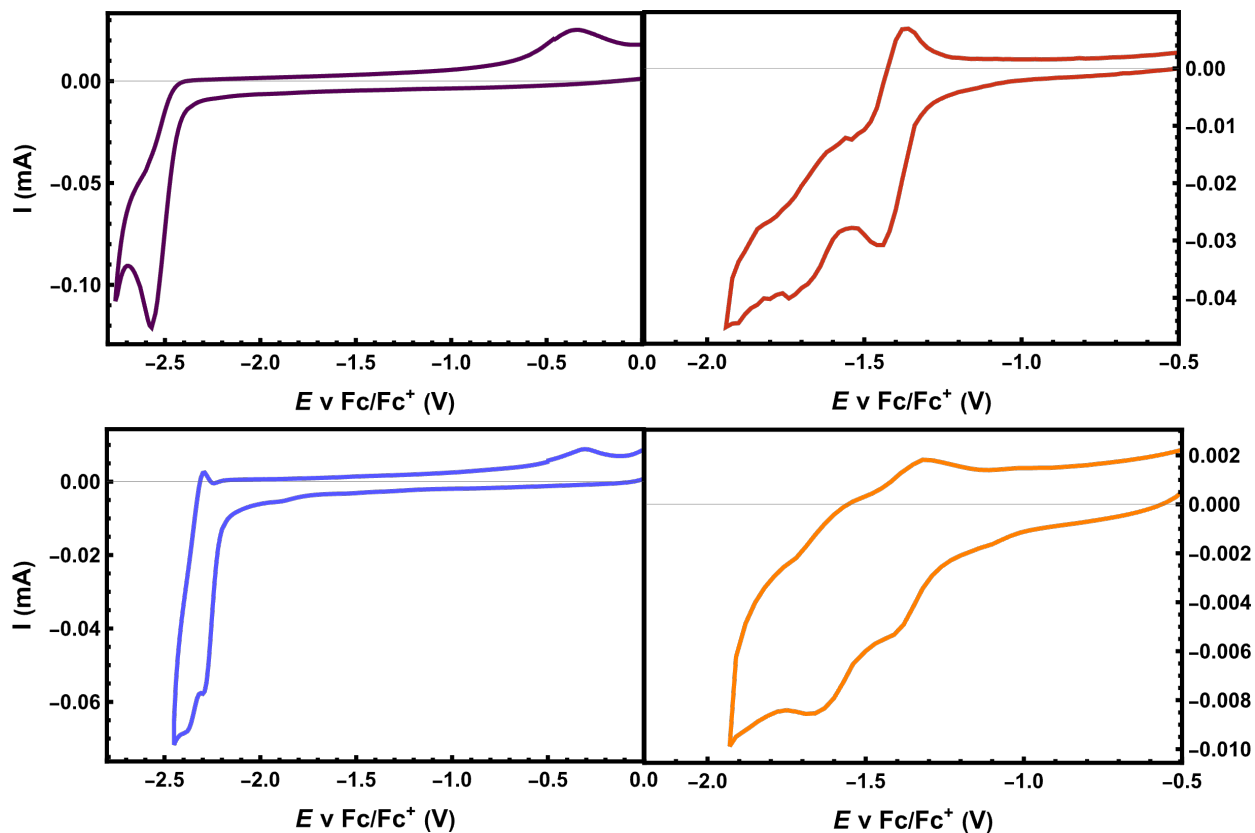


Figure III.6. Cyclic voltammograms of 2,2':6',2''-terpyridine (top left), **III.6** (top right), **III.4** (bottom left), **III.5** (bottom right) in acetonitrile; supporting electrolyte: 0.2 M Bu₄NPF₆, scan rate: 0.2 V/s. All potentials are referenced to the Fc/Fc⁺ redox couple.

III.6. Computational results

Computational results were obtained using the Gaussian 09 package with B3LYP/LANL2DZ as the functional and basis set.¹⁰⁶ Both complexes were investigated computationally using DFT methods to understand which processes are responsible for the optical and electrochemical properties. Starting with the molecular orbitals, Ir(tpy)(ppy)Cl (**III.6**) has a HOMO localized on the ppy ligand and LUMO localized on the tpy ligand, but the nanohoop complex has a HOMO localized on the bent phenylene portion of the nanohoop while the LUMO is localized on the tpy fragment on the nanohoop (Figure III.7).

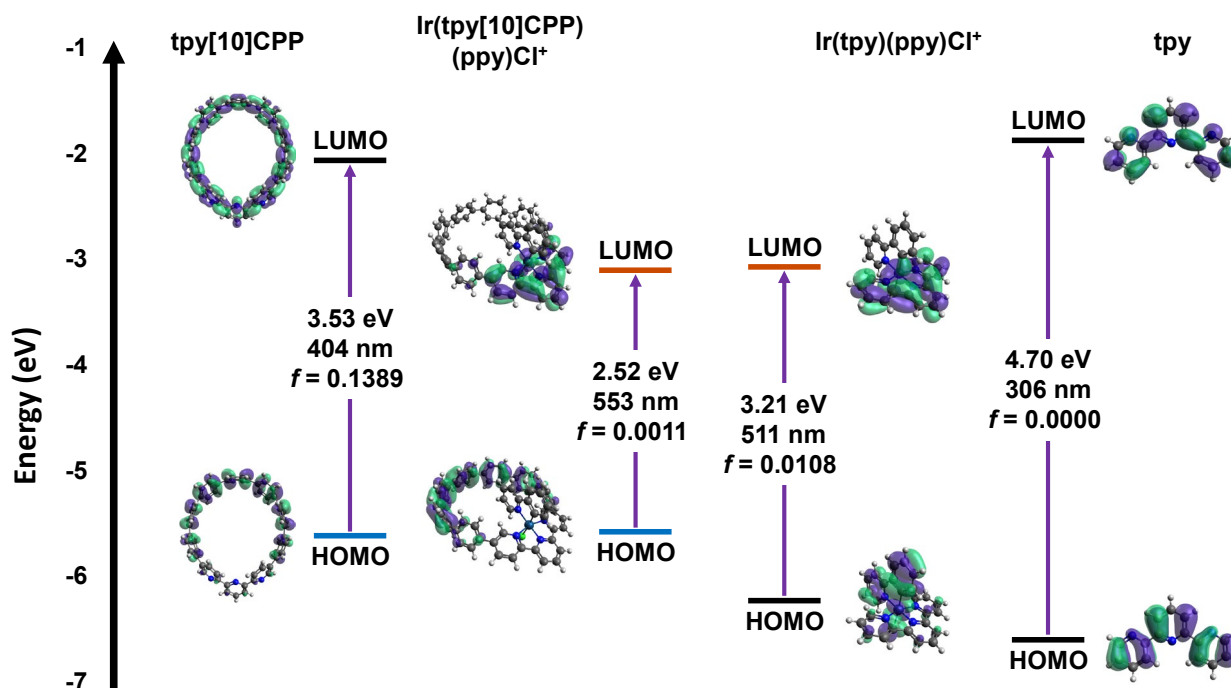


Figure III.7. TD-DFT calculations of **tpy[10]CPP**, **III.5**, **III.6**, and 2,2':6',2''-terpyridine (**tpy**) showing the HOMO-LUMO gap and individual energies. The predicted wavelength of the lowest transition is provided above the predicted oscillator strength. Images of the molecular orbitals are shown for each molecule (isosurface value of 0.03).

Energetically, the non-metalated ligands have larger HOMO-LUMO gaps and no discernable charge-transfer characteristics. Upon metalation to form the iridium complexes discussed, the HOMO-LUMO gaps decrease drastically (~1.5 eV for **III.6**). The nanohoop complex **III.5** retains the HOMO energy as the **tpy[10]CPP** but has a LUMO energy that aligns with the LUMO of **III.6**. This is consistent with D-A nanohoops since the HOMO is localized on the bent phenylene portion of the macrocycle. Nanohoop complexes with finely tuned energy gaps can be made following this principle, because the HOMO energy is controlled by the number of phenylenes. Smaller **tpy[n]CPPs** would make complexes with smaller HOMO-LUMO gaps—as is typical with all nanohoop analogues—but the LUMO will remain at the same energy level, localized onto the terpyridine-Ir center. The intensity of the absorption profiles for both the ligands and complexes can also be explained by the oscillator strengths of the lowest energy transition. Nanohoops have much stronger absorptions than their small molecule analogue and this is reflected by the oscillator strengths of 0.1389 for **tpy[10]CPP** and 0.0000 for 2,2':6',2''-terpyridine (smaller than four significant digits). Computationally, we can find nanohoop complexes with intense absorption profiles in the visible region as possible dyes in DSSC or absorption peaks at desirable wavelengths for photoredox catalysis.

III.7. Conclusion

A new type of nanohoop ligand incorporating a terpyridine fragment has been synthesized in moderate yields. This new ligand can bind metals in a tridentate binding motif towards the pore of the nanohoop. An iridium (III) 2-phenylpyridine complex **III.5** was successfully made using **tpy[10]CPP** and

characterized by ^1H NMR, UV-vis and fluorescence spectroscopy, ESI-MS, and cyclic voltammetry. These experimental results were compared to the small molecule analogue **III.6** to observe any emergent properties from the nanohoop complex. This is corroborated with TD-DFT simulations. Overall, the HOMO-LUMO gap decreases due to the increase HOMO energy level from the bent phenylene backbone of the nanohoop. The molar absorptivity is much larger for the nanohoop complex, as has been reported in the literature for nanohoop structures in comparison to their small molecule analogues. Surprisingly, the emission of the nanohoop complex is much less compared to the small molecule complex. This is likely due to intermolecular charge-transfer which dominates D-A nanohoos presented in the literature. Electrochemically, nanohoop complex **III.5** has similar reduction events to **III.6**, since the major contribution of the LUMO resides primarily on the terpyridine fragment on the nanohoop. We plan to explore more tpy[*n*]CPP complexes and possible synthetic routes to tpy[*n*]CPP catenanes in the future, with the hope of discovering novel charge-transfer interactions with metals binding within the pore of these macrocycles.

III.8. General experimental details

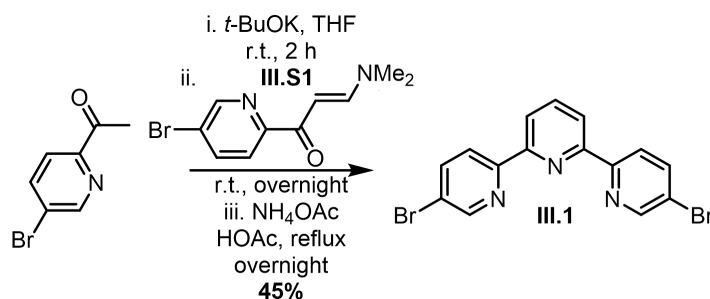
All glassware was flame dried and cooled under an inert atmosphere of nitrogen unless otherwise noted. Moisture sensitive reactions were carried out under nitrogen atmosphere using Schlenk and standard syringe/septa techniques. Tetrahydrofuran, dichloromethane, and 1,4-dioxane were dried by filtration through alumina according to the methods described by Grubbs.¹⁰⁷ Silica column chromatography was conducted with Zeochem Zeoprep 60 Eco 40-63 μm silica gel. Automated flash chromatography was performed using a Biotage Isolera One. Thin Layer Chromatography (TLC) was performed using Sorbent Technologies Silica Gel XHT TLC plates. Developed plates were visualized using UV light at wavelengths of 254 and 365 nm. ^1H NMR spectra were recorded at 500 MHz or 600 MHz on a Bruker Advance-III-HD NMR spectrometer. ^{13}C NMR spectra were recorded at 150 MHz on a Bruker Advance-III-HD NMR spectrometer. All ^1H NMR spectra were taken in CDCl_3 (referenced to TMS, δ 0.00 ppm, or residual chloroform, δ 7.26 ppm), methylene chloride- d_2 (referenced to residual methylene chloride, δ 5.32 ppm), or acetone- d_6 (referenced to residual acetone, δ 2.05 ppm). All ^{13}C NMR spectra were taken in CDCl_3 (referenced to chloroform, δ 77.16 ppm), methylene chloride- d_2 (referenced to methylene chloride, δ 53.84 ppm), or acetone- d_6 (referenced to residual acetone, δ 118.31 ppm). Mass spectra were obtained from University of Oregon CAMCOR using ASAP or ESI. HRMS was attempted for all compounds, but when not successful, LRMS is reported. Absorbance and fluorescence spectra were obtained in a 1 cm Quartz cuvette with dichloromethane or acetonitrile using an Agilent Cary 100 UV-Vis spectrometer and a Horiba Jobin Yvon Fluoromax-4 Fluorimeter. All reagents were obtained commercially unless otherwise noted. Compounds **III.S1**,¹²⁹ **III.S2**,¹³⁵ **III.6**,¹³⁴ and Pd SPhos Gen III¹¹¹ were prepared according to literature procedure.

III.8.1 Computational details

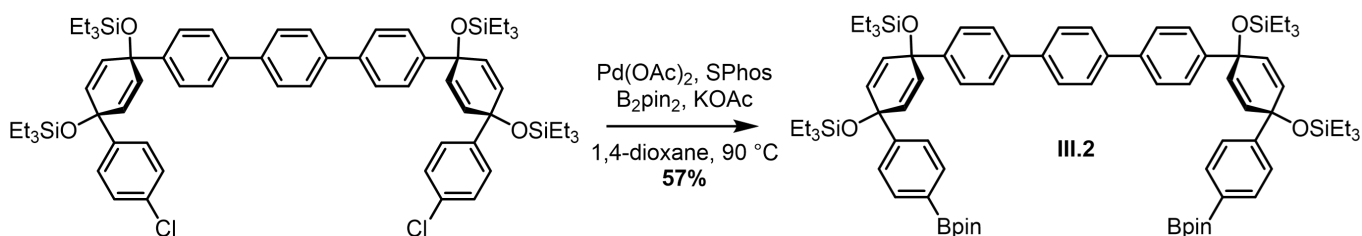
Using Gaussian09 software, computations were performed using Density Functional Theory (DFT) at the B3LYP/LANL2DZ level of theory.¹⁰⁶ All results were solvated using the self-consistent reaction field

using the default Polarizable Continuum Model method with the dielectric constant for dichloromethane or acetonitrile. All output files are available at: <https://figshare.com/s/3ede21ff78ea71473e86>

III.8.2. Synthesis and characterization

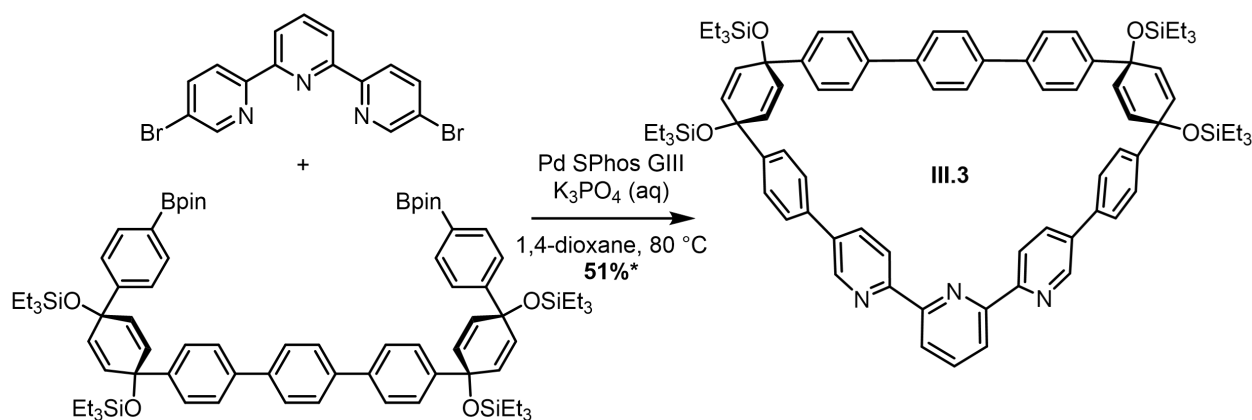


III.1 5,5''-dibromo-2,2':6',2''-terpyridine. Following a similar reported procedure, 3.38 g (16.9 mmol, 1 equiv.) of 5-bromo-2-acetylpyridine and 2.84 g (25.3 mmol, 1.5 equiv) of dry potassium tert-butoxide were added to a 250 mL flame-dried round bottom flask equipped with stirring. The contents were evacuated and backfilled with nitrogen three times and capped with a rubber septum under an atmosphere of nitrogen. 40 mL of dry THF was added and the mixture was stirred for at least 2 hours before adding a 20 mL solution of 4.30 g (16.9 mmol, 1 equiv.) **III.S1** in dry THF. The reaction was stirred overnight at room temperature. 13 g (169 mmol, 10 equiv.) of ammonium acetate and 40 mL of glacial acetic acid were added to the reaction flask, the mixture was refluxed open to air. The reaction was refluxed overnight and the THF in the reaction mixture was distilled or open to air to remove from the reaction. The mixture was cooled to room temperature and added to a saturated solution of sodium carbonate in DI water. The solution was completely neutralized before extracting three times with dichloromethane. The organic layer was washed with brine, dried over sodium sulfate, and the solvent was removed under reduced pressure to obtain a dark solid. Crude solids were purified via flash column chromatography on basic alumina with a gradient of 10% toluene in hexanes to 50% toluene in hexanes. The product fractions were concentrated to a pink solid (3.20 g, 49%). ¹H NMR (500 MHz, Chloroform-*d*) δ 8.74 (d, *J* = 2.3 Hz, 2H), 8.48 (d, *J* = 8.5 Hz, 2H), 8.43 (d, *J* = 7.8 Hz, 2H), 7.99 – 7.93 (m, 3H).

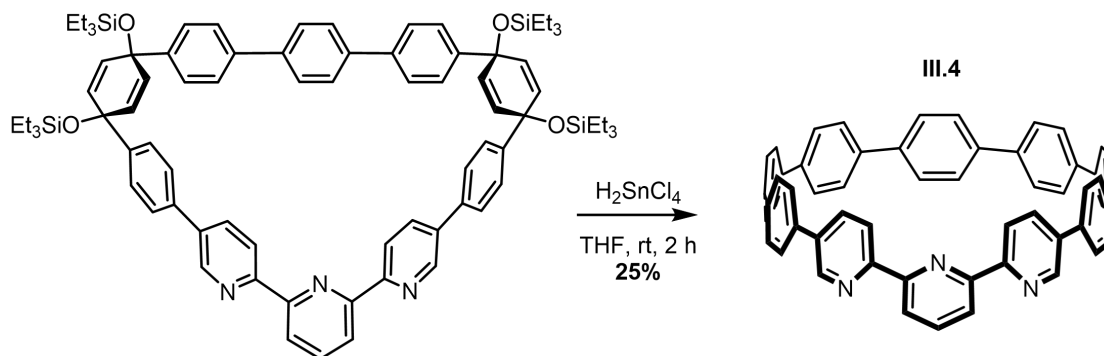


III.2. 3.50 g (3.10 mmol, 1 equiv.) of **III.S2**, 1.97 g (7.75 mmol, 2.5 equiv.) of bis(pinacolato)diboron, 0.035 g (0.155 mmol, 0.05 equiv.) of Pd(OAc)₂, 0.159 g (0.388 mmol, 0.125 equiv.) SPhos, and 1.83 g (18.6 mmol, 6 equiv.) of potassium acetate were loaded into a flame-dried round bottom flask equipped with stirring. The contents were evacuated and backfilled with nitrogen three times and capped with a rubber septum under an atmosphere of nitrogen. 8 mL of dry 1,4-dioxane were added and the mixture was heated

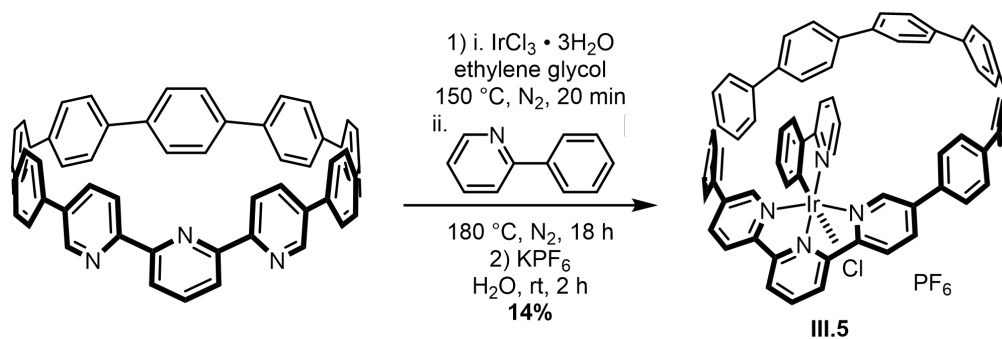
to 90 °C. The mixture was heated and stirred overnight. The reaction was cooled to room temperature and diluted with ethyl acetate before filtering through a pad of celite and eluted with more ethyl acetate. The solvent was removed under reduced pressure to obtain a dark oil that was sonicated in methanol to obtain a flocculant white solid. The solid was filtered to obtain the desired product. (2.30 g, 57%). ¹H NMR (500 MHz, Chloroform-*d*) δ 7.73 (d, *J* = 8.3 Hz, 4H), 7.65 (s, 4H), 7.54 (d, *J* = 8.5 Hz, 4H), 7.41 (d, *J* = 6.1 Hz, 4H), 7.40 (d, *J* = 6.0 Hz, 4H), 6.01 (s, 8H), 1.34 (s, 24H), 0.95 (dt, *J* = 16.1, 7.9 Hz, 36H), 0.62 (dq, *J* = 27.1, 7.9 Hz, 24H).



III.3. 0.503 g (0.384 mmol, 1 equiv.) of **III.2**, 0.150 g (0.384 mmol, 1 equiv.) of **III.1**, and 0.030 g (0.0384 mmol, 0.1 equiv.) of Pd SPhos GIII were added to a 500 mL round bottom flask equipped with stirring. The contents were evacuated and backfilled with nitrogen three times and capped with a rubber septum under an atmosphere of nitrogen. 255 mL of 1,4-dioxane was added and the mixture was sparged with nitrogen for 1 hour. The mixture was stirred and heated to 80 °C for 15 minutes before adding 25.5 mL of pre-sparged 2 M K₃PO₄ in water. The reaction was stirred under heat overnight. The mixture was cooled to room temperature and filtered through a pad of celite with a layer of sodium sulfate at the top via decanting the upper organic layer. The eluent was evaporated under reduced pressure to obtain a tan oil. The oil was sonicated in ethanol and cooled in the freezer before filtering a tan solid. The solid was not purified any further due to instability via chromatographic methods. (0.25* g, 51%*). ¹H NMR (500 MHz, Chloroform-*d*) δ 8.95 (d, *J* = 2.2 Hz, 2H), 8.39 (d, *J* = 8.2 Hz, 2H), 8.18 (d, *J* = 7.7 Hz, 2H), 8.03 (d, *J* = 7.7 Hz, 1H), 7.99 (dd, *J* = 8.3, 2.3 Hz, 2H), 7.67 (s, 4H), 7.50 (d, *J* = 2.9 Hz, 4H), 7.49 (d, *J* = 2.9 Hz, 4H), 7.39 (d, *J* = 8.4 Hz, 4H), 7.32 (d, *J* = 8.3 Hz, 4H), 6.11 – 6.05 (m, 8H), 0.99 (dt, *J* = 19.2, 8.0 Hz, 36H), 0.67 (dq, *J* = 24.1, 8.0 Hz, 24H).



III.4 tpy[10]CPP. 0.135 g (0.105 mmol, 1 equiv.) of **III.3** was added to a 25 mL round bottom flask. The contents were evacuated and backfilled with nitrogen three times and capped with a rubber septum under an atmosphere of nitrogen. 2.0 mL of dry THF was added and the mixture was stirred at room temperature. A solution of H_2SnCl_4 in THF was prepared by adding 248 mg (1.10 mmol) of $\text{SnCl}_2 \cdot 2\text{H}_2\text{O}$ into a 25 mL heart-shaped flask. 5 mL of dry THF was added to the heart-shaped flask under nitrogen along with 0.190 mL of concentrated (36%) HCl (aq). 2.1 mL (0.462 mmol, 4.2 equiv) of the H_2SnCl_4 solution was added dropwise. The mixture was stirred for one hour before quenching the reaction with 2 M NaOH in DI water. The reaction mixture was extracted five times with dichloromethane. Organic fractions were combined and washed with brine, dried over sodium sulfate, then the solvent was evaporated under reduced pressure to obtain a pale yellow solid. (20 mg, 25%). ^1H NMR (500 MHz, Methylene Chloride- d_2) δ 8.88 (d, $J = 2.2$ Hz, 2H), 8.06 (dd, $J = 7.9, 4.8$ Hz, 4H), 7.98 (dd, $J = 8.5, 7.0$ Hz, 1H), 7.74 (dd, $J = 8.3, 2.3$ Hz, 2H), 7.69 (d, $J = 8.6$ Hz, 4H), 7.66 (d, $J = 8.7$ Hz, 4H), 7.64 – 7.56 (m, 17H), 7.55 (d, $J = 8.5$ Hz, 3H). ^{13}C NMR (126 MHz, CD_2Cl_2) δ 157.59, 157.19, 146.95, 139.58, 139.37, 138.80, 138.70, 138.54, 138.14, 137.12, 136.83, 136.22, 128.59, 128.14, 128.08, 127.99, 127.96, 127.81, 127.79, 123.12, 120.64. HRMS (ASAP) (m/z): $[\text{M}+\text{H}]^+$ calculated for $\text{C}_{57}\text{H}_{37}\text{N}_3$, 764.3066; found 764.3019.



III.5. 0.020 g (0.0262 mmol, 1 equiv.) of **tpy[10]CPP** and 0.011 g (0.0288 mmol, 1.1 equiv.) of iridium (III) chloride trihydrate were loaded into a flame-dried round bottom flask equipped with stirring. The contents were evacuated and backfilled with nitrogen three times and capped with a rubber septum under an atmosphere of nitrogen. 3 mL of dried ethylene glycol stored over 3 Å molecular sieves was added to the flask, the mixture was heated to 150 °C, and stirred for 20 minutes before adding 0.005 mL (0.0314 mmol, 1.2 equiv.) of 2-phenylpyridine. The reaction was heated to 180 °C and stirred overnight. The mixture

was cooled to room temperature and poured into 3 mL of DI water with 0.048 g (0.262 mmol, 10 equiv.) of potassium hexafluorophosphate. The mixture was stirred at room temperature for 2 hours before diluting with 20 mL of DI water. 20 mL of dichloromethane was added to the mixture and the aqueous layer was extracted with dichloromethane two more times. The organic layers were combined and washed with brine, dried over sodium sulfate, and evaporated under reduced pressure to obtain a yellow solid. The solid was dissolved with acetone, filtered through a 0.1 μm syringe filter, diluted with hexanes, and filtered through a 0.1 μm syringe filter again. The filter was washed with acetone then evaporated under reduced pressure to obtain the product as a yellow solid. (4 mg, 14%). ^1H NMR (500 MHz, Acetone- d_6) δ 9.33 (d, J = 5.7 Hz, 1H), 8.86 (d, J = 8.2 Hz, 2H), 8.69 (d, J = 8.4 Hz, 2H), 8.60 – 8.51 (m, 2H), 8.28 (d, J = 8.2 Hz, 1H), 8.11 (s, 1H), 8.01 (s, 2H), 7.82 – 7.78 (m, 16H), 7.67 (t, J = 8.5 Hz, 8H), 7.49 (d, J = 2.1 Hz, 2H), 7.40 – 7.34 (m, 4H), 7.04 (t, J = 6.4 Hz, 1H), 7.00 (t, J = 7.2 Hz, 1H), 6.89 (t, J = 7.2 Hz, 1H), 6.21 (d, J = 7.6 Hz, 1H). ^{19}F NMR (471 MHz, Acetone) δ -71.70, -73.20. ^{31}P NMR (202 MHz, Acetone) δ -137.17, -140.66, -144.16, -147.65, -151.15. HRMS (ESI+) (m/z): [M-PF $_6$] $^+$ calculated for C $_{68}$ H $_{45}$ N $_4$ $^{193}\text{Ir}^+$, 1145.2962; found 1145.2981.

III.9. Bridge to Chapter 4

Since novel properties of nanohoop structures have a strong dependency on their inherent strain, methods to quantify and detail the strain of these structures is vital to future development of interesting functional materials. StrainViz has continued to be a reliable tool for quantifying the total and visualizing the local strain of macrocycles for in-depth analysis of how strain affects the optoelectronic and chemical properties of a variety of structures. My mentor Dr. Curtis Colwell developed this tool and taught me how to use it during my early graduate career, as well as let me contribute to the publication with some experimental work. The next chapter is this publication reformatted to introduce the tool before my work utilizing it to help explain the reactivities of alkyne-containing cycloparaphenylenes.

CHAPTER IV

STRAIN VISUALIZATION FOR STRAINED MACROCYCLES

IV.1. Introduction

Strain has a unique impact on molecular properties and reactivity. Macrocyclic strain is leveraged in chemical biology for bioorthogonal reactivity^{136,137} and in polymer chemistry for ring opening metathesis.^{138,139} Additionally, graphitic macrocycles, such as carbon nanohoops,¹⁴⁰ have enhanced solubility,^{49,141} remarkable photophysical properties,^{24,142} and reactivity^{143–146} that all arise from strain. These attributes, and improvements in methods for their synthesis,^{103,147–149} have caused a renewed interest in strained macrocyclic molecules. While methods for probing solubility and photophysical properties are well established, macrocyclic strain is a challenging characteristic to analyze and quantify. The best-known methods for calculating macrocyclic strain energy (the potential energy released upon breaking the macrocycle) compare heat of formation for strained and unstrained molecules in a theoretical strain releasing reaction.^{150–152} While combustion calorimetry can be used,^{153,154} computationally determined energies are now standard due to the quality of current computational methods and the challenge of obtaining accurate experimental results. It has become routine to report the calculated strain energy of new strained macrocycles with their synthesis due to the fundamental effects of this tension.

Total strain energies are commonly reported and the strain in specific parts of the molecule cannot be discerned. While the total strain energy does provide some information, it does not correlate perfectly to reactivity. For example, when the same amount of strain energy is spread over more atoms, the molecule is more stable than when it is concentrated in fewer atoms. If this is corrected for by dividing by the total atoms, non-participating atoms artificially lower the strain energy per atom determined. Local strain can sometimes be inferred in highly symmetric molecules, such as strain per phenylene in a cycloparaphenylene. However, non-symmetric molecules have unevenly distributed strain energy leading to locations of higher reactivity that may be unintuitive. Some alternative metrics have been devised to measure local strain. For example, the distortion of an aromatic ring, torsional angle in a biphenyl segment, and bond lengths can be compared to an unstrained comparative molecule.^{38,103} For non-planar π -systems, a measure of pyramidalization was developed that estimates relative strain in non-planar aromatics such as corannulene and fullerene.^{155,156} However, these measurements are not quantitative and, therefore, cannot be compared across molecules which limits their utility. Even when combining total strain calculation with these other metrics, it results in an incomplete depiction of molecular strain energy.

A method that determines strain both quantitatively and locally is quite useful. Therefore, a computational method was developed that identifies the quantity of strain energy local to every coordinate (bond, angle, and torsional angle) in a molecule. This strain visualization software is called StrainViz and has been made freely available. A similar method was previously reported for mechanochemistry where unstrained molecules are stretched and the tension that appears upon stretching is analyzed.¹⁵⁷ Attempts were made to apply this method to macrocycles by comparing stretched and unstretched macrocycles as well as conformational changes that induce stretching,^{158,159} however, the inherent strain was not

addressed. StrainViz can find this elusive strain energy. Our new method was evaluated to establish its accuracy using prior calculated strain energies and experimental reaction results from the literature. It is freely available on GitHub.¹⁶⁰ The resulting computational method provides an interactive and insightful strain map. Knowledge of specific strain location facilitates and enhances synthetic efforts towards strained macrocycles by providing the exact and specific impact on strain of structural changes in a molecule. As is demonstrated herein with StrainViz, it is now possible to make inferences about the local properties and reactivity in strained molecules.

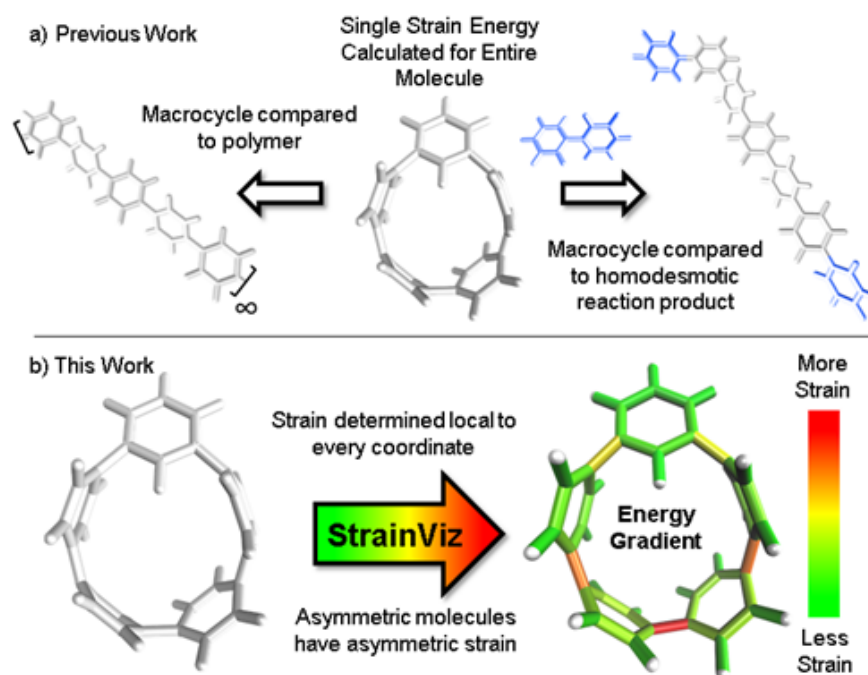


Figure IV.1. a) Strain energy is calculated by comparing the strained molecule to an unstrained polymer or homodesmotic reaction product resulting in a single strain energy for the entire molecule. b) StrainViz determines strain energy local to every coordinate.

IV.2. Computational methods

This new computational method is fundamentally an advancement on the use of a homodesmotic reaction to estimate strain energy (Figure IV.1, previous work pointing right).¹⁶¹ Here, the macrocyclic strain energy may be defined as the energy associated with deforming a linear molecular segment when included in a macrocycle. For example, the deformation of a phenylene when included in a cycloparaphenylene. To use a homodesmotic reaction to determine this quantity, the molecular geometry is optimized and the single point energy of the lowest energy conformation is determined ($E_{\text{macrocycle}}$). In this state, the molecule retains strain energy that cannot be realized until the molecule is broken so that tension is released. Breaking the molecule creates radicals at each side of the break that must be capped with a capping molecule that is similarly broken and placed at each end aiming to retain the local environment of the ends. Then, the lowest energy conformation of this strain released theoretical molecule (E_{linear}) is calculated and compared to the original molecule while accounting for the atoms added to cap the broken ends (E_{cap}) by determining the

single point energy of the capping molecule shown in blue in Figure IV.1. The difference in total energy between the starting materials and products of this theoretical homodesmotic reaction is the total strain energy (E_{strain}) in the macrocycle shown in Equation 1.

$$E_{\text{strain}} = (E_{\text{macrocycle}} + E_{\text{cap}}) - E_{\text{linear}} \quad (\text{Equation 1})$$

This is an example of how a homodesmotic reaction may be used for estimating strain energy. The homodesmotic reaction itself has been rigorously defined elsewhere.¹⁶²

It is also possible to disassemble the molecule into an infinite polymer and compare the repeating unit energies in both the macrocycle and the unstrained polymer.^{21,163} If it were possible to connect these geometries by creating a trajectory between the strained and unstrained states, one could comment on how the energy of each atom changes to release strain energy as the trajectory proceeds. Ideally, the trajectory would begin in the optimized geometry of the strained molecule and descend to an unstrained infinite polymer (Figure IV.2a). The macrocycle cannot be broken without changing the atomic environment and introducing additional strain into the analysis. A theoretical trajectory between the strained macrocycle and unstrained infinite polymer that isolates macrocyclic strain energy is therefore impossible.

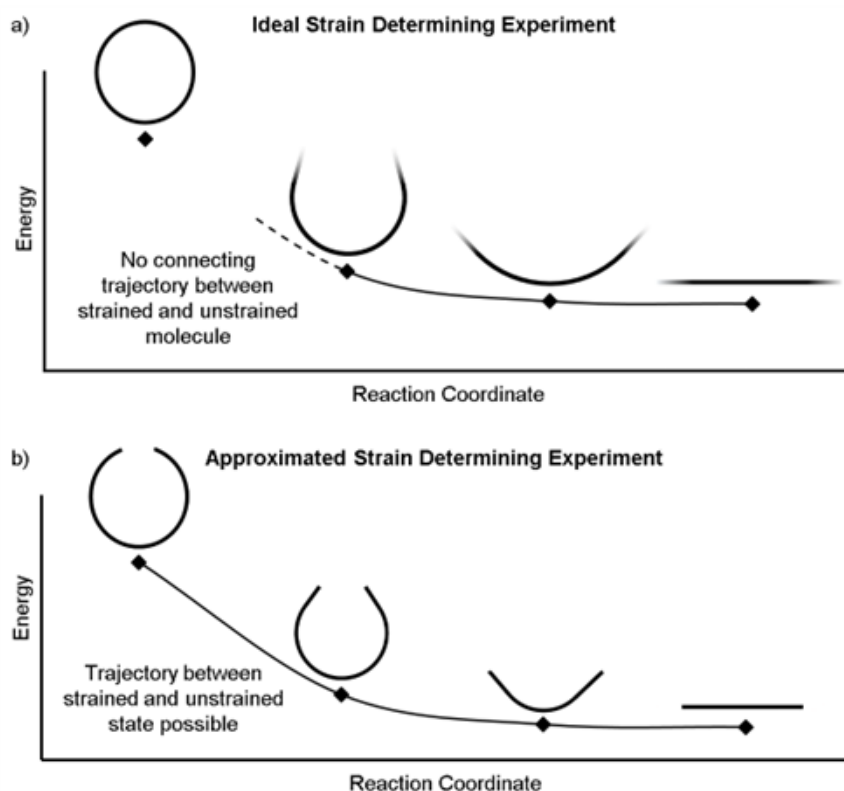


Figure IV.2. a) This ideal experiment begins with the strained macrocycle and ends with an infinite polymer where the strain has been released. b) By removing part of the molecule, the beginning and end geometries can now be connected by a strain releasing trajectory. This allows the local trajectory of each atom to be determined.

It is, however, possible to fragment the molecule so that it may descend into an unstrained state without introducing new strain. By deleting certain atoms, the trajectory shown in Figure IV.2b becomes possible and allows the initial geometry to share the location of its atoms (highlighted in the inset of Figure IV.3) with the strained molecule while still relaxing to an unstrained state upon geometry optimization. The trajectory of each atom accurately represents the trajectory of atoms in the strained molecule to atoms in an unstrained state. This approximates an ideal strain energy determining experiment by averaging these trajectories for multiple fragments.

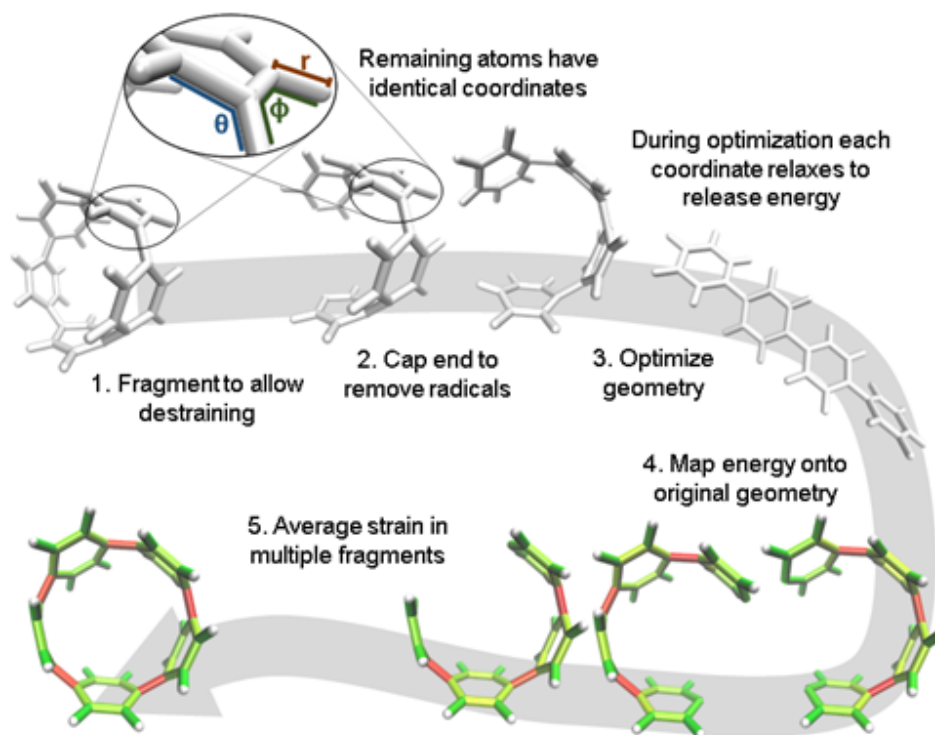


Figure IV.3. Workflow for strain analysis. The coordinates in each molecule fragment relax to release strain energy that is quantified per coordinate (r : bond length, θ : angle, ϕ : torsional angle).

In practice, a segment of the molecule is removed, such as a phenylene or ethylene, to create a fragment as shown in steps 1 and 2 of Figure IV.3. The choice of fragments does not appear to significantly impact overall strain energy determination; however, it can impact strain distribution. Therefore, obtaining accurate results requires as many symmetrically created fragments as possible. For example, when analyzing cycloparaphenylenes, there should be as many fragments as there are phenylenes to be removed. Once a fragment is removed the ends are capped with hydrogen atoms. This requires the segment removed to be at least two atoms (e.g. ethylene) to accommodate replacement with hydrogens. These capping hydrogen atoms are optimized by freezing all atoms in the fragment that match the initial geometry. This ensures they do not add additional strain to the fragment when the fragment is optimized. All fragments created for the analyses in this paper are in the supplementary information to remove any ambiguity.

The trajectory of each individual atom during this process follows the optimization algorithm given by the program used. In these studies, Gaussian09¹⁰⁶ was used with the quasi-Newton rational function optimization (RFO) method that is the default for Gaussian03 due to it converging more smoothly than the newer direct inversion in the iterative subspace (DIIS) method.¹⁶⁴ StrainViz can also be used with Orca, delivering similar results and being free for academic users.^{165,166} The energy of each atom is given by its relationship to other atoms via internal coordinates. The internal coordinates describe the distances and angles between atoms shown in a zoomed in image in Figure IV.3. There are three coordinates that together describe the position of every atom relative to each other: the distance between two atoms, the angle between three atoms, and the torsional angle between four atoms. The optimization algorithm minimizes the energy of the geometry by interrogating these internal coordinates and adjusting them to release energy. The algorithm estimates a force for each coordinate (F) and, depending on step size, assigns a displacement (Δx). It is also possible to define “strain” as the force and “strain energy” as the total energy associated with that force. Multiplying the force by the displacement, as shown in Equation 2, identifies the change in energy ($\Delta E_{\text{coord est}}$) each coordinate experiences in each step.

$$F\Delta x = \Delta E_{\text{coord est}} \quad (\text{Equation 2})$$

The energy determined from this specific calculation is only an estimate. The algorithm overestimates the total energy released for each displacement due to the necessary use of redundant internal coordinates.¹⁶⁷ Therefore, each step is scaled relative to the actual change in the single point energy calculated ($\Delta E_{\text{step actual}}$ in Equation 3) at each step.

$$\Delta E_{\text{coord actual}} \approx \Delta E_{\text{coord est}} (\Delta E_{\text{step actual}} / \Delta E_{\text{step est}}) \quad (\text{Equation 3})$$

Where $\Delta E_{\text{step est}}$ is the sum of all $\Delta E_{\text{coord est}}$ present. As the optimization proceeds, these energies become smaller until the relaxed geometry is found and ΔE approaches zero for all coordinates. For a given coordinate, summing the energy determined for each optimization step gives the total amount of energy stored in that internal coordinate.

After symmetrically fragmenting the molecule, optimizing the fragments, and analyzing the trajectory of the internal coordinates, this data must be displayed in a way that effectively communicates the information gathered. The effective color mapping scheme used for analyzing mechanical force was adopted.¹⁵⁸ The bond strain energy associated is simple to display because there is a single value per bond and the bonds are colored accordingly. For the energy associated with the angle between three atoms, the energy is divided in half among the two contributing bonds. Finally, for the torsional angle between four atoms, the energy is split evenly among the three bonds connecting the four contributing atoms. These maps are produced for bond, angle, and torsional strain energy in each fragment. Then the energies per

bond are averaged among every fragment containing that bond and a single map for each type of strain energy. Finally, the three types are summed and a total strain map is produced.

It is important to note that almost none of the above-mentioned processes are done manually. A package of freely available scripts on GitHub automate Gaussian input file creation, job submission, and VMD script generation.¹⁶⁰ Each analysis only requires the manual generation of an optimized geometry and appropriate fragments, StrainViz does the rest.

IV.3. Results and discussion

With a framework in place for analyzing strained molecules, it is important to check the assumptions made when creating this method. There are three main assumptions that underpin the validity of this computational method: 1) The fragments chosen accurately represent the base molecule. 2) The sum of all energies for all internal coordinates total to an energy that is corroborated by previous methods. 3) The local strain energy determined relates to reactivity. If these three assumptions are proven valid, then StrainViz is useful for determining strain energy.

IV.3.1. Fragments accurately represent the molecule

By using fragments to calculate strain energy in the molecule we lose the information provided by the portion omitted. Although it is not possible to compare the fragment directly with the base molecule, it is possible to identify differences when varying the fragment size. **[8]CPP** was analyzed using fragments of increasing size (Figure IV.4). From this analysis we will see how much information is lost dependent on the size of the omitted portion.

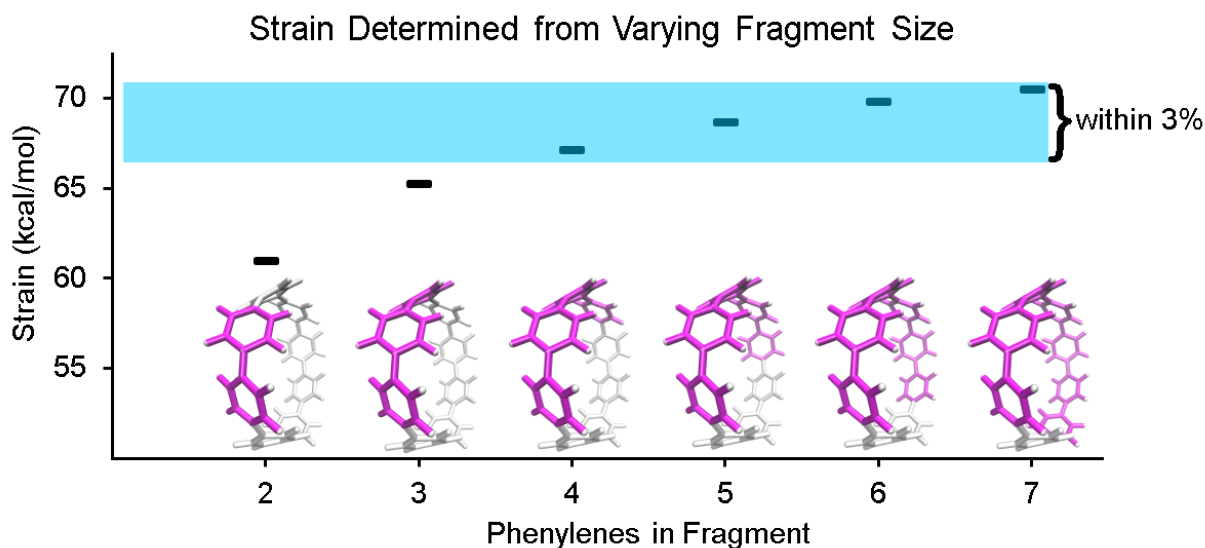


Figure IV.4. Fragments of **[8]CPP** having 2-7 phenylenes (highlighted in pink) were used in the strain analysis. Fragments retaining 50% or more of the molecule all determined strain energies within 3% of each other. All calculations were performed at the B3LYP/6-31G(d) level of theory unless otherwise noted.

When molecule fragments are being analyzed, the fragment size must be judiciously chosen to reduce the impact of edge effects where the molecule is cut. It has been previously seen, in the strain-induced retro-Huisgen cycloaddition of triazoles,¹⁶⁸ that when the edge atoms are connected to the triazole

by coordinates (torsional angle across an ethyl or propyl group), results do not match expectations. Therefore, the program does not include any coordinates that contain the end capping atoms or the atoms attached to them. This trims away forces at the ends of the geometry that are most susceptible to these edge effects. By doing so, the results become more relevant regardless of fragment size, but limits how small the fragments may be made. Despite this consideration, the chosen fragment size does still have an impact on the accuracy. Within each fragment, the variability of strain energy measurement for each bond from the analysis also increases with decreasing fragment size. The four largest **[8]CPP** fragment sizes, shown in Figure IV.4, all determine strain energies within 3% of their mean. These fragments are also internally consistent. Each individual strain energy determined for each bond is also within 3% of the mean. This consistency shows that when the fragments used are at least half the original molecule edge effects are minimal.

IV.3.2. Energies are expectedly similar to previous results

A relevant computational technique must deliver results that are relatively consistent with previously described techniques while providing new insight. Unfortunately, there is no computational benchmark or easily obtainable experimental data for strain and the amount determined can vary depending on the technique used. For example, **[12]CPP** has a range of strain energies depending on the computational technique (summarized in Table IV.1). Given this relatively wide range in the literature, there is significant room for error in any new computational method. However, when using a similar computational technique, (entries 1-4) the range narrows significantly even when using different levels of theory. Therefore, StrainViz will be compared directly to known examples using the homodesmotic reaction at the same level of theory. Values similar to previous reports should be expected.

Strain Energy	Theory	Reference
50 kcal/mol	B3LYP/6-31G(d)	<i>Yamago 2010</i>
48.1 kcal/mol	B3LYP/6-31G(d)	<i>Segawa 2010</i>
49.0 kcal/mol	B3LYP/6-31G(d)	<i>Bachrach 2010</i>
50.2 kcal/mol	M06-2X/6-31G(d)	<i>Bachrach 2010</i>
42 kcal/mol	Gaussian Pseudopotentials	<i>Rio 2016</i>
48.3 kcal/mol	B3LYP/6-31G(d)	This work

Table IV.1. Reported strain energies of **[12]CPP**.

A variety of molecules with macrocyclic strain energy were used in this analysis (Figure IV.5). Given that cycloparaphenylenes are well studied in this respect, cycloparaphenylenes having six to ten phenylenes were analyzed and compared to an analysis using homodesmotic reactions (Figure IV.5a).¹⁵⁰ Comparing these two analyses, we can see that the results are most similar at larger cycloparaphenylene sizes. This is consistent with the aforementioned accuracy of the StrainViz analysis where larger cycloparaphenylene fragments result in more accurate strain energy determinations. Analyzing Itami's carbon nanobelt resulted in even better matching with previous efforts (Figure IV.5b).⁴⁷ The high accuracy

may be owed to the fragment optimization trajectory quality. See supplementary information for further comments. A recently synthesized highly strained small cyclophane from the Bodwell group¹⁶⁹ and [2.2]paracyclophane¹⁷⁰ were also analyzed and confirm that StrainViz is consistent with prior computational efforts (Figure IV.5c).

The literature report of [2.2]paracyclophane does attempt to quantify the strain energy present in the phenylene and ethylene segments.¹⁷⁰ This was done in a similar manner to our method. The molecule was broken up and the strain energy in each fragment was determined by comparing single point energies of the strained and unstrained states. Their analysis, however, found different amounts of strain than their homodesmotic reaction; 10.2 kcal/mol per phenylene and 5.6 kcal/mol per ethylene summing to 31.6 kcal/mol, but 30.8 kcal/mol from a homodesmotic reaction using the ω B97X-D functional. This begs the question which analysis is more accurate. With our method, the local strain adds up to the total strain by definition.

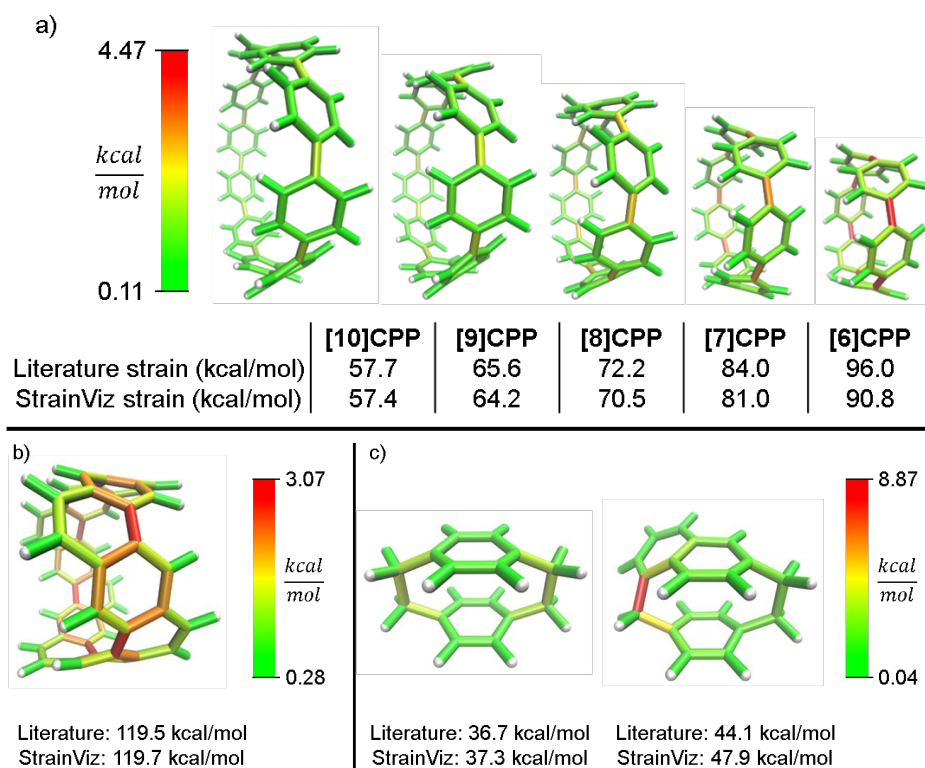


Figure IV.5. Literature examples of strain energy determinations compared to StrainViz analysis. a) Cycloparaphenylene strain determined by homodesmotic reactions.¹⁵⁰ b) carbon nanobelt strain energy extrapolated from increasing belt sizes.⁴⁷ c) [2.2]paracyclophane strain and Bodwell's more strained analogue determined by isodesmotic reaction B3LYP/6-31G(d,p)¹⁷⁰ and M06-2X/Def2TZVP¹⁶⁹ respectively.

By corroborating results found in the literature, we establish that StrainViz determines total strain energies that are reasonable. This shows that generating a map of local strain does not compromise the total strain analysis quality. More importantly, we see exactly where in the structure the strain is distributed. We hope to confirm that local strain is more instructive than total strain for reactivity.

IV.3.3. Local strain energy relates to reactivity

In a previous paper, we described the synthesis of cycloparaphenylenes having one phenylene switched from being *para* to *meta* connected.⁸⁵ We described the strain using homodesmotic reactions and concluded that the *meta*-cycloparaphenylenes are less strained than cycloparaphenylenes with an equal amount of phenylenes (Figure IV.6). A structural strain parameter from the crystal structure, the torsional angle between adjacent phenylenes, had values above and below comparable cycloparaphenylenes which hinted that strain may not be evenly distributed. Lacking a tool to directly locate and quantify strain at specific locations on the molecule, we could not at that time make any further claims about strain in these molecules. Now, StrainViz locates the strain and predicts the reactivity of *meta*-cycloparaphenylenes.

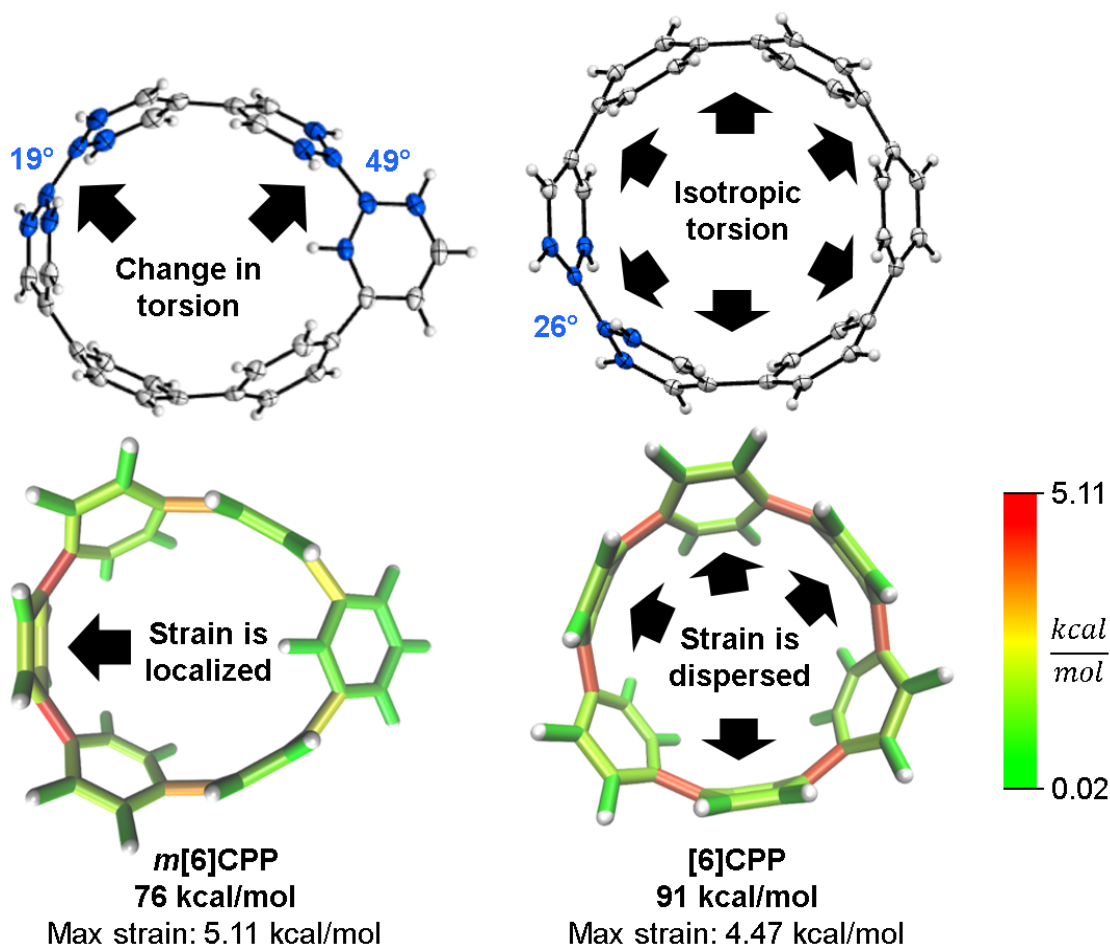
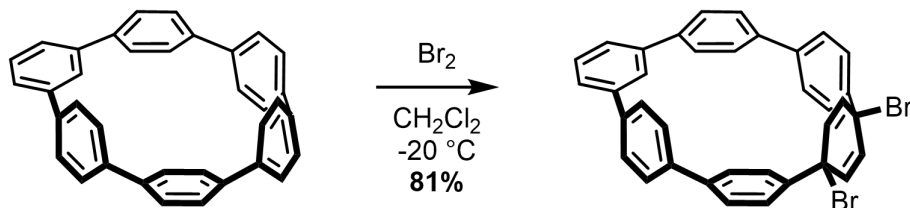


Figure IV.6. Torsional angles and total strain of [6]CPP and *m*[6]CPP. Changing connectivity from *para* to *meta* decreases total strain but increases local strain energy.

Analysis using StrainViz in Figure III.6 shows that strain is concentrated across from the *meta* phenylene. Changing a phenylene in a cycloparaphenylene from being *para* to *meta* connected relieves strain at that end of the molecule but adds strain at the opposite end. If this program provides a meaningful molecular strain analysis, then this high strain area should react faster in a strain relieving reaction. For example, bromination of a *meta*-cycloparaphenylene should occur exactly across from the *meta* phenylene

where the majority of the strain is located. Indeed, upon bromination of a *m*[6]CPP, bromination occurs exactly where predicted by our calculations (Scheme IV.1).



Scheme IV.1. Bromination of *m*[6]CPP.

Even more striking from the analysis is that despite *meta*-cycloparaphenylenes being less strained in total, they should be more reactive due to a higher amount of local strain relative to a cycloparaphenylene where strain is spread equally over the molecule. This phenomenon is seen clearly in the aforementioned publications by Yamago. In the case of either bromination¹⁴⁴ or C-C bond activation by platinum,¹⁴⁵ a reaction at one phenylene is followed by a faster second reaction. This is not consistent with the total quantity of strain present in each reacting molecule. A homodesmotic reaction of the starting cycloparaphenylene and singly brominated cycloparaphenylene shows that the second has much less strain energy. However, when analyzed using StrainViz as shown in Figure IV.7, it is clear that the singly brominated intermediate has more strain across from the first site of bromination and that the molecule has been activated to brominate the second time at a faster rate.

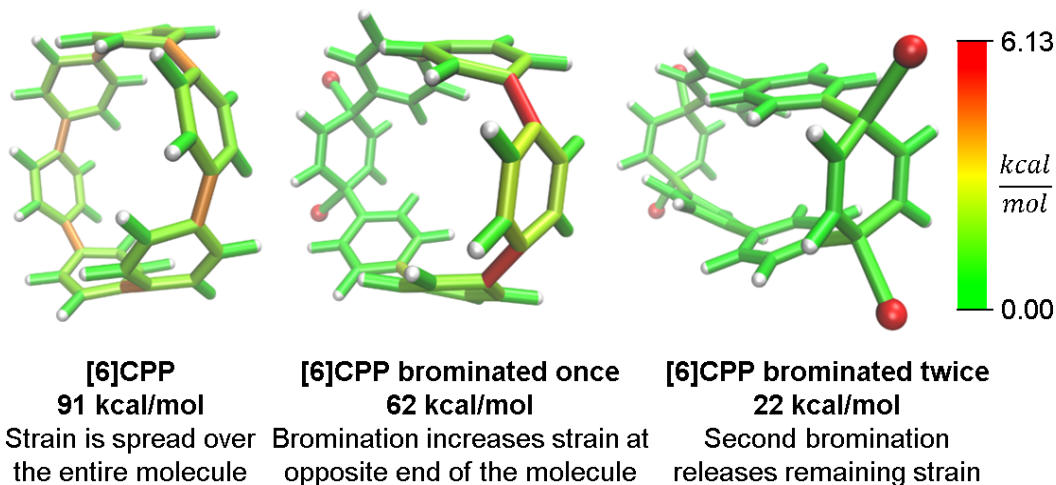


Figure IV.7. Strain release during bromination of [6]CPP. First bromination activates molecule to be more reactive in the second step.

Despite these specific examples of reactivity correlating extremely well to the strain energy present at certain locations in the molecule, it is important to note that the specific reaction taking place is being aided by relief of strain to effect the transformation. This is why it is not the bond with the highest determined strain energy that is broken during the reaction, but that the chemical reactivity occurring is preferred when in proximity to higher strain energy.

IV.4. Unique strain analysis of macrocycles from the literature

In addition to validating the method, we thought it instructive to provide use cases for StrainViz. Additional molecules from the literature were analyzed using this method to determine strain energies and the location of it as a heat map. The Tanaka group recently reported two strained nanobelt structures where one has a turn in it so that it forms a Möbius loop shown in Figure IV.8a.⁵⁵ This geometry is intriguing in that the turn introduces additional strain energy to the molecule. The non-Möbius geometry is strained similarly to the corresponding cycloparaphenylene, however, the Möbius geometry is quite different. Despite having five repeating units instead of four, it is more strained overall. The additional strain is introduced at the entry points to the turn. This is similar to a polymer knot where strain is mostly located at a choke point at the knot entry.^{171,172} Within the turn there is higher strain and outside of the turn there is significantly less. The symmetry of this Möbius molecule prevents direct comparison to a non-Möbius molecule, however, it is possible to instead study molecules with higher symmetry (Figure IV.8b). A Vögtle belt¹² has high enough symmetry to directly compare molecularly degenerate molecules with and without a Möbius turn. The Vögtle belt has evenly distributed strain resulting in relatively little at any single point. Adding a Möbius twist places extreme strain (four times as much) on two symmetrically separated bonds at the entrance and exit of the twist. In total, strain increases from 105 kcal/mol to 238 kcal/mol. This speaks to the challenge of synthesizing rigid Möbius molecules that are of fundamental interest.⁵²

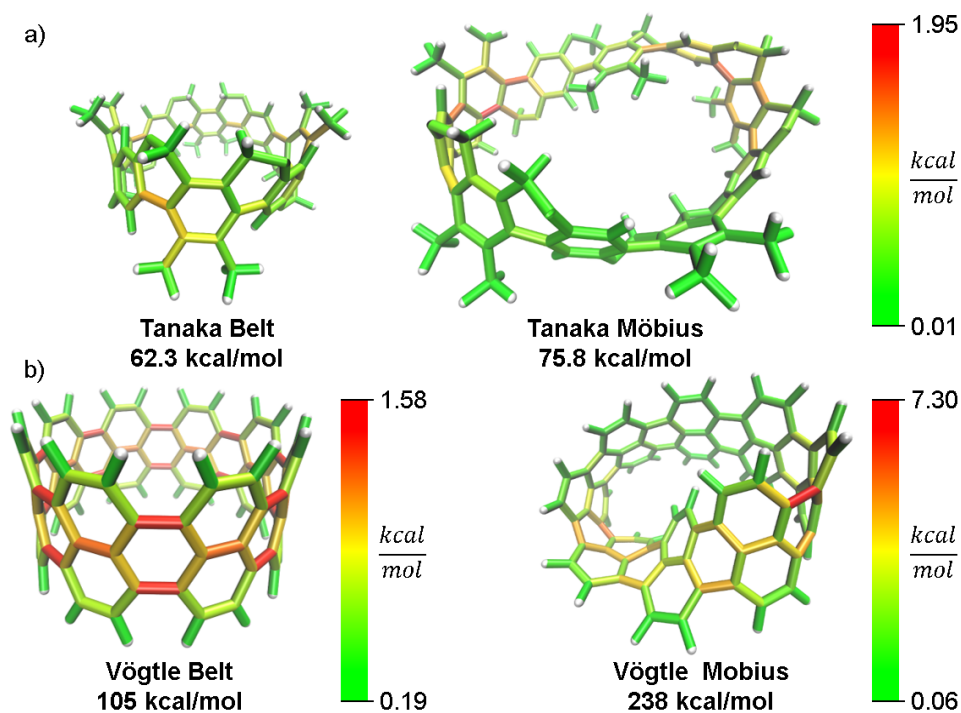


Figure IV.8. Möbius molecules have more strain due to an internal twist when compared to a non-Möbius belt. a) The Möbius molecule synthesized in the Tanaka group is more strained than the non-Möbius despite being a larger size. b) In a symmetric Möbius molecule, strain is centered at the twist entry point.

In addition to macrocyclic molecules, multimacrocylic molecules can be analyzed as long as each fragment fully releases all strain present. The Yamago group has reported a highly symmetric nanoball with multiple macrocyclic connections (Figure IV.9).¹⁷³ Analyzing a single panel shows that strain is spread relatively evenly around the periphery aside from some anisotropy induced by the C₂ symmetry of this lowest energy conformation. In the ball, however, it appears that there is more strain at the corners as opposed to the edges. This indicates that the three additional macrocycles in the ball add strain where they attach at the corners of a panel. As they do not apply force directly in the direction of any edges, the force is split between the edges and concentrates at the corners. This unique multimacrocylic strain contribution is easily apparent using this analysis.

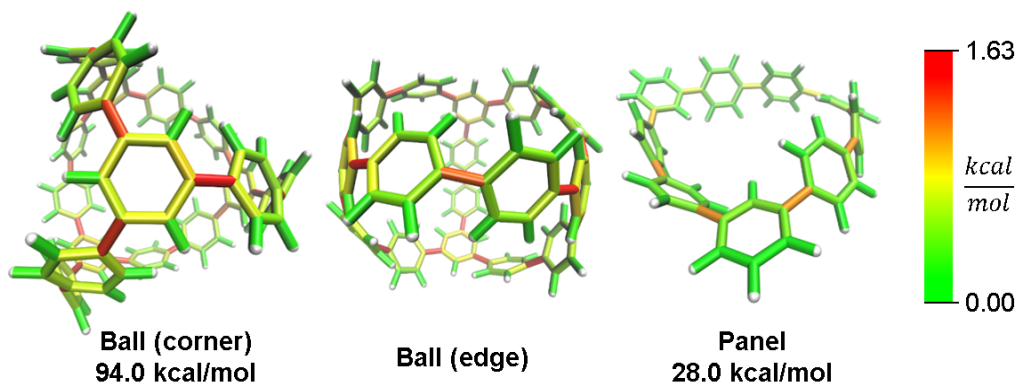


Figure IV.9. Strain energy present in Yamago's nanoball. More strain at the ball corners relative to the edge.

While this analysis was designed for analyzing curved aromatic molecules, it applies widely in the analysis of strained molecules. For example, strained hydrocarbons play a very important role as bioorthogonal reagents. Specifically, cyclooctynes and *trans*-cyclooctenes are used as reactive reagents for copper-free click reactivity in biological media. A previous Houk group analysis^{174,175} noted that a strain energy based analysis fails to accurately predict molecular reactivity and instead used a distortion/interaction model¹⁷⁶ to accurately predict reactivity. However, our novel analysis can correctly order the reactivity of these strained reagents using a local strain analysis. The analysis of cyclooctyne in Figure IV.10 reveals 13.7 kcal/mol of strain whereas *trans*-cyclooctene has 17.4 kcal/mol both have nearly the same proportion (42% and 41%) located at the reactive site. This is in agreement with the relative rate of reaction with a tetrazine of 30 and 13,000 M⁻¹s⁻¹ respectively. Furthermore, when comparing the more reactive *trans*-bicyclo[6.1.0]nonene to *trans*-cyclooctene in Figure IV.10, the total strain energy increases only slightly to 18.9 kcal/mol, however, the reaction rate increases 160 fold.¹⁷⁷ By increasing the macrocycle rigidity, the strain is shifted to the reactive alkene. The *trans*-cyclooctene has 7.2 kcal/mol of strain energy located in the alkene, whereas *trans*-bicyclo[6.1.0]nonene has 9.3 kcal/mol. This increases the reactivity more than would be predicted by total strain energy. Again, the StrainViz analysis provides the missing information that previous strain analyses lack. While this analysis does not provide accurate prediction of rates as the distortion/interaction model of the Houk group does,¹⁷⁶ it may be put to good use in informing the design of new strained bioorthogonal reagents by evaluating strain local to the reactive site.

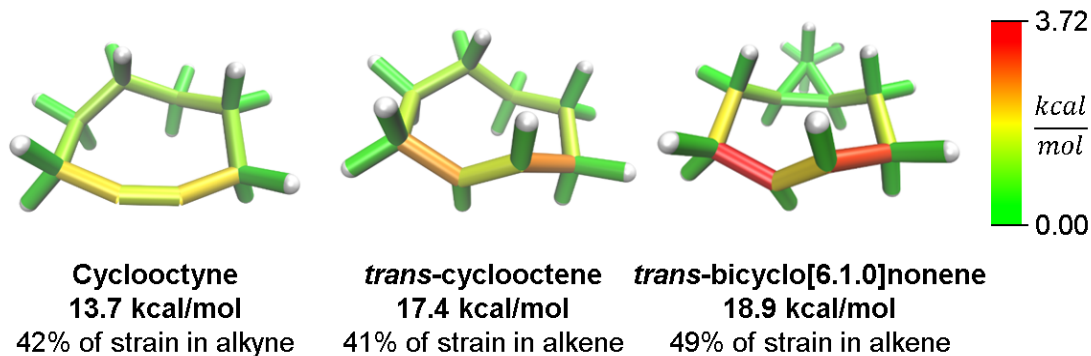


Figure IV.10. Strain energy in copper-free click reagents. *Trans*-cyclooctene is more strained than cyclooctyne but has similar strain distribution. Increasing rigidity by addition of a cyclopropyl fusion increases strain energy and shifts it to the reactive site.

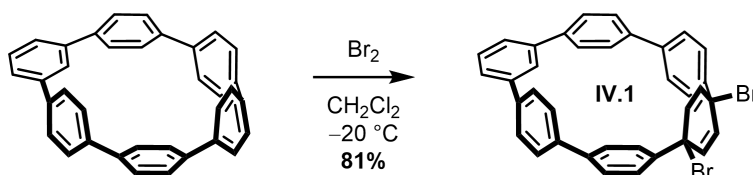
IV.5. Conclusions

A new computational method is reported for the determination of strain energy in macrocycles. This method improves on the current standard of using homodesmotic reactions to determine strain energy by locating contributions to the total strain. The robustness of the method was tested to show that fragment sizes of at least more than half of the molecule give accurate results. The method is accurate in that it delivers reasonable total strain energy relative to previous computational results. It is effective in strain promoted reaction prediction by successfully locating the site of bromination in unsymmetric molecules. Finally, a sampling of literature examples were analyzed with new insight gathered including design considerations for new strained bioorthogonal reagents. This new computational strain determination method is, therefore, broadly useful for the research of strained macrocycles.

IV.6. General experimental details

All glassware was flame dried and cooled under an inert atmosphere of nitrogen unless otherwise noted. Moisture sensitive reactions were carried out under nitrogen atmosphere using Schlenk and standard syringe/septa techniques. Dichloromethane was dried by filtration through alumina according to the methods described by Grubbs.¹⁰⁷ ¹H NMR spectra were recorded at 500 MHz on a Bruker Advance-III-HD NMR spectrometer. ¹³C NMR spectra were recorded at 125 MHz on a Bruker Advance-III-HD NMR spectrometer. All ¹H NMR spectra were taken in chloroform-*d* (referenced to TMS, δ 0.00 ppm). All ¹³C NMR spectra were taken in chloroform-*d* (referenced to chloroform, δ 77.16 ppm). All reagents were obtained commercially unless otherwise noted. Mass spectra were obtained from the University of Illinois at Urbana-Champaign Mass Spectrometry Lab using ESI on a Micromass 70-VSE.

IV.6.1. Synthesis and characterization



IV.1 diBr-*m*[6]CPP. Freshly synthesized *m*[6]CPP (8 mg, 17.5 nmol, 1 eq) was added to a flame dried 25 mL round bottom flask. The contents were evacuated and backfilled with nitrogen three times. Dichloromethane (6 mL) was added to the flask. This was cooled to -20 °C. A 50 mM solution of Br₂ (64.0 μL) in methylene chloride (50 mL) was prepared in a flame dried 100 mL pear shaped flask. The bromine solution (385 μL, 19.3 nmol, 1.1 eq) was added dropwise and the mixture was stirred at -20 °C for 20 min. The contents of the flask were passed through an Aura MT 0.45 μm PTFE syringe filter and evaporated under reduced pressure to obtain the product as an orange-red solid (8.7 mg, 81%). ¹H NMR (500 MHz, Chloroform-*d*) δ 7.49 – 7.40 (m, 3H), 7.36 (d, *J* = 8.5 Hz, 4H), 7.33 (d, *J* = 8.4 Hz, 4H), 7.18 (d, *J* = 8.5 Hz, 4H), 7.11 (d, *J* = 8.4 Hz, 4H), 6.38 (s, 4H), 4.65 (t, *J* = 1.7 Hz, 1H). ¹³C NMR (126 MHz, CDCl₃) δ 143.35, 142.82, 142.69, 141.66, 140.34, 139.15, 130.35, 130.27, 129.08, 127.32, 126.78, 121.81, 56.44, 1.17. HRMS (ESI-TOF) (*m/z*): [M-HBr]⁺ calculated for C₃₆H₂₃Br, 534.09831; found, 534.09804.

IV.7. Co-authored content

The work in Chapter 4 was co-authored with Curtis Colwell, Prof. Tim Stauch, and Prof. Ramesh Jasti and published under the title of “Strain Visualization for Strained Macrocycles” in *Chemical Science*.⁶⁸ I helped edit some of the manuscript, trialed the tutorial for running StrainViz analysis as mentored by Curtis Colwell, and performed the synthesis and bromination of *m*[6]CPP. Curtis Colwell wrote the manuscript, wrote the StrainViz software, and performed all computational analyses. Prof. Tim Stauch provided crucial mentorship and edited the manuscript. Prof. Ramesh Jasti edited the manuscript. Further permissions related to the use of material excerpted in this chapter should be directed to The Royal Chemical Society.

IV.8. Bridge to Chapter V

As our computational methods improve, we have the power to predict useful properties based on previously reported trends. Developing tools like StrainViz has improved our chemical intuition by explaining trends in reactivity based on how strain is localized in inherently strained molecules. Analyzing previously reported structures or new hypothetical structures can motivate scientists to propose and attempt their syntheses. The following chapters utilize StrainViz and other computational methods to either determine their strain-induced reactivities or approximate a trend in their supramolecular and optoelectronic properties.

CHAPTER V

COMPUTATIONAL ANALYSIS OF STRAIN PROMOTED REACTIVITIES

V.1. Background

Cyclic structures provide a suite of properties that are different or not present in their linear analogues, as has been echoed extensively in nanohoop literature.^{24,140} Computationally, this is important to catalogue as more cyclic compounds are being reported in literature and proposed as interesting avenues of research. As presented with the publication of the StrainViz software, inherently strained macrocycles possess reactivities that are directly related to their relative strain and how the strain is allocated throughout the structure.⁶⁸ Efforts to describe how strained molecules react and their rates have benefited from computational analyses of their distortion-interaction energies and their total and local strain energies as calculated by StrainViz.

“Click” reactions have made a definite impact in the scientific community with the publications of Sharpless, Meldal, and Bertozzi.^{136,137,178,179} As a result, they were awarded the Nobel prize in chemistry for their pioneering work in developing chemistry that has revolutionized biological labeling in the form of bioorthogonal chemistry. Reactive alkynes in general have become useful synthetic intermediates to more complex carbon nanostructures, polymers, and pharmacophores.^{15,180–183} It follows that development of novel strained alkynes or methods for synthesizing reactive alkynes can benefit the field by diversifying the possible structures available for chemists in these fields. Understanding how strain can be manipulated is, therefore, a powerful tool to that end.

Alkyne-included cycloparaphenylenes are good candidates for addressing the affect strain has in strain-promoted reactions due to their bottom-up synthetic accessibility and functional group tolerance.^{69,143} Functional groups can change the electronic properties of the nanohoops and, as a result, the interaction energies of cycloaddition reactions.^{137,184,185} The size of the nanohoop can be varied to control the inherent strain of the alkyne, increasing the reactivity with decreasing number of phenylenes.^{68,69} Fellow lab members Julia Fehr and Tara Clayton have successfully made a suite of alkyne-containing nanohoops that capture both of these affects. Herein summarizes the strain-induced reactivities of these molecules and their importance in the literature.

V.2. Experimental and Theoretical Elucidation of SPAAC Kinetics for Strained Alkyne-Containing Cycloparaphenylenes

The strain-promoted azide-alkyne click (SPAAC) reaction is a powerful tool for labeling biological targets via a robust bioorthogonal chemical reaction.^{136,137,184,185} By using more and more strained alkynes in the form of cyclooctyne or azacyclooctynones (Figure V.1a), chemists have tailored reaction rates to increase efficacy for labeling biological targets with fluorescent payloads. As more strained alkynes are developed, the competition between reaction rate and deleterious reaction pathways becomes one-sided in favor of less stable alkyne derivatives. Therin lies the challenge of making suitable reagents for precise and more niche biochemical labeling. Alkyne-included cycloparaphenylenes, $[n+1]$ CPPs, can address the synthetic scope of possible SPAAC reagents by acting as the strained alkyne and fluorophore in one

molecule. They also provide a modular scaffold because of their bottom-up synthetic methods. Functionalizing the phenylenes of CPPs can provide more control over the photophysical properties or reaction rates with greater fidelity. Computational analysis of total and local strain is warranted to help explain differences in the SPAAC reaction rates.

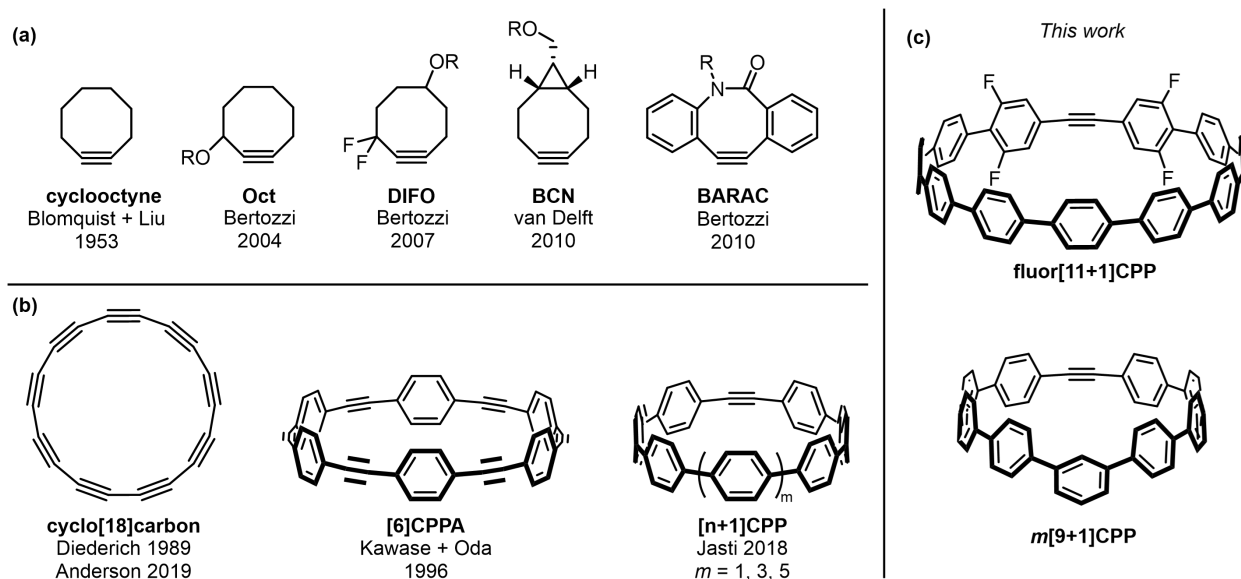


Figure V.1. (a) Examples of strained alkynes developed for copper-free click chemistry. (b) Strained alkynes in the field of carbon nanomaterials. (c) New strained alkyne-containing [n+1]CPPs described in this work.

V.2.1. Introduction

In this context, strained alkynes can be found within radially π -conjugated macrocycles. For instance, the elusive ‘all-carbon’ molecules, dubbed cyclo[n]carbons, have been the subject of much scientific interest. Diederich and coworkers first observed cyclo[18]carbon by time-of-flight mass spectrometry after laser flash heating of annulene precursors in 1989.¹⁵ More recently, in 2019, Anderson and coworkers observed cyclo[18]carbon on a NaCl-surface using high-resolution atomic force microscopy.¹⁸¹ [n]Cycloparaphenyleneacetylenes ([n]CPPAs), comprised of alternating C-C triple bonds and phenylene units, are also intriguing cyclic structures that were first synthesized by Oda and coworkers in 1996.¹⁸⁰ From their onset, [n]CPPAs have been shown to be notably unstable, with Oda noting that [6]CPPA “explosively decomposed at about 80 °C.” Recent work by Moore and Lee has introduced several different sizes and variations of the CPPA scaffold, including [3]CPP³A which can successfully undergo a triple SPAAC reaction with three equivalents of an azido-compound.^{186–188} Clearly, [n]CPPAs possess very interesting reactivity but some are relegated to the glovebox due to their low stability.^{186,188}

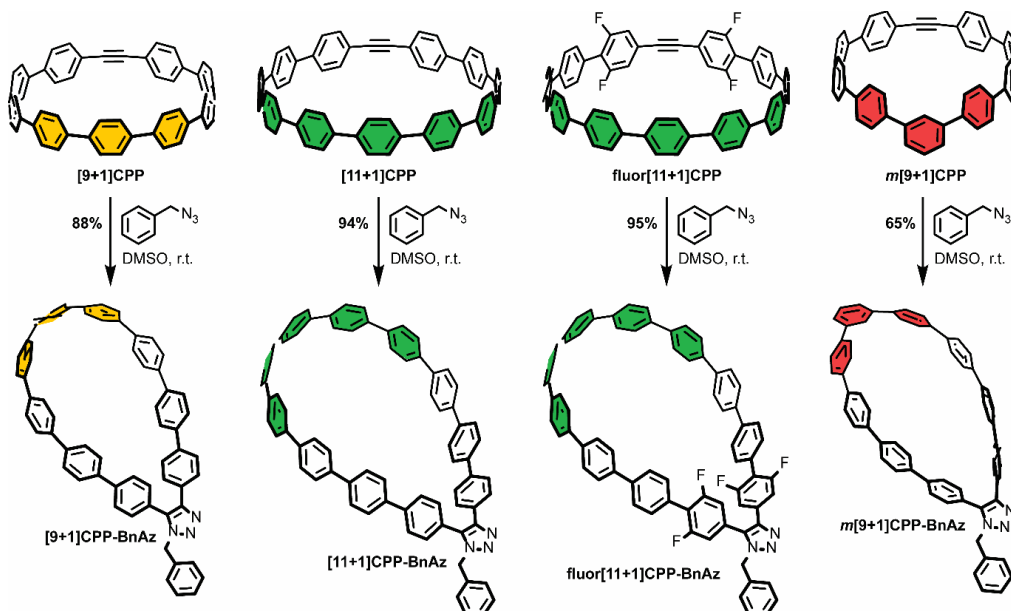
Our group has historically focused on a related, but generally more stable type of carbon nanomaterial: the cycloparaphenylene ([n]CPP) or carbon nanohoop.²¹ These molecules possess a radially-oriented π -system which allows for increased solubility in organic solvents, unique photophysical properties (including bright fluorescence for most carbon nanohoos), tunable frontier molecular orbitals (FMOs), and host-guest capabilities (e.g. complexation with C₆₀).²⁴ In 2018, we introduced a new subclass

of carbon nanohoops containing a single strained alkyne within the carbon backbone.¹⁴³ We refer to these structures as $[n+1]$ CPPs, where the n denotes the number of phenylene units in the molecule “+1” alkyne moiety (Figure V.1b). In that initial publication, we detailed the synthesis of three molecules—**[7+1]CPP**, **[9+1]CPP**, and **[11+1]CPP**—and demonstrated that these molecules (a) can undergo strain-promoted cycloadditions at the alkyne, (b) possess size-dependent (i.e. strain-dependent) levels of reactivity, and (c) maintain the photophysical properties typical of cycloparaphenylenes, including a common absorbance maximum, high molar absorptivities, bright fluorescence, and a size-dependent emission maximum. However, while **[9+1]CPP** and **[11+1]CPP** possessed good stability, **[7+1]CPP** was found to decompose quickly under ambient conditions.

Nonetheless, we were excited by the idea of a new strained alkyne scaffold that offered the radially-conjugated π -system of cyclic carbon nanomaterials, the synthetic manipulability of the well-studied cyclooctyne, and reasonable stability. Herein, we describe our efforts to (a) tune the reactivity of the $[n+1]$ CPP scaffold *via* organic synthesis, (b) fully characterize the photophysical properties of these molecules, (c) quantify the rate constants for each described $[n+1]$ CPP in the SPAAC reaction with benzyl azide, and (d) computationally illustrate the origin of these effects. In this work, we studied previously reported **[9+1]CPP** and **[11+1]CPP** as well as two new $[n+1]$ CPPs: ***m*[9+1]CPP** and **fluor[11+1]CPP** (Figure V.1c). In both cases, we observed heightened reactivity relative to the parent $[n+1]$ CPPs which can be explained with quantum mechanical calculations provided by Lopez and coworkers. Our ultimate aim in this study is to understand the structural perturbations that can lead to increased reactivity for this new strained alkyne scaffold.

V.2.2. Results and discussion

Detailed synthesis of the structures presented in this publication is elaborated in the referenced paper.⁶⁹ The structures chosen are based on the feasibility of their synthesis and stability of the resulting alkyne-containing cycloparaphenylene. The goal was to vary the number of phenylenes, append functional groups (addition of fluorine atoms), and change the bond order of the nanohoop to address strain and electronic dependent reaction rates for the SPAAC reaction (Scheme V.1). Each $[n+1]$ CPP was reacted with excess benzyl azide. The analysis of the reaction rates followed. Paired with the computational results of the reaction coordinate diagram and StrainViz analysis, we can ascertain the effect of each variable.



Scheme V.1. Strain-promoted azide-alkyne cycloaddition reactions between the $[n+1]$ CPPs described in this study and benzyl azide, a model compound. Yields were determined *in-situ* via quantitative ^1H NMR in comparison to an internal standard, dimethyl sulfone.

V.2.3. Kinetics of the SPAAC reaction with benzyl azide

We set out to quantify second-order rate constants for the SPAAC reaction of each $[n+1]$ CPP with benzyl azide and determine how the structure and electronic characteristics of the nano hoops change the rate of the reaction. To accomplish this, we combined each $[n+1]$ CPP with 2-12 equivalents of benzyl azide in deuterated DMSO at 25 °C and monitored the reaction *via* quantitative ^1H NMR. Concentrations were determined by comparison to an internal standard of known concentration (dimethyl sulfone). From the results, we determined second-order rate constants for each reaction as shown in Figure V.2.

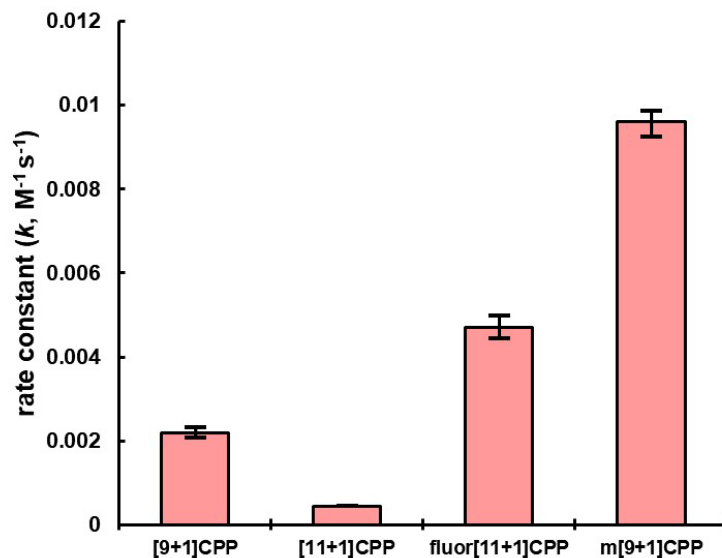


Figure V.2. SPAAC second-order rate constants for $[n+1]$ CPPs. These constants were measured *via* quantitative ^1H NMR in deuterated DMSO.

We found that the $[n+1]$ CPP structure directly impacted the observed SPAAC rate constants. We had shown previously that the smaller **[9+1]CPP** possesses heightened reactivity over larger **[11+1]CPP** towards tetracyanoethylene (TCNE) in a [2+2]cycloaddition-retrocyclization reaction.¹⁴³ The same holds true in this study, where we observed an almost five-fold increase in rate constant for **[9+1]CPP** ($2.2 \times 10^{-3} \text{ M}^{-1} \text{ s}^{-1}$) compared to **[11+1]CPP** ($4.5 \times 10^{-4} \text{ M}^{-1} \text{ s}^{-1}$). The electronically modulated **fluor[11+1]CPP**, exhibiting fluorine atoms at all four positions *meta* to the alkyne moiety, displayed a second-order rate constant of $4.7 \times 10^{-3} \text{ M}^{-1} \text{ s}^{-1}$ towards the SPAAC reaction with benzyl azide. This is an approximately 10-fold increase in comparison to **[11+1]CPP** just by fluorination of the scaffold. Lastly, we hypothesized that the *meta*-linked version of **[9+1]CPP**, ***m*[9+1]CPP**, would possess increased local strain at the alkyne due to its location opposite the *meta* linkage. We determined a second-order rate constant of $9.6 \times 10^{-3} \text{ M}^{-1} \text{ s}^{-1}$ for the SPAAC reaction of ***m*[9+1]CPP** with benzyl azide. This corresponds to a 4.4-fold increase compared to **[9+1]CPP** just by changing the connectivity of the macrocycle.

V.2.4. StrainViz methods for alkyne-containing nanohoops

Computations were performed using Gaussian09¹⁰⁶ at the B3LYP/6-31+G(d) level of theory. StrainViz calculations were performed using the scripts available through GitHub with an alternation to the “input_gen.py” script. Keywords “Opt=(rfo,NoSymm)” were added to account for the fragments with an alkyne. Output from individual StrainViz calculations were submitted with the maximum bond energy set as the highest strained bond between all four molecules. This setting recolors each bond to generate a comparative heat map. Replacing the “max(norm_values)” on line 171 in the “bond_scripts.py” with the max bond strain in the “total_bond.tcl” file, a recolored output is generated by rerunning the StrainViz script for each molecule. Running each fragment separate from the StrainViz script permits longer runtimes per fragment to avoid incomplete relaxation. Analysis of the triazole products did not provide any productive results beyond what was obtained from the $[n+1]$ CPPs.

V.2.5. Transition state geometry and energy methods

Computations were performed using Gaussian 16 program.¹⁸⁹ The reactions between each $[n+1]$ CPP and benzyl azide were optimized using M06-2X¹⁹⁰ and 6-31+G(d,p)¹⁹¹ basis set with the integral equation formalism variant of polarizable continuum model (IEF-PCM)¹⁹² with parameters for DMSO. Conformational searches of the 10 lowest energy conformers were determined for the reactants, intermediates, and transition states using the Conformer-Rotamer Ensemble Sampling Tool (CREST).¹⁹³ After locating the lowest energy transition structure, we ran intrinsic reaction coordinate (IRC) calculations and optimized the reactive conformers corresponding to the reactants and products. We performed a vibrational analysis and confirmed that each stationary point was a minima; we identified only positive vibrational frequencies. The optimized global minima transition structures showed only one negative vibrational frequency and was used to determine barrier heights and reaction energies.

V.2.6. Computational analysis of $[n+1]$ CPP reactivity

In order to better understand the relationship between $[n+1]$ CPP structure and the observed reactivity trends, we performed an in-depth computational analysis. First, we analyzed the ground state

geometries of each $[n+1]$ CPP with StrainViz to better understand the distribution of strain throughout each molecule (results displayed in **Figure V.3** and **Table V.1**).⁶⁸ A few trends can be observed. In each $[n+1]$ CPP maximum local strain is located at the alkyne. We also noted that **[11+1]CPP** and **fluor[11+1]CPP** displayed the lowest maximum local strains of 1.29 and 1.16 kcal mol⁻¹, respectively, while **m[9+1]CPP** has the highest local strain at the alkyne with 3.56 kcal mol⁻¹. For the unfunctionalized **[9+1]CPP**, **[11+1]CPP**, and **m[9+1]CPP**, it is clear from this analysis that the acuteness of the C-C≡C bond angle and therefore the local strain at the alkyne has a major effect on SPAAC rate constant. However, strain cannot account for the heightened reactivity of **fluor[11+1]CPP** in comparison to the similarly strained, unfunctionalized **[11+1]CPP**. We therefore turned to transition state structure analysis and the distortion- interaction model developed by Houk to provide a more detailed explanation of our results.^{176,194}

$[n+1]$ CPP	Total strain (kcal)	Max. local strain (kcal)
[9+1]CPP	58.0	2.94
[11+1]CPP	44.4	1.29
fluor[11+1]CPP	44.6	1.16
m[9+1]CPP	43.3	3.56

Table V.1. Summary of strain values (in kcal mol⁻¹) determined by StrainViz for each $[n+1]$ CPP.

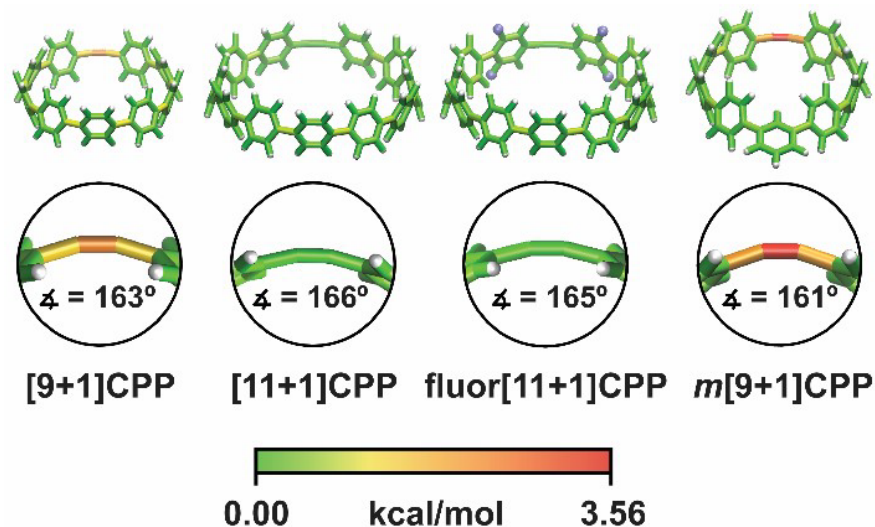


Figure V.3. Strain analysis of the $[n+1]$ CPPs described in this study with the StrainViz computational tool.

We computed the transition structures and activation free energies for the SPAAC of each $[n+1]$ CPP with benzyl azide (**Figure V.4a** and **Table V.2**). The transition structures are all concerted but asynchronous. The C-N_{internal} and C-N_{external} bond lengths in the $[n+1]$ CPP transition states range from 2.15-2.17 Å and 2.26-2.30 Å, respectively. This observed asynchronicity can be attributed to the larger orbital coefficient and nucleophilicity of the N_{internal} of benzyl azide with a natural bond orbital (NBO) charge of -0.40, in comparison to -0.078 for N_{external}. The computed activation free energies ($\Delta G^\ddagger_{\text{comp}}$) ranged from 23.0 to 25.3 kcal mol⁻¹. We observed an acceptable agreement between computations and experiments; when

plotting $\Delta G^{\ddagger}_{\text{exp}}$ against $\Delta G^{\ddagger}_{\text{comp}}$, we observed a linear correlation ($R^2 = 0.94$; $\Delta G^{\ddagger}_{\text{comp}} = 1.17 \Delta G^{\ddagger}_{\text{exp}} - 0.62$; see SI for details).

$[n+1]\text{CPP}$	$\Delta G^{\ddagger}_{\text{experimental}}$	$\Delta G^{\ddagger}_{\text{computational}}$
[9+1]CPP	21.1	24.2
[11+1]CPP	22.0	25.3
fluor[11+1]CPP	20.6	24.2
m[9+1]CPP	20.2	23.0

Table V.2. Activation free energies for the $[n+1]\text{CPPs}$ in this study; reported in kcal mol⁻¹.

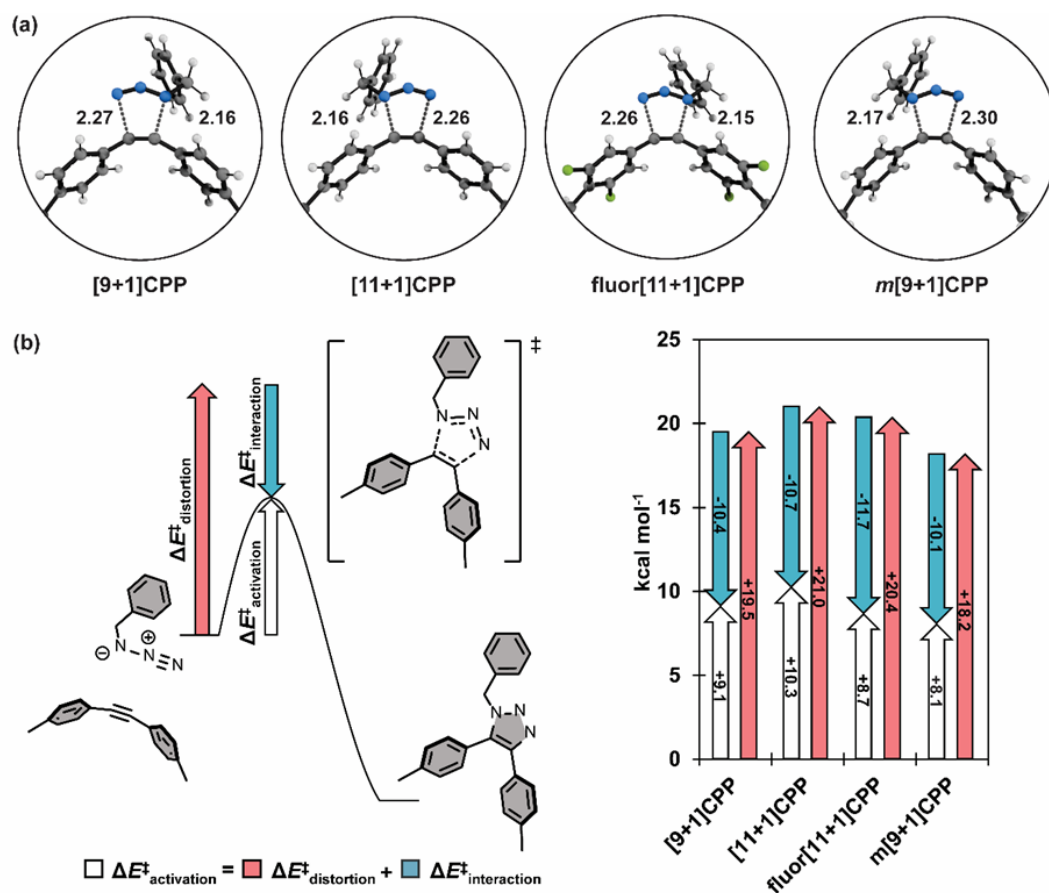


Figure V.4. (a) Transition state structures for each SPAAC reaction with benzyl azide; distances shown in Angstroms (Å). (b) Generalization of the distortion-interaction model and $\Delta E^{\ddagger}_{\text{activation}}$ of each SPAAC reaction broken down into its $\Delta E^{\ddagger}_{\text{distortion}}$ and $\Delta E^{\ddagger}_{\text{interaction}}$ components.

We next implemented the distortion/interaction model to understand the origin of the reactivity differences of the $[n+1]\text{CPPs}$ towards benzyl azide. The distortion/interaction model^{176,194} is an energy-decomposition scheme that has been used extensively to understand the origin of unimolecular^{195–198} and bimolecular^{199–203} reactions. The distortion/interaction model dissects activation energies into distortion and interaction energies. The distortion energy ($\Delta E^{\ddagger}_{\text{dist}}$) is the energy required to distort the reactants from their equilibrium geometries to their transition state geometries without allowing them to interact. The interaction

energy ($\Delta E_{\text{int}}^{\ddagger}$) captures the interactions between the two distorted reactants in the transition state. A generalization of the distortion-interaction model and a summary of the results of this analysis is displayed in **Figure V.4b**. We note that the activation electronic energies (i.e. ΔE^{\ddagger}) are different from the activation free energies (i.e. ΔG^{\ddagger}) because the electronic energies omit zero point energy and thermochemical energetic corrections. The distortion/interaction model uses energies without zero point energies because the distorted and frozen geometries of the cycloaddends are extracted from the optimized transition state structures. Notably, **fluor[11+1]CPP** has the highest $\Delta E_{\text{int}}^{\ddagger}$ of all the $[n+1]$ CPPs in this study (-11.7 kcal mol⁻¹). This, in conjunction with its slightly lower $\Delta E_{\text{dist}}^{\ddagger}$ (20.4 kcal mol⁻¹) relative to parent **[11+1]CPP** (21.0 kcal mol⁻¹), is responsible for the relatively low ΔE^{\ddagger} and superior SPAAC rate constant.

The reactivity trend for **[9+1]CPP**, **[11+1]CPP**, and **m[9+1]CPP** can also be explained via the distortion-interaction model. $[n+1]$ CPPs with more acute C-C \equiv C bond angles in the ground state geometry displayed slightly decreased $\Delta E_{\text{int}}^{\ddagger}$, but this was counteracted by significant lowering of $\Delta E_{\text{dist}}^{\ddagger}$ since less energy input was required to distort pre-bent reactants into their transition state geometries. This phenomenon is known as distortion-acceleration.

Finally, we sought to explain the large $\Delta E_{\text{int}}^{\ddagger}$ of **fluor[11+1]CPP** in comparison to the other $[n+1]$ CPPs in this study using FMO analysis.^{204–211} Tetrafluorination resulted in an overall lowering in energy of the HOMO-1 and LUMO orbitals in comparison to the parent **[11+1]CPP**. This leads to a smaller FMO gap with benzyl azide (6.64 eV for **fluor[11+1]CPP** vs. 6.85 eV for **[11+1]CPP**). In line with FMO theory, smaller FMO gaps lead to stronger orbital interactions in the transition state structure; this effect is captured in $\Delta E_{\text{int}}^{\ddagger}$. The $\Delta E_{\text{int}}^{\ddagger}$ values for **fluor[11+1]CPP** and **[11+1]CPP** are -11.7 vs. -10.7 kcal mol⁻¹. The 1.0 kcal mol⁻¹ increase in stabilizing interaction energy is caused by relatively strong FMO interactions of **fluor[11+1]CPP** with benzyl azide relative to **[11+1]CPP**.

V.2.7. Conclusion to SPAAC Rates of Alkyne-Containing Cycloparaphenylenes

We have expanded the $[n+1]$ CPP library to include two new molecules with unique properties: fluorinated **fluor[11+1]CPP** and *meta*-linked **m[9+1]CPP**. We fully characterized these two molecules as well as previously reported **[9+1]CPP** and **[11+1]CPP** computationally and via quantitative SPAAC reaction kinetics with benzyl azide. Finally, we extrapolated the effect of electron-withdrawing groups on the reactivity of the alkyne and directly modelled the strain via StrainViz. By changing a phenylene linkage or installing electron-withdrawing groups, it is possible to alter the strain of the alkyne and reactivity by as much as an order of magnitude via favorable electronic interaction in the SPAAC reaction. Understanding how the structure of these $[n+1]$ CPPs affect the reactivity encourage further investigation into other cyclization reactions or general transformation involving alkynes to produce interesting macrocyclic molecules.

V.2.8. Experimental details (computations)

All input files, fragment geometries, and output files are available for download *via* Figshare at https://figshare.com/projects/Supporting_Information_of_Computational_results_StrainViz_for_Experimental_and_Theoretical_Elucidation_of_SPAAC_Kinetics_for_Strained_Alkyne-Containing_Cycloparaphenylenes/155192.

V.3. Pinwheel-like Curved Aromatics from the Cyclotrimerization of Strained Alkyne-Containing Cycloparaphenylenes

Extended π -rich structures have intrigued chemists over the centuries because of the endless structure-property relationships that have motivated the discovery of novel aromatic or antiaromatic organic materials.^{15–17,62,173,212–217} Previous groups have teased out the intricate details of extended π -systems by alternating seven-, six-, five-, and even four-membered rings. Ring size and fusions seem to be the limiting factor in this, but the three-dimensional nature of space opens a realm of possible structures. The discovery of curved aromatics such as fullerenes, carbon nanotubes, and helicenes have provided us with a new metric to develop novel π -rich structures. Topologically unique nanocarbons have seen an explosion due to their strain-induced electronic properties, making them the best performing materials in the field.^{6,19,73}

V.3.1 Introduction

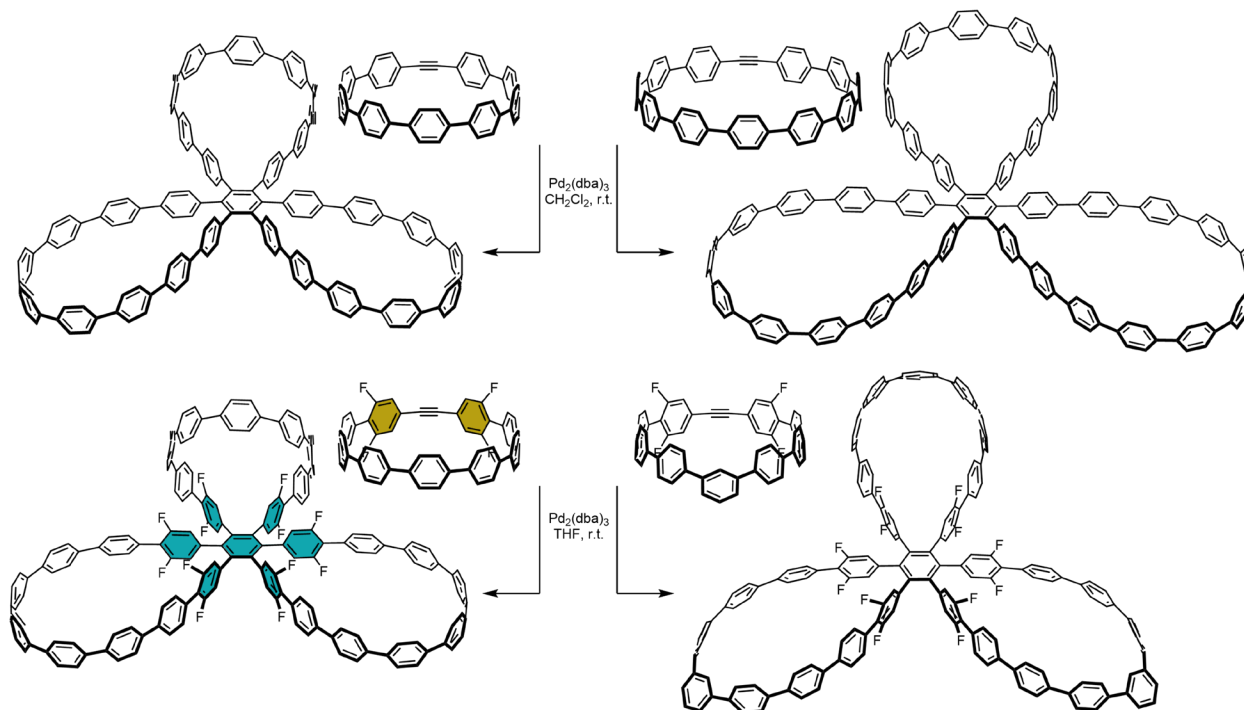
So called curved aromatic systems have continually been investigated to understand how modifications of the carbon backbone can produce more electronically relevant materials while maintaining the increased solubility and intrinsic host-guest properties.^{95,140,218,219} Cycloparaphenylenes (CPPs) are now a well-known curved nanocarbon structure that has seen a renaissance in their synthetic development. A variety of π -extended CPPs have been synthesized to understand how the inherent strain the nanohoop affect the electronic properties of pre-established polycyclic aromatic hydrocarbons (PAHs).²¹⁸ Notably, smaller sized CPPs—those with less phenyl units—polarize the effect of bending the functional units. It is therefore valuable to synthesize functionalized CPPs in more than one ring-size to understand the size-dependent and, in turn, strain-dependent properties. CPPs stand as an interesting structure alone, but recent works have established reactions on CPPs that make them a novel precursor to more complex carbon nanostructures.^{69,70,79,93,123,143}

Together with the concept of strain-driven properties, $[n+1]$ CPPs, where the $[n+1]$ represents a nanohoop with “ n ” phenylenes and one internal alkyne, have strain-promoted reactivities that are not present in flat analogues. Previous reports from our lab have established their reactivity in $[2+2]$ cycloadditions using tetracyanoethylene and $[3+2]$ cycloadditions with benzyl azide.^{69,143} The latter reports the strain and electronic dependent reaction rates of the SPAAC reaction. Computational investigation of the strain and reaction dynamics have shown that directing the strain onto the alkyne or aligning the FMOs with the transition state increase the rate of the SPAAC reaction.⁶⁹

In the process of investigating strain-promoted reactions, $[2+2+2]$ cyclotrimerization of alkynes was envisioned as a thermodynamic driving force towards a large curved π -system that would be difficult to assemble any other way.^{220–224} Metal-mediated cyclotrimerizations are efficient and result in interesting π -rich structures. Reacting $[n+1]$ CPPs this way should produce large pinwheel-like structures while maintaining some characteristic properties of CPPs due to the macrocyclic units surrounding the newly formed six-membered ring. The following text reports the successful trimerization of four $[n+1]$ CPP derivatives as well as their optical properties, solid state packing structure, and calculated electronic properties and strain.

V.3.2. Results and discussion

Synthesis of $[n+1]$ CPPs follow the same methods previously published by our lab.^{69,143} The methods to cyclotrimerize the alkyne were adapted from the literature using either $\text{Ni}(\text{COD})_2$, $\text{Pd}_2(\text{dba})_3$, or $\text{Rh}(\text{PPh}_3)_3\text{Cl}$ —also known as Wilkinson's catalyst.²²⁴ Palladium was determined to be the best catalyst for the trimerization reaction based on percent conversion and relative rates of reaction (Scheme V.2). This is in parallel with trimerization reactions in the literature with arynes. Typical unstrained alkynes have been shown to trimerize in good yields with nickel,²²⁵ but it was not as efficient with $[n+1]$ CPPs.



Scheme V.2. Synthesis of **[11+1] trimer**, **[9+1] trimer**, **fluor[9+1] trimer**, **meta-fluor[9+1] trimer** from their respective CPP.

We set out to characterize the electronic properties of the resulting trimers and their precursors and gain a deeper understanding of their strain-promoted reactivities. Computationally, we can predict which structures are more reactive by their increased local strain and compare the predicted electronic properties with experimental measurements to understand how the curved π -system affects the annulated structures.^{68–70,85,226} Although the electrochemical characterization was attempted, no redox events were observed electrochemically in dichloromethane. The trimers did retain their solubility in dichloromethane and dimethylsulfoxide enough for optical characterization. **Fluor[9+1] trimer** is emphasized because of its distinct optical properties from **fluor[9+1]CPP** which has some CT character as shown in Figure V.5.

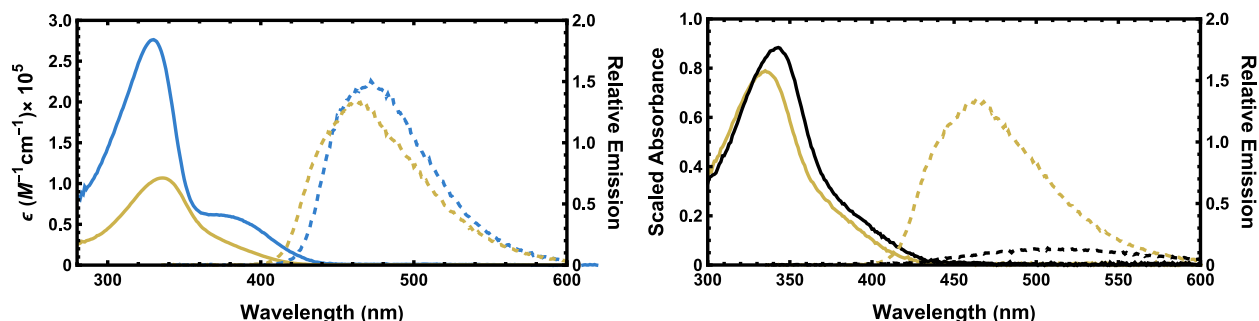


Figure V.5. Absorbance (solid) and emission (dashed) profiles of **fluor[9+1]CPP** (yellow) and **fluor[9+1] trimer** (blue) on the left in dichloromethane. Absorbance (solid) and emission (dashed) profile in dichloromethane (yellow) and dimethylsulfoxide (black).

In DMSO compared to DCM, **fluor[9+1]CPP** has a red-shifting absorbance and emission profile with a drastically lower emission intensity. Each trimer has roughly three times the molar absorptivity compared to the representative nanohoop. The lowest energy transition increases in intensity from the nanohoop to the trimer likely due to the increased orbital density localized on different lobes of the trimer instead of the being dispersed equivalently in the case of the nanohoop. Differences in orbital symmetry between molecular orbitals in the ground state geometry increase the number of allowed transitions, which increase the intensity of the lowest energy absorption compared to the nanohoop. Figure V.6 illustrates this concept in the case of **fluor[9+1]CPP** and **fluor[9+1] trimer** by the distribution of molecular orbitals and their respective orbital geometry.

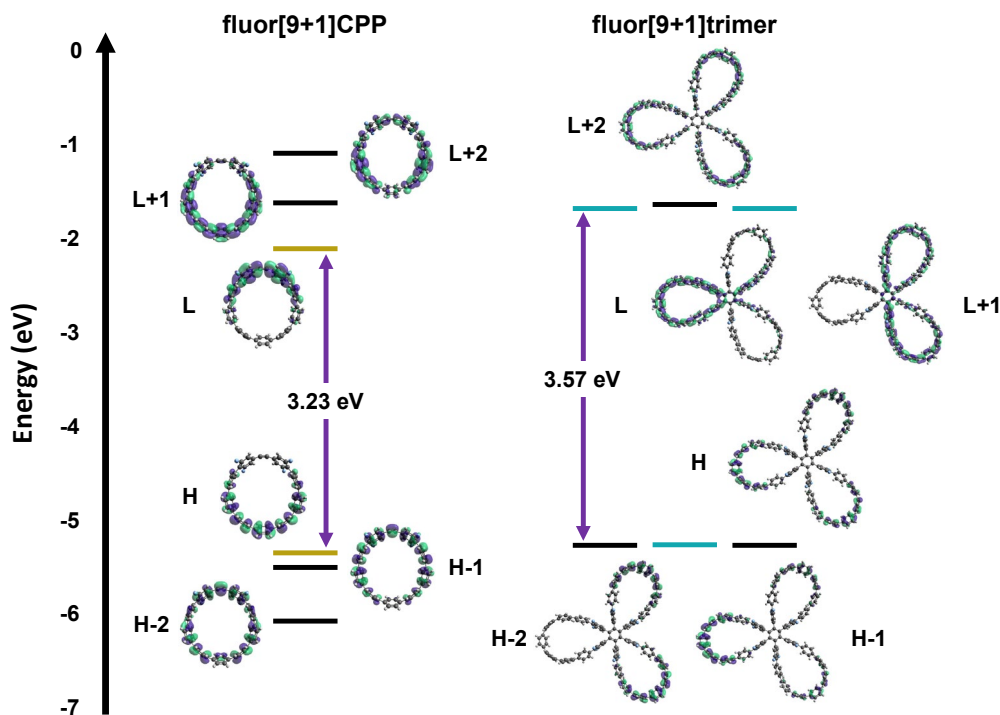


Figure V.6. Calculated orbital energies for **fluor[9+1]CPP** and **fluor[9+1] trimer** with the orbital geometries labelled and shown adjacent to each energy level (B3LYP/6-31G(d) level of theory, isosurface of 0.03).

V.3.3. Strain calculations

Calculations were performed with the Gaussian09 package at the B3LYP/6-31G(d) level of theory for all structures.¹⁰⁶ Optimized geometries were obtained by requesting Rational Function Optimization “rfo” methods in the command line. Each parent nanohoop and cyclotrimerized products were analyzed via StrainViz and referenced to the most strained structure, **meta-fluor[9+1]CPP**. Overall, the strain of each nanohoop is localized onto the alkyne, as seen in a previous paper from our group,⁶⁹ but becomes localized at the opposite end upon trimerization. This is consistent with our understanding of how strain is distributed in inherently strained macrocycles.^{68,226} Linear strips of phenylenes tend to localize the strain as the substitution pattern on the opposite side of the nanohoop changes from para to meta or ortho connectivity. Trimers, other than the **meta-fluoro[9+1] trimer**, have greater localized strain due to the change in connectivity from alkyne to ortho-phenylene. All of the trimers have total strain values equivalent to less-than-three-times the total strain of the precursor alkyne nanohoops, 130 kcal/mol for **fluor[9+1] trimer** versus 56 kcal/mol for **fluor[9+1]CPP**. Although the total strain decreases after trimerization, the local strain is increased for the para substituted alkyne nanohoops, 3.10 kcal/mol for **fluor[9+1] trimer** versus 2.78 kcal/mol **fluor[9+1]CPP** (Figure V.7). Understanding how the strain is allocated within the alkyne nanohoop and trimers could serve as a useful tool for altering the photophysical properties of these materials. As previously addressed in literature, localizing strain onto electron acceptors within a nanohoop can result in larger bathochromic shifts in the emission profile. Installation of multiple alkynes could provide reaction pathways to extended structures, and knowing how the strain is distributed with iterative reaction is important for designing such systems.

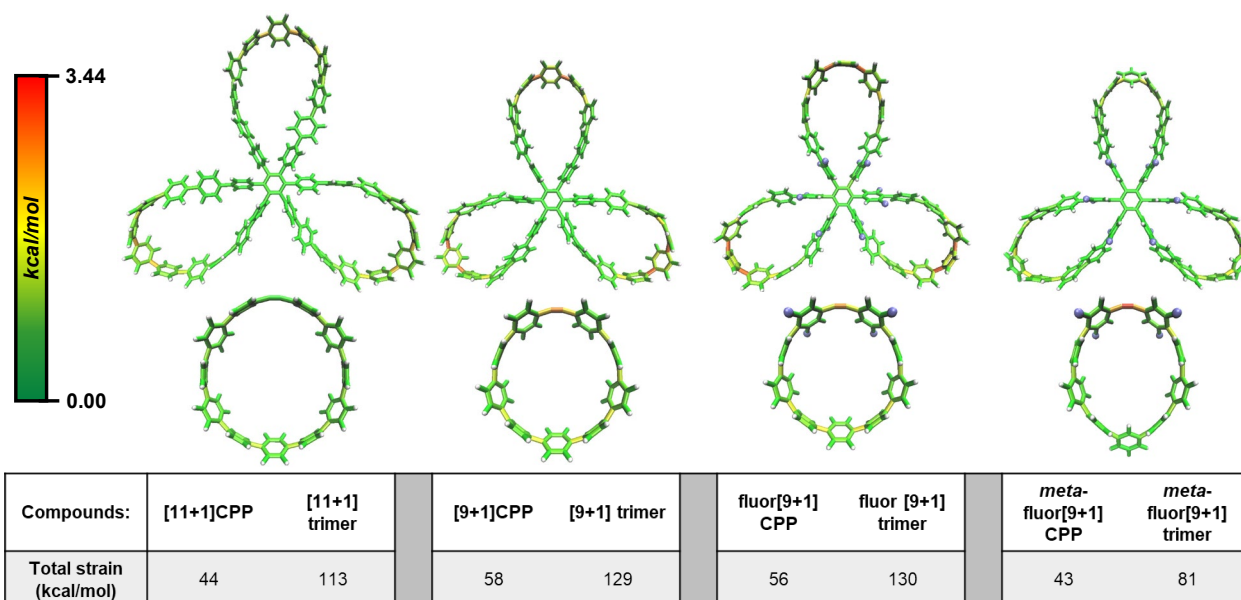


Figure V.7. StrainViz analysis of $[n+1]$ CPPs and their respective trimers at the B3LYP/6-31G(d) level of theory. Table of total strain for each shown below respective structures. Relative strain scale (in kcal/mol) shown on the left.

V.3.4. Conclusion to Cyclotrimerization of Alkyne-Containing Cycloparaphenylenes

$[n+1]$ CPPs have been shown to undergo strain-promoted reactions that would otherwise require elevated temperatures or activated substrates. A set of diverse nanohoops have been reported to undergo $[2+2+2]$ cyclotrimerizations with themselves to make large pinwheel-like structures. These large π -rich structures retain a common absorption seen from nanohoop derivatives but have much larger molar absorptivities. Computationally, we can characterize the total and local strain to help explain why the alkyne-containing cycloparaphenylenes react at ambient conditions and connect changes in the optical properties with changes in strain. Emergent properties of *meta*-fluor $[9+1]$ CPP and *meta*-fluor $[9+1]$ trimer were also investigated computationally to explain the solvent dependent fluorescence of the nanohoop and increase in the lowest energy absorption of the trimer. Cyclotrimerization of these alkyne-containing CPPs is a powerful tool for making extended π -rich structures. Studying them computationally can help guide the synthesis to large structures with desirable optoelectronic properties.

V.3.5. Experimental details (computations)

Computations were performed using Gaussian09 at the B3LYP/6-31G(d) level of theory.¹⁰⁶ Keywords “Opt=(rfo,NoSymm)” were added to account for the fragments with an alkyne and to ensure minimal negative energies in the case of the trimer fragments. The alkyne piece was present in one fragment for the *m*-fluor $[9+1]$ CPP StrainViz analysis because of the error associated with optimizing fragments with a 180° angle. Outputs from individual StrainViz calculations were submitted with the maximum bond energy set as the highest strained bond between all four molecules (*m*-fluor $[9+1]$ CPP) to generate a relative strain scale. This setting recolors each bond to generate a comparative heat map. Replacing the “max(norm_values)” on line 171 in the “bond_scripts.py” with the max bond strain in the “total_bond.tcl” file, a recolored output is generated by rerunning the StrainViz script for each molecule. All fragment geometries and output files will be available for download from the following link: <https://figshare.com/s/a9a9e03f19998b572ca7>

V.4. Co-authored content

The work in section V.2 was co-authored with Julia Fehr, Nathalie Myrthil, Anna Garrison, Prof. Steven Lopez, and Prof. Ramesh Jasti and published under the title “Experimental and Theoretical Elucidation of SPAAC Kinetics for Strained Alkyne-Containing Cycloparaphenylenes” in *Chemical Science*.⁶⁹ Section V.3 was co-authored with Julia Fehr, Tara Clayton, Dr. Lev Zakharov, and Prof. Ramesh Jasti and is being prepared for submission. For section V.2, Julia Fehr wrote the majority of the manuscript, performed all the experimental work, and made the figures. Nathalie Myrthil performed the reaction coordinate computations. Anna Garrison performed some experimental work with Julia Fehr. I helped write a portion of the computational section, performed all StrainViz calculations, and helped with editing. Prof. Ramesh Jasti and Prof. Steven Lopez edited the manuscript. The writing and computational work for section V.3 was done by me and represents a draft of a manuscript in preparation for publication with Julia Fehr and Tara Clayton as the first co-authors. I made the figures with help from Julia Fehr. All experimental work

was done by Julia Fehr and Tara Clayton. Optical data was collected by Julia Fehr. Dr. Lev Zakharov solved crystal structures of the **fluoro[9+1]** and **meta-fluor[9+1]** trimers. Prof. Ramesh Jasti edited the manuscript in preparation.

V.5. Bridge to Chapter 6

Computational investigation of the strain of nanohoops can act as a bridge to explain emergent optical properties. As the strain of the nanohoop increases the orbital energies converge to produce molecules with lower band gaps. In turn, we can also calculate the intermolecular interactions to explain binding affinities and link charge transfer properties just like in the case of single molecules. My work has expanded to provide computational evidence for host-guest interactions of functionalized nanohoops and optoelectronic properties that arise from nanohoops with increasing donor-acceptor character.

CHAPTER VI
 PREDICTING OPTICAL AND HOST-GUEST PROPERTIES OF FUNCTIONALIZED CARBON
 NANOHOOPS

VI.1. Background

Synthesis of functionalized carbon nanohoops was facilitated by the bottom-up synthetic methods developed by our lab.^{24,79,85,86,93,103,123} Nucleophilic addition of functionalized arenes into functional benzoquinone or semiquinone building blocks is routine, and thanks to the mild tin reduction conditions¹⁴⁷ our lab has successfully synthesized a wide range of functionalized carbon nanohoops. We can incorporate pyridines, pyrimidines, and thiophenes in place of phenylenes and append a range of alkyl or heteroatom substituents onto the phenylenes.^{82,92} Most carbon nanohoop derivatives are even stable enough to perform functional group conversions and metal-mediated reactions to derivatize them (Figure VI.1).^{70,124} Incremental placement of functionalized arenes allowed us to tease out subtle changes in the optical and electronic properties of carbon nanohoops.^{79,226} Among these properties we typically highlight the host-guest interactions, fluorescent properties, and electrochemical redox properties.^{86,93,95}

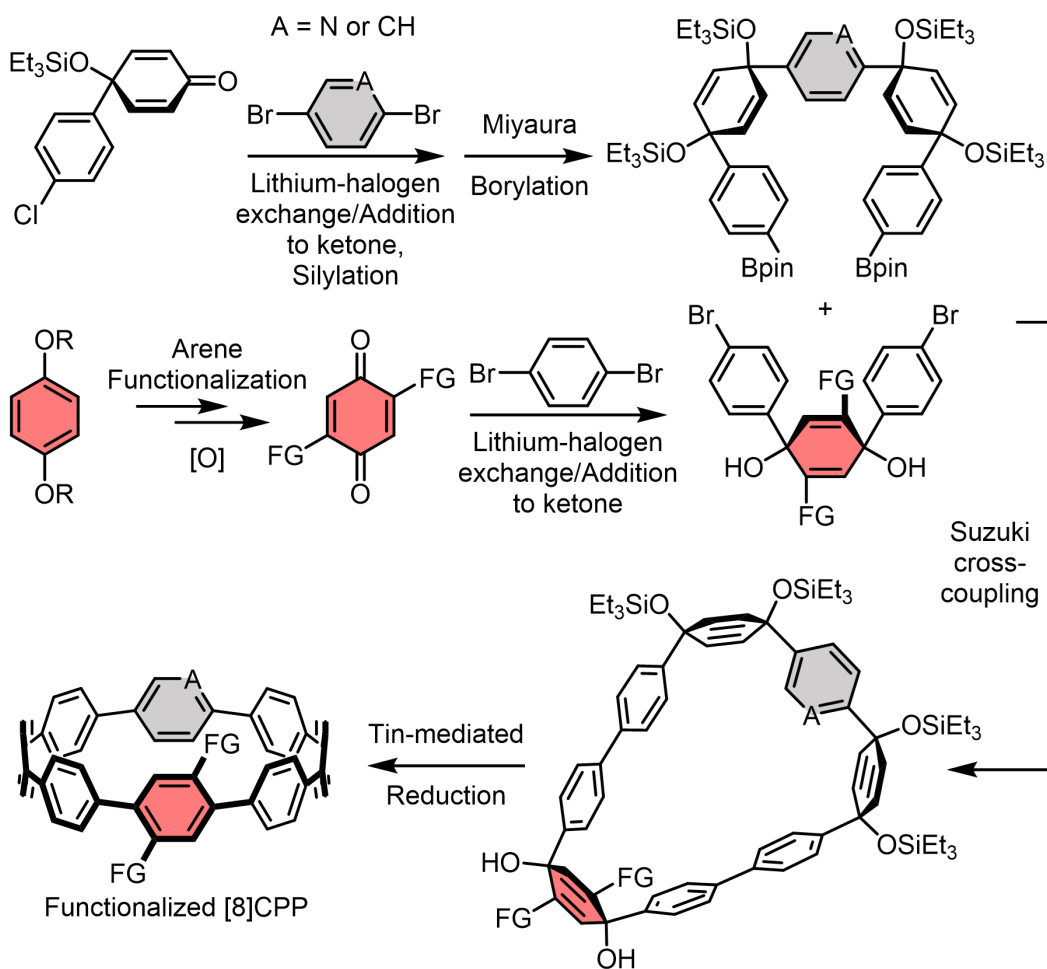


Figure VI.1. Typical synthetic route to functionalized cycloparaphenylenes with a variable pyridine in replacement of a phenylene.

Cycloparaphenylenes with 10 or more phenylenes are established guests for hosting fullerenes.^{95,219,227–232} There is even sufficient literature precedence for hosting functionalized or endotopic fullerenes, but much fewer examples of functionalized nanohoops hosting fullerenes. As a result, the effect on the binding constant from appending functional groups is not well-understood. Therefore, we will address the effect of appending esters and carboxylate groups onto [10]CPP and [12]CPP on their binding affinity with C₆₀ and PC₆₀BM, experimentally and computationally. We also observed host-guest interactions between CPPs experimentally via fluorescence titrations and computationally following the same methods with fullerenes and will present the results in the forthcoming sections. Computational experiments can be used to sample a large set of possible hosts to later explore experimentally.

Due to their bright fluorescence and small band gaps, electrochemical and optical properties of cycloparaphenylenes and their derivatives are continually being studied to address their performance as a viable material in future devices. The functional group tolerance of our lab's methods facilitates incorporation of redox active groups like fluorenone which can be further functionalized via the ketone on the fluorenone fragment. Size dependent properties of these nanohoops were investigated experimentally and computationally via the UV-vis absorbance, emission, DFT, TD-DFT, and cyclic voltammetry in the following sections. Size dependent and solvent dependent properties can be corroborated with computational results to highlight a trend in donor-acceptor systems or suggest a suitable synthetic target to explore experimentally.

VI.2. Synthesis of Water-Soluble Cycloparaphenylene and Their Supramolecular Chemistry in Aqueous Systems

Supramolecular chemistry specializes in non-covalent interactions (i.e. van der Waals forces, hydrogen bonds, hydrophobic forces, metal-ligand coordination, *etc.*) that drive self-assembly and the construction of complex materials of two or more chemical species. Importantly, since the discovery of crown ethers as hosts for metals in solution by Pedersen,²³³ alongside analogous work by Cram and Lehn, macrocycles have been a mainstay of supramolecular chemistry, particularly in the area of molecular recognition.^{234,235} Common macrocycles used in supramolecular chemistry include cyclodextrins, cucurbiturils, pillararenes, calixarenes, resorcinarenes and others, and systems produced with these macrocycles have found countless applications spanning many fields.^{236–247} In particular those macrocycles which can function in water, most notably cyclodextrins (CDs) and cucurbiturils (CBs), offer chemists a tool for developing a better understanding of the complex but ubiquitous solvent that is water via studying supramolecular chemistry in aqueous environments. Aqueous supramolecular chemistry has mainly been governed by the hydrophobic and Hofmeister effects; however, these phenomena are not very well understood at the molecular level making our understanding of aqueous supramolecular chemistry quite murky.^{248,249} Further, due to challenges in synthesizing water-soluble organic compounds, most of this research still takes place in organic solvents.²⁵⁰ Carbon nanomaterials have gained interest as possible guests to realize their intrinsic properties in an aqueous environment, but due to their carbon-rich nature are not soluble and covalent methods to solubilize them render their material properties less effective.⁴⁵

Despite this, supramolecular studies of CB and CD in aqueous environments has proven lucrative, resulting in a wide range of applications for these water soluble systems including: drug delivery and solubilization systems, water purification methods, imaging and sensing, as well as reaction containers for aqueous synthesis and tools for surface functionalization.^{237,239,242,243,248–250}

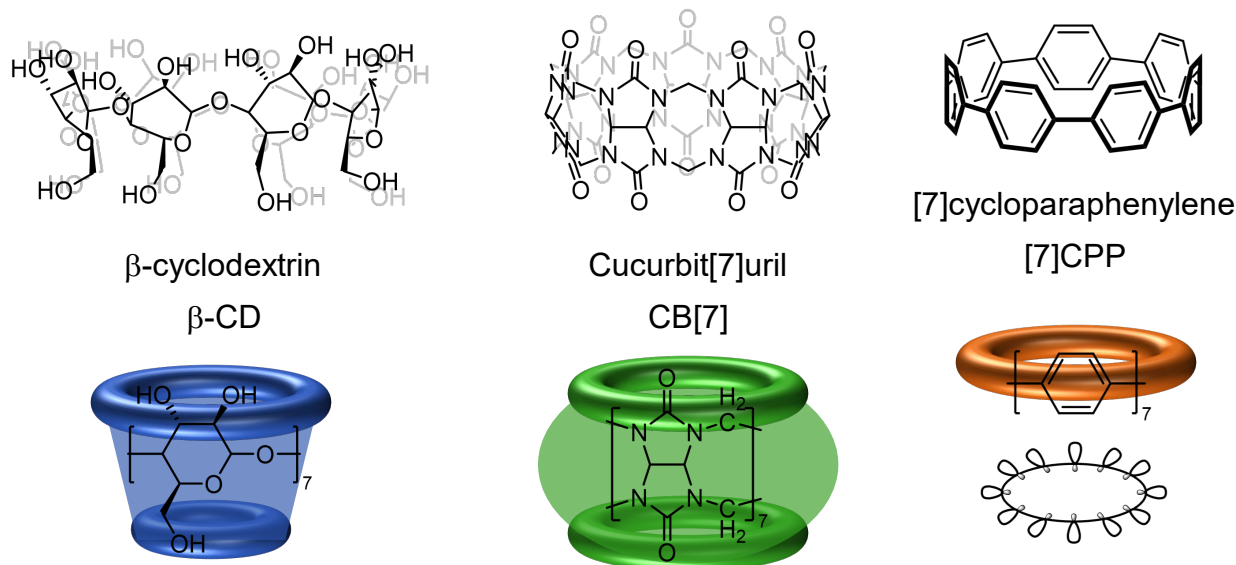


Figure VI.2. Established macrocyclic hosts like cyclodextrins (left) and cucurbiturils (center) have found utility in aqueous supramolecular chemistry. In contrast CPPs (right), while interesting in their own right, have found limited use in this area due to their functionally simple structure.

A relatively new family of macrocycles first synthesized in 2008, $[n]$ CPPs were long-standing synthetic targets due largely to interest in their structure representing a small molecule analogue of armchair CNTs and their unique optoelectronic properties that arise from the bent phenylene backbone.²¹ CPPs are macrocycles composed entirely of para-linked phenylenes and are colloquially dubbed “carbon nano hoops.” Since the synthesis of nano hoops has been well established, focus has shifted towards their potential applications and derivatization, including use in supramolecular chemistry. Due to the rigid nature of these phenylene-based macrocycles, they contain a shape-persistent pore and a radially oriented π -system capable of interacting with complementary guests, such as fullerenes or other carbon nanostructures.^{219,251} In contrast to macrocycles like CBs and CDs, nano hoops are selective to guest molecules with large π systems or C-H bonds in favorable alignment to the nano hoop π -system (i.e. π - π stacking, cation- π , anion- π , or CH- π interactions), which has allowed them to differentiate between larger guests that CBs and CDs do not bind well. Since their initial synthesis, researchers have developed methods to access a variety of functionalized nano hoops including π -extension of the backbone,²⁵¹ installation of electron-donor and -acceptor groups^{70,86} or pendant halides,²⁵² and heteroatom doping,⁹⁵ all of which can alter the optoelectronic and supramolecular properties.

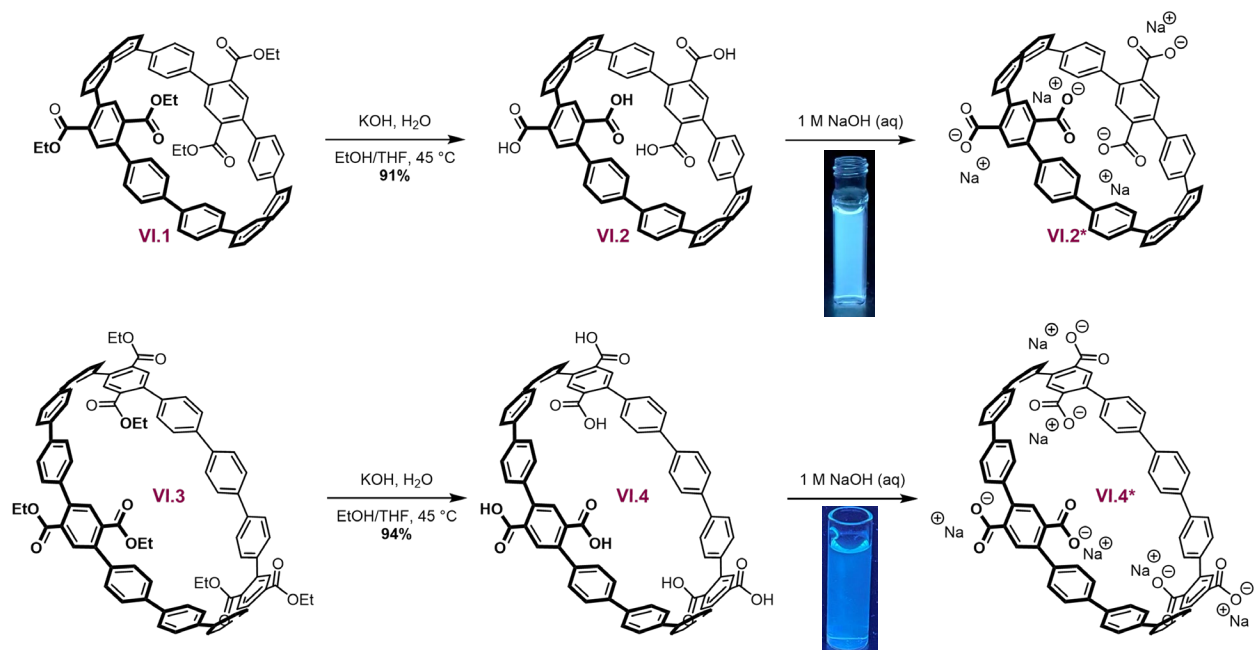
Tailoring the supramolecular properties of nano hoops via derivatization of the parent structure has proven quite effective.²⁵ In particular, nano hoops with appended electron-donating or with-drawing groups has proven a successful route to tailoring their molecular recognition properties. For example, two

independent studies on dimethoxybenzene-containing nanohoops have illustrated that incorporation of this electron-rich functionality allowed for complexation with cationic small molecules via cation- π and CH- π interactions.^{253,254} A recent publication by the von Delius group details the binding affinity for C₆₀ in aza[10]CPP and N-methylaza[10]CPP, concluding that the methylated CPP has a lower affinity due to the steric hinderance by the N-methyl group. Work from our lab in 2019 also illustrated that strategic incorporation of perfluoroarenes into the nanohoop backbone allowed for the creation of supramolecular CNT mimics via arene-perfluoroarene interactions.²⁵² Inspired by these successful efforts and the general interest in aqueous-based supramolecular chemistry, herein we present the synthesis of the first completely water-soluble CPP derivatives with which we can explore host-guest interactions of these pi-conjugated materials driven by the hydrophobic effect in aqueous media.

VI.2.1. Results and discussion

For this work, we first targeted a water-soluble [10]CPP derivative, due to its well-studied size-dependent interaction with C₆₀.^{227,255,256} We initially envisioned that solubility could be conferred from pendant sulfonate groups, inspired by the synthesis of the first biocompatible disulfonate-[8]CPP in 2018.¹⁰⁹ Due to the increase in nanohoop size, as well as the tendency of the disulfonated nanohoop to crash out of solution upon standing, we sought to investigate more effective and synthetically accessible solubilizing groups. We then found that installation of a robust ester group could readily be saponified to the carboxylate functionality.

Tetra-ester[10]CPP **VI.1** was saponified to obtain tetra-acid[10]CPP **VI.2**. From here, simple deprotonation of the acid-functionalized hoop with aqueous NaOH yields a fully water soluble nanohoop. Importantly, the water-soluble carboxylate-derivative **VI.2***, retains its fluorescence in water with a λ_{\max} of 470 nm. To account for the potential steric encumbrance around the nanohoop pore created by carboxylic acid substituents, and to enhance the solubility of the fullerene complexes, we next considered that a larger, more substituted [12]CPP derivative may fare better in aqueous studies. Using the same synthetic approach with ester-functionalized phenylenes, hexa-ester[12]CPP **VI.3** was made and saponified to reach hexa-acid[12]CPP **VI.4** which was completely soluble in water after deprotonation to **VI.4***, emitting with a λ_{\max} of 450 nm (Scheme VI.1). To determine whether our water-soluble nanohoop would still bind C₆₀ in aqueous media as predicted, fluorescence titrations were attempted via the method published by Yamago *et al.*²²⁷



Scheme VI.1. Conversion of tetra-ester[10]CPP **VI.1** to tetra-carboxylate[10]CPP **VI.2** and hexa-ester[12]CPP **VI.3** to hexa-carboxylate[12]CPP **VI.4** with inlays of their emissive properties in water.

It should be noted that alternate titration methods were also considered or attempted but were insufficient; NMR analysis is not sensitive enough to analyze associations of magnitudes greater than 10^6 M^{-1} , and ITC studies were prohibitive due to the partial precipitation of both C_{60} and nano hoop- C_{60} complexes resulting in irregular data over multiple trials. Additionally, these experiments were carried out with phenyl- C_{61} -butyric acid methyl ester (PCBM, a more soluble C_{60} derivative) as the guest molecule. In order to carry out titrations in aqueous media, solubility of both the host and guest must be achieved at the concentration regime of the experiment, which meant the use of co-solvents to work with fullerenes; the results are summarized in Table VI.1 below.

	Host	Host ID	Guest	Solvent	K_a (M^{-1})
1[†]	[10]CPP	–	C_{60}	Toluene	$2.79 (\pm 0.03) \times 10^6$
2	[10]CPP	–	PCBM	Toluene	$8.82 (\pm 0.04) \times 10^5$
3	$(CO_2^-)_4$ -[10]CPP	2*	C_{60}	20% EtOH/ H_2O	$2.03 (\pm 0.52) \times 10^6$
4	$(CO_2^-)_4$ -[10]CPP	2*	PCBM	20% EtOH/ H_2O	$1.78 (\pm 0.29) \times 10^7$
5	$(CO_2Et)_4$ -[10]CPP	1	PCBM	DMSO	$2.19 (\pm 0.34) \times 10^4$
6	[10]CPP	–	[5]CPP	Toluene	$6.91 (\pm 1.54) \times 10^5$
7	$(CO_2^-)_4$ -[10]CPP	2*	[5]CPP	H_2O	$3.20 (\pm 1.01) \times 10^5$
8	$(CO_2^-)_4$ -[10]CPP	2*	[7]CPP	H_2O	$1.64 (\pm 0.43) \times 10^6$
9	$(CO_2^-)_4$ -[10]CPP	2*	[9]CPP	H_2O	N/A

Table VI.1. Summary of titration results with [10]CPP, **1**, and **2*** with fullerene and nano hoop guests in varied solvents with associated binding affinities.

In general, titrations with C₆₀ not performed in toluene (Table VI.1 entry 3) were plagued by larger error, which is likely due to poor solubility of the complexes especially at higher concentrations. Despite this, we see that in the aqueous mixture the affinity for C₆₀ is maintained (Table VI.1 entry 1 vs 3); however, PCBM—with its enhanced solubility over C₆₀—in general resulted in more reliable titration data and led to an order of magnitude increase in affinity between the host-guest pair (Table VI.1 entry 4). Based on this result, we wanted to assess the broad utility of the hydrophobic effect as a means of driving host-guest interactions with nanohoops in water, and next turned our attention to the creation of nanohoop ring-in-ring complexes. While these types of complexes have been studied via theoretical models,^{256,257} there is far less evidence for their formation experimentally,^{258–260} likely in large part due to their decreased association affinity (on the order of 10¹⁻²) as reported by Yamago et al.²⁶¹

We found that fluorescence titrations once again led to characteristic fluorescence quenching as a function of guest concentration. As an initial test, we once again started with titrations in toluene using the parent [10]CPP host and were surprised to find the fluorescence quenching suggested higher association than previously reported (Table VI.1 entry 6) based on NMR chemical shifts reported in literature. Next, we assessed the affinity of [5] and [7]-[9]CPP in water. Unsurprisingly, the smaller nanohoop guests were more readily solubilized in water than fullerenes, and therefore all ring-in-ring complexes created with water-soluble host **2*** were carried out in water without the use of co-solvents. Interestingly, we saw that [5]- and [7]CPP were at least partly solubilized by our water soluble [10]CPP **2*** (Table VI.1 entries 7 and 8), which was seen visually by the slow change in color from clear to yellow of each solution, as well as a measurable decrease in fluorescence with the sequential addition of guest CPP. In contrast, theoretical work has repeatedly predicted the ideal guest size for [n]CPP being [n-5]CPP (e.g. [10]CPP \supset [5]CPP) based on optimized vdW interactions. This suggests that alternate orientations of the host and guest nanohoops are likely possible to accommodate a wider range of sizes. Importantly though, we see no quenching and assume no host-guest interactions when titrations are attempted with [9]CPP (Table VI.1 entry 9) as this guest is only one phenylene unit smaller than the host and, regardless of orientation, too large to be hosted adequately by **2***.

With the success of ring-in-ring complex formation in water, we wanted to further assess the broad viability of the hydrophobic effect as a means for driving guest association with nanohoop hosts. In particular, while the high association constant of the [10]CPP \supset fullerene systems measured in toluene was retained in aqueous media, we had initially expected an increase in association due to the hydrophobic effect driving the fullerenes into the pore of the nanohoop. With the hexacarboxylate-functionalized [12]CPP having a larger pore and more solubilizing groups, we repeated the fluorescence titrations with both fullerene compounds and smaller nanohoops, and we found that the association with C₆₀ increased when compared to titrations with the parent [12]CPP in toluene (Table VI.2 entry 10 vs 11). Most excitingly, we were able to measure the association of **4*** and PCBM at 1.53 \times 10⁶ M⁻¹ in only water without the use of any cosolvents (Table VI.2 entry 13). Next we carried out titrations with [6]-, aza-[6]-, [7]- and [9]CPP. Unsurprisingly, the water-soluble derivative of [12]CPP **4*** was able to host [9]CPP (Table 2-16) where **2***

failed to do so. The most interesting finding from all of the ring-in-ring complexes formed in water was that for both sizes of host, the guest with the highest affinity was larger than the guest predicted to have the best fit in previous works - the optimal pairs are [10]CPP \supset [5]CPP and [12]CPP \supset [7]CPP, however the water soluble [12]CPP \supset [9]CPP (**Table VI.2** entry 16) had higher K_a values by at least half an order of magnitude in water.

	Host	Host ID	Guest	Solvent	K_a (M^{-1})
10	[12]CPP	–	C ₆₀	Toluene	1.01 (± 0.11) $\times 10^6$
11	(CO ₂) ₆ -[12]CPP	4*	C ₆₀	20% EtOH/H ₂ O	1.85 (± 0.46) $\times 10^6$
12	(CO ₂) ₆ -[12]CPP	4*	PCBM	20% EtOH/H ₂ O	1.63 (± 0.29) $\times 10^7$
13	(CO ₂) ₆ -[12]CPP	4*	PCBM	Water	1.53 (± 0.24) $\times 10^6$
14	[12]CPP	–	[7]CPP	Toluene	6.67 (± 0.21) $\times 10^6$
15	(CO ₂) ₆ -[12]CPP	4*	[7]CPP	H ₂ O	9.83 (± 1.27) $\times 10^5$
16	(CO ₂) ₆ -[12]CPP	4*	[9]CPP	H ₂ O	3.55 (± 0.95) $\times 10^6$

Table VI.2. Summary of titration results with [12]CPP and 4* with fullerene and nanohoop guests in water and their associated binding affinity.

VI.2.2. Computational results

In an attempt to better understand these unexpected results that we obtained during titrations, we turned to DFT generated models of our water-soluble nanohoop and fullerene-complexes (see SI, section 4.) The interactions of the host CPP with each respective guest were calculated following published computational methods using solvation parameters for water in equilibrium. Multiple initial geometries were considered and the optimized structures with the most encapsulation or “Saturn-like” arrangement were used herein. Geometry optimizations support the interactions of host-guest complexes not already explored experimentally. Multiple ring-in-ring complexes form the “Saturn-like” complexes discussed in literature, and they present distortion and interaction energies within a similar range of their all-carbon counterparts. Distortion of the cycloparaphenylene backbone can support the binding of unconventional guests by contorting to increase π -contacts with the nanohoop. We measured the diameter of 2* and 4* for each guest and summarized the results in **Table VI.3** in Angstroms. Figures VI.3 and VI.4 show how the diameters of the nanohoops were measured from the computed geometries of hexa-carboxylate[12]CPP \supset C₆₀ and tetra-carboxy[10]CPP \supset C₆₀, respectively. Since larger nanohoops are less strained and, as a result, more flexible, they can accommodate and bind a larger selection of guests. However, the distortion of the larger nanohoops would impart a larger energetic cost to the interaction. Therefore, larger nanohoops will have a larger range of binding affinities for a given host unlike smaller nanohoops which bind a smaller selection of guests with a narrow range of affinities.

The distortion and interaction energies summarized in **Table VI.3** are used to compare the interaction energy of tetracarboxylate[10]CPP \supset C₆₀ (-58.32 kcal/mol) with other complexes, offering supporting evidence of host-guest interactions and benchmarking relative affinities of the interaction. Further computational experiments could identify suitable host-guest combinations within the regime of the

experimental examples discussed herein. Design of Matryoshka-like systems and multi-walled nanotube-nanoring can be further justified if the predicted binding affinities are within range of experimentally determined values.²⁵⁹ In-line with our experimental results, we saw that the host nano hoops, especially in the case of **4*** were able to distort their naturally spherical geometry to more ovalar geometries in order to maximize vdW interactions with smaller guest molecules like C₆₀.

Host	Guest	Distortion of host (Å) [x, y]	E _{interaction} (kcal)
2*	C ₆₀	[-0.048, 0.137]	-58.32
4*	C ₆₀	[-2.196, 1.767]	-41.67
4*	[6]CPP	[-0.253, 0.229]	-53.01
4*	[7]CPP	[-0.497, 0.176]	-57.87
4*	[8]CPP	[-1.552, 1.401]	-56.04
4*	[9]CPP	[0.174, -0.154]	-49.25
4*	[10]CPP	[-0.515, 0.321]	-48.04

Table VI.3. Summary of interaction energies for the predicted host-guest complexes and their distorted diameters as illustrated in Figures VI.3 and VI.4 in Angstroms.

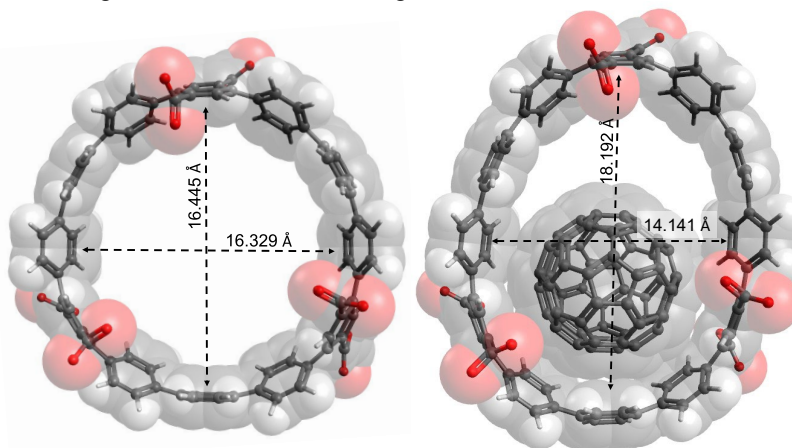


Figure VI.3. DFT models of **4*** and **4***⊃C₆₀ in water highlighting the deformation of the larger nano hoop to optimize vdW interactions between host and guest.

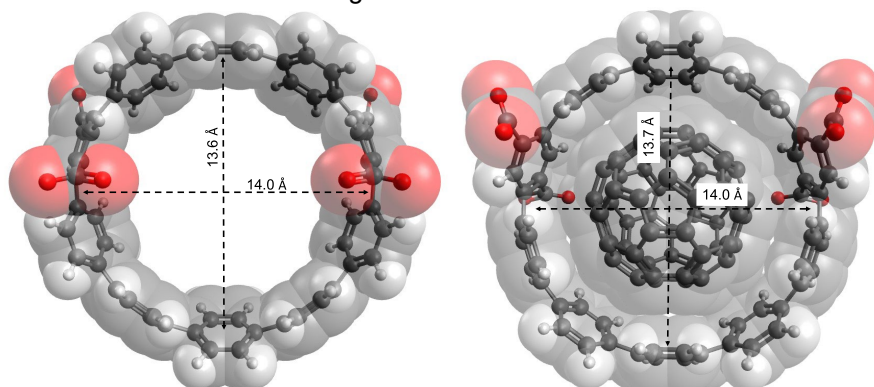


Figure VI.4. DFT models of **2*** and **2***⊃C₆₀ in water illustrating the tight binding of the complementary π-surfaces to optimize vdW interactions between host and guest.

VI.2.3. Conclusion to host-guest properties

The development of water-soluble carboxylate-functionalized nanohoops has allowed for exploration of a supramolecular interaction new to nanohoops: the hydrophobic effect. Excitingly, this hydrophobic driving force seems to be a broadly applicable strategy for creation of nanohoop host-guest complexes. Importantly for nanohoop-supramolecular complexes outside of those with fullerenes, exploitation of the hydrophobic effect has a large impact on the association affinity of these complexes with K_a s for ring-in-ring structures increasing by more than 4 orders of magnitude. In addition, studying these complexes in water offers an opportunity to learn more about the nature of π - π interactions in aqueous media which could have broader utility in the world of supramolecular chemistry. Based off the successes discussed herein, in the future we hope to explore more host-guest interactions of nanohoops in water, including the use of functionalized nanohoop guests like fluorinated- and methylated-aza[n]CPPs. Additionally, very recent work from the Bruns group has shown that small molecule polycyclic aromatic hydrocarbons can also interact with nanohoop hosts via CH- π interactions.²⁶² Based on this work, guests like corannulene and coronene should fit well with the water-soluble hosts discussed herein and provide further evidence of broad applicability of the hydrophobic effect for driving host-guest complexation of nanohoops.

VI.2.4. Experimental details (computational)

All computations were performed with the Gaussian 09 suite.¹⁰⁶ The structures were optimized at ω B97X-D/6-31G(d,p), a density functional that accounts for dispersion.²⁶³ Keywords “NoSymm” were added to account for redundant displacement. All results were solvated using the self-consistent reaction field using the default Polarizable Continuum Model method with the dielectric constant for water. For optimization of the supramolecular complexes, the guest molecule (C_{60} , [n]CPP or corannulene) was placed in proximity to the host molecule (“carboxylate[n]CPP”) and then optimized to an arbitrary minimum. Generally, all obtained structures represent a local energy minimum giving rise to only real vibrational frequencies, and those most closely resembling the previously predicted “planetary orbit” geometries are reported herein (Figure VI.5).

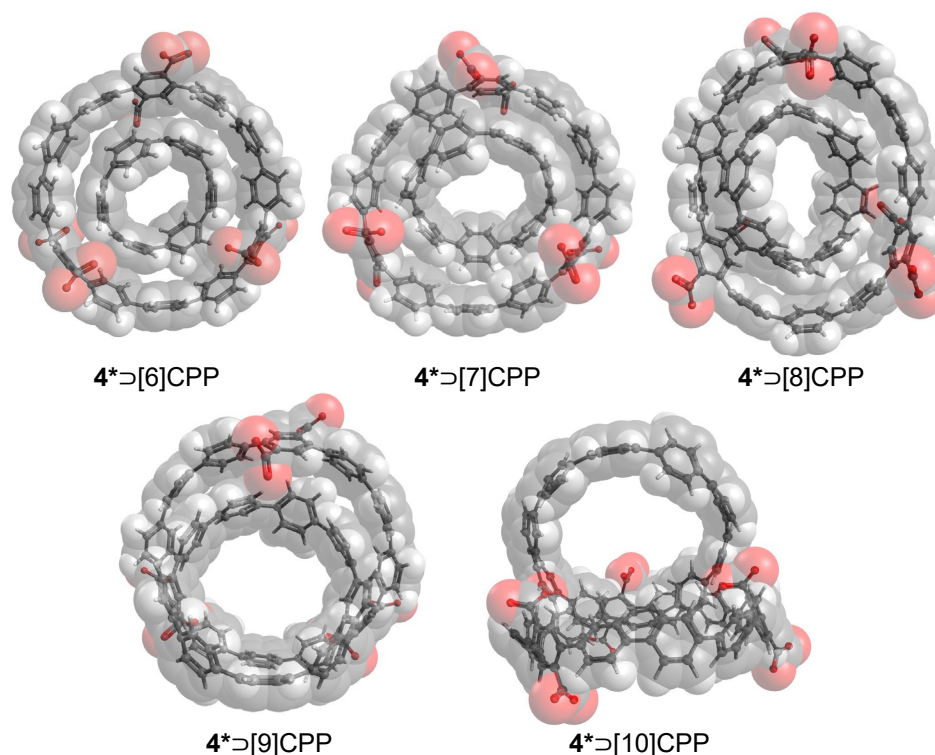


Figure VI.5. Geometries of the ring-in-ring complexes optimized computationally using Gaussian 09 at the ω B97X-D/6-31G(d,p) level of theory and the self-consistent reaction field using the default Polarizable Continuum Model method with the dielectric constant for water.

VI.3. Synthesis and Properties of Fluorenone-containing Cycloparaphenylenes and Their Late-Stage Transformations

Macrocyclic conjugated systems containing donor-acceptor (D-A) moieties have become of increasing interest in recent years as they are being explored for potential applications in organic electronics,^{264–266} in photodetectors,²⁶⁷ and in photovoltaics.²⁶⁸ Conjugated macrocycles with radially oriented π -systems are rather rare and less studied. CPPs belong to this subdivision; they are cyclic molecules consisting of paraphenylene units linked together into a hoop and are the smallest possible armchair carbon nanotubes, so-called nano hoops.²¹ They exhibit absorption and fluorescence properties that can be tuned by the number of phenylene units, alternate linkages (*para* vs *meta*) along with various functionalizations along the peripheries.^{140,269–273}

CPPs are continuously being explored by introducing a range of structural components into the nano hoop backbone,^{49,273–277} by incorporation into larger structures,^{123,214,278} or by bridging the phenylene rings with either carbon atoms or heteroatoms.^{89,96,97,279–284} To date, however, very few structures have been reported where phenylene units within the ring are replaced by electron rich or poor heteroaromatic or fused ring systems of donor (D) or acceptor (A) character.^{25,78,79,83,86,95} Due to the bending of the backbone of the CPPs, the associated HOMO energies are elevated, which in turn makes the pi-backbone an inherent donor.²²⁶ By introducing an electron acceptor unit within the nano hoop, D-A motifs can accordingly be

obtained.^{78,79,83,86,95} Indeed, D-A nano hoops often show interesting optical properties, such as redshifted absorption and emission bands.

Some D-A conjugated nano hoops that have been reported to date are shown in Figure VI.6, including **Me-Py**[*n*]**CPP**·OTf (*n* = 8, 10),^{79,95} **BT**[10]**CPP**,⁸⁶ **TT-F**[10]**CP**,⁸³ **AQ**[12]**CP**,⁷⁸ and **TCAQ**[12]**CP**,⁷⁸ with Py = pyridinium, BT = benzothiadiazole, TT = tetrathiophene, AQ = anthraquinone, and TCAQ = tetracyanoanthraquinodimethane. More structures which can be considered D-A nano hoops have been synthesized,^{80,81,84,87,285} but for the purpose of this work we have chosen to focus on nano hoops in which only one acceptor unit is incorporated and where the donor is the CPP π -backbone. Here **TT-F**[10]**CP** (**F** = fluorenone) is, however, an exception as it has thiophene units integrated as electron donors. Moreover, while nano hoops **AQ**[12]**CP** and **TCAQ**[12]**CP** maintain an all-phenylene backbone as the donor, the radial conjugation is actually ‘broken’ for these by cross-conjugation.

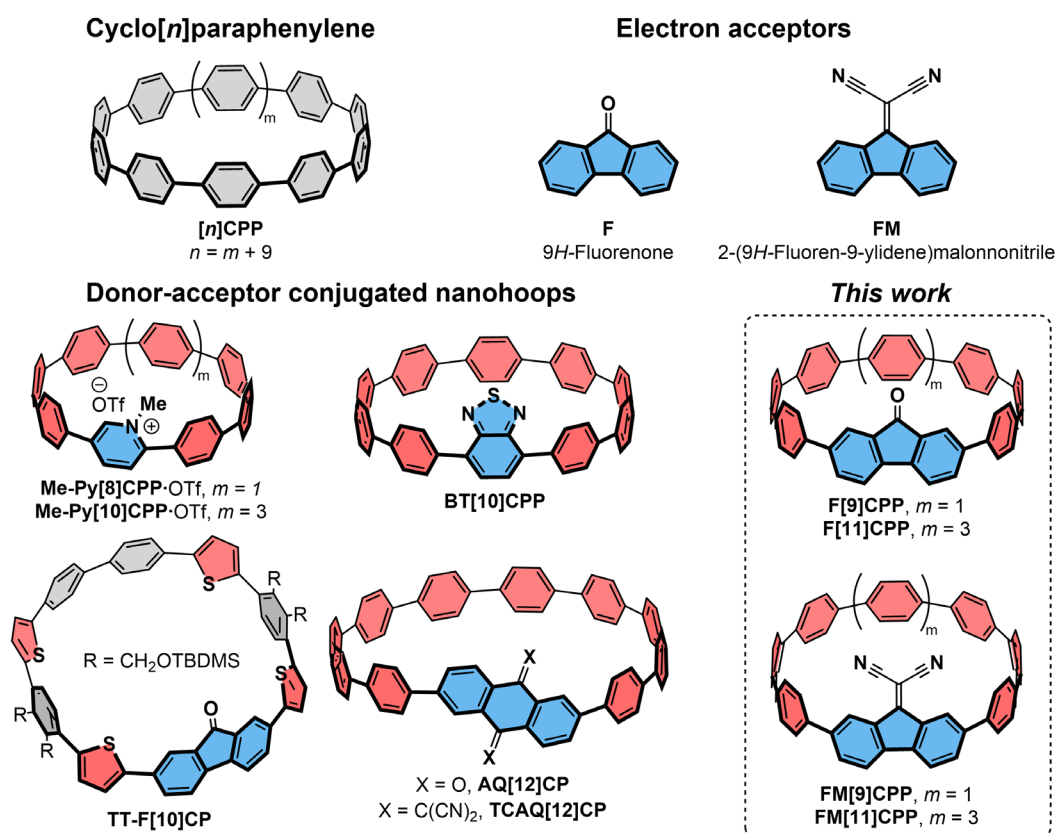


Figure VI.6. Top: [*n*]Cycloparaphenylene ([*n*]CPP) and the electron acceptors selected for this study. Bottom, left: Known donor-acceptor conjugated nano hoops. Bottom, right: New structures described herein. Number in brackets corresponds to the number of aromatic rings in the nano hoop. CPP stands for cycloparaphenylene (phenylene in this case meaning aromatic ring, e.g. pyridinium, benzothiadiazole), CP just stands for cyclophenylene as not all rings in the structures are *para*-substituted (phenylene in this case meaning aromatic ring, e.g. thiophene).

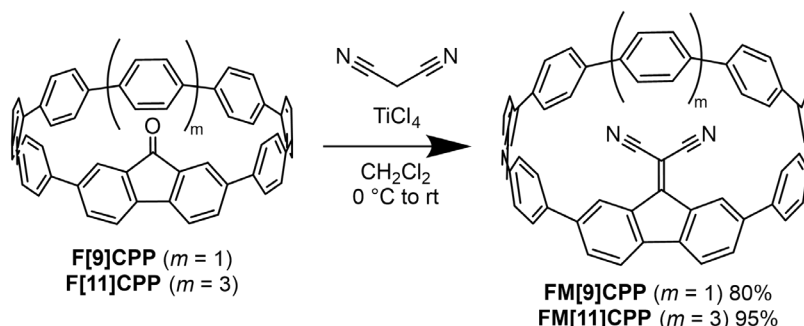
The limited number of donor-acceptor CPP compounds makes it difficult to generalize what controls optical properties. Specifically, the **BT** unit results in a redshifted emission and high quantum yield,⁸⁶

whereas the **TCAQ** unit induces an even more redshifted emission, but now with a drastically diminished quantum yield.⁷⁸ With the **Me-Py** unit integrated, the CPP is likewise nearly non-emissive in the case of **Me-Py[8]CPP·OTf**.⁷⁹ Upon a size-increase to **Me-Py[10]CPP·OTf**⁹⁵ a significant blueshift of the emission is observed in agreement with the general size-dependent properties of $[n]$ CPPs.¹⁴⁰ When it comes to redox properties, establishment of correlations between redox potentials as a function of ring size of donor-acceptor CPPs is suffering from either lack of reported oxidations (as is the case of **Me-Py[8]CPP** and **Me-Py[10]CPP**) or an irreversible reduction (**Me-Py[10]CPP**).

More structures clearly need to be investigated to rationally design donor-acceptor nano hoop structures for various applications. The overall aim of this paper is therefore to systematically elucidate the effects of the fluorenone and the related acceptor motif 2-(9H-fluoren-9-ylidene)malononitrile (**FM**) in radially conjugated CPPs with an all-phenylene backbone as the donor. We present here the synthesis of four such new CPPs of two different sizes and with one of two different acceptor units. Specifically, we have synthesized two sizes of CPPs with 9 and 11 phenylene-rings of which two are bridged by a carbonyl moiety, corresponding to the incorporation of a 9-fluorenone within the backbone. The fluorenone both serves as an acceptor, but also as a convenient synthetic handle for further functionalization, which was exemplified with the Knoevenagel reaction by introduction of the strongly electron-accepting malononitrile unit. This yielded the series of four compounds shown in Figure VI.6 (bottom, right).

VI.3.1. Results and discussion

With the two new $F[n]$ CPPs ($n = 9, 11$) in hand, the introduction of dicyanovinylidene units was accomplished by subjecting **F[9]CPP** and **F[11]CPP** to Knoevenagel condensations with malononitrile in the presence of TiCl_4 (Scheme VI.2).⁷⁸ Gratifyingly, these reactions gave in high yields the fluorenylidene-malononitrile-containing $\text{FM}[n]$ CPPs (**FM[9]CPP** 80%, **FM[11]CPP** 95%).



Scheme VI.2. Synthesis of $\text{FM}[n]$ CPPs ($n = 9, 11$) by Knoevenagel condensations.

VI.3.2. Experimental and theoretical absorption and fluorescence results

The optical properties of the new D-A nano hoops were explored in order to determine whether these differ from the simple addition of spectra of the parent compounds or whether new properties arise by the fusion. The UV-Vis absorption spectra of all four compounds in CH_2Cl_2 show a similar and intense absorption peak around 330-340 nm (Figure VI.8). Similar transitions are observed in the parent **[9]**- and **[11]CPP**. However, a new red-shifted low-intensity transition emerges around 500-600 nm, which is neither observed for **[9]CPP**, **[11]CPP**, fluorenone (**F**) nor 2-(9H-fluoren-9-ylidene)malononitrile (**FM**). Thus, this

feature is not intrinsic to any of the individual building blocks, but of an emergent feature of the D-A system. This lowest electronic transition is expected to have a large degree of charge-transfer character on account of the donor-acceptor nature of the nano hoops. The calculated HOMO and LUMO orbitals dominating the first transition, shown in Figure VI.7, supports this hypothesis as the HOMO is largely localized on the PP fragment and the LUMO on the acceptor (using the Gaussian 09 program package and the B3LYP/def2tzvp level of theory¹⁰⁶). The limited orbital overlap (*i.e.*, atoms sharing both orbitals) suggests only a weak oscillator strength in agreement with the low experimental molar absorption coefficients $\epsilon \approx 2 \times 10^3 \text{ M}^{-1}\text{cm}^{-1}$ of the CT transition. The nature of this band was further investigated by recording spectra in solvents of different polarities: CH₂Cl₂, toluene, and DMSO. The shoulder follows the polarity of the solvent with the lowest-energy absorption occurring in DMSO. The nature of the low-energy CT transitions was investigated further using emission spectroscopy for **F[9]CPP** and **F[11]CPP**. Compounds **FM[9]CPP** and **FM[11]CPP** are non-emissive and thus were not further analyzed. The emission spectra of **F[9]CPP** in a range of solvents are shown in Figure VI.9. Neither compound **F[9]CPP** nor **F[11]CPP** are strong emitters, in line with their donor-acceptor characters. Compound **F[11]CPP** has a higher relative fluorescence quantum yield, roughly by a factor of 2 vs **F[9]CPP**, but the same trends were observed for both **F[9]CPP** and **F[11]CPP**. A significant redshift in the emission compared to the parent compounds (**[9]-**, **[11]CPP** and **F**) is observed, which is attributed to a charge-transfer state. The emission also shows solvent dependence. Emissions in the polar solvents DMSO and CH₂Cl₂ are very similar even though their difference in polarity is significant. The emission in toluene and heptane is more blue-shifted in agreement with solvent polarity effects. Finally, the emission maxima in chlorobenzene lie in-between the others, in agreement with the solvent polarity, where the overall trend in lowering of the emission energy in more polar solvents is observed. The trend observed in relative quantum yields (toluene > heptane > chlorobenzene > DMSO > CH₂Cl₂) matches the trend in fluorescence lifetimes. This suggests that changes in fluorescence intensity is mainly due to the increase in non-radiative relaxation in the more polar solvents.

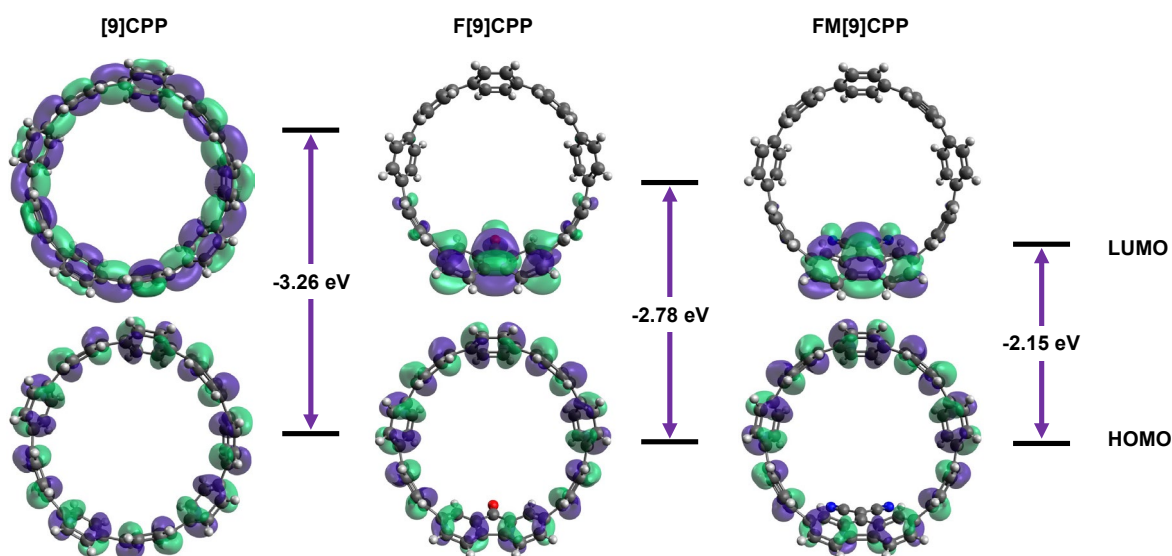


Figure VI.7. FMOs of **[9]CPP**, **F[9]CPP**, and **FM[9]CPP** calculated at the B3LYP/def2TZVP level of theory.

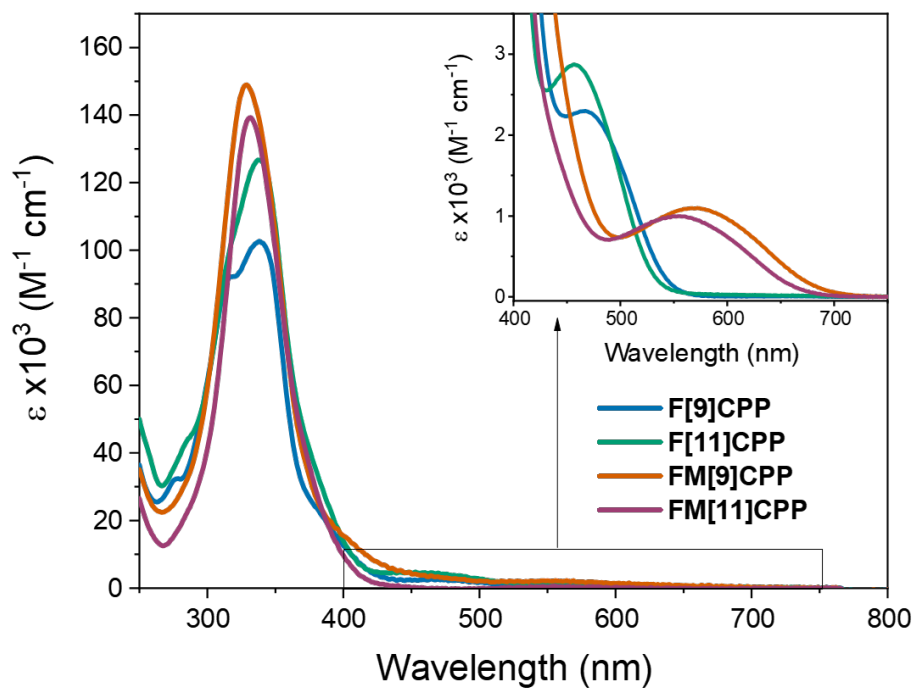


Figure VI.8. UV-Vis absorption spectra of compounds **F[9]CPP** (blue), **F[11]CPP** (green), **FM[9]CPP** (red), and **FM[11]CPP** (purple) in dichloromethane. Insert: Zoom of most red-shifted absorption bands.

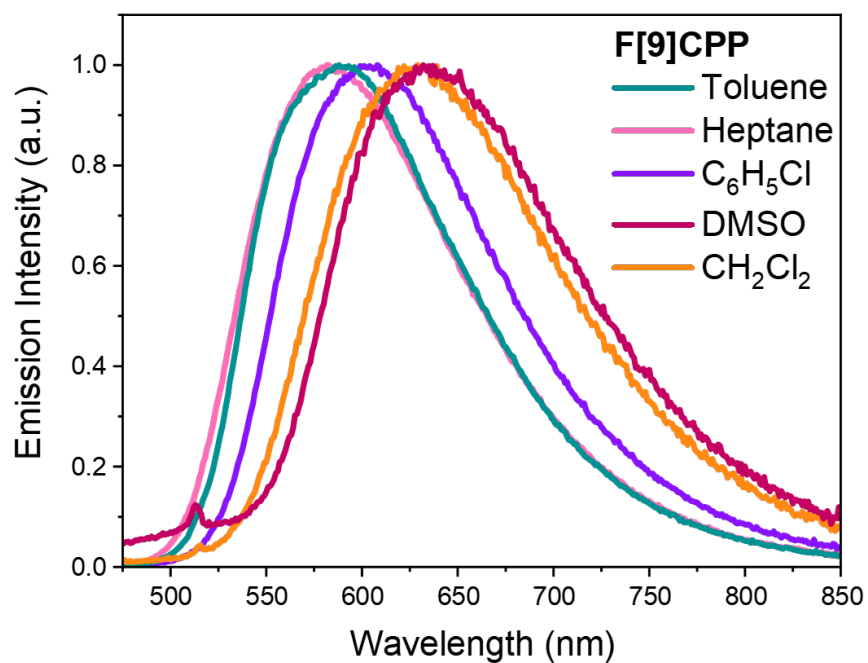


Figure VI.9. Emission spectra of compound **F[9]CPP** in toluene (green), heptane (5% CH_2Cl_2) (pink), chlorobenzene (purple), DMSO (red) and CH_2Cl_2 (orange). All compounds were excited at 450 nm.

VI.3.3. Experimental and theoretical electrochemical results

To further elucidate the donor and acceptor strengths of the compounds, the four macrocycles were subjected to electrochemical experiments. Cyclic voltammograms of **F[9]CPP**, **F[11]CPP**, **FM[9]CPP**, and **FM[11]CPP** are shown in Figure VI.10, and the electrochemical data summarized in Table VI.4, along with the data for **F**, **FM**, **[9]-** and **[11]CPP**. The electrochemical experiments revealed an oxidation event that turned out to be dependent on ring size rather than acceptor strength, with the oxidations occurring at higher potential for the larger rings. Oxidations are also observed for the parent **[9]-** and **[11]CPPs**, at slightly lower positive potentials, suggesting that the incorporation of accepting units makes the oxidation slightly harder. This is in good agreement with the computational results showing that the energy of the HOMO is largely contributed to by the phenylene backbone, and that the energy level of the HOMO is higher for smaller rings, allowing for easier oxidation, as shown in Figure VI.11. All compounds show reversible reductions at similar potentials to that of **F** and **FM**, with respect to their incorporated acceptor, again in agreement with the fact that the acceptor is the main contributor to the LUMO energy level, as shown in Figure VI.11. It is noteworthy, however, that the fluorenone is a stronger acceptor when introduced in the CPP nano hoops, and at the same time the acceptor strength increases with ring size (**F[9]CPP** vs **F[11]CPP**). Less significant differences in acceptor strengths are seen for the **FM**, **FM[9]CPP** and **FM[11]CPP** compounds.

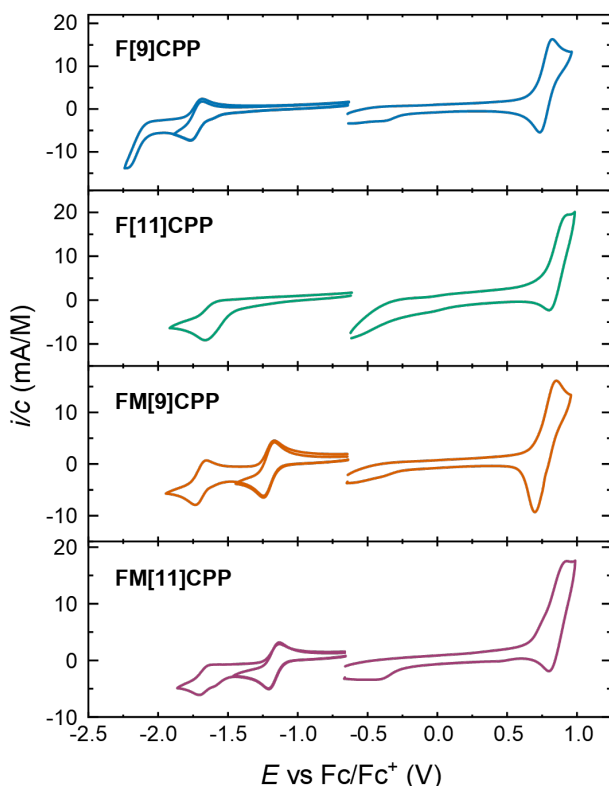


Figure VI.10. Cyclic voltammograms of compounds **F[9]CPP** (blue), **F[11]CPP** (green), **FM[9]CPP** (red), and **FM[11]CPP** (purple) in CH_2Cl_2 at 0.5 mM; supporting electrolyte: 0.1 M Bu_4NPF_6 , scan rate: 0.1 V/s. All potentials are depicted against the Fc/Fc^+ redox couple.

Compound	$E_{\text{red1}} / \text{V}$	$E_{\text{red1}} / \text{V}$	$E_{\text{red1}} / \text{V}$	$E_{\text{red1}} / \text{V}$
F	-1.80	-2.36 ^[a]	-	-
FM	-1.20	-1.79	-	-
F[9]CPP	-1.75	-2.16 ^[a]	0.77	-
F[11]CPP	-1.67 ^[b]	-2.08 ^[a]	0.86 ^[b]	-
FM[9]CPP	-1.22	-1.71	0.79	1.14 ^[a]
FM[11]CPP	-1.19	-1.69 ^[a]	0.85 ^[b]	-
[9]CPP^[c]	-	-	0.72	-
[11]CPP^[c]	-	-	0.83	-

Table VI.4. Electrochemical data from differential pulse voltammetry of compounds **F**, **FM**, **F[9]CPP**, **F[11]CPP**, **FM[9]CPP**, **M[11]CPP**, **[9]CPP** and **[11]CPP** in CH_2Cl_2 ; potentials in volts vs Fc/Fc^+ ; concentrations of 0.5 mM; supporting electrolyte: 0.1 M Bu_4NPF_6 . [a] Irreversible redox event. [b] Not perfectly reversible. [c] Ref. 286, recorded in 1,2-dichloroethane, V versus Fc/Fc^+ , supporting electrolyte: 0.1 m Bu_4NPF_6 .

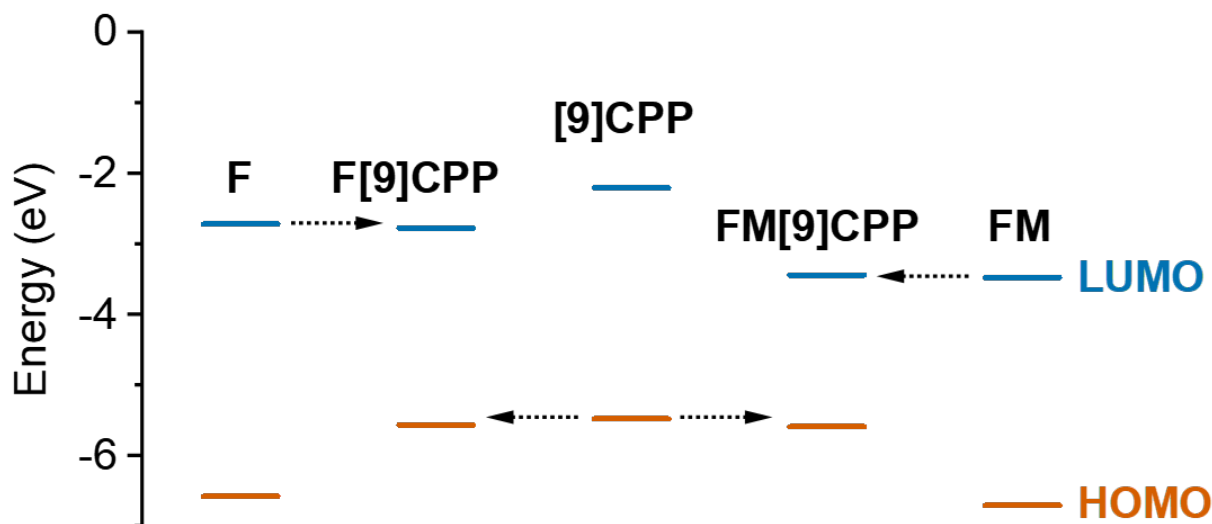


Figure VI.11. Calculated HOMO (orange) and LUMO (blue) energies for compounds **F**, **FM**, **F[9]CPP**, **FM[9]CPP** and **[9]CPP**. Arrows indicate contributing orbitals to the HOMO and LUMO energies of the fused compounds **F[9]CPP** and **FM[9]CPP**. Orbital energies were calculated at the B3LYP/def2tzvp level of theory. Similar observations are observed for the compounds **F[11]CPP**, **FM[11]CPP**, and **[11]CPP** (see Table VI.5).

Compounds **FM[9]CPP** and **FM[11]CPP** both show a second reduction event similar to that of **FM**; however, in the case of **FM[11]CPP** it is irreversible. The difference in potential between the first reduction event and the first oxidation event is shown in Table VI.5; it transpires that the gap is largely dependent on the acceptor, and no significant change is observed by the expansion of the rings. This difference in potentials is in good agreement with the optical gap calculated from the shoulder peak (shown in the insert of Figure VI.8) as well as the calculated HOMO-LUMO gap, as summarized in Table VI.5.

Compound	HOMO / eV	LUMO / eV	$E_{\text{gap-comp}} / \text{eV}$	$E_{\text{ox}} - E_{\text{red}} / \text{V}^{[a]}$	$E_{\text{shoulder}} / \text{eV}^{[b]}$
F	-6.55	-2.71	3.85	N/A	-
FM	-6.68	-3.46	3.22	N/A	-
F[9]CPP	-5.54	-2.76	2.78	2.52	2.66
F[11]CPP	-5.57	-2.77	2.80	2.53	2.71
FM[9]CPP	-5.57	-3.43	2.15	2.01	2.18
FM[11]CPP	-5.61	-3.44	2.17	2.04	2.24
[9]CPP	-5.55	-2.19	3.26	N/A	-
[11]CPP	-5.54	-2.13	3.40	N/A	-

Table VI.5. Experimental and computational (comp) values. [a] From Table 1. [b] Energy of shoulder from longest-wavelength absorption.

In order to better understand the electrochemical and photophysical observations, the energies of the molecular orbitals were calculated at a B3LYP/def2tzvp level of theory. The calculated frontier orbitals support the proposed D-A character, as the acceptor dominates the contribution to the LUMO energy; the LUMO energy of **F** is very close to that of **F[9]CPP** and **F[11]CPP**, and the same is observed for the **FM**, **FM[9]CPP** and **FM[11]CPP** series. These observations are illustrated in Figure VI.11 and summarized in Table VI.5. Similarly, the energy of the HOMO orbital is dependent on the all-phenylene backbone as the energies do not deviate much from that of the parent structures **[9]-** and **[11]CPP**. As a result of the above, we see a significant reduction of the calculated HOMO-LUMO gap, which is supported by both the electrochemical and photophysical measurements.

VI.3.4. Conclusion to optoelectronic properties

In conclusion, four new radially conjugated donor-acceptor based CPPs of varying acceptor strengths (9-fluorenone vs 2-(9H-fluoren-9-ylidene)malononitrile) and donor strengths (two different ring sizes) were prepared, namely the macrocycles **F[9]CPP**, **FM[9]CPP**, **FM[9]CPP**, and **FM[11]CPP**. High-yielding, late-stage functionalizations of the carbonyl-bridged **F[n]CPPs** by Knoevenagel reactions with malononitrile were successfully demonstrated, and the identities of the CPPs were confirmed by X-ray crystallographic structures, revealing slightly elliptical structures and a slight tilting of the fluorenylidene units towards the inside of the ring.

A new, characteristic absorption band was attributed to the D-A character of these compounds, which was supported by computational data as well as fluorescence emission data for the fluorenone CPPs. Furthermore, electrochemical and computational results suggest that the phenylene backbones contribute

to the HOMOs of the new systems and that the incorporated acceptors contribute to the LUMOs. Gratifyingly, all four CPP compounds exhibited reversible reductions and quasi-reversible oxidations, illustrating their convenient multi-redox characteristics. We anticipate that the late-stage functionalization of the fluorenone-incorporated CPPs can lead to a range of new systems as the ketone functionality provides an excellent handle for further derivatization without breaking radial conjugation.

VI.3.5. Experimental details (computational)

Using Gaussian09 software, computations were performed using Density Functional Theory (DFT) at the CAM-B3LYP/def2-TZVP level of theory.¹⁰⁶ All results were solvated using the self-consistent reaction field using the default Polarizable Continuum Model method with the dielectric constant for dichloromethane, dimethyl sulfoxide, or toluene, respectively. Excited-state calculations were performed using Time-Dependent DFT (TD-DFT) with the ground state optimized geometry. Absorption and emission profiles were calculated as vertical energy transitions using “NSTATES=6” for the first 6 lowest-energy transitions. Orbital energy calculations were collected at the B3LYP/def2-TZVP level of theory; dichloromethane solvation was included via the default Polarizable Continuum Model method. GaussSum was used to generate calculated spectra available in the Supporting Information (thermal broadening set to 1500 cm⁻¹).²⁸⁷ All output files are available at:

https://figshare.com/projects/Supporting_information_of_computational_results_for_Synthesis_and_Properties_of_Fluorenone-containing_Cyclo-paraphenylenes_and_Their_Late-Stage_Transformation/170619

VI.4. Co-authored content

The work in section V.2 was co-authored with Dr. Claire Otteson and Prof. Ramesh Jasti and is being prepared for submission. Section V.3 was co-authored with Viktor Pedersen, Dr. Nicolaj Kofod, Dr. Bo Laursen, Prof. Ramesh Jasti, and Prof. Dr. Mogens Nielsen and published under the title “Synthesis and Properties of Fluorenone-containing Cycloparaphenylenes and Their Late-Stage Transformation” to *Chemistry, a European Journal*.⁷⁰ In section V.2, Dr. Claire Otteson performed all the synthesis, gathered all the experimental data, and drafted the majority of the manuscript. The figures were drafted with most work done by Dr. Otteson. I performed all the computational experiments, assisted with the computationally relevant figures, wrote the computational sections, and helped with editing. Prof. Ramesh Jasti edited the manuscript in preparation. In section V.3, Viktor Pedersen performed the all the synthesis, drafted most of the figures, and drafted most of the manuscript. Dr. Nicolaj Kofod collected all the optical data. I performed all the computational experiments, drafted computationally relevant figures, and helped with editing. Dr. Bo Laursen, Prof. Ramesh Jasti, and Prof. Dr. Mogens Nielsen edited the manuscript.

VI.5. Bridge to Conclusion

This exhaustive demonstration of the utility of computational chemistry to describe a variety of optoelectronic, reactive, and strain-related properties illustrates the need to continue modeling nanohoop structures to predict these properties and motivate the development of functionalized nanohoops. Continued development of nanohoop syntheses will present an opportunity for their applications in future devices, but computational investigation can help narrow the range of target molecules to study first.

CONCLUDING REMARKS

Overall, development of future materials will rely on the continued development of novel organic materials. As the number of carbon structures are catalogued, introduction of nitrogen atoms diversifies the type of structures and electron accepting character by quaternization of the nitrogen center. Computational chemistry is a powerful tool to explore possible structures within the realm of synthetic reason to target structures with intrinsically interesting electronic properties that differ from their all-carbon counterparts. This will remain a necessary step in future research as a way to narrow down the ever-expanding library of possible electronically active organic molecules. Computational methods have continued to serve experimentalists in order to explain differences in electronic properties and chemical reactivities.

REFERENCES CITED

- (1) Köhler, A.; Bäessler, H. *Electronic Processes in Organic Semiconductors: An Introduction*, 1st ed.; Wiley, 2015. <https://doi.org/10.1002/9783527685172>
- (2) Swager, T. M. *50th Anniversary Perspective : Conducting/Semiconducting Conjugated Polymers. A Personal Perspective on the Past and the Future*. *Macromolecules* **2017**, *50* (13), 4867–4886. <https://doi.org/10.1021/acs.macromol.7b00582>
- (3) Mazzio, K. A.; Luscombe, C. K. The Future of Organic Photovoltaics. *Chem. Soc. Rev.* **2015**, *44* (1), 78–90. <https://doi.org/10.1039/C4CS00227J>
- (4) Herges, R. Magnetic Properties of Aromatic Compounds and Aromatic Transition States. In *The Chemical Bond*; Frenking, G., Shaik, S., Eds.; Wiley, 2014; pp 383–420. <https://doi.org/10.1002/9783527664658.ch13>
- (5) Muñoz-García, A. B.; Benesperi, I.; Boschloo, G.; Concepcion, J. J.; Delcamp, J. H.; Gibson, E. A.; Meyer, G. J.; Pavone, M.; Pettersson, H.; Hagfeldt, A.; Freitag, M. Dye-Sensitized Solar Cells Strike Back. *Chem. Soc. Rev.* **2021**, *50* (22), 12450–12550. <https://doi.org/10.1039/D0CS01336F>
- (6) Hiramoto, M.; Kubo, M.; Shinmura, Y.; Ishiyama, N.; Kaji, T.; Sakai, K.; Ohno, T.; Izaki, M. Bandgap Science for Organic Solar Cells. *Electronics* **2014**, *3* (2), 351–380. <https://doi.org/10.3390/electronics3020351>
- (7) Imran, M.; Wehrmann, C. M.; Chen, M. S. Open-Shell Effects on Optoelectronic Properties: Antiambipolar Charge Transport and Anti-Kasha Doublet Emission from a *N*-Substituted Bisphenalenyl. *J. Am. Chem. Soc.* **2020**, *142* (1), 38–43. <https://doi.org/10.1021/jacs.9b10677>
- (8) Wehrmann, C. M.; Imran, M.; Pointer, C.; Fredin, L. A.; Young, E. R.; Chen, M. S. Spin Multiplicity Effects in Doublet *versus* Singlet Emission: The Photophysical Consequences of a Single Electron. *Chem. Sci.* **2020**, *11* (37), 10212–10219. <https://doi.org/10.1039/D0SC04211K>
- (9) Ball, M.; Zhong, Y.; Fowler, B.; Zhang, B.; Li, P.; Etkin, G.; Paley, D. W.; Decatur, J.; Dalsania, A. K.; Li, H.; Xiao, S.; Ng, F.; Steigerwald, M. L.; Nuckolls, C. Macrocyclization in the Design of Organic N-Type Electronic Materials. *J. Am. Chem. Soc.* **2016**, *138* (39), 12861–12867. <https://doi.org/10.1021/jacs.6b05474>
- (10) Housecroft, C. E.; Constable, E. C. Solar Energy Conversion Using First Row D-Block Metal Coordination Compound Sensitizers and Redox Mediators. *Chem. Sci.* **2022**, *13* (5), 1225–1262. <https://doi.org/10.1039/D1SC06828H>
- (11) Schröder, A.; Mekelburger, H.-B.; Vögtle, F. Belt-, Ball-, and Tube-Shaped Molecules. In *Cyclophanes*; Weber, E., Ed.; Topics in Current Chemistry; Springer-Verlag: Berlin/Heidelberg, 1994; Vol. 172, pp 179–201. <https://doi.org/10.1007/BFb0025270>
- (12) Vögtle, F.; Schröder, A.; Karbach, D. Strategy for the Synthesis of Tube-Shaped Molecules. *Angew. Chem. Int. Ed. Engl.* **1991**, *30* (5), 575–577. <https://doi.org/10.1002/anie.199105751>
- (13) Weber, E. *Cyclophanes*; Topics in Current Chemistry; Springer-Verlag Springer e-books: Berlin, Heidelberg, 1994.

- (14) Herges, R. Fully Conjugated Beltenes (Belt-Like and Tubular Aromatics). In *Modern Cyclophane Chemistry*; Gleiter, R., Hopf, H., Eds.; Wiley, 2004; pp 337–358.
<https://doi.org/10.1002/3527603964.ch13>
- (15) Diederich, F.; Rubin, Y.; Knobler, C. B.; Whetten, R. L.; Schriver, K. E.; Houk, K. N.; Li, Y. All-Carbon Molecules: Evidence for the Generation of Cyclo[18]Carbon from a Stable Organic Precursor. *Science* **1989**, *245* (4922), 1088–1090. <https://doi.org/10.1126/science.245.4922.1088>
- (16) Kroto, H. W.; Heath, J. R.; O'Brien, S. C.; Curl, R. F.; Smalley, R. E. C₆₀: Buckminsterfullerene. *Nature* **1985**, *318* (6042), 162–163. <https://doi.org/10.1038/318162a0>
- (17) Iijima, S. Helical Microtubules of Graphitic Carbon. *Nature* **1991**, *354* (6348), 56–58.
<https://doi.org/10.1038/354056a0>
- (18) Rao, C. N. R.; Govindaraj, A. Carbon Nanotubes. In *Nanotubes and Nanowires*; The Royal Society of Chemistry, 2011; pp 1–242. <https://doi.org/10.1039/9781849732840-00001>
- (19) Sgobba, V.; Guldi, D. M. Carbon Nanotubes—Electronic/Electrochemical Properties and Application for Nanoelectronics and Photonics. *Chem. Soc. Rev.* **2009**, *38* (1), 165–184.
<https://doi.org/10.1039/B802652C>
- (20) Heilbronner, E. Molecular Orbitals in homologen Reihen mehrkerniger aromatischer Kohlenwasserstoffe: I. Die Eigenwerte von LCAO-MO's in homologen Reihen. *Helv. Chim. Acta* **1954**, *37* (3), 921–935. <https://doi.org/10.1002/hlca.19540370336>
- (21) Jasti, R.; Bhattacharjee, J.; Neaton, J. B.; Bertozzi, C. R. Synthesis, Characterization, and Theory of [9]-, [12]-, and [18]Cycloparaphenylene: Carbon Nanohoop Structures. *J. Am. Chem. Soc.* **2008**, *130* (52), 17646–17647. <https://doi.org/10.1021/ja807126u>
- (22) Takaba, H.; Omachi, H.; Yamamoto, Y.; Bouffard, J.; Itami, K. Selective Synthesis of [12]Cycloparaphenylene. *Angew. Chem. Int. Ed.* **2009**, *48* (33), 6112–6116.
<https://doi.org/10.1002/anie.200902617>
- (23) Yamago, S.; Watanabe, Y.; Iwamoto, T. Synthesis of [8]Cycloparaphenylene from a Square-Shaped Tetranuclear Platinum Complex. *Angew. Chem. Int. Ed.* **2010**, *49* (4), 757–759.
<https://doi.org/10.1002/anie.200905659>
- (24) Darzi, E. R.; Jasti, R. The Dynamic, Size-Dependent Properties of [5]–[12]Cycloparaphenylenes. *Chem. Soc. Rev.* **2015**, *44* (18), 6401–6410. <https://doi.org/10.1039/C5CS00143A>
- (25) Hermann, M.; Wassy, D.; Esser, B. Conjugated Nanohoops Incorporating Donor, Acceptor, Hetero- or Polycyclic Aromatics. *Angew. Chem. Int. Ed.* **2021**, *60* (29), 15743–15766.
<https://doi.org/10.1002/anie.202007024>
- (26) Guo, Q.-H.; Qiu, Y.; Wang, M.-X.; Fraser Stoddart, J. Aromatic Hydrocarbon Belts. *Nat. Chem.* **2021**, *13* (5), 402–419. <https://doi.org/10.1038/s41557-021-00671-9>
- (27) Chen, Z.; Jiang, D.; Lu, X.; Bettinger, H. F.; Dai, S.; Schleyer, P. V. R.; Houk, K. N. Open-Shell Singlet Character of Cyclacenes and Short Zigzag Nanotubes. *Org. Lett.* **2007**, *9* (26), 5449–5452.
<https://doi.org/10.1021/ol7023339>

- (28) Houk, K. N.; Lee, P. S.; Nendel, M. Polyacene and Cyclacene Geometries and Electronic Structures: Bond Equalization, Vanishing Band Gaps, and Triplet Ground States Contrast with Polyacetylene. *J. Org. Chem.* **2001**, *66* (16), 5517–5521. <https://doi.org/10.1021/jo010391f>
- (29) Choi, H. S.; Kim, K. S. Structures, Magnetic Properties, and Aromaticity of Cyclacenes. *Angew. Chem. Int. Ed.* **1999**, *38* (15), 2256–2258. [https://doi.org/10.1002/\(SICI\)1521-3773\(19990802\)38:15<2256::AID-ANIE2256>3.0.CO;2-B](https://doi.org/10.1002/(SICI)1521-3773(19990802)38:15<2256::AID-ANIE2256>3.0.CO;2-B)
- (30) Florey, A.; Vogel, P. 2,3,5,6-Tetramethylidene-Bicyclo[2.2.1]Heptane (Preliminary Communication). *Helv. Chim. Acta* **1975**, *58* (5), 1488–1492. <https://doi.org/10.1002/hlca.19750580528>
- (31) Kohnke, F. H.; Slawin, A. M. Z.; Stoddart, J. F.; Williams, D. J. Molecular Belts and Collars in the Making: A Hexaepoxyoctacosahydro[12]Cyclacene Derivative. *Angew. Chem. Int. Ed. Engl.* **1987**, *26* (9), 892–894. <https://doi.org/10.1002/anie.198708921>
- (32) Ashton, P. R.; Isaacs, N. S.; Kohnke, F. H.; Mathias, J. P.; Stoddart, J. F. Stereoregular Oligomerization by Repetitive Diels–Alder Reactions. *Angew. Chem. Int. Ed. Engl.* **1989**, *28* (9), 1258–1261. <https://doi.org/10.1002/anie.198912581>
- (33) Ashton, P. R.; Isaacs, N. S.; Kohnke, F. H.; Slawin, A. M. Z.; Spencer, C. M.; Stoddart, J. F.; Williams, D. J. Towards the Making of [12]Collarene. *Angew. Chem. Int. Ed. Engl.* **1988**, *27* (7), 966–969. <https://doi.org/10.1002/anie.198809661>
- (34) Ashton, P. R.; Brown, G. R.; Isaacs, N. S.; Giuffrida, D.; Kohnke, F. H.; Mathias, J. P.; Slawin, A. M. Z.; Smith, D. R.; Stoddart, J. F.; Williams, D. J. Molecular LEGO. 1. Substrate-Directed Synthesis via Stereoregular Diels–Alder Oligomerizations. *J. Am. Chem. Soc.* **1992**, *114* (16), 6330–6353. <https://doi.org/10.1021/ja00042a009>
- (35) Girreser, U.; Giuffrida, D.; Kohnke, F. H.; Mathias, J. P.; Philp, D.; Stoddart, J. F. The Structure-Directed Synthesis of Cyclacene and Polyacene Derivatives. *Pure Appl. Chem.* **1993**, *65* (1), 119–125. <https://doi.org/10.1351/pac199365010119>
- (36) Segawa, Y.; Yagi, A.; Ito, H.; Itami, K. A Theoretical Study on the Strain Energy of Carbon Nanobelts. *Org. Lett.* **2016**, *18* (6), 1430–1433. <https://doi.org/10.1021/acs.orglett.6b00365>
- (37) Kayahara, E.; Patel, V. K.; Yamago, S. Synthesis and Characterization of [5]Cycloparaphenylene. *J. Am. Chem. Soc.* **2014**, *136* (6), 2284–2287. <https://doi.org/10.1021/ja413214q>
- (38) Evans, P. J.; Darzi, E. R.; Jasti, R. Efficient Room-Temperature Synthesis of a Highly Strained Carbon Nano-hoop Fragment of Buckminsterfullerene. *Nat. Chem.* **2014**, *6* (5), 404–408. <https://doi.org/10.1038/nchem.1888>
- (39) Matsui, K.; Fushimi, M.; Segawa, Y.; Itami, K. Synthesis, Structure, and Reactivity of a Cylinder-Shaped Cyclo[12]Orthophenylene[6]Ethyne: Toward the Synthesis of Zigzag Carbon Nanobelts. *Org. Lett.* **2016**, *18* (20), 5352–5355. <https://doi.org/10.1021/acs.orglett.6b02702>
- (40) Schulz, F.; García, F.; Kaiser, K.; Pérez, D.; Guitián, E.; Gross, L.; Peña, D. Exploring a Route to Cyclic Acenes by On-Surface Synthesis. *Angew. Chem. Int. Ed.* **2019**, *58* (27), 9038–9042. <https://doi.org/10.1002/anie.201902784>

- (41) Shi, T.-H.; Guo, Q.-H.; Tong, S.; Wang, M.-X. Toward the Synthesis of a Highly Strained Hydrocarbon Belt. *J. Am. Chem. Soc.* **2020**, *142* (10), 4576–4580. <https://doi.org/10.1021/jacs.0c00112>
- (42) Han, Y.; Dong, S.; Shao, J.; Fan, W.; Chi, C. Synthesis of a Sidewall Fragment of a (12,0) Carbon Nanotube. *Angew. Chem. Int. Ed.* **2021**, *60* (5), 2658–2662. <https://doi.org/10.1002/anie.202012651>
- (43) Cheung, K. Y.; Watanabe, K.; Segawa, Y.; Itami, K. Synthesis of a Zigzag Carbon Nanobelt. *Nat. Chem.* **2021**, *13* (3), 255–259. <https://doi.org/10.1038/s41557-020-00627-5>
- (44) Chen, H.; Xia, Z.; Miao, Q. Synthesis, Aromatization and Cavitates of an Oxanorbornene-Fused Dibenzo[de,qr]Tetracene Nanobox. *Chem. Sci.* **2022**, *13* (8), 2280–2285 <https://doi.org/10.1039/D1SC06553J>.
- (45) Nakamura, E.; Tahara, K.; Matsuo, Y.; Sawamura, M. Synthesis, Structure, and Aromaticity of a Hoop-Shaped Cyclic Benzenoid [10]Cyclophenacene. *J. Am. Chem. Soc.* **2003**, *125* (10), 2834–2835. <https://doi.org/10.1021/ja029915z>
- (46) Li, Y.; Xu, D.; Gan, L. Selective Multiamination of C₇₀ Leading to Curved π Systems with 60, 58, 56, and 50 π Electrons. *Angew. Chem. Int. Ed.* **2016**, *55* (7), 2483–2487. <https://doi.org/10.1002/anie.201510872>
- (47) Povie, G.; Segawa, Y.; Nishihara, T.; Miyauchi, Y.; Itami, K. Synthesis of a Carbon Nanobelt. *Science* **2017**, *356* (6334), 172–175. <https://doi.org/10.1126/science.aam8158>
- (48) Povie, G.; Segawa, Y.; Nishihara, T.; Miyauchi, Y.; Itami, K. Synthesis and Size-Dependent Properties of [12], [16], and [24]Carbon Nanobelts. *J. Am. Chem. Soc.* **2018**, *140* (31), 10054–10059. <https://doi.org/10.1021/jacs.8b06842>
- (49) Golder, M. R.; Colwell, C. E.; Wong, B. M.; Zakharov, L. N.; Zhen, J.; Jasti, R. Iterative Reductive Aromatization/Ring-Closing Metathesis Strategy toward the Synthesis of Strained Aromatic Belts. *J. Am. Chem. Soc.* **2016**, *138* (20), 6577–6582. <https://doi.org/10.1021/jacs.6b02240>
- (50) Cheung, K. Y.; Gui, S.; Deng, C.; Liang, H.; Xia, Z.; Liu, Z.; Chi, L.; Miao, Q. Synthesis of Armchair and Chiral Carbon Nanobelts. *Chem* **2019**, *5* (4), 838–847. <https://doi.org/10.1016/j.chempr.2019.01.004>
- (51) Segawa, Y.; Watanabe, T.; Yamanoue, K.; Kuwayama, M.; Watanabe, K.; Pirillo, J.; Hijikata, Y.; Itami, K. Synthesis of a Möbius Carbon Nanobelt. *Nat. Synth.* **2022**, *1* (7), 535–541. <https://doi.org/10.1038/s44160-022-00075-8>
- (52) Herges, R. Topology in Chemistry: Designing Möbius Molecules. *Chem. Rev.* **2006**, *106* (12), 4820–4842. <https://doi.org/10.1021/cr0505425>
- (53) Ajami, D.; Oeckler, O.; Simon, A.; Herges, R. Synthesis of a Möbius Aromatic Hydrocarbon. *Nature* **2003**, *426* (6968), 819–821. <https://doi.org/10.1038/nature02224>

- (54) Stępień, M.; Latos-Grażyński, L.; Sprutta, N.; Chwalisz, P.; Szterenber, L. Expanded Porphyrin with a Split Personality: A Hückel–Möbius Aromaticity Switch. *Angew. Chem. Int. Ed.* **2007**, *46* (41), 7869–7873. <https://doi.org/10.1002/anie.200700555>
- (55) Nishigaki, S.; Shibata, Y.; Nakajima, A.; Okajima, H.; Masumoto, Y.; Osawa, T.; Muranaka, A.; Sugiyama, H.; Horikawa, A.; Uekusa, H.; Koshino, H.; Uchiyama, M.; Sakamoto, A.; Tanaka, K. Synthesis of Belt- and Möbius-Shaped Cycloparaphenylenes by Rhodium-Catalyzed Alkyne Cyclotrimerization. *J. Am. Chem. Soc.* **2019**, *141* (38), 14955–14960. <https://doi.org/10.1021/jacs.9b06197>
- (56) Hummelen, J. C.; Knight, B.; Pavlovich, J.; González, R.; Wudl, F. Isolation of the Heterofullerene C₅₉N as Its Dimer (C₅₉N)₂. *Science* **1995**, *269* (5230), 1554–1556. <https://doi.org/10.1126/science.269.5230.1554>
- (57) Anthony, J. E. Functionalized Acenes and Heteroacenes for Organic Electronics. *Chem. Rev.* **2006**, *106* (12), 5028–5048. <https://doi.org/10.1021/cr050966z>
- (58) Takase, M.; Enkelmann, V.; Sebastiani, D.; Baumgarten, M.; Müllen, K. Annularly Fused Hexapyrrolohexaazacoronenes: An Extended π System with Multiple Interior Nitrogen Atoms Displays Stable Oxidation States. *Angew. Chem. Int. Ed.* **2007**, *46* (29), 5524–5527. <https://doi.org/10.1002/anie.200701452>
- (59) Kawahara, K. P.; Matsuoka, W.; Ito, H.; Itami, K. Synthesis of Nitrogen-Containing Polyaromatics by Aza-Annulative π -Extension of Unfunctionalized Aromatics. *Angew. Chem. Int. Ed.* **2020**, *59* (16), 6383–6388. <https://doi.org/10.1002/anie.201913394>
- (60) Jeon, I.; Noh, H.; Baek, J. Nitrogen-Doped Carbon Nanomaterials: Synthesis, Characteristics and Applications. *Chem. Asian J.* **2020**, *15* (15), 2282–2293. <https://doi.org/10.1002/asia.201901318>
- (61) Stępień, M.; Gońka, E.; Żyła, M.; Sprutta, N. Heterocyclic Nanographenes and Other Polycyclic Heteroaromatic Compounds: Synthetic Routes, Properties, and Applications. *Chem. Rev.* **2017**, *117* (4), 3479–3716. <https://doi.org/10.1021/acs.chemrev.6b00076>
- (62) Borissov, A.; Maurya, Y. K.; Moshniaha, L.; Wong, W.-S.; Żyła-Karwowska, M.; Stępień, M. Recent Advances in Heterocyclic Nanographenes and Other Polycyclic Heteroaromatic Compounds. *Chem. Rev.* **2022**, *122* (1), 565–788. <https://doi.org/10.1021/acs.chemrev.1c00449>
- (63) Sondheimer, A. Zur Kenntniss Eines Körpers Mit Achtgliedrigem Ringe. *Ber. Dtsch. Chem. Ges.* **1896**, *29* (2), 1272–1275. <https://doi.org/10.1002/cber.18960290220>
- (64) Zhu, J.; Han, Y.; Ni, Y.; Li, G.; Wu, J. Facile Synthesis of Nitrogen-Doped [(6.)_m8]_n Cyclacene Carbon Nanobelts by a One-Pot Self-Condensation Reaction. *J. Am. Chem. Soc.* **2021**, *143* (7), 2716–2721. <https://doi.org/10.1021/jacs.1c00409>
- (65) Zhang, F.; Du, X.; Zhang, D.; Wang, Y.; Lu, H.; Chen, C. A Green Fluorescent Nitrogen-Doped Aromatic Belt Containing a [6]Cycloparaphenylene Skeleton. *Angew. Chem. Int. Ed.* **2021**, *60* (28), 15291–15295. <https://doi.org/10.1002/anie.202104259>

- (66) Sato, H.; Suizu, R.; Kato, T.; Yagi, A.; Segawa, Y.; Awaga, K.; Itami, K. N-Doped Nonalternant Aromatic Belt *via* a Six-Fold Annulative Double N-Arylation. *Chem. Sci.* **2022**, *13* (34), 9947–9951. <https://doi.org/10.1039/D2SC02647C>
- (67) Price, T. W.; Jasti, R. Carbon Nanobelts Do the Twist. *Nat. Synth.* **2022**, *1* (7), 502–503. <https://doi.org/10.1038/s44160-022-00083-8>
- (68) Colwell, C. E.; Price, T. W.; Stauch, T.; Jasti, R. Strain Visualization for Strained Macrocycles. *Chem. Sci.* **2020**, *11* (15), 3923–3930. <https://doi.org/10.1039/D0SC00629G>
- (69) Fehr, J. M.; Myrthil, N.; Garrison, A. L.; Price, T. W.; Lopez, S. A.; Jasti, R. Experimental and Theoretical Elucidation of SPAAC Kinetics for Strained Alkyne-Containing Cycloparaphenylenes. *Chem. Sci.* **2023**, *14* (11), 2839–2848. <https://doi.org/10.1039/D2SC06816H>
- (70) Pedersen, V. B. R.; Price, T. W.; Kofod, N.; Zakharov, L. N.; Laursen, B. W.; Jasti, R.; Nielsen, M. B. Synthesis and Properties of Fluorenone-containing Cyclo-paraphenylenes and Their Late-Stage Transformation. *Chem. Eur. J.* **2023**, e202303490. <https://doi.org/10.1002/chem.202303490>
- (71) Griggs, S.; Marks, A.; Bristow, H.; McCulloch, I. N-Type Organic Semiconducting Polymers: Stability Limitations, Design Considerations and Applications. *J. Mater. Chem. C* **2021**, *9* (26), 8099–8128. <https://doi.org/10.1039/D1TC02048J>
- (72) Ostroverkhova, O. Organic Optoelectronic Materials: Mechanisms and Applications. *Chem. Rev.* **2016**, *116* (22), 13279–13412. <https://doi.org/10.1021/acs.chemrev.6b00127>
- (73) Xu, Z.; Zhou, Z.; Li, B.; Wang, G.; Leu, P. W. Identification of Efficient Active Sites in Nitrogen-Doped Carbon Nanotubes for Oxygen Reduction Reaction. *J. Phys. Chem. C* **2020**, *124* (16), 8689–8696. <https://doi.org/10.1021/acs.jpcc.9b11090>
- (74) Liang, Y.; Wang, H.; Diao, P.; Chang, W.; Hong, G.; Li, Y.; Gong, M.; Xie, L.; Zhou, J.; Wang, J.; Regier, T. Z.; Wei, F.; Dai, H. Oxygen Reduction Electrocatalyst Based on Strongly Coupled Cobalt Oxide Nanocrystals and Carbon Nanotubes. *J. Am. Chem. Soc.* **2012**, *134* (38), 15849–15857. <https://doi.org/10.1021/ja305623m>
- (75) Jeong, H. M.; Lee, J. W.; Shin, W. H.; Choi, Y. J.; Shin, H. J.; Kang, J. K.; Choi, J. W. Nitrogen-Doped Graphene for High-Performance Ultracapacitors and the Importance of Nitrogen-Doped Sites at Basal Planes. *Nano Lett.* **2011**, *11* (6), 2472–2477. <https://doi.org/10.1021/nl2009058>
- (76) Gao, Y.; Huang, L.; Cao, Y.; Richter, M.; Qi, J.; Zheng, Q.; Yang, H.; Ma, J.; Chang, X.; Fu, X.; Palma, C.-A.; Lu, H.; Zhang, Y.-Y.; Cheng, Z.; Lin, X.; Ouyang, M.; Feng, X.; Du, S.; Gao, H.-J. Selective Activation of Four Quasi-Equivalent C–H Bonds Yields N-Doped Graphene Nanoribbons with Partial Corannulene Motifs. *Nat. Commun.* **2022**, *13* (1), 6146. <https://doi.org/10.1038/s41467-022-33898-2>
- (77) Ding, Y.; Kopold, P.; Hahn, K.; Van Aken, P. A.; Maier, J.; Yu, Y. Facile Solid-State Growth of 3D Well-Interconnected Nitrogen-Rich Carbon Nanotube–Graphene Hybrid Architectures for Lithium–Sulfur Batteries. *Adv. Funct. Mater.* **2016**, *26* (7), 1112–1119. <https://doi.org/10.1002/adfm.201504294>

- (78) Kuwabara, T.; Orii, J.; Segawa, Y.; Itami, K. Curved Oligophenylenes as Donors in Shape-Persistent Donor–Acceptor Macrocycles with Solvatofluorochromic Properties. *Angew. Chem. Int. Ed.* **2015**, *54* (33), 9646–9649. <https://doi.org/10.1002/anie.201503397>
- (79) Darzi, E. R.; Hirst, E. S.; Weber, C. D.; Zakharov, L. N.; Lonergan, M. C.; Jasti, R. Synthesis, Properties, and Design Principles of Donor–Acceptor Nanohoops. *ACS Cent. Sci.* **2015**, *1* (6), 335–342. <https://doi.org/10.1021/acscentsci.5b00269>
- (80) Nishigaki, S.; Fukui, M.; Sugiyama, H.; Uekusa, H.; Kawauchi, S.; Shibata, Y.; Tanaka, K. Synthesis, Structures, and Photophysical Properties of Alternating Donor–Acceptor Cycloparaphenylenes. *Chem. Eur. J.* **2017**, *23* (30), 7227–7231. <https://doi.org/10.1002/chem.201701547>
- (81) Ball, M.; Fowler, B.; Li, P.; Joyce, L. A.; Li, F.; Liu, T.; Paley, D.; Zhong, Y.; Li, H.; Xiao, S.; Ng, F.; Steigerwald, M. L.; Nuckolls, C. Chiral Conjugated Corrals. *J. Am. Chem. Soc.* **2015**, *137* (31), 9982–9987. <https://doi.org/10.1021/jacs.5b05698>
- (82) Thakellapalli, H.; Farajidizaji, B.; Butcher, T. W.; Akhmedov, N. G.; Popp, B. V.; Petersen, J. L.; Wang, K. K. Syntheses and Structures of Thiophene-Containing Cycloparaphenylenes and Related Carbon Nanohoops. *Org. Lett.* **2015**, *17* (14), 3470–3473. <https://doi.org/10.1021/acs.orglett.5b01514>
- (83) Thakellapalli, H.; Li, S.; Farajidizaji, B.; Baughman, N. N.; Akhmedov, N. G.; Popp, B. V.; Wang, K. K. Synthesis and Properties of Conjugated Macrocycles Containing 2,7-Bis(2-thienyl)-9H-fluoren-9-one Units. *Org. Lett.* **2017**, *19* (10), 2674–2677. <https://doi.org/10.1021/acs.orglett.7b01019>
- (84) Li, C.; Wang, C.; Guo, Y.; Jin, Y.; Yao, N.; Wu, Y.; Zhang, F.; Li, W. A Diketopyrrolopyrrole-Based Macrocyclic Conjugated Molecule for Organic Electronics. *J. Mater. Chem. C* **2019**, *7* (13), 3802–3810. <https://doi.org/10.1039/C9TC00377K>
- (85) Lovell, T. C.; Colwell, C. E.; Zakharov, L. N.; Jasti, R. Symmetry Breaking and the Turn-on Fluorescence of Small, Highly Strained Carbon Nanohoops. *Chem. Sci.* **2019**, *10* (13), 3786–3790. <https://doi.org/10.1039/C9SC00169G>
- (86) Lovell, T. C.; Garrison, Z. R.; Jasti, R. Synthesis, Characterization, and Computational Investigation of Bright Orange-Emitting Benzothiadiazole [10]Cycloparaphenylene. *Angew. Chem. Int. Ed.* **2020**, *59* (34), 14363–14367. <https://doi.org/10.1002/anie.202006350>
- (87) Qiu, Z.; Tang, C.; Wang, X.; Ju, Y.; Chu, K.; Deng, Z.; Hou, H.; Liu, Y.; Tan, Y. Tetra-benzothiadiazole-based [12]Cycloparaphenylene with Bright Emission and Its Supramolecular Assembly. *Angew. Chem. Int. Ed.* **2020**, *59* (47), 20868–20872. <https://doi.org/10.1002/anie.202008505>
- (88) Qiu, Z.; He, M.; Chu, K.; Tang, C.; Chen, X.; Zhu, L.; Zhang, L.; Sun, D.; Qian, J.; Tan, Y. Well-Defined Segment of Carbon Nanotube with Bright Red Emission for Three-Photon Fluorescence Cerebrovascular Imaging. *Adv. Opt. Mater.* **2021**, *9* (19), 2100482. <https://doi.org/10.1002/adom.202100482>

- (89) Li, S.; Aljhdli, M.; Thakellapalli, H.; Farajidizaji, B.; Zhang, Y.; Akhmedov, N. G.; Milsmann, C.; Popp, B. V.; Wang, K. K. Synthesis and Structure of a Functionalized [9]Cycloparaphenylene Bearing Three Indeno[2,1-*a*]fluorene-11,12-dione-2,9-diyl Units. *Org. Lett.* **2017**, *19* (15), 4078–4081. <https://doi.org/10.1021/acs.orglett.7b01866>
- (90) Ito, H.; Mitamura, Y.; Segawa, Y.; Itami, K. Thiophene-Based, Radial π -Conjugation: Synthesis, Structure, and Photophysical Properties of Cyclo-1,4-phenylene-2',5'-thienylenes. *Angew. Chem. Int. Ed.* **2015**, *54* (1), 159–163. <https://doi.org/10.1002/anie.201409389>
- (91) Matsui, K.; Segawa, Y.; Itami, K. Synthesis and Properties of Cycloparaphenylene-2,5-Pyridylidene: A Nitrogen-Containing Carbon Nanoring. *Org. Lett.* **2012**, *14* (7), 1888–1891. <https://doi.org/10.1021/ol3005112>
- (92) Hines, D. A.; Darzi, E. R.; Hirst, E. S.; Jasti, R.; Kamat, P. V. Carbon Nanohoops: Excited Singlet and Triplet Behavior of Aza[8]CPP and 1,15-Diaza[8]CPP. *J. Phys. Chem. A* **2015**, *119* (29), 8083–8089. <https://doi.org/10.1021/acs.jpca.5b04404>
- (93) Van Raden, J. M.; Darzi, E. R.; Zakharov, L. N.; Jasti, R. Synthesis and Characterization of a Highly Strained Donor–Acceptor Nanohoop. *Org. Biomol. Chem.* **2016**, *14* (24), 5721–5727. <https://doi.org/10.1039/C6OB00133E>
- (94) Van Raden, J. M.; Louie, S.; Zakharov, L. N.; Jasti, R. 2,2'-Bipyridyl-Embedded Cycloparaphenylenes as a General Strategy To Investigate Nanohoop-Based Coordination Complexes. *J. Am. Chem. Soc.* **2017**, *139* (8), 2936–2939. <https://doi.org/10.1021/jacs.7b00359>
- (95) Schwer, F.; Zank, S.; Freiburger, M.; Kaur, R.; Frühwald, S.; Robertson, C. C.; Görling, A.; Drewello, T.; Guldi, D. M.; Von Delius, M. Synthesis and C₆₀ Binding of Aza[10]CPP and N-Methylaza[10]CPP. *Org. Mater.* **2022**, *4* (02), 7–17. <https://doi.org/10.1055/a-1814-7686>
- (96) Li, Y.; Segawa, Y.; Yagi, A.; Itami, K. A Nonalternant Aromatic Belt: Methylene-Bridged [6]Cycloparaphenylene Synthesized from Pillar[6]Arene. *J. Am. Chem. Soc.* **2020**, *142* (29), 12850–12856. <https://doi.org/10.1021/jacs.0c06007>
- (97) Kono, H.; Li, Y.; Zanasi, R.; Monaco, G.; Summa, F. F.; Scott, L. T.; Yagi, A.; Itami, K. Methylene-Bridged [6]-, [8]-, and [10]Cycloparaphenylenes: Size-Dependent Properties and Paratropic Belt Currents. *J. Am. Chem. Soc.* **2023**, *145* (16), 8939–8946. <https://doi.org/10.1021/jacs.2c13208>
- (98) Izuhara, D.; Swager, T. M. Poly(Pyridinium Phenylene)s: Water-Soluble N-Type Polymers. *J. Am. Chem. Soc.* **2009**, *131* (49), 17724–17725. <https://doi.org/10.1021/ja906513u>
- (99) Izuhara, D.; Swager, T. M. Poly(3-hexylthiophene)-*block*-poly(pyridinium phenylene)s: Block Polymers of p- and n-Type Semiconductors. *Macromolecules* **2011**, *44* (8), 2678–2684. <https://doi.org/10.1021/ma102566u>
- (100) Luo, C.; Gandeepan, P.; Jayakumar, J.; Parthasarathy, K.; Chang, Y.; Cheng, C. Rh^{III}-Catalyzed C–H Activation: A Versatile Route towards Various Polycyclic Pyridinium Salts. *Chem. Eur. J.* **2013**, *19* (42), 14181–14186. <https://doi.org/10.1002/chem.201302290>

- (101) Zhang, G.; Yang, L.; Wang, Y.; Xie, Y.; Huang, H. An Efficient Rh/O₂ Catalytic System for Oxidative C–H Activation/Annulation: Evidence for Rh(I) to Rh(III) Oxidation by Molecular Oxygen. *J. Am. Chem. Soc.* **2013**, *135* (24), 8850–8853. <https://doi.org/10.1021/ja404414q>
- (102) Xu, K.; Fu, Y.; Zhou, Y.; Hennesdorf, F.; Machata, P.; Vincon, I.; Weigand, J. J.; Popov, A. A.; Berger, R.; Feng, X. Cationic Nitrogen-Doped Helical Nanographenes. *Angew. Chem. Int. Ed.* **2017**, *56* (50), 15876–15881. <https://doi.org/10.1002/anie.201707714>
- (103) Darzi, E. R.; White, B. M.; Loventhal, L. K.; Zakharov, L. N.; Jasti, R. An Operationally Simple and Mild Oxidative Homocoupling of Aryl Boronic Esters To Access Conformationally Constrained Macrocycles. *J. Am. Chem. Soc.* **2017**, *139* (8), 3106–3114. <https://doi.org/10.1021/jacs.6b12658>
- (104) Hashimoto, S.; Kayahara, E.; Mizuhata, Y.; Tokitoh, N.; Takeuchi, K.; Ozawa, F.; Yamago, S. Synthesis and Physical Properties of Polyfluorinated Cycloparaphenylenes. *Org. Lett.* **2018**, *20* (18), 5973–5976. <https://doi.org/10.1021/acs.orglett.8b02715>
- (105) Xia, J.; Jasti, R. Synthesis, Characterization, and Crystal Structure of [6]Cycloparaphenylene. *Angew. Chem. Int. Ed.* **2012**, *51* (10), 2474–2476. <https://doi.org/10.1002/anie.201108167>
- (106) Gaussian 09, Revision A.02, M. J. Frisch, G. W. Trucks, H. B. Schlegel, G. E. Scuseria, M. A. Robb, J. R. Cheeseman, G. Scalmani, V. Barone, G. A. Petersson, H. Nakatsuji, X. Li, M. Caricato, A. Marenich, J. Bloino, B. G. Janesko, R. Gomperts, B. Mennucci, H. P. Hratchian, J. V. Ortiz, A. F. Izmaylov, J. L. Sonnenberg, D. Williams-Young, F. Ding, F. Lipparini, F. Egidi, J. Goings, B. Peng, A. Petrone, T. Henderson, D. Ranasinghe, V. G. Zakrzewski, J. Gao, N. Rega, G. Zheng, W. Liang, M. Hada, M. Ehara, K. Toyota, R. Fukuda, J. Hasegawa, M. Ishida, T. Nakajima, Y. Honda, O. Kitao, H. Nakai, T. Vreven, K. Throssell, J. A. Montgomery, Jr., J. E. Peralta, F. Ogliaro, M. Bearpark, J. J. Heyd, E. Brothers, K. N. Kudin, V. N. Staroverov, T. Keith, R. Kobayashi, J. Normand, K. Raghavachari, A. Rendell, J. C. Burant, S. S. Iyengar, J. Tomasi, M. Cossi, J. M. Millam, M. Klene, C. Adamo, R. Cammi, J. W. Ochterski, R. L. Martin, K. Morokuma, O. Farkas, J. B. Foresman, and D. J. Fox, Gaussian, Inc., Wallingford CT, 2016.
- (107) Pangborn, A. B.; Giardello, M. A.; Grubbs, R. H.; Rosen, R. K.; Timmers, F. J. Safe and Convenient Procedure for Solvent Purification. *Organometallics* **1996**, *15* (5), 1518–1520. <https://doi.org/10.1021/om9503712>
- (108) Pelter, A.; Elgandy, S. Phenolic Oxidation with (Diacetoxyiodo)Benzene. *Tetrahedron Lett.* **1988**, *29* (6), 677–680. [https://doi.org/10.1016/S0040-4039\(00\)80182-3](https://doi.org/10.1016/S0040-4039(00)80182-3)
- (109) White, B. M.; Zhao, Y.; Kawashima, T. E.; Branchaud, B. P.; Pluth, M. D.; Jasti, R. Expanding the Chemical Space of Biocompatible Fluorophores: Nanohoops in Cells. *ACS Cent. Sci.* **2018**, *4* (9), 1173–1178. <https://doi.org/10.1021/acscentsci.8b00346>
- (110) Prasad, A. S. B.; Kanth, J. V. B.; Periasamy, M. Convenient Methods for the Reduction of Amides, Nitriles, Carboxylic Esters, Acids and Hydroboration of Alkenes Using NaBH₄/I₂ system. *Tetrahedron* **1992**, *48* (22), 4623–4628. [https://doi.org/10.1016/S0040-4020\(01\)81236-9](https://doi.org/10.1016/S0040-4020(01)81236-9)

- (111) Bruno, N. C.; Tudge, M. T.; Buchwald, S. L. Design and Preparation of New Palladium Precatalysts for C–C and C–N Cross-Coupling Reactions. *Chem. Sci.* **2013**, *4* (3), 916–920. <https://doi.org/10.1039/C2SC20903A>
- (112) Grätzel, M. Dye-Sensitized Solar Cells. *J. Photochem. Photobiol. C* **2003**, *4* (2), 145–153. [https://doi.org/10.1016/S1389-5567\(03\)00026-1](https://doi.org/10.1016/S1389-5567(03)00026-1)
- (113) Sauvage, J. P.; Collin, J. P.; Chambron, J. C.; Guillerez, S.; Coudret, C.; Balzani, V.; Barigelletti, F.; De Cola, L.; Flamigni, L. Ruthenium(II) and Osmium(II) Bis(Terpyridine) Complexes in Covalently-Linked Multicomponent Systems: Synthesis, Electrochemical Behavior, Absorption Spectra, and Photochemical and Photophysical Properties. *Chem. Rev.* **1994**, *94* (4), 993–1019. <https://doi.org/10.1021/cr00028a006>
- (114) Scarborough, C. C.; Lancaster, K. M.; DeBeer, S.; Weyhermüller, T.; Sproules, S.; Wieghardt, K. Experimental Fingerprints for Redox-Active Terpyridine in $[\text{Cr}(\text{Tpy})_2](\text{PF}_6)_n$ ($n = 3-0$), and the Remarkable Electronic Structure of $[\text{Cr}(\text{Tpy})_2]^{1-}$. *Inorg. Chem.* **2012**, *51* (6), 3718–3732. <https://doi.org/10.1021/ic2027219>
- (115) Luca, O. R.; Crabtree, R. H. Redox-Active Ligands in Catalysis. *Chem. Soc. Rev.* **2013**, *42* (4), 1440–1459. <https://doi.org/10.1039/C2CS35228A>
- (116) Hill, S. P.; Hanson, K. Harnessing Molecular Photon Upconversion in a Solar Cell at Sub-Solar Irradiance: Role of the Redox Mediator. *J. Am. Chem. Soc.* **2017**, *139* (32), 10988–10991. <https://doi.org/10.1021/jacs.7b05462>
- (117) Han, F. S.; Higuchi, M.; Kurth, D. G. Metallosupramolecular Polyelectrolytes Self-Assembled from Various Pyridine Ring-Substituted Bisterpyridines and Metal Ions: Photophysical, Electrochemical, and Electrochromic Properties. *J. Am. Chem. Soc.* **2008**, *130* (6), 2073–2081. <https://doi.org/10.1021/ja710380a>
- (118) Saccone, D.; Magistris, C.; Barbero, N.; Quagliotto, P.; Barolo, C.; Viscardi, G. Terpyridine and Quaterpyridine Complexes as Sensitizers for Photovoltaic Applications. *Materials* **2016**, *9* (3), 137. <https://doi.org/10.3390/ma9030137>
- (119) Kubota, N.; Segawa, Y.; Itami, K. η^6 -Cycloparaphenylene Transition Metal Complexes: Synthesis, Structure, Photophysical Properties, and Application to the Selective Monofunctionalization of Cycloparaphenylenes. *J. Am. Chem. Soc.* **2015**, *137* (3), 1356–1361. <https://doi.org/10.1021/ja512271p>
- (120) Kayahara, E.; Patel, V. K.; Mercier, A.; Kündig, E. P.; Yamago, S. Regioselective Synthesis and Characterization of Multinuclear Convex-Bound Ruthenium- $[\eta]$ Cycloparaphenylene ($n = 5$ and 6) Complexes. *Angew. Chem. Int. Ed.* **2016**, *55* (1), 302–306. <https://doi.org/10.1002/anie.201508003>
- (121) Van Raden, J. M.; White, B. M.; Zakharov, L. N.; Jasti, R. Nanohoop Rotaxanes from Active Metal Template Syntheses and Their Potential in Sensing Applications. *Angew. Chem. Int. Ed.* **2019**, *58* (22), 7341–7345. <https://doi.org/10.1002/anie.201901984>

- (122) Heras Ojea, M. J.; Van Raden, J. M.; Louie, S.; Collins, R.; Pividori, D.; Cirera, J.; Meyer, K.; Jasti, R.; Layfield, R. A. Spin-Crossover Properties of an Iron(II) Coordination Nanohoop. *Angew. Chem. Int. Ed.* **2021**, *60* (7), 3515–3518. <https://doi.org/10.1002/anie.202013374>
- (123) May, J. H.; Van Raden, J. M.; Maust, R. L.; Zakharov, L. N.; Jasti, R. Active Template Strategy for the Preparation of π -Conjugated Interlocked Nanocarbons. *Nat. Chem.* **2023**, *15* (2), 170–176. <https://doi.org/10.1038/s41557-022-01106-9>
- (124) Kamin, A. A.; Clayton, T. D.; Otteson, C. E.; Gannon, P. M.; Krajewski, S.; Kaminsky, W.; Jasti, R.; Xiao, D. J. Synthesis and Metalation of Polycatechol Nanohoos Derived from Fluorocycloparaphenylenes. *Chem. Sci.* **2023**, *14* (36), 9724–9732. <https://doi.org/10.1039/D3SC03561A>
- (125) Klein, Y. M.; Prescimone, A.; Constable, E. C.; Housecroft, C. E. 4,2':6',4"- and 3,2':6',3"-Terpyridines: The Conflict between Well-Defined Vectorial Properties and Serendipity in the Assembly of 1D-, 2D- and 3D-Architectures. *Materials* **2017**, *10* (7), 728. <https://doi.org/10.3390/ma10070728>
- (126) Wei, C.; He, Y.; Shi, X.; Song, Z. Terpyridine-Metal Complexes: Applications in Catalysis and Supramolecular Chemistry. *Coord. Chem. Rev.* **2019**, *385*, 1–19. <https://doi.org/10.1016/j.ccr.2019.01.005>
- (127) Schubert, U. S.; Winter, A.; Newkome, G. R. *Terpyridine-Based Materials: For Catalytic, Optoelectronic and Life Science Applications*, 1st ed.; Wiley, 2011. <https://doi.org/10.1002/9783527639625>
- (128) Shaw, M. H.; Twilton, J.; MacMillan, D. W. C. Photoredox Catalysis in Organic Chemistry. *J. Org. Chem.* **2016**, *81* (16), 6898–6926. <https://doi.org/10.1021/acs.joc.6b01449>
- (129) Zhang, C.; Wang, W.; Zhu, X.; Chen, L.; Luo, H.; Guo, M.; Liu, D.; Liu, F.; Zhang, H.; Li, Q.; Lin, J. Synthesis of Indolizines via Tf₂O-Mediated Cascade Reaction of Pyridyl-enaminones with Thiophenols/Thioalcohols. *Org. Lett.* **2023**, *25* (7), 1192–1197. <https://doi.org/10.1021/acs.orglett.3c00177>
- (130) Jameson, D. L.; Guise, L. E. An Improved, Two-Step Synthesis of 2,2':6',2"-Terpyridine. *Tetrahedron Lett.* **1991**, *32* (18), 1999–2002. [https://doi.org/10.1016/S0040-4039\(00\)78891-5](https://doi.org/10.1016/S0040-4039(00)78891-5)
- (131) Ziessel, R.; Grosshenny, V.; Hissler, M.; Stroh, C. *Cis*-[Ru(2,2':6',2"-Terpyridine)(DMSO)Cl₂]: Useful Precursor for the Synthesis of Heteroleptic Terpyridine Complexes under Mild Conditions. *Inorg. Chem.* **2004**, *43* (14), 4262–4271. <https://doi.org/10.1021/ic049822d>
- (132) Flamigni, L.; Ventura, B.; Barigelletti, F.; Baranoff, E.; Collin, J.; Sauvage, J. Luminescent Iridium(III)-Terpyridine Complexes – Interplay of Ligand Centred and Charge Transfer States. *Eur. J. Inorg. Chem.* **2005**, *2005* (7), 1312–1318. <https://doi.org/10.1002/ejic.200400801>
- (133) Yuan, B.; Liu, J.; Guan, R.; Jin, C.; Ji, L.; Chao, H. Endoplasmic Reticulum Targeted Cyclometalated Iridium(III) Complexes as Efficient Photodynamic Therapy Photosensitizers. *Dalton Trans.* **2019**, *48* (19), 6408–6415. <https://doi.org/10.1039/C9DT01072F>

- (134) Chirdon, D. N.; Transue, W. J.; Kagalwala, H. N.; Kaur, A.; Maurer, A. B.; Pintauer, T.; Bernhard, S. [Ir(N^NN)(C^NN)L]⁺: A New Family of Luminophores Combining Tunability and Enhanced Photostability. *Inorg. Chem.* **2014**, *53* (3), 1487–1499. <https://doi.org/10.1021/ic402411>
- (135) Maust, R. L. Leveraging Macrocyclic Architectures in the Development of Polymeric Carbon Nanomaterials. Dissertation, University of Oregon, Eugene, OR, 2021.
- (136) Agard, N. J.; Prescher, J. A.; Bertozzi, C. R. A Strain-Promoted [3 + 2] Azide–Alkyne Cycloaddition for Covalent Modification of Biomolecules in Living Systems. *J. Am. Chem. Soc.* **2004**, *126* (46), 15046–15047. <https://doi.org/10.1021/ja044996f>
- (137) Baskin, J. M.; Prescher, J. A.; Laughlin, S. T.; Agard, N. J.; Chang, P. V.; Miller, I. A.; Lo, A.; Codelli, J. A.; Bertozzi, C. R. Copper-Free Click Chemistry for Dynamic *in Vivo* Imaging. *Proc. Natl. Acad. Sci. U.S.A.* **2007**, *104* (43), 16793–16797. <https://doi.org/10.1073/pnas.0707090104>
- (138) Bielawski, C. W.; Grubbs, R. H. Living Ring-Opening Metathesis Polymerization. *Prog. Polym. Sci.* **2007**, *32* (1), 1–29. <https://doi.org/10.1016/j.progpolymsci.2006.08.006>
- (139) Walker, R.; Conrad, R. M.; Grubbs, R. H. The Living ROMP of *Trans*-Cyclooctene. *Macromolecules* **2009**, *42* (3), 599–605. <https://doi.org/10.1021/ma801693q>
- (140) Leonhardt, E. J.; Jasti, R. Emerging Applications of Carbon Nanohoops. *Nat. Rev. Chem.* **2019**, *3* (12), 672–686. <https://doi.org/10.1038/s41570-019-0140-0>
- (141) Kayahara, E.; Cheng, Y.; Yamago, S. Short-Step Synthesis of Large Cycloparaphenylenes. *Chem. Lett.* **2018**, *47* (9), 1108–1111. <https://doi.org/10.1246/cl.180486>
- (142) Iwamoto, T.; Watanabe, Y.; Sakamoto, Y.; Suzuki, T.; Yamago, S. Selective and Random Syntheses of [n]Cycloparaphenylenes (n = 8–13) and Size Dependence of Their Electronic Properties. *J. Am. Chem. Soc.* **2011**, *133* (21), 8354–8361. <https://doi.org/10.1021/ja2020668>
- (143) Schaub, T. A.; Margraf, J. T.; Zakharov, L.; Reuter, K.; Jasti, R. Strain-Promoted Reactivity of Alkyne-Containing Cycloparaphenylenes. *Angew. Chem. Int. Ed.* **2018**, *57* (50), 16348–16353. <https://doi.org/10.1002/anie.201808611>
- (144) Kayahara, E.; Qu, R.; Yamago, S. Bromination of Cycloparaphenylenes: Strain-Induced Site-Selective Bis-Addition and Its Application for Late-Stage Functionalization. *Angew. Chem. Int. Ed.* **2017**, *56* (35), 10428–10432. <https://doi.org/10.1002/anie.201704982>
- (145) Kayahara, E.; Hayashi, T.; Takeuchi, K.; Ozawa, F.; Ashida, K.; Ogoshi, S.; Yamago, S. Strain-Induced Double Carbon–Carbon Bond Activations of Cycloparaphenylenes by a Platinum Complex: Application to the Synthesis of Cyclic Diketones. *Angew. Chem. Int. Ed.* **2018**, *57* (35), 11418–11421. <https://doi.org/10.1002/anie.201806591>
- (146) Miki, K.; Ohe, K. π-Conjugated Macrocycles Bearing Angle-Strained Alkynes. *Chem. Eur. J.* **2020**, *26* (12), 2529–2575. <https://doi.org/10.1002/chem.201904114>
- (147) Patel, V. K.; Kayahara, E.; Yamago, S. Practical Synthesis of [n]Cycloparaphenylenes (n = 5, 7–12) by H₂SnCl₄-Mediated Aromatization of 1,4-Dihydroxycyclo-2,5-diene Precursors. *Chem. Eur. J.* **2015**, *21* (15), 5742–5749. <https://doi.org/10.1002/chem.201406650>

- (148) Hayase, N.; Miyauchi, Y.; Aida, Y.; Sugiyama, H.; Uekusa, H.; Shibata, Y.; Tanaka, K. Synthesis of [8]Cycloparaphenylene-octacarboxylates via Rh-Catalyzed Stepwise Cross-Alkyne Cyclotrimerization. *Org. Lett.* **2017**, *19* (11), 2993–2996. <https://doi.org/10.1021/acs.orglett.7b01231>
- (149) Darzi, E. R.; Sisto, T. J.; Jasti, R. Selective Syntheses of [7]–[12]Cycloparaphenylenes Using Orthogonal Suzuki–Miyaura Cross-Coupling Reactions. *J. Org. Chem.* **2012**, *77* (15), 6624–6628. <https://doi.org/10.1021/jo3011667>
- (150) Segawa, Y.; Omachi, H.; Itami, K. Theoretical Studies on the Structures and Strain Energies of Cycloparaphenylenes. *Org. Lett.* **2010**, *12* (10), 2262–2265. <https://doi.org/10.1021/ol1006168>
- (151) Bachrach, S. M. *Computational Organic Chemistry*, Second edition.; Wiley: Hoboken, New Jersey, 2014.
- (152) Daoust, K. J.; Hernandez, S. M.; Konrad, K. M.; Mackie, I. D.; Winstanley, J.; Johnson, R. P. Strain Estimates for Small-Ring Cyclic Allenes and Butatrienes. *J. Org. Chem.* **2006**, *71* (15), 5708–5714. <https://doi.org/10.1021/jo060698k>
- (153) Roux, M. V.; Dávalos, J. Z.; Jiménez, P.; Notario, R.; Castaño, O.; Chickos, J. S.; Hanshaw, W.; Zhao, H.; Rath, N.; Liebman, J. F.; Farivar, B. S.; Bashir-Hashemi, A. Cubane, Cuneane, and Their Carboxylates: A Calorimetric, Crystallographic, Computational, and Conceptual Coinvestigation. *J. Org. Chem.* **2005**, *70* (14), 5461–5470. <https://doi.org/10.1021/jo050471+>
- (154) De Meijere, A.; Kozhushkov, S. I.; Rauch, K.; Schill, H.; Verevkin, S. P.; Kümmerlin, M.; Beckhaus, H.-D.; Rüdhardt, C.; Yufit, D. S. Heats of Formation of [2.2]Paracyclophane-1-Ene and [2.2]Paracyclophane-1,9-Diene – An Experimental Study. *J. Am. Chem. Soc.* **2003**, *125* (49), 15110–15113. <https://doi.org/10.1021/ja0374628>
- (155) Haddon, R. C.; Scott, L. T. π -Orbital Conjugation and Rehybridization in Bridged Annulenes and Deformed Molecules in General: π -Orbital Axis Vector Analysis. *Pure Appl. Chem.* **1986**, *58* (1), 137–142. <https://doi.org/10.1351/pac198658010137>
- (156) Haddon, R. C. Chemistry of the Fullerenes: The Manifestation of Strain in a Class of Continuous Aromatic Molecules. *Science* **1993**, *261* (5128), 1545–1550. <https://doi.org/10.1126/science.261.5128.1545>
- (157) Stauch, T.; Dreuw, A. Quantum Chemical Strain Analysis For Mechanochemical Processes. *Acc. Chem. Res.* **2017**, *50* (4), 1041–1048. <https://doi.org/10.1021/acs.accounts.7b00038>
- (158) Stauch, T.; Günther, B.; Dreuw, A. Can Strained Hydrocarbons Be “Forced” To Be Stable? *J. Phys. Chem. A* **2016**, *120* (36), 7198–7204. <https://doi.org/10.1021/acs.jpca.6b05461>
- (159) Slavov, C.; Yang, C.; Heindl, A. H.; Stauch, T.; Wegner, H. A.; Dreuw, A.; Wachtveitl, J. Twist and Return–Induced Ring Strain Triggers Quick Relaxation of a (Z)-Stabilized Cyclobisazobenzene. *J. Phys. Chem. Lett.* **2018**, *9* (16), 4776–4781. <https://doi.org/10.1021/acs.jpcllett.8b02159>
- (160) Colwell, C. E. *StrainViz*. <https://github.com/CurtisColwell/StrainViz.git>

- (161) Bachrach, S. M. The Group Equivalent Reaction: An Improved Method for Determining Ring Strain Energy. *J. Chem. Educ.* **1990**, *67* (11), 907. <https://doi.org/10.1021/ed067p907>
- (162) Wheeler, S. E.; Houk, K. N.; Schleyer, P. V. R.; Allen, W. D. A Hierarchy of Homodesmotic Reactions for Thermochemistry. *J. Am. Chem. Soc.* **2009**, *131* (7), 2547–2560. <https://doi.org/10.1021/ja805843n>
- (163) Rio, J.; Erbahar, D.; Rayson, M.; Briddon, P.; Ewels, C. P. Cyclotetrahalo-p-Phenylenes: Simulations of Halogen Substituted Cycloparaphenylenes and Their Interaction with C₆₀. *Phys. Chem. Chem. Phys.* **2016**, *18* (33), 23257–23263. <https://doi.org/10.1039/C6CP03376H>
- (164) Li, X.; Frisch, M. J. Energy-Represented Direct Inversion in the Iterative Subspace within a Hybrid Geometry Optimization Method. *J. Chem. Theory Comput.* **2006**, *2* (3), 835–839. <https://doi.org/10.1021/ct050275a>
- (165) Neese, F. The ORCA Program System. *WIREs Comput Mol Sci* **2012**, *2* (1), 73–78. <https://doi.org/10.1002/wcms.81>
- (166) Neese, F. Software Update: The ORCA Program System, Version 4.0. *WIREs Comput Mol Sci* **2018**, *8* (1), e1327. <https://doi.org/10.1002/wcms.1327>
- (167) Avdoshenko, S. M.; Konda, S. S. M.; Makarov, D. E. On the Calculation of Internal Forces in Mechanically Stressed Polyatomic Molecules. *J. Chem. Phys.* **2014**, *141* (13), 134115. <https://doi.org/10.1063/1.4896944>
- (168) Stauch, T.; Dreuw, A. Force-Induced Retro-Click Reaction of Triazoles Competes with Adjacent Single-Bond Rupture. *Chem. Sci.* **2017**, *8* (8), 5567–5575. <https://doi.org/10.1039/C7SC01562C>
- (169) Biswas, S.; Qiu, C. S.; Dawe, L. N.; Zhao, Y.; Bodwell, G. J. Contractive Annulation: A Strategy for the Synthesis of Small, Strained Cyclophanes and Its Application in the Synthesis of [2](6,1)Naphthaleno[1]Paracyclophane. *Angew. Chem. Int. Ed.* **2019**, *58* (27), 9166–9170. <https://doi.org/10.1002/anie.201904673>
- (170) Bachrach, S. M. DFT Study of [2.2]-, [3.3]-, and [4.4]Paracyclophanes: Strain Energy, Conformations, and Rotational Barriers. *J. Phys. Chem. A* **2011**, *115* (11), 2396–2401. <https://doi.org/10.1021/jp111523u>
- (171) Saitta, A. M.; Soper, P. D.; Wasserman, E.; Klein, M. L. Influence of a Knot on the Strength of a Polymer Strand. *Nature* **1999**, *399* (6731), 46–48. <https://doi.org/10.1038/19935>
- (172) Stauch, T.; Dreuw, A. Knots “Choke Off” Polymers upon Stretching. *Angew. Chem. Int. Ed.* **2016**, *55* (2), 811–814. <https://doi.org/10.1002/anie.201508706>
- (173) Kayahara, E.; Iwamoto, T.; Takaya, H.; Suzuki, T.; Fujitsuka, M.; Majima, T.; Yasuda, N.; Matsuyama, N.; Seki, S.; Yamago, S. Synthesis and Physical Properties of a Ball-like Three-Dimensional π -Conjugated Molecule. *Nat. Commun.* **2013**, *4* (1), 2694. <https://doi.org/10.1038/ncomms3694>

- (174) Liu, F.; Liang, Y.; Houk, K. N. Theoretical Elucidation of the Origins of Substituent and Strain Effects on the Rates of Diels–Alder Reactions of 1,2,4,5-Tetrazines. *J. Am. Chem. Soc.* **2014**, *136* (32), 11483–11493. <https://doi.org/10.1021/ja505569a>
- (175) Bach, R. D. Ring Strain Energy in the Cyclooctyl System. The Effect of Strain Energy on [3 + 2] Cycloaddition Reactions with Azides. *J. Am. Chem. Soc.* **2009**, *131* (14), 5233–5243. <https://doi.org/10.1021/ja8094137>
- (176) Bickelhaupt, F. M.; Houk, K. N. Analyzing Reaction Rates with the Distortion/Interaction-Activation Strain Model. *Angew. Chem. Int. Ed.* **2017**, *56* (34), 10070–10086. <https://doi.org/10.1002/anie.201701486>
- (177) Taylor, M. T.; Blackman, M. L.; Dmitrenko, O.; Fox, J. M. Design and Synthesis of Highly Reactive Dienophiles for the Tetrazine–*trans*-Cyclooctene Ligation. *J. Am. Chem. Soc.* **2011**, *133* (25), 9646–9649. <https://doi.org/10.1021/ja201844c>
- (178) Kolb, H. C.; Finn, M. G.; Sharpless, K. B. Click Chemistry: Diverse Chemical Function from a Few Good Reactions. *Angew. Chem. Int. Ed.* **2001**, *40* (11), 2004–2021. [https://doi.org/10.1002/1521-3773\(20010601\)40:11<2004::AID-ANIE2004>3.0.CO;2-5](https://doi.org/10.1002/1521-3773(20010601)40:11<2004::AID-ANIE2004>3.0.CO;2-5)
- (179) Tornøe, C. W.; Christensen, C.; Meldal, M. Peptidotriazoles on Solid Phase: [1,2,3]-Triazoles by Regiospecific Copper(I)-Catalyzed 1,3-Dipolar Cycloadditions of Terminal Alkynes to Azides. *J. Org. Chem.* **2002**, *67* (9), 3057–3064. <https://doi.org/10.1021/jo011148j>
- (180) Kawase, T.; Darabi, H. R.; Oda, M. Cyclic [6]- and [8]Paraphenylacetylenes. *Angew. Chem. Int. Ed. Eng.* **1996**, *35* (22), 2664–2666. <https://doi.org/10.1002/anie.199626641>
- (181) Kaiser, K.; Scriven, L. M.; Schulz, F.; Gawel, P.; Gross, L.; Anderson, H. L. An Sp-Hybridized Molecular Carbon Allotrope, Cyclo[18]Carbon. *Science* **2019**, *365* (6459), 1299–1301. <https://doi.org/10.1126/science.aay1914>
- (182) Yang, H.; Jin, Y.; Du, Y.; Zhang, W. Application of Alkyne Metathesis in Polymer Synthesis. *J. Mater. Chem. A* **2014**, *2* (17), 5986. <https://doi.org/10.1039/c3ta14227b>
- (183) Talele, T. T. Acetylene Group, Friend or Foe in Medicinal Chemistry. *J. Med. Chem.* **2020**, *63* (11), 5625–5663. <https://doi.org/10.1021/acs.jmedchem.9b01617>
- (184) Bettens, T.; Alonso, M.; Geerlings, P.; De Proft, F. The Hunt for Reactive Alkynes in Bio-Orthogonal Click Reactions: Insights from Mechanochemical and Conceptual DFT Calculations. *Chem. Sci.* **2020**, *11* (5), 1431–1439. <https://doi.org/10.1039/C9SC04507D>
- (185) Jewett, J. C.; Sletten, E. M.; Bertozzi, C. R. Rapid Cu-Free Click Chemistry with Readily Synthesized Biarylazacyclooctynones. *J. Am. Chem. Soc.* **2010**, *132* (11), 3688–3690. <https://doi.org/10.1021/ja100014q>
- (186) Lee, S.; Chénard, E.; Gray, D. L.; Moore, J. S. Synthesis of Cycloparaphenyleneacetylene via Alkyne Metathesis: C₇₀ Complexation and Copper-Free Triple Click Reaction. *J. Am. Chem. Soc.* **2016**, *138* (42), 13814–13817. <https://doi.org/10.1021/jacs.6b08752>

- (187) Zhou, X.; Thompson, R. R.; Fronczek, F. R.; Lee, S. Size-Selective Synthesis of Large Cycloparaphenyleneacetylene Carbon Nanohoops Using Alkyne Metathesis. *Org. Lett.* **2019**, *21* (12), 4680–4683. <https://doi.org/10.1021/acs.orglett.9b01563>
- (188) Zhou, X.; Kwon, H.; Thompson, R. R.; Herman, R. J.; Fronczek, F. R.; Bruns, C. J.; Lee, S. Scalable Synthesis of [8]Cycloparaphenyleneacetylene Carbon Nanohoop Using Alkyne Metathesis. *Chem. Commun.* **2021**, *57* (83), 10887–10890. <https://doi.org/10.1039/D1CC04776K>
- (189) Gaussian 16, Revision C.01, Frisch, M. J.; Trucks, G. W.; Schlegel, H. B.; Scuseria, G. E.; Robb, M. A.; Cheeseman, J. R.; Scalmani, G.; Barone, V.; Petersson, G. A.; Nakatsuji, H.; Li, X.; Caricato, M.; Marenich, A. V.; Bloino, J.; Janesko, B. G.; Gomperts, R.; Mennucci, B.; Hratchian, H. P.; Ortiz, J. V.; Izmaylov, A. F.; Sonnenberg, J. L.; Williams-Young, D.; Ding, F.; Lipparini, F.; Egidi, F.; Goings, J.; Peng, B.; Petrone, A.; Henderson, T.; Ranasinghe, D.; Zakrzewski, V. G.; Gao, J.; Rega, N.; Zheng, G.; Liang, W.; Hada, M.; Ehara, M.; Toyota, K.; Fukuda, R.; Hasegawa, J.; Ishida, M.; Nakajima, T.; Honda, Y.; Kitao, O.; Nakai, H.; Vreven, T.; Throssell, K.; Montgomery, J. A., Jr.; Peralta, J. E.; Ogliaro, F.; Bearpark, M. J.; Heyd, J. J.; Brothers, E. N.; Kudin, K. N.; Staroverov, V. N.; Keith, T. A.; Kobayashi, R.; Normand, J.; Raghavachari, K.; Rendell, A. P.; Burant, J. C.; Iyengar, S. S.; Tomasi, J.; Cossi, M.; Millam, J. M.; Klene, M.; Adamo, C.; Cammi, R.; Ochterski, J. W.; Martin, R. L.; Morokuma, K.; Farkas, O.; Foresman, J. B.; Fox, D. J. Gaussian, Inc., Wallingford CT, 2016.
- (190) Zhao, Y.; Truhlar, D. G. The M06 Suite of Density Functionals for Main Group Thermochemistry, Thermochemical Kinetics, Noncovalent Interactions, Excited States, and Transition Elements: Two New Functionals and Systematic Testing of Four M06-Class Functionals and 12 Other Functionals. *Theor. Chem. Acc.* **2008**, *120* (1), 215–241. <https://doi.org/10.1007/s00214-007-0310-x>
- (191) Ditchfield, R.; Hehre, W. J.; Pople, J. A. Self-Consistent Molecular-Orbital Methods. IX. An Extended Gaussian-Type Basis for Molecular-Orbital Studies of Organic Molecules. *J. Chem. Phys.* **1971**, *54* (2), 724–728. <https://doi.org/10.1063/1.1674902>
- (192) Tomasi, J.; Mennucci, B.; Cammi, R. Quantum Mechanical Continuum Solvation Models. *Chem. Rev.* **2005**, *105* (8), 2999–3094. <https://doi.org/10.1021/cr9904009>
- (193) Pracht, P.; Bohle, F.; Grimme, S. Automated Exploration of the Low-Energy Chemical Space with Fast Quantum Chemical Methods. *Phys. Chem. Chem. Phys.* **2020**, *22* (14), 7169–7192. <https://doi.org/10.1039/C9CP06869D>
- (194) Ess, D. H.; Houk, K. N. Distortion/Interaction Energy Control of 1,3-Dipolar Cycloaddition Reactivity. *J. Am. Chem. Soc.* **2007**, *129* (35), 10646–10647. <https://doi.org/10.1021/ja0734086>
- (195) Kochhar, G. S.; Mosey, N. J. Differences in the Abilities to Mechanically Eliminate Activation Energies for Unimolecular and Bimolecular Reactions. *Sci. Rep.* **2016**, *6* (1), 23059. <https://doi.org/10.1038/srep23059>
- (196) de Cózar, A. Diastereoselectivity on Intramolecular Alder-Ene Reaction of 1,6-Dienes. *ChemPhysChem* **23** (23), e202200377. <https://doi.org/10.1002/cphc.202200377>

- (197) Fernández, I.; Bickelhaupt, F. M.; Cossío, F. P. Type-I Dyotropic Reactions: Understanding Trends in Barriers. *Chem. Eur. J.* **2012**, *18* (39), 12395–12403. <https://doi.org/10.1002/chem.201200897>
- (198) Velasco-Juárez, E.; Arpa, E. M. A Novel Partitioning Scheme for the Application of the Distortion/Interaction - Activation Strain Model to Intramolecular Reactions. *Theor. Chem. Acc.* **2021**, *140* (8), 107. <https://doi.org/10.1007/s00214-021-02803-3>
- (199) Lopez, S. A.; Houk, K. N. Alkene Distortion Energies and Torsional Effects Control Reactivities, and Stereoselectivities of Azide Cycloadditions to Norbornene and Substituted Norbornenes. *J. Org. Chem.* **2013**, *78* (5), 1778–1783. <https://doi.org/10.1021/jo301267b>
- (200) Liu, F.; Paton, R. S.; Kim, S.; Liang, Y.; Houk, K. N. Diels–Alder Reactivities of Strained and Unstrained Cycloalkenes with Normal and Inverse-Electron-Demand Dienes: Activation Barriers and Distortion/Interaction Analysis. *J. Am. Chem. Soc.* **2013**, *135* (41), 15642–15649. <https://doi.org/10.1021/ja408437u>
- (201) Paton, R. S.; Kim, S.; Ross, A. G.; Danishefsky, S. J.; Houk, K. N. Experimental Diels–Alder Reactivities of Cycloalkenones and Cyclic Dienes Explained through Transition-State Distortion Energies. *Angew. Chem. Int. Ed.* **2011**, *50* (44), 10366–10368. <https://doi.org/10.1002/anie.201103998>
- (202) Lopez, S. A.; Munk, M. E.; Houk, K. N. Mechanisms and Transition States of 1,3-Dipolar Cycloadditions of Phenyl Azide with Enamines: A Computational Analysis. *J. Org. Chem.* **2013**, *78* (4), 1576–1582. <https://doi.org/10.1021/jo302695n>
- (203) Fell, J. S.; Martin, B. N.; Houk, K. N. Origins of the Unfavorable Activation and Reaction Energies of 1-Azadiene Heterocycles Compared to 2-Azadiene Heterocycles in Diels–Alder Reactions. *J. Org. Chem.* **2017**, *82* (4), 1912–1919. <https://doi.org/10.1021/acs.joc.6b02524>
- (204) Ess, D. H.; Houk, K. N. Distortion/Interaction Energy Control of 1,3-Dipolar Cycloaddition Reactivity. *J. Am. Chem. Soc.* **2007**, *129* (35), 10646–10647. <https://doi.org/10.1021/ja0734086>
- (205) Ess, D. H.; Jones, G. O.; Houk, K. N. Conceptual, Qualitative, and Quantitative Theories of 1,3-Dipolar and Diels–Alder Cycloadditions Used in Synthesis. *Adv. Synth. Catal.* **2006**, *348* (16–17), 2337–2361. <https://doi.org/10.1002/adsc.200600431>
- (206) Houk, K. N. Frontier Molecular Orbital Theory of Cycloaddition Reactions. *Acc. Chem. Res.* **1975**, *8* (11), 361–369. <https://doi.org/10.1021/ar50095a001>
- (207) Houk, K. N.; Sims, Joyner.; Watts, C. R.; Luskus, L. J. Origin of Reactivity, Regioselectivity, and Periselectivity in 1,3-Dipolar Cycloadditions. *J. Am. Chem. Soc.* **1973**, *95* (22), 7301–7315. <https://doi.org/10.1021/ja00803a018>
- (208) Houk, K. N.; Sims, Joyner.; Duke, R. E.; Strozier, R. W.; George, J. K. Frontier Molecular Orbitals of 1,3 Dipoles and Dipolarophiles. *J. Am. Chem. Soc.* **1973**, *95* (22), 7287–7301. <https://doi.org/10.1021/ja00803a017>

- (209) Schoenebeck, F.; Ess, D. H.; Jones, G. O.; Houk, K. N. Reactivity and Regioselectivity in 1,3-Dipolar Cycloadditions of Azides to Strained Alkynes and Alkenes: A Computational Study. *J. Am. Chem. Soc.* **2009**, *131* (23), 8121–8133. <https://doi.org/10.1021/ja9003624>
- (210) Houk, K. N.; Paddon-Row, M. N.; Rondan, N. G.; Wu, Y.-D.; Brown, F. K.; Spellmeyer, D. C.; Metz, J. T.; Li, Y.; Loncharich, R. J. Theory and Modeling of Stereoselective Organic Reactions. *Science* **1986**, *231* (4742), 1108–1117. <https://doi.org/10.1126/science.3945819>
- (211) Ess, D. H.; Houk, K. N. Theory of 1,3-Dipolar Cycloadditions: Distortion/Interaction and Frontier Molecular Orbital Models. *J. Am. Chem. Soc.* **2008**, *130* (31), 10187–10198. <https://doi.org/10.1021/ja800009z>
- (212) Cai, J.; Ruffieux, P.; Jaafar, R.; Bieri, M.; Braun, T.; Blankenburg, S.; Muoth, M.; Seitsonen, A. P.; Saleh, M.; Feng, X.; Müllen, K.; Fasel, R. Atomically Precise Bottom-up Fabrication of Graphene Nanoribbons. *Nature* **2010**, *466* (7305), 470–473. <https://doi.org/10.1038/nature09211>
- (213) Hayase, N.; Nogami, J.; Shibata, Y.; Tanaka, K. Synthesis of a Strained Spherical Carbon Nanocage by Regioselective Alkyne Cyclotrimerization. *Angew. Chem. Int. Ed.* **2019**, *58* (28), 9439–9442. <https://doi.org/10.1002/anie.201903422>
- (214) Li, P.; Zakharov, L. N.; Jasti, R. A Molecular Propeller with Three Nanohoop Blades: Synthesis, Characterization, and Solid-State Packing. *Angew. Chem. Int. Ed.* **2017**, *56* (19), 5237–5241. <https://doi.org/10.1002/anie.201700935>
- (215) Schaub, T. A.; Prantl, E. A.; Kohn, J.; Bursch, M.; Marshall, C. R.; Leonhardt, E. J.; Lovell, T. C.; Zakharov, L. N.; Brozek, C. K.; Waldvogel, S. R.; Grimme, S.; Jasti, R. Exploration of the Solid-State Sorption Properties of Shape-Persistent Macrocyclic Nanocarbons as Bulk Materials and Small Aggregates. *J. Am. Chem. Soc.* **2020**, *142* (19), 8763–8775. <https://doi.org/10.1021/jacs.0c01117>
- (216) Scott, L. T.; Hashemi, M. M.; Meyer, D. T.; Warren, H. B. Corannulene. A Convenient New Synthesis. *J. Am. Chem. Soc.* **1991**, *113* (18), 7082–7084. <https://doi.org/10.1021/ja00018a082>
- (217) Rudebusch, G. E.; Zafra, J. L.; Jorner, K.; Fukuda, K.; Marshall, J. L.; Arrechea-Marcos, I.; Espejo, G. L.; Ponce Ortiz, R.; Gómez-García, C. J.; Zakharov, L. N.; Nakano, M.; Ottosson, H.; Casado, J.; Haley, M. M. Diindeno-Fusion of an Anthracene as a Design Strategy for Stable Organic Biradicals. *Nat. Chem.* **2016**, *8* (8), 753–759. <https://doi.org/10.1038/nchem.2518>
- (218) Wang, J.; Zhang, X.; Jia, H.; Wang, S.; Du, P. Large π -Extended and Curved Carbon Nanorings as Carbon Nanotube Segments. *Acc. Chem. Res.* **2021**, *54* (22), 4178–4190. <https://doi.org/10.1021/acs.accounts.1c00505>
- (219) Xu, Y.; Von Delius, M. The Supramolecular Chemistry of Strained Carbon Nanohoops. *Angew. Chem. Int. Ed.* **2020**, *59* (2), 559–573. <https://doi.org/10.1002/anie.201906069>
- (220) Reppe, W.; Schlichting, O.; Klager, K.; Toepel, T. Cyclisierende Polymerisation von Acetylen I Über Cyclooctatetraen. *Justus Liebigs Ann. Chem.* **1948**, *560* (1), 1–92. <https://doi.org/10.1002/jlac.19485600102>

- (221) Heller, B.; Hapke, M. The Fascinating Construction of Pyridine Ring Systems by Transition Metal-Catalysed [2 + 2 + 2] Cycloaddition Reactions. *Chem. Soc. Rev.* **2007**, *36* (7), 1085. <https://doi.org/10.1039/b607877j>
- (222) Tietze, L. F.; Brasche, G.; Gericke, K. M. *Domino Reactions in Organic Synthesis*; Wiley-VCH: Weinheim, 2006.
- (223) Kotha, S.; Brahmachary, E.; Lahiri, K. Transition Metal Catalyzed [2+2+2] Cycloaddition and Application in Organic Synthesis. *Eur. J. Org. Chem.* **2005**, *2005* (22), 4741–4767. <https://doi.org/10.1002/ejoc.200500411>
- (224) Saito, S.; Yamamoto, Y. Recent Advances in the Transition-Metal-Catalyzed Regioselective Approaches to Polysubstituted Benzene Derivatives. *Chem. Rev.* **2000**, *100* (8), 2901–2916. <https://doi.org/10.1021/cr990281x>
- (225) Xue, F.; Loh, Y. K.; Song, X.; Teo, W. J.; Chua, J. Y. D.; Zhao, J.; Hor, T. S. A. Nickel-Catalyzed Facile [2+2+2] Cyclotrimerization of Unactivated Internal Alkynes to Polysubstituted Benzenes. *Chem. Asian J.* **2017**, *12* (1), 168–173. <https://doi.org/10.1002/asia.201601469>
- (226) Lovell, T. C.; Fosnacht, K. G.; Colwell, C. E.; Jasti, R. Effect of Curvature and Placement of Donor and Acceptor Units in Cycloparaphenylenes: A Computational Study. *Chem. Sci.* **2020**, *11* (44), 12029–12035. <https://doi.org/10.1039/D0SC03923C>
- (227) Iwamoto, T.; Watanabe, Y.; Sadahiro, T.; Haino, T.; Yamago, S. Size-Selective Encapsulation of C₆₀ by [10]Cycloparaphenylene: Formation of the Shortest Fullerene-Peapod. *Angew. Chem. Int. Ed.* **2011**, *50* (36), 8342–8344. <https://doi.org/10.1002/anie.201102302>
- (228) Iwamoto, T.; Watanabe, Y.; Takaya, H.; Haino, T.; Yasuda, N.; Yamago, S. Size- and Orientation-Selective Encapsulation of C₇₀ by Cycloparaphenylenes. *Chem. Eur. J.* **2013**, *19* (42), 14061–14068. <https://doi.org/10.1002/chem.201302694>
- (229) Iwamoto, T.; Slanina, Z.; Mizorogi, N.; Guo, J.; Akasaka, T.; Nagase, S.; Takaya, H.; Yasuda, N.; Kato, T.; Yamago, S. Partial Charge Transfer in the Shortest Possible Metallofullerene Peapod, La@C₈₂@[11]Cycloparaphenylene. *Chem. Eur. J.* **2014**, *20* (44), 14403–14409. <https://doi.org/10.1002/chem.201403879>
- (230) Xu, Y.; Wang, B.; Kaur, R.; Minameyer, M. B.; Bothe, M.; Drewello, T.; Guldi, D. M.; von Delius, M. A Supramolecular [10]CPP Junction Enables Efficient Electron Transfer in Modular Porphyrin–[10]CPP⊃Fullerene Complexes. *Angew. Chem. Int. Ed.* **2018**, *57* (36), 11549–11553. <https://doi.org/10.1002/anie.201802443>
- (231) Xu, Y.; Kaur, R.; Wang, B.; Minameyer, M. B.; Gsänger, S.; Meyer, B.; Drewello, T.; Guldi, D. M.; Von Delius, M. Concave–Convex π–π Template Approach Enables the Synthesis of [10]Cycloparaphenylene–Fullerene [2]Rotaxanes. *J. Am. Chem. Soc.* **2018**, *140* (41), 13413–13420. <https://doi.org/10.1021/jacs.8b08244>
- (232) Steudel, F. M.; Ubasart, E.; Leanza, L.; Pujals, M.; Parella, T.; Pavan, G. M.; Ribas, X.; Von Delius, M. Synthesis of C₆₀/[10]CPP-Catenanes by Regioselective, Nanocapsule-Templated Bingel Bis-

- Addition. *Angew. Chem. Int. Ed.* **2023**, *62* (42), e202309393.
<https://doi.org/10.1002/anie.202309393>
- (233) Pedersen, C. J. Cyclic Polyethers and Their Complexes with Metal Salts. *J. Am. Chem. Soc.* **1967**, *89* (26), 7017–7036. <https://doi.org/10.1021/ja01002a035>
- (234) Cram, D. J.; Cram, J. M. Host-Guest Chemistry: Complexes between Organic Compounds Simulate the Substrate Selectivity of Enzymes. *Science* **1974**, *183* (4127), 803–809.
<https://doi.org/10.1126/science.183.4127.803>
- (235) Lehn, J.-M. Supramolecular Chemistry: Receptors, Catalysts, and Carriers. *Science* **1985**, *227* (4689), 849–856. <https://doi.org/10.1126/science.227.4689.849>
- (236) Liu, Z.; Nalluri, S. K. M.; Stoddart, J. F. Surveying Macrocyclic Chemistry: From Flexible Crown Ethers to Rigid Cyclophanes. *Chem. Soc. Rev.* **2017**, *46* (9), 2459–2478.
<https://doi.org/10.1039/C7CS00185A>
- (237) Li, J.; Loh, X. J. Cyclodextrin-Based Supramolecular Architectures: Syntheses, Structures, and Applications for Drug and Gene Delivery. *Advanced Drug Delivery Reviews* **2008**, *60* (9), 1000–1017. <https://doi.org/10.1016/j.addr.2008.02.011>
- (238) Helttunen, K.; Shahgaldian, P. Self-Assembly of Amphiphilic Calixarenes and Resorcinarenes in Water. *New J. Chem.* **2010**, *34* (12), 2704. <https://doi.org/10.1039/c0nj00123f>
- (239) Bhasikuttan, A. C.; Pal, H.; Mohanty, J. Cucurbit[n]uril Based Supramolecular Assemblies: Tunable Physico-Chemical Properties and Their Prospects. *Chem. Commun.* **2011**, *47* (36), 9959.
<https://doi.org/10.1039/c1cc12091c>
- (240) Ogoshi, T.; Yamagishi, T. Pillararenes: Versatile Synthetic Receptors for Supramolecular Chemistry. *Eur. J. Org. Chem.* **2013**, *2013* (15), 2961–2975.
<https://doi.org/10.1002/ejoc.201300079>
- (241) Rebilly, J.-N.; Reinaud, O. Calixarenes and Resorcinarenes as Scaffolds for Supramolecular Metallo-Enzyme Mimicry. *Supramol. Chem.* **2014**, *26* (7–8), 454–479.
<https://doi.org/10.1080/10610278.2013.877137>
- (242) Barrow, S. J.; Kasera, S.; Rowland, M. J.; Del Barrio, J.; Scherman, O. A. Cucurbituril-Based Molecular Recognition. *Chem. Rev.* **2015**, *115* (22), 12320–12406.
<https://doi.org/10.1021/acs.chemrev.5b00341>
- (243) Healy, B.; Yu, T.; C. Da Silva Alves, D.; Okeke, C.; Breslin, C. B. Cyclodextrins as Supramolecular Recognition Systems: Applications in the Fabrication of Electrochemical Sensors. *Materials* **2021**, *14* (7), 1668. <https://doi.org/10.3390/ma14071668>
- (244) Ogoshi, T.; Yamagishi, T.; Nakamoto, Y. Pillar-Shaped Macrocyclic Hosts Pillar[n]arenes: New Key Players for Supramolecular Chemistry. *Chem. Rev.* **2016**, *116* (14), 7937–8002.
<https://doi.org/10.1021/acs.chemrev.5b00765>

- (245) Wang, M.-X. Coronarenes: Recent Advances and Perspectives on Macrocyclic and Supramolecular Chemistry. *Sci. China Chem.* **2018**, *61* (8), 993–1003. <https://doi.org/10.1007/s11426-018-9328-8>
- (246) Gaeta, C.; Wang, D.-X. Editorial: New Macrocycles and Their Supramolecular Perspectives. *Front. Chem.* **2020**, *8*, 128. <https://doi.org/10.3389/fchem.2020.00128>
- (247) Yu, J.; Qi, D.; Li, J. Design, Synthesis and Applications of Responsive Macrocycles. *Commun. Chem.* **2020**, *3* (1), 189. <https://doi.org/10.1038/s42004-020-00438-2>
- (248) Murray, J.; Kim, K.; Ogoshi, T.; Yao, W.; Gibb, B. C. The Aqueous Supramolecular Chemistry of Cucurbit[n]urils, Pillar[n]arenes and Deep-Cavity Cavitands. *Chem. Soc. Rev.* **2017**, *46* (9), 2479–2496. <https://doi.org/10.1039/C7CS00095B>
- (249) Cremer, P. S.; Flood, A. H.; Gibb, B. C.; Mobley, D. L. Collaborative Routes to Clarifying the Murky Waters of Aqueous Supramolecular Chemistry. *Nat. Chem.* **2018**, *10* (1), 8–16. <https://doi.org/10.1038/nchem.2894>
- (250) Pairault, N.; Barat, R.; Tranoy-Opalinski, I.; Renoux, B.; Thomas, M.; Papot, S. Rotaxane-Based Architectures for Biological Applications. *Comptes Rendus Chimie* **2016**, *19* (1–2), 103–112. <https://doi.org/10.1016/j.crci.2015.05.012>
- (251) Huang, Q.; Zhuang, G.; Jia, H.; Qian, M.; Cui, S.; Yang, S.; Du, P. Photoconductive Curved-Nanographene/Fullerene Supramolecular Heterojunctions. *Angew. Chem. Int. Ed.* **2019**, *58* (19), 6244–6249. <https://doi.org/10.1002/anie.201900084>
- (252) Leonhardt, E. J.; Van Raden, J. M.; Miller, D.; Zakharov, L. N.; Alemán, B.; Jasti, R. A Bottom-Up Approach to Solution-Processed, Atomically Precise Graphitic Cylinders on Graphite. *Nano Lett.* **2018**, *18* (12), 7991–7997. <https://doi.org/10.1021/acs.nanolett.8b03979>
- (253) Della Sala, P.; Talotta, C.; Caruso, T.; De Rosa, M.; Soriente, A.; Neri, P.; Gaeta, C. Tuning Cycloparaphenylene Host Properties by Chemical Modification. *J. Org. Chem.* **2017**, *82* (18), 9885–9889. <https://doi.org/10.1021/acs.joc.7b01588>
- (254) Lu, D.; Zhuang, G.; Jia, H.; Wang, J.; Huang, Q.; Cui, S.; Du, P. A Novel Symmetrically Multifunctionalized Dodecamethoxy-Cycloparaphenylene: Synthesis, Photophysical, and Supramolecular Properties. *Org. Chem. Front.* **2018**, *5* (9), 1446–1451. <https://doi.org/10.1039/C8QO00033F>
- (255) Xia, J.; Bacon, J. W.; Jasti, R. Gram-Scale Synthesis and Crystal Structures of [8]- and [10]CPP, and the Solid-State Structure of C₆₀@[10]CPP. *Chem. Sci.* **2012**, *3* (10), 3018. <https://doi.org/10.1039/c2sc20719b>
- (256) Bachrach, S. M.; Zayat, Z.-C. “Planetary Orbit” Systems Composed of Cycloparaphenylenes. *J. Org. Chem.* **2016**, *81* (11), 4559–4565. <https://doi.org/10.1021/acs.joc.6b00339>
- (257) Fomine, S.; Zolotukhin, M. G.; Guadarrama, P. “Russian Doll” Complexes of [n]Cycloparaphenylenes: A Theoretical Study. *J. Mol. Model.* **2012**, *18* (9), 4025–4032. <https://doi.org/10.1007/s00894-012-1402-7>

- (258) Peña-Álvarez, M.; Fanetti, S.; Falsini, N.; Novelli, G.; Casado, J.; G. Baonza, V.; Taravillo, M.; Parsons, S.; Bini, R.; Citroni, M. Linear, Non-Conjugated Cyclic and Conjugated Cyclic Paraphenylene under Pressure. *Molecules* **2019**, *24* (19), 3496. <https://doi.org/10.3390/molecules24193496>
- (259) Minameyer, M. B.; Xu, Y.; Frühwald, S.; Görling, A.; Von Delius, M.; Drewello, T. Investigation of Cycloparaphenylenes (CPPs) and Their Noncovalent Ring-in-Ring and Fullerene-in-Ring Complexes by (Matrix-Assisted) Laser Desorption/Ionization and Density Functional Theory. *Chem. Eur. J.* **2020**, *26* (40), 8729–8741. <https://doi.org/10.1002/chem.202001503>
- (260) Zhao, C.; Liu, F.; Feng, L.; Nie, M.; Lu, Y.; Zhang, J.; Wang, C.; Wang, T. Construction of a Double-Walled Carbon Nanoring. *Nanoscale* **2021**, *13* (9), 4880–4886. <https://doi.org/10.1039/D0NR08931A>
- (261) Hashimoto, S.; Iwamoto, T.; Kurachi, D.; Kayahara, E.; Yamago, S. Shortest Double-Walled Carbon Nanotubes Composed of Cycloparaphenylenes. *ChemPlusChem* **2017**, *82* (7), 1015–1020. <https://doi.org/10.1002/cplu.201700097>
- (262) Kwon, H.; Bruns, Carson. J. All-Hydrocarbon, All-Conjugated Cycloparaphenylene-Polycyclic Aromatic Hydrocarbon Host-Guest Complexes Stabilized by CH- π Interactions. *Nano Res.* **2022**, *15* (6), 5545–5555. <https://doi.org/10.1007/s12274-022-4145-5>
- (263) Chai, J.-D.; Head-Gordon, M. Long-Range Corrected Hybrid Density Functionals with Damped Atom-Atom Dispersion Corrections. *Phys. Chem. Chem. Phys.* **2008**, *10* (44), 6615. <https://doi.org/10.1039/b810189b>
- (264) Ball, M.; Zhang, B.; Zhong, Y.; Fowler, B.; Xiao, S.; Ng, F.; Steigerwald, M.; Nuckolls, C. Conjugated Macrocycles in Organic Electronics. *Acc. Chem. Res.* **2019**, *52* (4), 1068–1078. <https://doi.org/10.1021/acs.accounts.9b00017>
- (265) Ball, M.; Nuckolls, C. Stepping into the Light: Conjugated Macrocycles with Donor-Acceptor Motifs. *ACS Cent. Sci.* **2015**, *1* (8), 416–417. <https://doi.org/10.1021/acscentsci.5b00339>
- (266) Seitz, P.; Bhosale, M.; Rzesny, L.; Uhlmann, A.; Wössner, J. S.; Wessling, R.; Esser, B. Conjugated Nanohoop Polymers Based on Antiaromatic Dibenzopentalenes for Charge Storage in Organic Batteries. *Angew. Chem. Int. Ed.* **2023**, *62* (43), e202306184. <https://doi.org/10.1002/anie.202306184>
- (267) Zhang, B.; Trinh, M. T.; Fowler, B.; Ball, M.; Xu, Q.; Ng, F.; Steigerwald, M. L.; Zhu, X.-Y.; Nuckolls, C.; Zhong, Y. Rigid, Conjugated Macrocycles for High Performance Organic Photodetectors. *J. Am. Chem. Soc.* **2016**, *138* (50), 16426–16431. <https://doi.org/10.1021/jacs.6b10276>
- (268) Zhang, S.-Q.; Liu, Z.-Y.; Fu, W.-F.; Liu, F.; Wang, C.-M.; Sheng, C.-Q.; Wang, Y.-F.; Deng, K.; Zeng, Q.-D.; Shu, L.-J.; Wan, J.-H.; Chen, H.-Z.; Russell, T. P. Donor-Acceptor Conjugated Macrocycles: Synthesis and Host-Guest Coassembly with Fullerene toward Photovoltaic Application. *ACS Nano* **2017**, *11* (11), 11701–11713. <https://doi.org/10.1021/acsnano.7b06961>

- (269) Quernheim, M.; Golling, F. E.; Zhang, W.; Wagner, M.; Räder, H.; Nishiuchi, T.; Müllen, K. The Precise Synthesis of Phenylene-Extended Cyclic Hexa-*peri*-hexabenzocoronenes from Polyarylated [n]Cycloparaphenylenes by the Scholl Reaction. *Angew. Chem. Int. Ed.* **2015**, *54* (35), 10341–10346. <https://doi.org/10.1002/anie.201500392>
- (270) Wassy, D.; Pfeifer, M.; Esser, B. Synthesis and Properties of Conjugated Nanohoops Incorporating Dibenzo[a,e]pentalenes: [2]DBP[12]CPPs. *J. Org. Chem.* **2020**, *85* (1), 34–43. <https://doi.org/10.1021/acs.joc.9b01195>
- (271) Volkmann, J.; Kohrs, D.; Bernt, F.; Wegner, H. A. Synthesis of a Substituted [10]Cycloparaphenylene through [2+2+2] Cycloaddition. *Eur. J. Org. Chem.* **2022**, *2022* (4), e202101357. <https://doi.org/10.1002/ejoc.202101357>
- (272) Shudo, H.; Kuwayama, M.; Shimasaki, M.; Nishihara, T.; Takeda, Y.; Mitoma, N.; Kuwabara, T.; Yagi, A.; Segawa, Y.; Itami, K. Perfluorocycloparaphenylenes. *Nat. Commun.* **2022**, *13* (1), 3713. <https://doi.org/10.1038/s41467-022-31530-x>
- (273) Bernt, F.; Wegner, H. A. Substituted *meta*[n]Cycloparaphenylenes: Synthesis, Photophysical Properties and Host–Guest Chemistry. *Chem. Eur. J.* **2023**, *29* (42), e202301001. <https://doi.org/10.1002/chem.202301001>
- (274) Kayahara, E.; Nakano, M.; Sun, L.; Ishida, K.; Yamago, S. Syntheses of Tetrasubstituted [10]Cycloparaphenylenes by a Pd-catalyzed Coupling Reaction. Remarkable Effect of Strain on the Oxidative Addition and Reductive Elimination. *Chem. Asian J.* **2020**, *15* (16), 2451–2455. <https://doi.org/10.1002/asia.202000711>
- (275) Jiang, H.-W.; Tanaka, T.; Mori, H.; Park, K. H.; Kim, D.; Osuka, A. Cyclic 2,12-Porphyrinylene Nanorings as a Porphyrin Analogue of Cycloparaphenylenes. *J. Am. Chem. Soc.* **2015**, *137* (6), 2219–2222. <https://doi.org/10.1021/ja513102m>
- (276) Wassy, D.; Hermann, M.; Wössner, J. S.; Frédéric, L.; Pieters, G.; Esser, B. Enantiopure Nanohoops through Racemic Resolution of Diketo[n]CPPs by Chiral Derivatization as Precursors to DBP[n]CPPs. *Chem. Sci.* **2021**, *12* (30), 10150–10158. <https://doi.org/10.1039/D1SC02718B>
- (277) Lu, D.; Wu, H.; Dai, Y.; Shi, H.; Shao, X.; Yang, S.; Yang, J.; Du, P. A Cycloparaphenylene Nanoring with Graphenic Hexabenzocoronene Sidewalls. *Chem. Commun.* **2016**, *52* (44), 7164–7167. <https://doi.org/10.1039/C6CC03002E>
- (278) Senthilkumar, K.; Kondratowicz, M.; Lis, T.; Chmielewski, P. J.; Cybińska, J.; Zafra, J. L.; Casado, J.; Vives, T.; Crassous, J.; Favereau, L.; Stępień, M. Lemniscular [16]Cycloparaphenylene: A Radially Conjugated Figure-Eight Aromatic Molecule. *J. Am. Chem. Soc.* **2019**, *141* (18), 7421–7427. <https://doi.org/10.1021/jacs.9b01797>
- (279) Kayahara, E.; Qu, R.; Kojima, M.; Iwamoto, T.; Suzuki, T.; Yamago, S. Ligand-Controlled Synthesis of [3]- and [4]Cyclo-9,9-dimethyl-2,7-fluorenes through Triangle- and Square-Shaped Platinum Intermediates. *Chem. Eur. J.* **2015**, *21* (52), 18939–18943. <https://doi.org/10.1002/chem.201504369>

- (280) Lucas, F.; Sicard, L.; Jeannin, O.; Rault-Berthelot, J.; Jacques, E.; Quinton, C.; Poriel, C. [4]Cyclo-*N*-ethyl-2,7-carbazole: Synthesis, Structural, Electronic and Charge Transport Properties. *Chem. Eur. J.* **2019**, *25* (32), 7740–7748. <https://doi.org/10.1002/chem.201901066>
- (281) Lucas, F.; Rault-Berthelot, J.; Quinton, C.; Poriel, C. Synthesis and Electronic Properties of Bridged [8]-, [12]- and [16]-cyclo-*para*-phenylenes. *J. Mater. Chem. C* **2022**, *10* (37), 14000–14009. <https://doi.org/10.1039/D2TC00881E>
- (282) Lucas, F.; Brouillac, C.; McIntosh, N.; Giannini, S.; Rault-Berthelot, J.; Lebreton, C.; Beljonne, D.; Cornil, J.; Jacques, E.; Quinton, C.; Poriel, C. Electronic and Charge Transport Properties in Bridged versus Unbridged Nanohoops: Role of the Nanohoop Size. *Chem. Eur. J.* **2023**, *29* (41), e202300934. <https://doi.org/10.1002/chem.202300934>
- (283) Brouillac, C.; Lucas, F.; Tondelier, D.; Rault-Berthelot, J.; Lebreton, C.; Jacques, E.; Quinton, C.; Poriel, C. [4]-Cyclo-2,7-Carbazole as Host Material in High-Efficiency Phosphorescent OLEDs: A New Perspective for Nanohoops in Organic Electronics. *Adv. Opt. Mater.* **2023**, *11* (3), 2202191. <https://doi.org/10.1002/adom.202202191>
- (284) Kayahara, E.; Zhai, X.; Yamago, S. Synthesis and Physical Properties of [4]cyclo-3,7-dibenzo[*b,d*]thiophene and its *S,S*-dioxide. *Can. J. Chem.* **2017**, *95* (4), 351–356. <https://doi.org/10.1139/cjc-2016-0474>
- (285) Chen, D.; Wada, Y.; Kusakabe, Y.; Sun, L.; Kayahara, E.; Suzuki, K.; Tanaka, H.; Yamago, S.; Kaji, H.; Zysman-Colman, E. A Donor–Acceptor 10-Cycloparaphenylene and Its Use as an Emitter in an Organic Light-Emitting Diode. *Org. Lett.* **2023**, *25* (6), 998–1002. <https://doi.org/10.1021/acs.orglett.3c00127>
- (286) Segawa, Y.; Šenel, P.; Matsuura, S.; Omachi, H.; Itami, K. [9]Cycloparaphenylene: Nickel-Mediated Synthesis and Crystal Structure. *Chem. Lett.* **2011**, *40* (4), 423–425. <https://doi.org/10.1246/cl.2011.423>
- (287) O'boyle, N. M.; Tenderholt, A. L.; Langner, K. M. Cclib: A Library for Package-independent Computational Chemistry Algorithms. *J. Comput. Chem.* **2008**, *29* (5), 839–845. <https://doi.org/10.1002/jcc.20823>